AGSO JOURNAL

OF AUSTRALIAN GEOLOGY & GEOPHYSICS

VOLUME 16, NUMBER 5

AGSO Journal of Australian Geology & Geophysics

Editor: Ian Hodgson, Corporate Publications, Australian Geological Survey Organisation
Editor of this number: Geoff Bladon

Information for contributors

From the end of volume 17, the *AGSO Journal of Australian Geology & Geophysics* will merge with the *Australian Journal of Earth Sciences* (*AJES*). The *AJES* is published by Blackwell Science for the Geological Society of Australia Inc. The editorial board of the *AGSO Journal of Australian Geology & Geophysics* is confident that the new combined journal, part of Blackwell's internationally recognised stable of quality scientific journals, will be well placed to keep Australian research at the leading edge of international geoscience.

As volume 17 is a series of special thematic issues, which are all fully committed, the Editor is unable to accept further unsolicited contributions. However, the Editor of the *Australian Journal of Earth Sciences* will be pleased to consider manuscripts for publication. Contributions should be sent to A.E. Cockbain, PO Box 8114, Angelo Street, South Perth, WA 6151, Australia (tel. and fax 09 367 7037; email: tcockbai@cyllene.uwa.edu.au).

AGSO JOURNAL

OF AUSTRALIAN GEOLOGY & GEOPHYSICS

VOLUME 16, NUMBER 5

ISSN 1320–1271

Copies of the AGSO Journal can be purchased from the Australian Geological Survey Organisation (GPO Box 378, Canberra ACT 2601; tel. 06 249 9642, fax 06 249 9982).

Other matters concerning the Journal should be sent to the Editor, AGSO Journal

Editor, AGSO Journal: Ian Hodgson
Editor of this number of the AGSO Journal: Geoff Bladon
Cover design, and figures inscribed with an index number (bottom right-hand corner), prepared by AGSO Spatial Information & Mapping Services Section
Prepared for publication by Lin Kay

Printed in Australia by National Capital Printing, Fyshwick, A.C.T. 2609

AUSTRALIAN GOVERNMENT PUBLISHING SERVICE CANBERRA 1997

Month of issue, May 1997

Front-cover illustration:

An irregular body and dyke of garnet-bearing leucogneiss intruding charnockite at the eastern end of Mount McCarthy, at the eastern end of the Porthos Range, northern Prince Charles Mountains, Antarctica. Both the leucogneiss and the charnockite display a well-developed lineation (L_6: Fitzsimons & Thost 1992), and are within a D_6 high-strain zone. Zircons from the leucogneiss yield a SHRIMP U–Pb age of ca 990 Ma, which Kinny et al. (this volume) interpret as an intrusive age. The figure at the base of the cliff (Ian Fitzsimons) indicates the scale. Photo by Doug Thost, AGSO, 1988.

AGSO Journal of Australian Geology & Geophysics, 16(5), 621–636

Mafic dyke swarms of the western Musgrave Block, central Australia: their geochemistry, origin, and relationships to the Giles Complex

John W. Sheraton[1] & Shen-su Sun[1]

Several petrographically and geochemically distinct suites of mafic dykes crop out in the Mesoproterozoic Musgrave Block. Intergranular dolerites (group A), as well as the voluminous Giles Complex layered mafic–ultramafic intrusions and Tollu Group basaltic volcanics, were formed by large-scale melting of heterogeneous enriched (ε_{Nd} −2.3 to −1.4) subcontinental lithospheric mantle about 1080 Ma ago, more than 100 m.y. after the 1200-Ma regional high-grade metamorphism of the Musgrave Block country rocks. The coeval Kulgera (eastern Musgrave Block) and Stuart (Arunta Block) dyke swarms are chemically and isotopically similar. Slightly younger (~1000 Ma), particularly heterogeneous olivine dolerites (group C) were also derived from a similarly enriched source. Mantle heterogeneity was apparently both lateral (as group C dolerites show significant geographical variations) and vertical (because chemically distinct dyke suites of similar age crop out in the same area).

Microgabbro dykes and sills associated with troctolitic intrusions of the Giles Complex are compositionally similar to both gabbronorite intrusions of the Giles Complex and to group A dolerite dykes therein. The least fractionated microgabbros are probably representative of an evolved magma that was parental to the major gabbroic intrusions of the Giles Complex, and underwent some degree of high-pressure pyroxene ± olivine fractionation. They cannot be directly parental to the leucotroctolite cumulates, which reflect much more extensive high-pressure fractionation before they were emplaced.

Quartz dolerites emplaced 800 Ma ago (group B) were derived by higher-pressure partial melting of a much less enriched (ε_{Nd} +2.8 to +3.8), homogeneous asthenospheric mantle source, probably related to mantle-plume activity. They are virtually identical chemically and isotopically with dykes, including the Amata (eastern Musgrave Block) and Gairdner (Gawler Craton) dyke swarms, that crop out over a distance of more than 1000 km.

Introduction

Mafic dyke swarms are common throughout the western part of the Mesoproterozoic Musgrave Block, in central Australia (Fig. 1), where they intrude high-grade metamorphic rocks, granitic rocks, and Giles Complex mafic–ultramafic intrusions. Such dykes commonly define periods of crustal extension and form useful stratigraphic markers. Dyke compositions provide information — including compositional variations with time — about their mantle source regions.

The western Musgrave Block (Fig. 2) was the focus of a major AGSO field project conducted within the framework of the National Geoscience Mapping Accord in 1987–1994. It consists of high-grade (mainly granulite-facies) metamorphic rocks of both igneous and sedimentary origin (Stewart & Glikson 1991; Glikson et al. 1995, 1996). Felsic orthogneiss is the most abundant component, whereas rocks of clearly sedimentary origin — such as metapelites, quartzites, and calc-silicates — are much less common. Metamorphosed mafic igneous rocks (mafic granulite), although widespread, are volumetrically minor. Igneous protoliths of felsic orthogneiss in the Tomkinson Ranges area were emplaced between 1550 and 1300 Ma ago. Regional high-grade metamorphism (>750°C, 0.5 ± 0.1 GPa*) accompanied by two penetrative deformational events (D_1 and D_2) occurred at about 1200 Ma (Gray 1978; Maboko et al. 1991; Sun & Sheraton 1992; Glikson et al. 1995, 1996). The metamorphic rocks are intruded by major layered mafic–ultramafic bodies of the Giles Complex, as well as a variety of granitic rocks and mafic dykes.

The post-D_2, pre-D_3 Giles Complex forms the largest exposures of deep-seated layered mafic–ultramafic intrusions in Australia (Nesbitt et al. 1970; Glikson et al. 1990; Ballhaus & Glikson 1995). It apparently was emplaced about 1080 Ma ago (Glikson et al. 1996), when the country rocks were still deep in the crust (0.6 ± 0.1 GPa for the Wingellina Hills intrusion; Ballhaus & Berry 1991). Contemporaneous mafic to felsic volcanic rocks of the Tollu Group (Bentley Supergroup), dated at 1078 ± 5 Ma (Glikson et al. 1996), were emplaced apparently in cauldron subsidence structures in granitic basement rocks to the west of the Tomkinson Ranges (Daniels 1974). The formation of open to isoclinal upright folds (D_3),

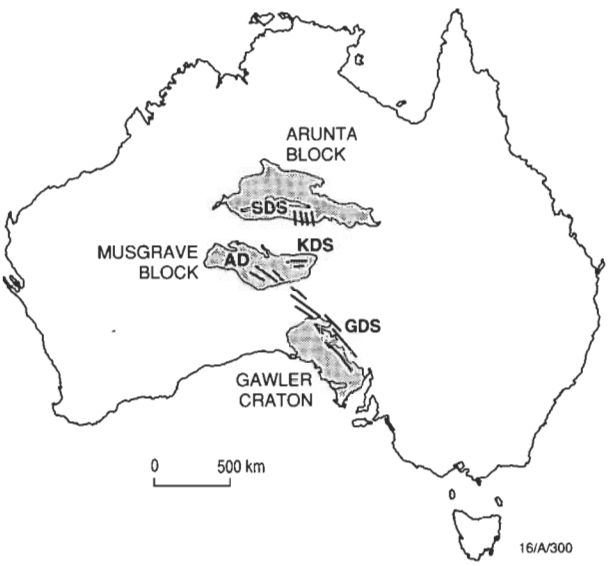

Figure 1. Location of the Mesoproterozoic Musgrave Block in relation to the Palaeoproterozoic Arunta Block and Archaean–Mesoproterozoic Gawler Craton. Also indicated are the distributions of dolerite dyke swarms: KDS, Kulgera dyke swarm; SDS, Stuart dyke swarm; AD, Amata dykes; GDS, Gairdner dyke swarm (after Zhao & McCulloch 1993a).

the emplacement of several suites of mafic dykes, and at least four episodes of mylonite/retrograde-shear-zone formation (D_{4-7}) followed the emplacement of the Giles Complex (Clarke 1992; Clarke et al. 1995a). D_3 was accompanied by extensive recrystallisation in some areas, including much of the western part of the Hinckley Range gabbronorite intrusion. Pressure–temperature estimates suggest that D_3 might have occurred at initial pressures as high as 1.1 GPa, possibly a consequence of crustal thickening associated with the emplacement of the Giles Complex, followed by decompression to 0.45 ± 1 GPa (Clarke et al. 1995a), although the geological significance of these data remain to be established. Present knowledge of the geological history of the western Musgrave Block is summarised in Table 1.

Structural and petrological criteria enabled Clarke et al. (1995a) to identify three generations of post-Giles Complex

* 0.1 GPa = 1 kb.

[1] Minerals Division, Australian Geological Survey Organisation, GPO Box 378, Canberra, ACT 2601

mafic dykes (types A, B, and C) in the Mount Aloysius and Champ de Mars areas of the western Musgrave Block (Fig. 2). The oldest (type A) apparently postdates the Hinckley Range gabbronorite of the Giles Complex and associated granitoids, but was deformed by D_3. Types B and C dolerites postdate D_3. Although chemical data support these groupings, several other chemically distinct types of mafic dyke are also present. Thus, Nesbitt et al. (1970) were able to distinguish four post-Giles Complex suites of dolerite dykes (A–D) in the eastern Tomkinson Ranges.

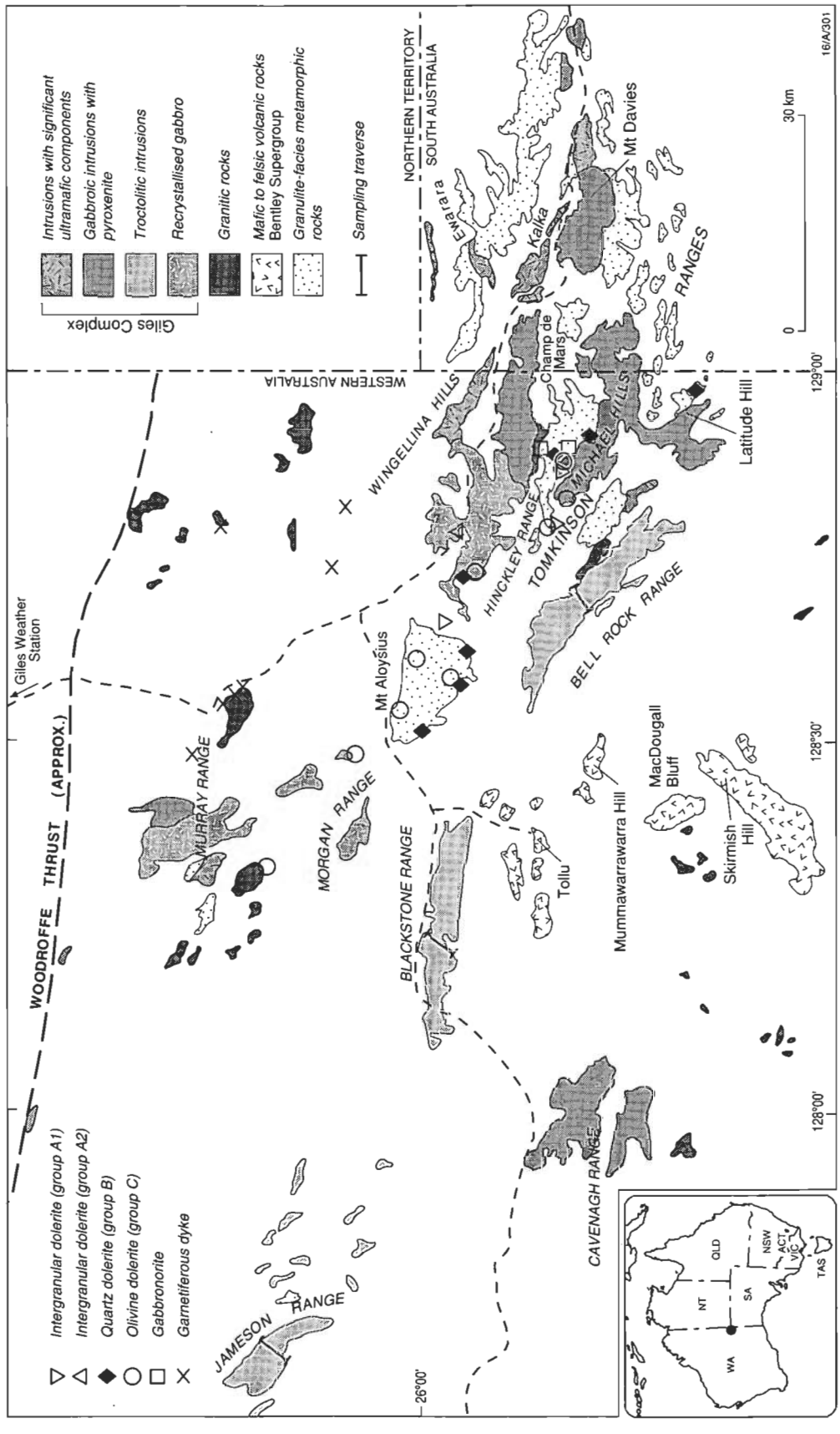

Figure 2. Geological sketch map of the western Musgrave Block, showing the main Giles Complex intrusions and the locations and groupings of analysed mafic dykes (based on Glikson et al. 1995).

Table 1. Simplified geological history of the western Musgrave Block (modified from Glikson et al. 1995; and based on age data in Glikson et al. 1996 and Clarke et al. 1995b).

		Approx. age (Ma)
1.	Emplacement of granitic rocks (protoliths of felsic orthogneiss); deposition of sediments	1300–1550
2.	Granulite-facies metamorphism (>750°C, 0.5 ± 0.1 GPa) emplacement of orthopyroxene granites; regional penetrative deformation (D_1 and D_2)	1200
3.	Emplacement of granitic and syenitic rocks	1190
4.	*Emplacement of Giles Complex mafic–ultramafic bodies and associated granitic rocks (at ~6 GPa), group A intergranular dolerite dykes, gabbronorite dykes, and Tollu Group mafic to felsic volcanic rocks*	1080
5.	Formation of upright, open to isoclinal folds (D_3), and extensive recrystallisation in some areas (650–700°C, up to 1.1 GPa, reducing to 0.45 ± 0.1 GPa)	
6.	*Emplacement of group C olivine dolerite dykes*	~1000
7.	*Emplacement of group B quartz dolerite dykes*	820
8.	Formation of ultramylonite zones (D_4, D_5) under greenschist to amphibolite-facies conditions	
9.	Formation of major E–W ultramylonite/pseudotachylite zones (including the Woodroffe Thrust; D_6), and localised high-pressure recrystallisation (750°C, 1.4 ± 0.1 GPa), during the Petermann Ranges Orogeny	~550
10.	Formation of retrograde shear zones (D_7)	

Dolerite dykes in the central and eastern Musgrave Block have given two distinct Sm–Nd mineral isochron ages: 1090 ± 32 Ma for the Kulgera (also known as the Alcurra) dyke swarm (similar to the age of the Stuart dyke swarm in the Arunta Block, 1076 ± 33 Ma), and 790 ± 40 and 797 ± 49 Ma for dykes at Amata (similar to the age of the Gairdner dyke swarm in the Gawler Craton, 867 ± 47 and 802 ± 35 Ma; Zhao & McCulloch 1993a; Fig. 1).

This paper describes the geochemistry and origin of mafic dykes in the western Tomkinson Ranges, and discusses possible correlations with the Giles Complex and Mummawarrawarra Basalt (part of the Tollu Group), as well as with dyke swarms elsewhere in central Australia. Even though the dykes of type B have been shown to be younger than those of type C, the A to C terminology of Clarke et al. (1995a) has been retained, because it has already been used in a number of papers (e.g., Glikson et al. 1995). The geographical distribution of the various dyke groups is shown in Figure 2.

Field relations and petrography

Intergranular dolerite dykes (group A)

These dykes appear to be equivalent, at least in part, to type A of Clarke et al. (1995a), although two chemically distinct subgroups (A1 and A2) have been recognised. They are commonly foliated along the margins, and have various orientations, but group A1 dykes in the Champ de Mars area are mostly northwest-trending. In the western Champ de Mars, a group A dyke is cut by a group C dolerite.

Group A1 dykes, which crop out in the Champ de Mars area and at Mount Aloysius, have intergranular textures, commonly with zoned plagioclase phenocrysts, and are thus texturally distinct from the younger dolerites. Apart from recrystallisation along the contacts, the textures are primary igneous, rather than metamorphic (i.e., granoblastic). Two aphyric dykes have essentially similar granular textures which may also be of igneous origin, although recrystallisation during deformation cannot be discounted. Intergranular dolerites contain clinopyroxene and orthopyroxene (about 20% each), plagioclase (andesine–labradorite: 55–60%), Fe–Ti oxides (1–5%), and apparently primary reddish brown biotite (up to 4%). One group A1 dyke has given an Sm–Nd mineral–whole-rock isochron age of about 1100 Ma (Glikson et al. 1996). These dykes thus presumably crystallised at considerable crustal depths during the waning stages of high-grade metamorphism and deformation, at about the same time as the Giles Complex was emplaced (?pre- to syn-D_3).

Intergranular dolerite dykes (group A2) cutting the northern part of the Hinckley Range gabbronorite intrusion are petrographically similar to group A1, but generally have more plagioclase (~65%), less clinopyroxene (~10%), and little or no biotite. Most of these dykes contain plagioclase phenocrysts. They cross-cut igneous layering in the gabbronorite (Clarke et al. 1995a), but chemical data suggest they are genetically related to this intrusion; thus, they might be only slightly younger than it (see below).

Olivine dolerite dykes (group C)

Olivine dolerites are mostly northeast- (rarely northwest-) trending, and mostly thinner (1–2 m) and finer-grained than those of group B. Their textures range from subophitic to porphyritic, and they contain olivine and plagioclase phenocrysts. Coarser-grained dykes contain plagioclase (50–60%), clinopyroxene (20–35%), olivine (5–12%), opaque minerals (Fe–Ti oxides + pyrite: 4–6%), and biotite (up to 4%). Olivine is commonly partly serpentinised, and, in some dykes, clinopyroxene is partly altered. A group C dyke from the western Hinckley Range has given an Sm–Nd mineral–whole-rock isochron age of about 1000 Ma (Glikson et al. 1996); although this is not statistically significantly younger than the group A dolerites, field and petrographic evidence suggest that the group C dykes are younger (i.e., post-D_3). These dykes may be equivalent to the type D olivine dolerites of Nesbitt et al. (1970).

Quartz dolerite dykes (group B)

These are northwest-trending, post-D_3, pre-D_{4-7} dykes, commonly 3–5 (but up to 30) m thick. They have typical medium-grained subophitic textures, although some are rather altered and cut by thin mylonite zones. Plagioclase (labradorite: 55–60%), clinopyroxene (35–40%), Fe–Ti oxides (2–4%), and

quartz (up to 2%) are the main constituents, but minor biotite and hornblende are commonly present; in some dykes, clinopyroxene is largely uralitised. These dykes have been dated at 824 ± 4 Ma (U–Pb zircon age: Glikson et al. 1996), similar to the age of the Amata dykes (Zhao & McCulloch 1993a).

Other mafic dykes in the Hinckley Range area

A 130-m-thick northeast-trending gabbronorite dyke in western Champ de Mars has a gabbroic to subophitic texture and consists of labradorite (60–75%), orthopyroxene (15–24%), clinopyroxene (8–14%), opaque minerals (2%), and minor biotite and apatite. It is cut by a group B dolerite, and has given a U–Pb zircon age of 1058 ± 14 Ma (Glikson et al. 1996). A petrographically similar gabbronorite dyke occurs near the contact of the Hinckley Range gabbronorite.

Mafic dykes north of the western Tomkinson Ranges contain high-pressure garnet-bearing assemblages, apparently formed during Cambrian metamorphism and deformation (D_6) associated with the development of the Woodroffe Thrust (Clarke et al. 1995a; Stewart 1995). These generally undeformed dykes contain centimetre-scale garnet-rich aggregates in a fine-grained granoblastic matrix of hornblende, clinopyroxene, plagioclase, and Fe–Ti oxides, so they are difficult to correlate petrographically with the unmetamorphosed dykes. However, chemical data show that most of the recognised groups (including the 800-Ma group B) are represented (see below).

Mummawarrawarra Basalt and associated dykes

The Mummawarrawarra Basalt (Tollu Group) in the Mummawarrawarra Hill–MacDougall Bluff area includes a variety of fine-grained amygdaloidal basalts and basaltic andesites with textures ranging from hypocrystalline to subophitic. Plagioclase is commonly sericitised or saussuritised, and mafic minerals are replaced by chlorite, epidote, and/or amphibole; relict clinopyroxene is rare. Vesicles contain mixtures of quartz, chlorite, epidote, and zeolites.

Dykes of basalt and basaltic andesite which intrude Tollu Group felsic volcanics near Tollu are fine- to medium-grained, and contain abundant amphibole and minor quartz. Petrographically varied dykes in the granitic basement underlying the Tollu Group at MacDougall Bluff include subtrachytic, moderately quartz-rich basaltic andesite and orthopyroxene-bearing subophitic dolerite. Most of these dykes are east–west-trending.

Sills and dykes associated with the Giles Complex intrusions

The Bell Rock troctolite intrusion contains olivine microgabbro sills and dykes, of which some are clearly intrusive into the cumulates; others, however, appear to be gradational, and apparently were emplaced before the host rocks had completely crystallised (Glikson et al. 1995). The microgabbros are commonly fine- to medium-grained, and their mineralogy is similar to that of the host cumulates (Ballhaus 1992; Ballhaus & Glikson 1995). Their textures range from cumulus to subophitic or gabbroic, and some have chilled margins. Most are olivine + plagioclase-phyric, and contain interstitial clinopyroxene, Fe–Ti oxides, and, in some rocks, biotite. Ballhaus & Glikson (1995) suggested that such bodies might represent high-pressure fractionated melts similar to those which were parental to the exposed Giles Complex intrusions.

A few similar sills and dykes also occur in the Jameson Range and Blackstone Range troctolites, although only one was sampled from each of the sampling traverses across these bodies. A 25-cm dyke from Jameson Range contains plagioclase and altered ?olivine phenocrysts, whereas a plagioclase-phyric sill from Blackstone Range is olivine-free.

Some of the analysed gabbroic rocks from the western part of the Hinckley Range gabbronorite may also be sills or dykes, but their field relations are unclear, as this part of the intrusion has been extensively recrystallised to mafic granulite. Such rocks range from fresh subophitic olivine dolerite (or microgabbro) to plagioclase-phyric intergranular two-pyroxene dolerite, texturally similar to group A dykes, and show various degrees of recrystallisation to granoblastic textures. The more intensely recrystallised rocks contain abundant brownish green hornblende and lesser amounts of biotite. Similar conformable layers, sills, and dykes of microgabbro were interpreted by Ballhaus (1992) and Ballhaus & Glikson (1995) as chilled variants of the layered cumulus sequences. One recrystallised sample has given a U–Pb zircon age of about 1070 Ma (Glikson et al. 1996), consistent with this interpretation.

Geochemistry

Fifty-nine samples of mafic dykes and nine of Mummawarrawarra Basalt were analysed for major and trace elements. FeO was determined volumetrically, Li by atomic absorption spectrophotometry, and the remaining elements by X-ray fluorescence spectrometry (XRF) according to the methods of Norrish & Hutton (1969) and Norrish & Chappell (1977). Further details of methods and accuracy are presented by Cruikshank & Pyke (1993). Representative analyses are presented in Table 2, and a complete list is available from the first author.

Intergranular dolerites (group A)

Group A1 dolerites are moderately evolved [*mg*, or atomic 100Mg/(Mg + 0.85total Fe) = 56–63] Ol or slightly Q-normative tholeiites. They have LILE (large-ion lithophile elements: K, Rb, Ba, Pb, Th, and U) and LREE (light rare-earth elements) markedly enriched relative to HFSE (high-field-strength elements: P, Nb, Zr, Ti, etc.), so that their LILE/Zr and Ce/Zr ratios are much higher than estimated for the primordial mantle (Fig. 3); in contrast, their P/Zr and Ti/Zr are significantly lower. Their S contents are quite high (700–1120 ppm: Fig. 4). Spidergrams of group A1 dolerites show quite fractionated patterns, large negative Nb anomalies, and, for some, small negative Sr anomalies, suggesting some degree of plagioclase fractionation (Fig. 5).

Sheraton et al. (1990) considered that the high LILE contents and Sr- and Nd-isotopic compositions of many continental tholeiites are better explained by derivation from enriched mantle source regions rather than direct crustal assimilation, although some degree of contamination is quite possible. Ratios of many incompatible elements (LILE, LREE, and some HFSE) are commonly more or less constant (as shown by pairs of elements defining lines of unit slope on logarithmic plots like Fig. 3), and are therefore considered to approximate those of the mantle source. On this basis, the type A1 dolerites were apparently derived from strongly enriched mantle, consistent with moderately low ε_{Nd} (–2.2 for one sample: Glikson et al. 1996).

Group A2 dolerites from the northern Hinckley Range are slightly more evolved (*mg* 49–59) and more strongly Q-normative than group A1, and have higher Sr, K/Rb, Ti/Zr, and P/Zr, and lower Sc and Rb/Zr (Fig. 3). Their spidergrams are characterised by the presence of marked positive Sr anomalies (Fig. 5), suggesting some degree of plagioclase accumulation. Their unusually high P/Zr is unlikely to be due to cumulus processes, because their P_2O_5 contents are much lower than those required to saturate a mafic melt (Watson 1979). Hence, these dolerites might have been derived from an apatite-rich mantle source, such as that postulated to be present beneath southeastern Australia (Menzies & Wass 1983). Group A2 dykes cannot have been comagmatic with those of group A1, and were presumably derived from a distinct but similarly enriched mantle source region.

Olivine dolerites (group C)

Most group C dolerites are moderately primitive, having high *mg* (58–74), Cr (373–793 ppm), and Ni (202–329 ppm), apart from two samples which are more evolved (*mg* 46 and 48); they also have high S (690–1670 ppm), reflecting the presence of late pyrite. Group C dykes are strongly Ol-normative tholeiitic or, rarely, transitional dolerites with trace-element characteristics broadly similar to group A1 dykes, but quite different from group B (Figs. 3–5). Their LILE/Zr and Ce/Zr are higher, whereas their Ti/Zr, Nb/Zr, and P/Zr are mostly lower, than primordial mantle.

Four group C dykes from the Champ de Mars area and western Hinckley Range are characterised by low Ti/Zr, K/Zr, Zn/Zr, and, in particular, Nb/Zr, compared with those from Mount Aloysius. Moreover, in the two most evolved (low-*mg*) group C dykes, P/Zr is high, and Sr shows much more variation than in the other dyke groups. Group C dykes thus form a chemically quite heterogeneous suite, implying derivation from a hetrogeneous mantle source, and they could be of more than one age. Although their mantle source was generally similar to that of group A1 dykes, their similar incompatible-element abundances, coupled with more primitive SiO_2-undersaturated compositions, indicate lower degrees of melting at higher pressures (Green 1973). The two most evolved (low *mg*) dykes have normative Ol contents similar to the other group C dykes, suggesting even lower degrees of melting.

Whereas group C dykes share some geochemical similarities with olivine tholeiites of the Kulgera and Stuart dyke swarms (Zhao & McCulloch 1993b), they also show geochemical contrasts with them; for example, most group C dykes have higher P_2O_5 and Zr, and lower Nb/Zr (Figs. 3 and 5). However, these differences are not surprising in view of the marked heterogeneity within group C in the small area of the western Tomkinson Ranges, and their possible differences in age. Nevertheless, group C dykes were apparently derived from a generally similarly enriched heterogeneous mantle source to that of the Kulgera and Stuart dykes, whose ε_{Nd} of –3.0 to +1.9 and –9.9 to –5.1 respectively (Zhao & McCulloch 1993b) compares with +1.9 for a single (low-K/Zr) group C dyke (Glikson et al. 1996). A trend of decreasing Nb/Zr with decreasing Nb in the group C dykes (Fig. 3) might be real or, instead, an artefact of the imprecise Nb XRF analyses near the detection limit (2 ppm), but it does appear to be supported by spark-source mass-spectrometry data for the Kulgera and Stuart dykes (Zhao 1992).

Quartz dolerites (group B)

Group B dolerites are slightly Q-normative tholeiites with *mg* 51–61, but are chemically distinct from any of the groups A or C dyke suites. In particular, they have lower S contents (50–370 ppm) and LILE/Zr ratios, and higher Cu. Apart from slightly lower P/Zr, their incompatible-element/Zr ratios are similar to those estimated for primordial mantle (Sun & McDonough 1989; Fig. 3). Their spidergrams are moderately flat, and have small Nb anomalies (Fig. 5). These dykes were therefore derived from a much less enriched mantle source, consistent with their high ε_{Nd} values (+2.8 to +3.8; Glikson et al. 1996).

Group B dolerites are chemically and isotopically virtually identical with the coeval Amata and Gairdner dykes (Zhao et al. 1994). This is evident from their similar incompatible-element ratios (Fig. 3) and spidergrams (Fig. 5). Even some of the small differences may be more apparent than real, because much of the scatter for elements such as Nb, La, and Ce in group B dykes probably reflects analytical uncertainties near the XRF detection limits. In contrast, the trace-element data for the Amata dykes were obtained by the more precise ICP–MS method. ε_{Nd} values for the Amata and Gairdner dykes are +2.4 to +4.3 and +2.6 to +4.1 respectively (Zhao et al. 1994). There is thus little doubt that group B dolerites, together with the Amata dykes, represent the northwestern extension into the Musgrave Block of the Gairdner dyke swarm in the Gawler Craton and adjacent Stuart Shelf, a correlation supported by their similar northwesterly trends.

Other mafic dykes in the Hinckley Range area

The thick gabbronorite dyke at western Champ de Mars is a slightly Q-normative tholeiite which does not appear to be related to any of the main dyke groups, from which it can be distinguished by — for example — different S/Zr, Pb/Zr, and K/Zr ratios. Nevertheless, like groups A and C dykes, this dyke was probably derived by melting of moderately enriched mantle with high LILE/Zr and Ce/Zr (Fig. 6) and low ε_{Nd} (–2.3; Glikson et al. 1996). Spidergrams of it are not unlike those of groups A1 and C (cf. Figs. 5 and 8), but its S content is much lower (190–290 ppm; Figs. 4 and 7). Two samples from the centre of this dyke are relatively fractionated compared with the margin; they have lower *mg* (49–51 compared with 61), FeO, MnO, MgO, Sc, V, Cr, Ni, and Zn, and higher Na_2O, K_2O, Ba, Sr, Pb, La, and Ce, but other elements are similar. Most incompatible-element ratios are more-or-less uniform throughout the dyke, except for P/Zr, which is slightly higher in samples from the centre. The degrees of SiO_2 saturation of these two samples are much the same as those of the marginal samples, suggesting that pyroxene — possibly with some plagioclase, but not olivine — dominated fractionation.

The other gabbronorite dyke — near the contact of the Hinckley Range intrusion — is Ol-normative (*mg* 57), and has higher Ti/Zr, P/Zr, and Rb/Zr. Hence, although broadly similar in composition, it cannot be directly related to the western Champ de Mars gabbronorite dyke.

The garnetiferous ('eclogitic') dykes, affected by Cambrian metamorphism, are compositionally varied. Some are virtually identical in composition with group B, indicating that even high-grade metamorphism inducing the development of quite different mineral assemblages does not necessarily result in significant chemical changes. Sheraton (1984) showed that deformation is an important factor in determining such changes, although the formation of high-pressure garnet-bearing assemblages commonly results in LILE depletion. Other garnetiferous dykes are compositionally similar to the gabbronorites. Yet others are more akin to group C olivine dolerites, from which they generally differ — however — in having much lower K/Zr, Rb/Zr, Pb/Zr, and Ce/Zr and higher Ba/Zr; unless these differences can be ascribed to metamorphism, these otherwise similar garnetiferous dykes may not be related to the group C dykes to the south. One such dyke has ε_{Nd} (at 1000 Ma) of +4.7, appreciably higher than that (+1.9) of the only isotopically analysed group C dolerite (Glikson et al. 1996).

Mummawarrawarra Basalt and associated dykes

Most Mummawarrawarra Basalt samples are strongly Q-normative tholeiites, ranging from basalt, through basaltic andesite, to andesite on the alkali–SiO_2 classification of Le Maitre (1989). They tend to be quite fractionated (*mg* 45–59), and their spidergrams have large negative Nb, Sr, P, and Ti anomalies (Fig. 5). Their LILE contents, in particular, show much greater variation than those of the samples in each of the dolerite dyke groups; this variation is probably due to alteration processes, and to the highly amygdaloidal nature of the volcanics. Nevertheless, their consistently high LILE/Zr ratios (Fig. 3) and low ε_{Nd} (–1.4) imply that the Mummawarrawarra Basalt was derived from an enriched mantle source, generally similar to those of groups A1 and C and the gabbronorite dykes. However, their S contents (20–120 ppm) are much lower than those of groups A1 and C, and significantly lower than the gabbronorite dykes (Figs. 4 and 7).

Table 2. Chemical analyses of representative mafic dykes and other mafic igneous rocks of the western Musgrave Block.

Sample no.	*91988086*	*91989151A*	*91988025*	*91988097*	*90984054*	*90984068*	*91989396*	*91989384*
Locality	*W Champ de Mars*	*N Hinckley Range*	*W Hinckley Range*	*W Champ de Mars*	*W Champ de Mars*	*W Champ de Mars*	*MacDougall Bluff*	*Tollu camp*
Lithology	*Intergran. dolerite*	*Intergran. dolerite*	*Dolerite*	*Quartz dolerite*	*Olivine dolerite*	*Olivine dolerite*	*Basaltic andesite*	*Basaltic andesite*
Group	*A1*	*A2*	*B*	*B*	*C*	*C*		
SiO_2	49.35	51.91	49.13	50.55	48.59	47.24	53.92	53.45
TiO_2	0.85	1.39	1.56	1.91	1.22	1.35	1.74	2.32
Al_2O_3	14.83	15.77	14.12	13.24	16.14	14.50	14.64	13.39
Fe_2O_3	4.32	1.78	2.07	1.77	3.14	4.18	4.16	3.09
FeO	6.88	8.48	10.25	11.47	7.03	7.35	7.71	9.43
MnO	0.16	0.13	0.17	0.18	0.16	0.16	0.18	0.15
MgO	8.53	6.72	7.58	6.50	9.02	10.90	3.05	3.25
CaO	11.04	8.41	11.43	10.55	10.22	9.93	6.78	5.93
Na_2O	2.34	3.24	2.17	2.23	2.48	2.17	1.72	3.65
K_2O	0.56	0.51	0.26	0.33	0.72	0.76	0.94	1.54
P_2O_5	0.11	0.23	0.13	0.15	0.23	0.18	0.12	0.39
LOI	0.77	0.67	0.73	1.24	0.69	0.88	4.16	2.58
Rest	0.32	0.36	0.24	0.25	0.39	0.43	0.28	0.29
Total	100.06	99.60	99.84	100.37	100.03	100.03	99.40	99.46
O=F,S,Cl	0.04	0.05	0.01	0.02	0.05	0.06	0.02	0.00
Total	**100.02**	**99.55**	**99.83**	**100.35**	**99.98**	**99.97**	**99.38**	**99.46**
	CIPW norms							
Q	–	1.01	–	2.93	–	–	16.05	6.02
Or	3.31	3.01	1.54	1.95	4.25	4.49	5.55	9.10
Ab	19.80	27.42	18.36	18.87	20.99	18.36	14.55	30.89
An	28.31	26.98	28.02	25.14	30.78	27.58	29.45	15.60
Di	21.02	10.84	22.85	21.67	14.95	16.61	2.87	9.49
Hy	12.73	23.67	19.95	21.21	9.63	6.86	19.90	17.12
Ol	9.05	–	1.94	–	12.94	18.88	–	–
Mt	2.60	2.44	2.93	3.16	2.38	2.69	2.77	2.95
Il	1.61	2.64	2.96	3.63	2.32	2.56	3.30	4.41
Ap	0.26	0.54	0.31	0.36	0.54	0.43	0.28	0.92
	Trace elements in parts per million							
Ba	264	239	48	41	344	279	708	483
Li	10	5	10	10	6	9	29	4
Rb	15	5	9	11	19	14	38	88
Sr	160	459	176	189	226	346	267	211
Pb	4	<2	3	<2	7	4	13	8
Th	2	<2	<2	<2	<2	<2	2	14
U	<0.5	<0.5	0.5	<0.5	1.0	<0.5	<0.5	1.5
Zr	86	83	96	125	150	106	132	416
Hf	3	<2	3	<2	4	3	4	9
Nb	2	2	5	6	4	6	5	29
Y	23	20	26	32	30	19	41	65
La	9	11	9	17	20	12	21	40
Ce	26	19	18	29	33	31	22	78
Nd	10	15	12	20	18	9	12	42
Sc	38	24	38	42	39	33	31	26
V	299	228	377	393	223	277	257	247
Cr	384	389	203	176	526	606	21	59
Ni	205	197	135	99	234	329	32	41
Cu	33	112	179	249	86	77	38	193
Zn	80	92	94	115	83	93	120	144
Ga	16	19	19	20	16	18	19	23
As	1.5	1.5	<0.5	1.5	<0.5	<0.5	1.0	2.0
S	850	1010	270	310	1060	1180	430	10
mg	62.4	58.3	56.8	51.1	65.7	67.3	35.8	35.8
K/Rb	310	847	240	249	315	451	205	145
K/Ba	17.6	17.7	45	67	17.4	23	11.0	26
K/Zr	54	51	22	22	40	60	59	31
Ti/Nb	2500	4200	1900	1900	1800	1300	2100	480
Ti/Zr	59	100	97	92	49	76	79	33
P/Zr	5.6	12.1	5.9	5.2	6.7	7.4	4.0	4.1
(Ce/Y)n	2.8	2.4	1.7	2.3	2.8	4.1	1.3	3.0
Sr/Sr*	0.70	2.03	0.89	0.59	0.69	1.39	1.21	0.27
Nb/Nb*	0.17	0.17	0.63	0.47	0.21	0.38	0.22	0.72

mg, atomic 100Mg/Mg + 0.85 total Fe); LOI, loss on ignition.
(Ce/Y)n, 2.5Ce/Y; Sr/Sr*, Sr/(5.77Ce + 7.74Nd); Nb/Nb*, Nb/(12.82K_2O + 0.507La); i.e., all primordial-mantle-normalised.

Table 2 (cont.).

Sample no.	*90980007B*	*90980008*	*91988093*	*91988094*	*88982029*	*88982034*	*91988052*	*91980111*
Locality	*Mummawar-rawarra H.*	*Mummawar-rawarra H.*	*W Champ de Mars*	*W Champ de Mars*	*SE Bell Rock Ra.*	*SE Bell Rock Ra.*	*W Hinckley Range*	*N Hinckley Range*
Lithology	*Amygdal. andesite*	*Basaltic andesite*	*Gabbronor-ite margin*	*Gabbronor-ite centre*	*Microgabb-ro sill*	*Microgabb-ro sill*	*Microgabb-ronorite*	*Microgabb-ronorite*
Group	*Tollu Gp*	*Tollu Gp*			*?Giles*	*?Giles*	*?Giles*	*Giles*
SiO_2	57.90	54.13	51.32	50.77	48.30	46.78	48.03	50.20
TiO_2	0.76	1.27	0.64	0.75	0.73	0.87	1.21	1.62
Al_2O_3	15.04	14.15	16.78	21.03	15.57	18.75	16.34	15.48
Fe_2O_3	3.13	3.23	1.78	1.53	1.87	1.69	2.45	2.99
FeO	4.11	7.84	8.00	7.09	8.86	9.30	8.69	8.95
MnO	0.11	0.15	0.15	0.11	0.16	0.13	0.16	0.17
MgO	3.45	4.22	7.13	3.92	9.49	8.47	8.47	6.11
CaO	7.64	7.89	10.79	10.75	11.72	9.83	10.72	8.63
Na_2O	2.33	2.42	2.35	2.80	1.95	2.51	2.25	2.92
K_2O	3.00	2.00	0.54	0.72	0.21	0.38	0.45	1.36
P_2O_5	0.17	0.23	0.07	0.11	0.06	0.12	0.14	0.21
LOI	2.13	1.99	0.86	0.48	0.69	0.86	0.88	0.68
Rest	0.27	0.30	0.20	0.19	0.32	0.18	0.32	0.29
Total	100.04	99.82	100.61	100.25	99.93	99.87	100.11	99.61
O=F,S,Cl	0.00	0.01	0.01	0.01	0.03	0.01	0.05	0.03
Total	**100.04**	**99.81**	**100.60**	**100.24**	**99.90**	**99.86**	**100.06**	**99.58**
	CIPW norms							
Q	11.08	7.13	0.37	0.29	–	–	–	–
Or	17.73	11.82	3.19	4.25	1.24	2.25	2.66	8.04
Ab	19.72	20.48	19.89	23.69	16.50	21.24	19.04	24.71
An	21.72	21.84	33.64	42.69	33.11	38.77	33.16	25.11
Di	12.48	13.18	15.91	8.24	20.05	7.52	15.59	13.48
Hy	11.20	17.40	22.82	16.67	13.23	5.36	12.02	15.44
Ol	–	–	–	–	10.65	19.15	11.11	5.37
Mt	1.67	2.60	2.32	2.05	2.55	2.62	2.63	2.81
Il	1.44	2.41	1.22	1.42	1.39	1.65	2.30	3.08
Ap	0.40	0.54	0.17	0.26	0.14	0.28	0.33	0.50
	Trace elements in parts per million							
Ba	938	756	214	306	75	96	188	563
Li	5	2	9	8	3	6	9	5
Rb	58	60	12	12	2	9	9	44
Sr	239	215	181	272	132	278	229	276
Pb	20	18	4	6	<2	<2	3	9
Th	8	8	3	<2	<2	<2	<2	<2
U	<0.5	1.0	1.0	<0.5	<0.5	1.0	<0.5	<0.5
Zr	177	286	49	62	38	60	73	122
Hf	5	6	<2	<2	<2	<2	<2	4
Nb	6	9	3	<2	2	6	4	4
Y	29	45	17	19	21	14	24	34
La	22	34	9	11	3	7	10	13
Ce	47	75	17	23	9	15	16	28
Nd	20	34	13	13	6	7	5	14
Sc	25	32	33	25	43	20	41	30
V	173	268	232	172	262	134	296	265
Cr	128	15	189	54	705	63	193	131
Ni	62	85	140	81	220	243	236	123
Cu	49	134	98	69	148	41	140	48
Zn	71	123	72	71	81	86	88	103
Ga	16	19	17	19	17	23	18	20
As	<0.5	1.5	<0.5	<0.5	<0.5	<0.5	1.0	<0.5
S	70	120	190	270	700	300	1020	520
mg	51.1	45.2	60.9	49.3	65.4	62.1	62.0	52.4
K/Rb	429	277	374	498	872	350	415	257
K/Ba	27	22	21	19.5	23	33	19.9	20
K/Zr	141	58	91	96	46	53	51	93
Ti/Nb	760	850	1300	>2300	2200	870	1800	2500
Ti/Zr	26	27	78	73	115	87	99	80
P/Zr	4.2	3.5	6.2	7.7	6.9	8.7	8.4	7.5
(Ce/Y)n	4.1	4.2	2.5	3.0	1.1	2.7	1.7	2.1
Sr/Sr*	0.56	0.31	0.91	1.17	1.34	1.98	1.75	1.02
Nb/Nb*	0.12	0.21	0.26	<0.14	0.47	0.71	0.37	0.17

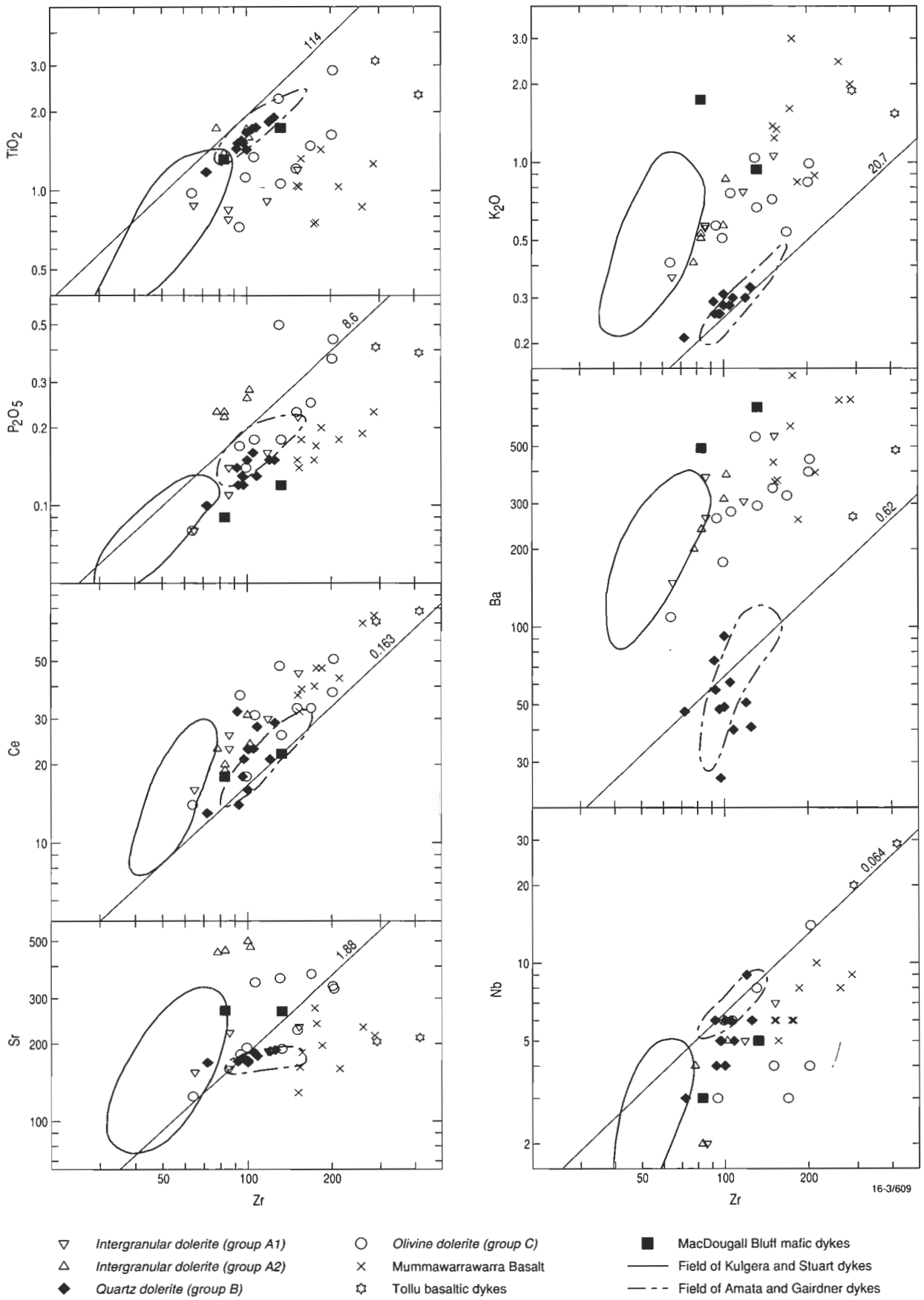

Figure 3. Logarithmic plots of various incompatible elements against Zr for dolerite dykes and the Mummawarrawarra Basalt. The fields of Kulgera + Stuart and Amata + Gairdner dykes are based on data in Zhao (1992), Zhao et al. (1994), and the AGSO 'ROCKCHEM' database. The lines of unit slope have constant element/Zr ratio, and estimated primordial mantle ratios (after Sun & McDonough 1989) are indicated. Such lines are also those for which the bulk mineral–melt distribution coefficient (K_d) is zero. The K_d value can be estimated from the expression K_d = 1 – slope (Allègre et al. 1977); for some elements, it is much higher than zero (e.g., ~0.7–1.0 for Sr in many dyke groups, in which it reflects plagioclase fractionation).

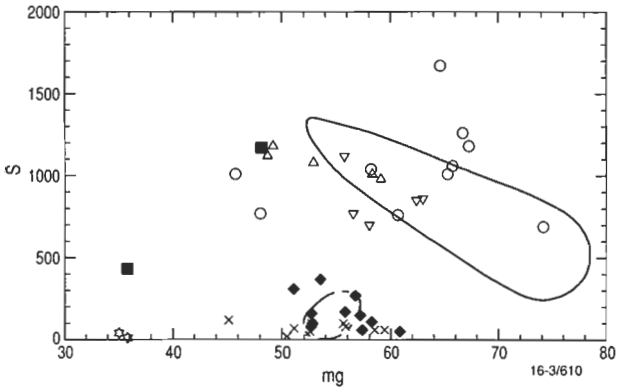

Figure 4. Plot of S against *mg* for dolerite dykes and the Mummawarrawarra Basalt. Symbols as in Figure 3.

Basaltic and basaltic andesite (quartz tholeiite) dykes which intrude Tollu Group felsic volcanics near Tollu have compositions that are generally similar to the Mummawarrawarra Basalt. However, as they are more strongly fractionated (*mg* 35–36) than the mafic volcanics, they are unlikely to be direct feeders for them. Moreover, they have higher Nb/Zr and lower Ba/Zr, K/Rb, and S (10–40 ppm; Figs. 3 and 4). Their spidergrams show marked negative Sr anomalies, consistent with plagioclase fractionation, but they have smaller Nb, P, and Ti anomalies than the Mummawarrawarra Basalt (Fig. 5). These dykes thus appear to have been derived from a mantle source similar to that of the basalts, but may not be directly related to them.

Mafic dykes in granitic basement at MacDougall Bluff are also highly evolved quartz tholeiites (*mg* 36–48). However, their LREE and HFSE contents are lower, and LILE are similar or even higher, than those in the Tollu dykes, so that their LILE/Zr ratios are much higher (Figs. 3 and 5); their S contents (430–1170 ppm) are also much higher (Fig. 4). Hence, although derived from enriched mantle, the MacDougall Bluff dykes do not appear to be closely related to either the Tollu dykes or Mummawarrawarra Basalt or, indeed, to any of the dyke suites in the western Hinckley Range area.

Clarke et al. (1995a) suggested that type A dolerites represent feeders to the mafic volcanics of the Bentley Supergroup (e.g., Mummawarrawarra Basalt). The much more fractionated compositions of the volcanics make direct correlations uncertain, but both were derived from very similar mantle source regions, so a genetic relationship — if not a strictly comagmatic origin — is quite plausible.

Sills and dykes associated with the Giles Complex intrusions

Microgabbro sills and dykes in the Bell Rock troctolite intrusion are mostly strongly Ol-normative tholeiites (*mg* 57–66), although olivine mg (Mg/[Mg + Fe]) values (Ballhaus 1992) suggest that at least some contain cumulus olivine. Like the previously described dyke suites (apart from group B), they are characterised by high LILE/Zr and Ce/Zr, but have HFSE/Zr similar to (not lower than) primordial mantle (Fig. 6). Their S contents (mostly 700–1000 ppm; Fig. 7) and K/Rb ratios (350–1100) also tend to be high. These compositional features are broadly similar to those of the leucotroctolites and gabbronorites with the least-developed cumulus features in the host intrusions (Fig. 6). Their spidergrams show prominent positive Sr anomalies, consistent with plagioclase accumulation, whereas the host rocks show much stronger cumulus characteristics, namely marked Sr (plagioclase) and Ti (titanomagnetite) enrichment relative to other incompatible elements (Fig. 8). In terms of source characteristics, they show a marked similarity to group A2 dykes, although these are more fractionated (Q-normative, *mg* 49–59) and have slightly higher P/Zr. However, group A2 dykes also show positive Sr anomalies, indicative of plagioclase accumulation (Fig. 5).

The Blackstone Range sill and Jameson Range dyke are both Ol-normative tholeiites, but are more evolved than the Bell Rock sills and dykes in terms of their high incompatible-element contents, low *mg* (46–48), and negative Sr anomalies. These characteristics might reflect lower degrees of melting of mantle sources similar to or, for the Jameson Range dyke, somewhat less LILE-enriched than that of the Bell Rock microgabbros (Fig. 6).

Three of the gabbroic rocks in the western part of the Hinckley Range intrusion are olivine tholeiites with moderately high *mg* (62–66) and S (960–1020 ppm). Their incompatible-element contents and ratios are mostly indistinguishable from those of the Bell Rock sills and dykes (Fig. 6), but their spidergrams are less irregular, and do not show the cumulus features (Sr enrichment, HFSE depletion) of the latter (Fig. 8). A fourth recrystallised gabbro (with a preliminary U–Pb zircon ion-microprobe age of 1070 Ma; Glikson et al. 1996) is more fractionated (*mg* 57), and has higher Ce/Zr, lower Ti/Zr and P/Zr, and a more irregular spidergram (Figs. 6 and 8); it may therefore be unrelated to the other west Hinckley Range rocks.

Gabbronorites in the north Hinckley Range are compositionally quite similar to those from the west, apart from being more evolved (*mg* 52–58) and having slightly lower Ti/Zr and Nb/Zr (Figs. 6 and 8). A recrystallised sample has ε_{Nd} of –1.4 (Glikson et al. 1996).

Discussion

Relationships to the Giles Complex

The presence of microgabbro sills and dykes with phenocryst assemblages (olivine + plagioclase) similar to the host cumulates in the Bell Rock and other troctolitic intrusions led Ballhaus (1992) and Ballhaus & Glikson (1995) to suggest that they either represent chilled variants of or are parental to the layered sequences. The lack of precise geochronological data precludes conclusive proof of such relationships, but similar ages of group A1 and gabbronorite dykes, and gabbronorites from the western and northern Hinckley Range, are consistent with at least some of the dykes being feeders to higher-level Giles Complex intrusions.

As already shown, the microgabbro sills and dykes in the Bell Rock intrusion are chemically similar to gabbroic rocks of the Hinckley Range intrusion. They also bear a marked resemblance to group A2 dykes in the northern Hinckley Range, although these have slightly higher P/Zr. These similarities strongly suggest a common (but not necessarily comagmatic) origin for the dykes and the gabbroic components of the Giles Complex in the Hinckley Range. However, clear relationships between the microgabbro sills and dykes and the troctolitic intrusions (Bell Rock, Blackstone Range, and Jameson Range) are more difficult to establish, because there are significant compositional gaps between, for example, the Bell Rock sills and dykes and the host layered sequences (Fig. 6). The layered sequences have prominent cumulus features, whereas the microgabbro sills and dykes and group A2 dykes show evidence of only minor plagioclase (and possibly olivine and titanomagnetite) accumulation (Figs. 5 and 8). Nevertheless, the Bell Rock leucotroctolites and the microgabbros were apparently derived from a similarly enriched mantle source, because most incompatible-element ratios of the less cumulus samples are similar to those of the dykes. Only Sr/Zr, Ti/Zr, and probably Nb/Zr are significantly higher, which can be explained by plagioclase and titanomagnetite accumulation. The Jameson Range leucotroctolites show similar features, and, although their LILE contents are somewhat higher, the LILE/Zr ratios of the least cumulus samples are

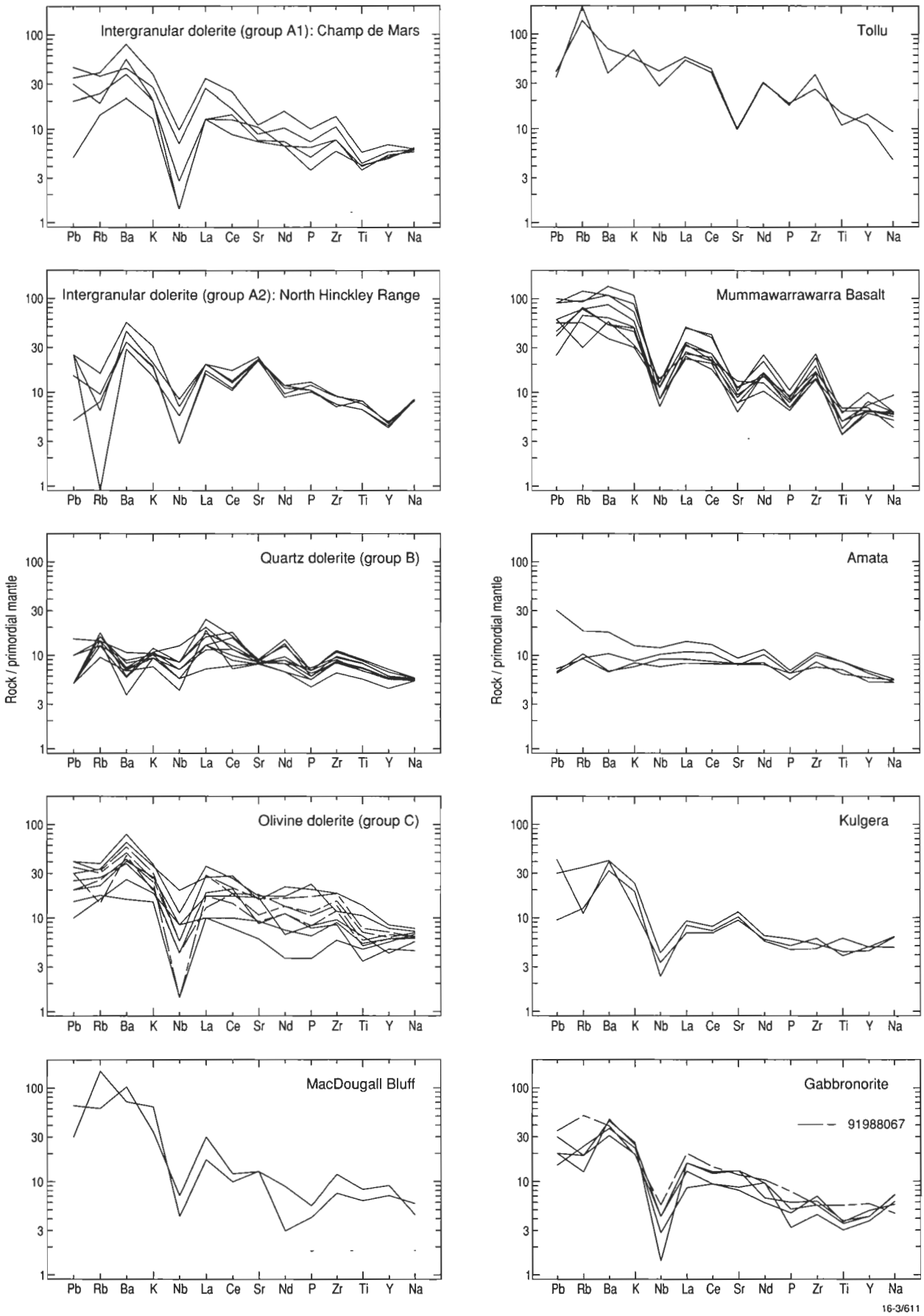

Figure 5. Primordial mantle-normalised incompatible-element abundance diagrams (spidergrams) for dolerite and gabbronorite dykes and the Mummawarrawarra Basalt. The broken lines for group C are the low Ti/Zr subgroup. Data for the Kulgera and Amata dykes are after Zhao (1992) and Zhao et al. (1994) respectively. Normalising values (Pb, 0.20; Rb, 0.63; Ba, 6.91; Th, 0.092; U, 0.022; K, 230; Nb, 0.71; La, 0.70; Ce, 1.81; Sr, 20.9; Nd, 1.35; P, 95; Zr, 11.1; Ti, 1270; Y, 4.52; Na, 2890 ppm) are after Sun & McDonough (1989).

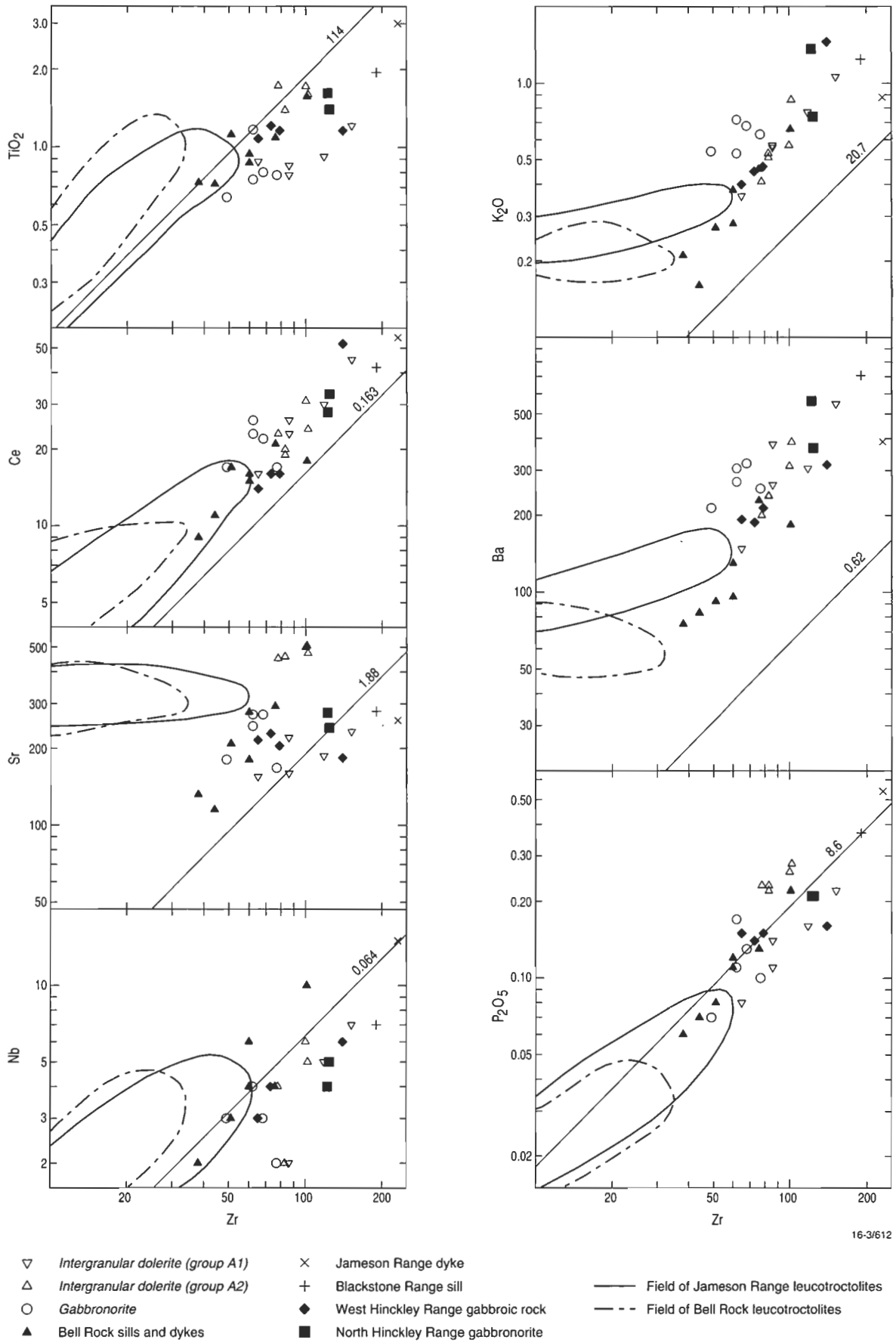

Figure 6. Logarithmic plots of various incompatible elements against Zr for groups A1, A2, and the gabbronorite dykes and sills associated with the Giles Complex intrusions. The fields of leucotroctolite cumulates from the Bell Rock and Jameson Range intrusions are based on data in the AGSO 'ROCKCHEM' database. Note the moderately large K_d values (≤1) for K_2O, Ba, and Sr for the leucotroctolites.

similar to those of Bell Rock (Fig. 6).

If Zr is assumed to be incompatible, logarithmic plots of other incompatible elements against Zr should define lines of unit slope (i.e., lines of constant ratio, corresponding to bulk distribution coefficients, K_d, of zero; Allègre et al. 1977). For the Bell Rock leucotroctolites, K_d values for Ce and P (Fig. 6), as well as for Y and S, are close to zero; for Sr, the K_d is about 1.0, consistent with plagioclase-dominated accumulation, but for the LILEs it is much higher (~0.7–1.0) than expected for such a process, suggesting involvement of an additional phase — such as biotite. However, Ballhaus (1992) described biotite as being of late or postmagmatic origin, so the relative LILE enrichment in the cumulates is possibly a deuteric or even a metamorphic effect. The K_ds for Ti and Nb in the Bell Rock leucotroctolites are difficult to estimate, but samples with less cumulus characters (higher Zr, etc.) have relatively high Ti/Zr (and possibly Nb/Zr) and may thus be more enriched in Fe–Ti oxides. In other words, there appears to be an inverse correlation between plagioclase and titanomagnetite accumulation. Of the compatible elements (not plotted here), Ni has a K_d of around 2, consistent with olivine accumulation; V shows a similar trend to Ti and Nb, suggesting vanadiferous titanomagnetite accumulation; and Cr shows little correlation with Zr. The estimated K_d for Sc is about 0.7, suggesting some pyroxene control, but petrographic evidence indicates olivine+plagioclase-dominated fractionation, so that fractionation of pyroxene might have occurred before emplacement. Early clinopyroxene fractionation could also account for the marked Y depletion relative to other HFSE (Fig. 8). Ballhaus & Glikson (1995) proposed that the parent magmas of the Giles Complex intrusions experienced various degrees of high-pressure (probably >1 GPa) orthopyroxene–clinopyroxene ± olivine fractionation at significantly greater depths before they were emplaced.

Most of the microgabbro dykes and sills in the troctolitic intrusions thus appear to be more closely related to the gabbroic bodies, like Hinckley Range, than to the troctolitic bodies themselves. They are, in fact, virtually indistinguishable from dykes cutting the gabbros, except that the more evolved microgabbros show some Sr enrichment (plagioclase accumulation) and Y depletion (?clinopyroxene fractionation). Their S contents are generally similar to those of the dykes cutting the gabbros, whereas those of most Giles Complex layered sequences are very low (≤ 100 ppm). However, this can be explained, at least to a large extent, by the strongly cumulus nature of the intrusions. As suggested by Ballhaus (1992) and Ballhaus & Glikson (1995), these microgabbros probably represent fractionated parental liquids derived by high-pressure pyroxene ± olivine fractionation of primitive mantle melts. According to these authors, the gabbroic rocks cannot be directly parental to the troctolitic cumulates, which require a more strongly fractionated parental melt depleted in normative clinopyroxene. Nevertheless, both the gabbroic and troctolitic parent magmas may have separated at different stages from the evolving high-pressure melt. Clearly, both were ultimately derived from similarly enriched mantle source regions.

The least fractionated microgabbros in the Bell Rock intrusion may well be representative of such evolved magmas that were parental to the gabbroic intrusions. Sample 88982029 (Table 2) has a moderately flat, regular spidergram showing only slight Sr enrichment and no Y depletion — i.e., no significant cumulus features. It is broadly similar to Sun &

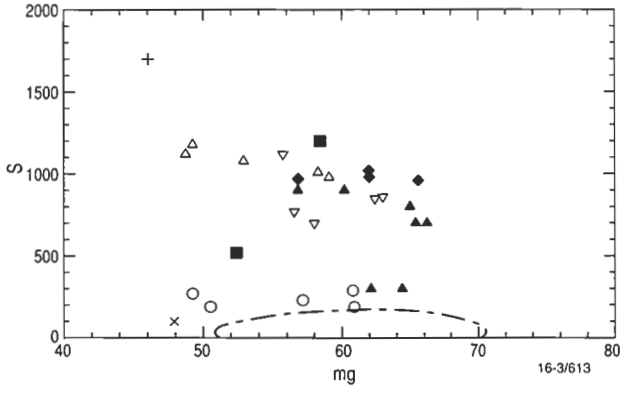

Figure 7. Plot of S against *mg* for groups A1, A2, and the gabbronorite dykes and sills associated with Giles Complex intrusions. Symbols as in Figure 6, except that only the Bell Rock leucotroctolite field is shown.

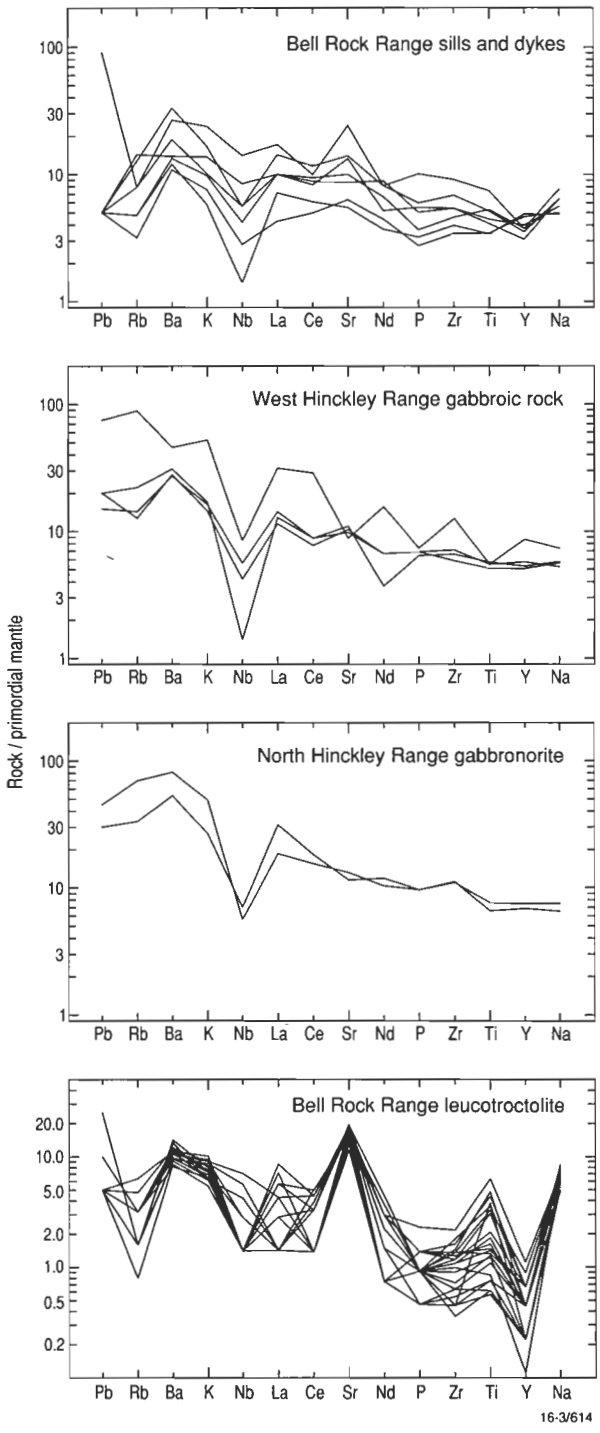

Figure 8. Spidergrams for microgabbro sills and dykes in the Bell Rock intrusion, Hinckley Range gabbroic rocks, and Bell Rock leucotroctolite. Note the change of scale for the leucotroctolite.

Sheraton's (1992) estimated Giles parent magma, but is slightly more evolved and has lower LREE and Zr. Both estimates are characterised by low HFSE, indicating magma generation by large degrees of mantle melting at moderately shallow depths. Unlike the troctolitic rocks, such compositions imply only small degrees of high-pressure fractionation. *mg* values (65 for 88982029) and Cr and Ni contents (705 and 220 ppm respectively) are not far removed from those of primary olivine tholeiite magmas in equilibrium with mantle pyrolite (Ringwood 1975; Frey et al. 1978).

Nesbitt et al. (1970) suggested that the Tollu Group volcanics might be genetically related to the Giles Complex. However, the compositional relationships between the Giles Complex and its associated dykes and the Mummawarrawarra Basalt are uncertain, because of the degrees of fractionation and alteration and the highly vesicular nature of the volcanics. Both the intrusive and extrusive rocks were derived from similarly enriched mantle source regions, and are of similar age, so that at least an indirect association is likely. The basaltic rocks have relatively low P/Zr, Ti/Zr, and Nb/Zr, which can be attributed to extensive fractionation, but whether these rocks were derived directly from any of the parent magmas of the Giles intrusions is unclear. The low S contents of the Mummawarrawarra Basalt probably reflect loss of S during extrusion (Wallace & Carmichael 1992).

Origin of the 1000–1100-Ma magmas

The group A1 dolerites, the ca 1080-Ma Giles Complex and its associated dykes and sills, and the Mummawarrawarra Basalt and its associated dykes, as well as the somewhat younger (at least in part) group C olivine dolerites, were all derived by the melting of an enriched source, probably subcontinental lithospheric mantle. This assertion is indicated by these rocks having LILE/Zr and LREE/Zr ratios much higher than the estimated primordial mantle (Sun & McDonough 1989), whereas their HFSE/Zr ratios are similar to or less than primordial mantle values. Their spidergram patterns thus reflect moderate to strong fractionation, and generally have marked negative Nb anomalies, consistent with metasomatic enrichment of the mantle source by a LILE- (and LREE-) rich fluid or melt — possibly derived by the dehydration or partial melting of subducted sedimentary rocks (Rogers et al. 1987; Nelson & McCulloch 1989). Under hydrous melting conditions, Nb would be retained in residual Ti-oxide minerals (ilmenite, rutile, sphene, or perovskite), which is thought to account for the negative Nb anomalies of island-arc basalts (Saunders et al. 1980; Arculus 1987). This process could explain the low Nb/Zr and Ti/Zr of many Musgrave mafic dyke suites (Fig. 3).

Although the various dyke suites are broadly similar in composition, there are marked chemical differences between them, and some (notably group C) are markedly heterogeneous. Groups A1, A2, and B show essentially constant ratios for many of their incompatible elements (i.e., they plot on lines of unit slope in Fig. 3). Plots of other elements approximate to lines of lower slope; for example, Sr has a K_d of about 1, indicating fractionation of plagioclase, and trends for Sc (K_d ~1) and Y (K_d ~0.3–0.6; not shown) are consistent with clinopyroxene fractionation. More compatible elements (V, Cr, and Ni) have even higher K_d values. The scatter shown by the Mummawarrawarra Basalt may be due largely to alteration and the presence of abundant amygdales, but, for group C dykes, which show moderately large variations in both major- and trace-element compositions, the differences are presumably of primary magmatic origin.

There are several possible explanations for these variations. Some crustal contamination is quite probable, particularly for LILE, although Sheraton et al. (1990) asserted that most of the compositional variations of continental tholeiite suites can be explained by partial melting and fractional crystallisation processes applied to a magma derived from heterogeneous lithospheric mantle sources; Zhao & McCulloch (1993b) also dismissed the involvement of major crustal contamination in the generation of the magmas that produced the Stuart and Kulgera dyke swarms. Different degrees of melting are implied by the fact that group C olivine tholeiites have similar (or even higher) absolute abundances of most incompatible elements compared with the more evolved (lower *mg*, quartz tholeiitic) group A2 and gabbronorite. More complex processes, such as dynamic partial melting (Langmuir et al. 1977), RTF (periodically replenished, tapped, and fractionated) magma chambers (O'Hara & Mathews 1981; Cox 1988), and possibly disequilibrium melting (Bédard 1989), also might have been important, but would not have significantly affected incompatible-element, as opposed to compatible/incompatible-element, ratios. Chemical and isotopic data for the Stuart dyke swarm (e.g., plots of Ce v. Ti/Zr, and trace element v. initial ε_{Nd}) are consistent with a two-component mixing process, possibly between a depleted mantle source and an older slab-derived trondhjemitic melt (J-X. Zhao, University of Queensland, personal communication 1995).

Hence, most of the incompatible-element heterogeneity shown by the various dyke suites probably reflects mantle-source heterogeneity, ultimately caused by subduction processes. For example, the unusually high P/Zr of group A2 might have originated from the melting of an apatite-rich source, and the widely varying Nb/Zr, Ce/Zr, Ti/Zr, and LILE/Zr ratios of group C also suggest source heterogeneity. Such chemical heterogeneity is reflected both laterally (as group C shows considerable geographical compositional variations) and vertically (as several chemically distinct suites of similar age crop out in the same area). Heterogeneity is also a feature of both the Kulgera and Stuart dyke swarms, for which ε_{Nd} ranges from –9.9 to +1.9 (Zhao & McCulloch 1993b); this range compares with –2.3 to +1.9 for single samples of groups A1 and C and the gabbronorite dykes (Glikson et al. 1996).

Most of the dykes, including those probably genetically related to the Giles Complex gabbroic intrusions, have S contents (700–1200 ppm) typical of those of continental tholeiites (Figs. 4 and 7). Such S contents are close to saturation levels for mafic magmas (Czamanske & Moore 1977), although group A2 and the Bell Rock dykes (as well as the Kulgera and Stuart dykes) show negative correlations with *mg*, suggesting that the magmas may not have been completely S-saturated. If the Giles parent magmas were S-saturated, this would severely restrict their economic potential for platinum-group-element (PGE) mineralisation (Sun et al. 1991; Wyborn & Sun 1994). Determination of Se (to quantify possible S loss) and PGEs are needed, to define this potential. The much lower S of the Mummawarrawarra Basalt (and two high-level dykes near Tollu) can be explained by S loss during ascent and eruption (Wallace & Carmichael 1992).

Zhao & McCulloch (1993b) pointed out that Sm–Nd whole-rock isochron ages and corresponding ε_{Nd} values for the Stuart (1853 ± 189 Ma, ε_{Nd} –4.2 ± 4.2) and Kulgera (1589 ± 165 Ma, ε_{Nd} +1.7 ± 3.6) dykes are similar to those of the associated continental crust. Nd T_{DM} model ages of felsic ortho- and paragneisses in the western Musgrave Block are 1615–1901 Ma, and their ε_{Nd} values (at 1080 Ma) are –2.5 to –4.8 (Glikson et al. 1996). This suggests that metasomatic enrichment of the lithospheric mantle (presumably subduction-related) was coeval with crust formation in the area. Similar correlations between source enrichment and continental crust formation have been demonstrated for many other dyke swarms, including those in the Bunger Hills, East Antarctica (Sheraton et al. 1990).

The ultimate cause of the extensive mantle-melting event

which produced the Giles Complex intrusions, dykes, and mafic volcanics at about 1080 Ma is unclear. Surprisingly, this magmatism postdates the peak (in terms of the formation of the regional foliation) of the ca 1200-Ma granulite-facies metamorphism in the area by more than 100 Ma. Hence, the Giles Complex magmatism cannot have been the direct cause of this event, although some mafic magmatism occurred soon after metamorphism: a small (~1 km across) body of biotite leucogabbronorite in the western Champ de Mars has a U–Pb zircon age of 1176 ± 5 Ma (Sheraton & Sun 1995; Glikson et al. 1996). Thus, high-grade metamorphism may have resulted from mafic underplating at that time. Nevertheless, the country rocks were still deep in the crust when the Giles Complex was emplaced: a pressure of 0.6 ± 0.1 GPa was estimated by Ballhaus & Berry (1991) for the Wingellina Hills intrusion, although pressures were lower to the southwest (C.G. Ballhaus, University of Mainz, Germany, personal communication 1995). The apparently large pressure increase, to about 1.1 GPa at 650–700°C in the Hinckley Range area soon after this event, may have been a consequence of crustal thickening related to the emplacement of the voluminous mafic–ultramafic magmas (Clarke et al. 1995a; Glikson et al. 1995). The intrusion of the Giles magmas caused extensive intracrustal melting, which produced a variety of granitic bodies — including rapakivi granites (Sheraton & Sun 1995).

A major thermal perturbation was clearly necessary to account for the scale of melting involved in the formation of the Giles Complex. Zhao & McCulloch (1993b) suggested that either lithospheric thinning allowed hot asthenospheric mantle to flow beneath the lithosphere and cause decompression melting, or underplating of refractory mantle diapirs or hot mantle plumes caused dehydration melting of the lithosphere. Mathur & Shaw (1982) envisaged the intracratonic Musgrave mobile belt to have begun as a zone of incipient crustal fracture or rifting, accompanied by voluminous mafic–ultramafic magmatism.

Origin of the 800-Ma magmas

Group B dolerites were derived from a source quite different from the 1000–1100-Ma dykes and the Giles Complex. In most respects, this source was apparently similar to estimated primordial mantle (Fig. 3), and had ε_{Nd} in the range +2.8 to +3.8 (Glikson et al. 1996). It was also much more homogeneous than that of the older mafic rocks, particularly as the Amata and Gairdner dykes have virtually identical compositions (ε_{Nd} +2.4 to +4.3: Zhao et al. 1994). This implies a homogeneous mantle-source region more than 1000 km across. Only Ba/Zr and possibly Ce/Zr show significant variations which cannot be attributed to analytical uncertainties. These variations are unlikely to be due to crustal assimilation, because other LILEs do not show such variations, and are presumably source characteristics. Whatever their cause, the large-scale compositional homogeneity of the 800-Ma dykes militates against significant crustal assimilation, and suggests an asthenospheric — rather than lithospheric — mantle source. Low Al_2O_3 (13.2–14.8%) is consistent with moderately high-pressure melting. Low S (50–370 ppm) is difficult to explain, even by assuming high degrees of melting at high temperatures (HFSE contents are similar to those of less fractionated Ol-normative dykes), but may be a result of high oxygen fugacity (Wallace & Carmichael 1992; Carroll & Webster 1994). Alternatively, some S might have been lost during emplacement at high crustal levels, although emplacement pressures are unknown.

Zhao et al. (1994) postulated that the 800-Ma magmas were derived by decompressional melting of a large-scale asthenospheric mantle plume, which resulted sequentially in domal uplift of the overlying crust, rifting, crustal extension, thinning, and, ultimately, thermal subsidence and basin formation in central-southern Australia. They considered that the northwest-trending dykes were emplaced along the axis of the failed arm of a triple junction located above the plume head in the Adelaide Geosyncline.

Although such an evolution seems quite plausible, it might be incompatible with the chronology of events. In particular, the initiation of the Amadeus Basin might have significantly predated the 800-Ma magmatism, particularly if the volcanics in the Bitter Springs Formation, which occur near the base of the Amadeus Basin, are the same age as the Amata dykes (Shaw 1991; Shaw et al. 1991), as suggested from chemical criteria by Zhao et al. (1994). Hence, the relationships of the postulated mantle-plume activity and associated magmatism to basin formation in central Australia, at least, remain to be clarified.

Park et al. (1995) suggested that the Gairdner dykes represent part of a giant radiating dyke swarm which also included dykes of western North America and was emplaced into a Neoproterozoic supercontinent. However, the North American dykes might be appreciably younger (U–Pb and $^{40}Ar/^{39}Ar$ ages are ~780 Ma) than the Australian examples.

Conclusions

Voluminous layered mafic–ultramafic intrusions of the Giles Complex, various mafic dykes (including group A intergranular dolerites), and the Tollu Group basaltic volcanics were all formed by large-scale melting of heterogeneous enriched (ε_{Nd} –2.3 to –1.4) subcontinental lithospheric mantle about 1080 Ma ago. This was more than 100 Ma after regional high-grade metamorphism of the Musgrave Block, but occurred while the country rocks were still at similar crustal depths (~20 km in the Hinckley Range area). The coeval Kulgera (eastern Musgrave Block) and Stuart (Arunta Block) dyke swarms are chemically and isotopically similar. Slightly younger (~1000 Ma) group C olivine dolerites are particularly heterogeneous, but were derived from similarly enriched sources. Mantle heterogeneity was apparently both lateral and vertical.

Microgabbro dykes and sills associated with the Bell Rock leucotroctolite intrusion are compositionally similar to both the Hinckley Range gabbronorite intrusion and group A2 dolerite dykes therein. The least fractionated microgabbros are probably representative of an evolved magma, parental to the gabbroic intrusions, which underwent some degree of high-pressure pyroxene ± olivine fractionation. They cannot be directly parental to the leucotroctolite cumulates, whose source was much more extensively fractionated at high pressure before emplacement.

Group B quartz dolerites (800 Ma) were derived by higher-pressure partial melting of a much less enriched (ε_{Nd} +2.8 to +3.8), homogeneous asthenospheric mantle source, probably related to mantle-plume activity. They are virtually identical chemically and isotopically with dykes, including the Amata (eastern Musgrave Block) and Gairdner (Gawler Craton) dyke swarms, that crop out over a distance of more than 1000 km.

Acknowledgments

We thank John Pyke, Bill Pappas, and Elizabeth Webber for chemical analyses; Chris Ballhaus, Alfredo Camacho, Nigel Duncan, John Foden, Andrew Glikson, and Jian-Xin Zhao for invaluable comments on the manuscript; and Angie Jaensch for drafting some of the figures.

References

Allègre, C.J., Treuill, M., Minster, J-F., Minster, B. & Albarede, F., 1977. Systematic use of trace elements in igneous processes. Part 1: Fractional crystallisation processes in volcanic suites. Contributions to Mineralogy and Petrology, 60, 57–75.

Arculus, R.J., 1987. The significance of source versus process in the tectonic control of magma genesis. Journal of Volcanology and Geothermal Research, 32, 1–12.

Ballhaus, C.G., 1992. Petrology of the layered mafic/ultramafic Giles Complex, Western Musgrave Block, Western Australia. Australian Geological Survey Organisation, Record 1992/73.

Ballhaus, C.G. & Berry, R.F., 1991. Crystallization pressure and cooling history of the Giles layered igneous complex, central Australia. Journal of Petrology, 28, 1–28.

Ballhaus, C.G. & Glikson, A.Y., 1995. The petrology of layered mafic–ultramafic intrusions of the Giles Complex, western Musgrave Block, Western Australia. AGSO Journal of Australian Geology & Geophysics, 16, 69–89.

Bédard, J.H., 1989. Disequilibrium mantle melting. Earth and Planetary Science Letters, 91, 359–366.

Carroll, M.R. & Webster, J.D., 1994. Solubilities of sulfur, noble gases, nitrogen, chlorine, and fluorine in magmas. In: Carroll, M.R. & Holloway, J.R. (Editors), Volatiles in magmas. Reviews in Mineralogy, Mineralogical Society of America, 30, 231–279.

Clarke, G.L., 1992. Field relationships and tectonic history of the Hinckley Gabbro, felsic to mafic granulites and granitoids, west Hinckley Range and Champ-de-Mars areas, Tomkinson Ranges, Musgrave Block, WA. Bureau of Mineral Resources, Australia, Record 1992/33.

Clarke, G.L., Buick, I.S., Glikson, A.Y. & Stewart, A.J., 1995a. Structural and pressure–temperature evolution of host rocks of the Giles Complex, western Musgrave Block, central Australia: evidence for multiple high-pressure events. AGSO Journal of Australian Geology & Geophysics, 16, 127–146.

Clarke, G.L., Sun, S.-s. & White, R.W., 1995b. Grenville-age belts and associated older terranes in Australia and Antarctica. AGSO Journal of Australian Geology & Geophysics, 16, 25–39.

Cox, K.G., 1988. Numerical modelling of a randomized RTF magma chamber: a comparison with continental flood basalt sequences. Journal of Petrology, 29, 681–697.

Cruikshank, B.I. & Pyke, J.G., 1993. Analytical methods used in Mineral and Land Use Program's geochemical laboratory. Australian Geological Survey Organisation, Record 1993/26.

Czamanske, G.K. & Moore, J.G., 1977. Composition and phase chemistry of sulfide globules in basalt from the Mid-Atlantic Ridge rift valley near 37°N lat. Geological Society of America Bulletin, 88, 587–599.

Daniels, J.L., 1974. The geology of the Blackstone region, Western Australia. Geological Survey of Western Australia, Bulletin 123.

Frey, F.A., Green, D.H. & Roy, S.D., 1978. Integrated models of basalt petrogenesis: a study of quartz tholeiites to olivine melilitites from south eastern Australia utilizing geochemical and experimental petrological data. Journal of Petrology, 19, 463–513.

Glikson, A.Y., Ballhaus, C. & Pharaoh, T.C., 1990. The Giles Complex, central Australia: new insights into tectonics and metamorphism. BMR Research Newsletter, 12, 18–20.

Glikson, A.Y., Ballhaus, C., Clarke, G.L., Sheraton, J.W., Stewart, A.J. & Sun, S.-s., 1995. Geological framework and crustal evolution of the Giles mafic–ultramafic complex and environs, western Musgrave Block, central Australia. AGSO Journal of Australian Geology & Geophysics, 16, 41–67.

Glikson, A.Y., Stewart, A.J., Ballhaus, C., Clarke, G.L., Feeken, E.H.J., Leven, J.H., Sheraton, J.W. & Sun, S.-s., 1996. Geology of the western Musgrave Block, central Australia, with particular reference to the mafic–ultramafic Giles Complex. Australian Geological Survey Organisation, Bulletin 239.

Green, D.H., 1973. Experimental melting studies on a model upper mantle composition at high pressure under water-saturated and water-undersaturated conditions. Earth and Planetary Science Letters, 19, 37–53.

Gray, C.M., 1978. Geochronology of granulite-facies gneisses in the western Musgrave Block, central Australia. Journal of the Geological Society of Australia, 25, 403–414.

Langmuir, C.H., Bender, J.F., Bence, A.E. & Hanson, G.N., 1977. Petrogenesis of basalts from the FAMOUS area: Mid-Atlantic Ridge. Earth and Planetary Science Letters, 36, 133–156.

Le Maitre, R.W., 1989. A classification of igneous rocks and glossary of terms. Blackwell, Oxford.

Maboko, M.A.H., Williams, I.S. & Compston, W., 1991. Zircon U–Pb chronometry of the pressure and temperature history of granulites in the Musgrave Ranges, central Australia. Journal of Geology, 99, 675–697.

Mathur, S.P. & Shaw, R.D., 1982. Australian orogenic belts: evidence for evolving plate tectonics. Earth Evolution Sciences, 2, 281–308.

Menzies, M.A. & Wass, S.Y., 1983. CO_2 and LREE-rich mantle below eastern Australia: a REE and isotopic study of alkaline magmas and apatite-rich mantle xenoliths from the Southern Highlands Province, Australia. Earth and Planetary Science Letters, 65, 287–302.

Nelson, D.R., & McCulloch, M.T., 1989. Enriched mantle components and mantle recycling of sediments. In: Ross, J. (Editor), Kimberlites and related rocks. Volume 1: their composition, occurrence, origin and emplacement. Geological Society of Australia, Special Publication 14, 560–570.

Nesbitt, R.W., Goode, A.D.T., Moore, A.C. & Hopwood, T.P., 1970. The Giles Complex, central Australia: a stratified sequence of mafic and ultramafic intrusions. Geological Society of South Africa, Special Publication 1, 547–564.

Norrish, K. & Chappell, B.W., 1977. X-ray fluorescence spectrometry. In: Zussman, J. (Editor), Physical methods in determinative mineralogy. Academic Press, London, 201–272.

Norrish, K. & Hutton, J.T., 1969. An accurate X-ray spectrographic method for the analysis of a wide range of geological samples. Geochimica et Cosmochimica Acta, 33, 431–453.

O'Hara, M.J. & Mathews, R.E., 1981. Geochemical evolution in an advancing, periodically replenished, continuously fractionated magma chamber. Journal of the Geological Society of London, 138, 237–277.

Park, J.K., Buchan, K.L. & Harlan, S.S., 1995. A proposed giant radiating dyke swarm fragmented by the separation of Laurentia and Australia based on paleomagnetism of ca. 780 Ma mafic intrusions in western North America. Earth and Planetary Science Letters, 132, 129–139.

Ringwood, A.E., 1975. Composition and petrology of the Earth's mantle. McGraw–Hill, New York.

Rogers, N.W., Hawkesworth, C.J., Mattey, D.P., & Harmon, R.S., 1987. Sediment subduction and the source of potassium in orogenic leucitites. Geology, 15, 451–453.

Saunders, A.D., Tarney, J. & Weaver, S.D., 1980. Transverse geochemical variations across the Antarctic Peninsula: implications for the generation of calc-alkaline magmas. Earth and Planetary Science Letters, 46, 344–360.

Shaw, R.D., 1991. The tectonic development of the Amadeus Basin, central Australia. In: Korsch, R.J. & Kennard, J.M. (Editors), Geological and geophysical studies in the Amadeus Basin, central Australia. Bureau of Mineral

Resources, Australia, Bulletin 236, 429–461.

Shaw, R.D., Etheridge, M.A. & Lambeck, K., 1991. Development of the Late Proterozoic to mid-Palaeozoic, intracratonic Amadeus Basin in central Australia: a key to understanding tectonic forces in plate interiors. Tectonics, 10, 688–721.

Sheraton, J.W., 1984. Chemical changes associated with high-grade metamorphism of mafic rocks in the East Antarctic Shield. Chemical Geology, 47, 135–147.

Sheraton, J.W., Black, L.P., McCulloch, M.T. & Oliver, R.L., 1990. Age and origin of a compositionally varied mafic dyke swarm in the Bunger Hills, East Antarctica. Chemical Geology, 85, 215–246.

Sheraton, J.W. & Sun, S.-s., 1995. Geochemistry and origin of felsic igneous rocks of the western Musgrave Block. AGSO Journal of Australian Geology & Geophysics, 16, 107–125.

Stewart, A.J., 1995. Western extension of the Woodroffe Thrust, Musgrave Block, central Australia. AGSO Journal of Australian Geology & Geophysics, 16, 147–153.

Stewart, A.J. & Glikson, A.Y., 1991. The felsic metamorphic/igneous core complexes hosting the Giles Complex. BMR Research Newsletter, 14, 6–16.

Sun. S.-s. & McDonough, W.F., 1989. Chemical and isotopic systematics of oceanic basalts: implications for mantle composition and processes. In: Saunders, A.D. & Norry, M.J. (Editors), Magmatism in ocean basins. Geological Society of London, Special Publication 42, 313–345.

Sun, S.-s. & Sheraton, J.W., 1992. Zircon U/Pb chronology, tectono-thermal and crust-forming events in the Tomkinson Ranges, Musgrave Block, central Australia. AGSO Research Newsletter, 17, 9–11.

Sun, S.-s., Wallace, D.A., Hoatson, D.M., Glikson, A.Y. & Keays, R.R., 1991. Use of geochemistry as a guide to platinum group element potential of mafic–ultramafic rocks: examples from the west Pilbara Block and Halls Creek Mobile Zone, Western Australia. Precambrian Research, 50, 1–35.

Wallace, P. & Carmichael, I.S.E., 1992. Sulfur in basaltic magmas. Geochimica et Cosmochimica Acta, 56, 1863–1874.

Watson, E.B., 1979. Apatite saturation in basic to intermediate magmas. Geophysical Research Letters, 6, 937–940.

Wyborn, D. & Sun, S.-s., 1994. Sulphur-undersaturated magmatism — a key factor for generating magma-related copper–gold deposits. AGSO Research Newsletter, 21, 7–8.

Zhao, J.-X., 1992. Proterozoic crust–mantle evolution in central Australia: geochemical and isotopic constraints. PhD Thesis, Australian National University, Canberra (unpublished).

Zhao, J.-X. & McCulloch, M.T., 1993a. Sm–Nd isochron ages of Late Proterozoic dyke swarms in Australia: evidence for two distinctive events of mafic magmatism and crustal extension. Chemical Geology (Isotope Geoscience Section), 109, 341–354.

Zhao, J.-X. & McCulloch, M.T., 1993b. Melting of a subduction-modified continental lithospheric mantle: evidence from Late Proterozoic mafic dike swarms in central Australia. Geology, 21, 463–466.

Zhao, J.-X., McCulloch, M.T. & Korsch, R.J., 1994. Characterisation of a plume-related ~800 Ma magmatic event and its implications for basin formation in central-southern Australia. Earth and Planetary Science Letters, 121, 349–367.

AGSO Journal of Australian Geology & Geophysics, 16(5). 637–654

Zircon U–Pb ages and geochemistry of igneous and metamorphic rocks in the northern Prince Charles Mountains, Antarctica

P.D. Kinny[1], L.P. Black[2], & J.W. Sheraton[2]

High-grade metamorphic and felsic igneous rocks from the northern Prince Charles Mountains, East Antarctica, have been characterised geochemically and dated from SHRIMP zircon geochronological data. Around 980 Ma ago, voluminous magmas representing a combination of mantle-derived and intracrustal melts, including orthopyroxene–quartz monzonite ('charnockite') on Loewe Massif and granitic and syenitic intrusions on Mount Collins, were emplaced during a regional high-grade tectonothermal event. Garnet leucogneiss sheets on Mount McCarthy, the products of local partial melting, were also emplaced at about this time. The geology of Fisher Massif is exceptional in that a ca 1280-Ma metavolcanic sequence and coeval granodiorite have been metamorphosed only up to the lower amphibolite facies, and intruded by a ca 1020-Ma biotite granite. None of the analysed samples shows in its isotopic systematics the effects of 500-Ma events, prominent elsewhere in East Antarctica. Rare inherited components 1850–1900 Ma old were found in some samples. A paragneiss on Mount Meredith yielded 2500–2800-Ma and 1800–2100-Ma detrital zircon populations.

Introduction

The Prince Charles Mountains (PCM) occupy a vast (600 × 300 km) region of MacRobertson Land, East Antarctica. They extend from the head of the Lambert glacier (lat. 75°S) north to the Amery Ice Shelf (lat. 70°S) between longitudes 60 and 70°E. They comprise sharp peaks and steep-sided massifs rising to 1000 m above the local ice surface. Their more northerly exposures are dominated by granulite-facies rocks that are part of an extensive but sparsely exposed Meso- to Neoproterozoic basement. These rocks were previously correlated with the Rayner Complex of Enderby and Kemp Land, and basement rocks of the Mawson and Prydz Bay coastlines (Fig. 1). To the south, the rocks of the PCM are of lower metamorphic grade, and include Archaean granitic basement and probably Proterozoic metasedimentary cover sequences (Tingey 1982, 1991).

Fitzsimons & Thost (1992) described basement geological relationships in the northern PCM, specifically in the Athos, Porthos, and Aramis Ranges. The Porthos and Aramis Ranges are composed primarily of homogeneous felsic orthogneiss and intrusives enclosing minor mafic and ultramafic boudins and rare metasediments. In the Athos Range and on Jetty Peninsula, paragneiss is more abundant. Granulite-facies assemblages attributed to a regional 1000-Ma event indicate peak conditions of 0.6 to 0.7 GPa and 700 to 800°C (Fitzsimons & Thost 1992). Late in the metamorphic history, early flat-lying structures were redeformed into upright folds and shears, and discordant leucogneiss bodies (representing locally derived partial melts) and large orthopyroxene-bearing granite ('charnockite') plutons were emplaced (Fitzsimons & Thost 1992).

Farther south, the outcrops are geologically quite distinct from those in the more northerly ranges. Fisher Massif (Fig. 1), for example, comprises a low- to medium-grade metavolcanic sequence and granitic intrusions, and a layered metagabbro complex crops out on Mount Willing (Tingey 1982, 1991; Fedorov et al. 1987).

Other descriptions of geological relations in the northern PCM have been published recently by McKelvey & Stephenson (1990; Radok Lake area), Manton et al. (1992; Jetty Peninsula), Kamenev et al. (1993; summary of extensive mapping by Russian geologists throughout the PCM), and Hand et al. (1994; Else Platform).

By current standards, age relations in and around the PCM are poorly established. This paper seeks to redress this deficiency by presenting new U–Pb zircon geochronological data for ten samples collected from Mount McCarthy, Loewe Massif, Fisher Massif, Mount Collins, and Mount Meredith (Fig. 1) during the 1990–91 summer field season. Ages have been obtained via the SHRIMP ion-probe technique (Compston et al. 1984, 1992), for which analytical notes are presented in the Appendix. Geochemical data for all samples presented in Table 1 show that most are I-type granites (derived by the melting of igneous source rocks) according to the classification of Chappell & White (1974). These rocks are diopside- (Di) or only slightly corundum- (C) normative and have ASI (alumina saturation indices: atomic Al/[Na + K + Ca]) <1.1, which is consistent with the common occurrence of hornblende, titanite, and allanite. However, sample 91286403 from Mount McCarthy might be of S-type origin (derived by the melting of sedimentary source rocks), and samples 91286412 and 13 from Mount Meredith are paragneiss.

Previous geochronology

Arriens (1975) presented (and Tingey 1982, 1991 revised) reconnaissance Rb–Sr ages from across the PCM. His total-rock isochron ages in the northern PCM and northern parts of the southern PCM range from 550 to 1090 Ma; many are ca 1000 Ma. Biotite and muscovite evince ages of 400 to 660 Ma; most are clustered around 500 Ma. From these data, Tingey (1982) postulated a major metamorphic episode in the northern PCM about 1000 Ma ago, and a widespread 500-Ma thermal event that reset mineral isotope systems and generated cross-cutting granitic pegmatites and stocks.

In contrast, a large part of the area that Arriens sampled in the southern PCM preserves late Archaean Rb–Sr isochron ages, indicating the presence of a large Archaean craton and less isotopic disturbance by 1000-Ma events in that area. A map in Tingey (1982) shows an inferred inlier of Archaean basement characterised by tholeiitic dyke swarms in the area encompassing Fisher Massif, Mount Collins, and Mount Willing (northern PCM; Fig. 1). Tingey correlated these dykes with similar-looking dykes of probable Palaeo- to Mesoproterozoic age which cut the Archaean rocks of the southern PCM, but recent geochemical studies show that they are unrelated (J.W. Sheraton, unpublished data).

More recent geochronology on Jetty Peninsula and Else Platform (Manton et al. 1992) has yielded Rb–Sr mineral isochron and conventional U–Pb zircon ± monazite ages of granulite-facies gneiss, two suites of intrusive granitic rocks, and a pegmatite. Zircons from the gneiss gave a U–Pb concordia upper intercept age of 1000 + 14/–11 Ma, interpreted as dating the granulite-facies metamorphism. One of the granite suites (gneissic leucogranite) gave ages of 940 + 24/–17 Ma (U–Pb zircon) and 718 ± 32 Ma (Rb–Sr); the other (biotite granite) did not yield an interpretable zircon age, but gave Rb–Sr mineral isochron ages of ca 480 Ma, similar to the projected lower intercept ages of some of the zircon discordia. Monazites

[1] Department of Applied Physics, Curtin University of Technology, GPO Box U1987, Perth, Western Australia, 6001.

[2] Minerals Division, Australian Geological Survey Organisation, GPO Box 378, Canberra, ACT 2601.

from both granites yielded ages between 530 and 540 Ma. Concordant U–Pb ages ranging from 495 to 505 Ma were obtained from the pegmatite. Manton et al. (1992) also cited Pb-isotope ages ranging from 830 to 968 Ma (Yakovlev et al. 1986) for orthopyroxene-bearing rocks in the Jetty Peninsula–Radok Lake area.

Mikhalsky et al. (1992) reported an Sm–Nd isochron age of 1233 ± 160 Ma, and a ca 1000-Ma metamorphic resetting age for mineral separates from nine samples of the layered gabbronorite complex on Mount Willing. They also documented conventional U–Pb zircon data for three granitic rocks from Mount Collins, from which they interpreted a crystallisation age of 1400 ± 80 Ma and subsequent disturbances between 700 and 900 Ma. Beliatsky et al. (1994) presented conventional multigrain zircon U–Pb data for mixed samples of low-grade metavolcanic rocks from Fisher Massif. They obtained discordia ages from five fractions indicating igneous emplacement at ca 1300 Ma, and a much older discordant point with a $^{207}Pb/^{206}Pb$ age of ca 2560 Ma from a sample of rhyodacite interpreted as having a clastic component.

Hensen et al. (1992) reported an Rb–Sr whole-rock age of 882 ± 140 Ma for intrusive charnockitic rocks of the Porthos Range. More recently, Zhou & Hensen (1995) applied Sm–Nd dating of whole-rock–garnet pairs to a leucogneiss sheet at Mount McCarthy. They interpreted their isochron age of ca 1150 Ma as reflecting contamination by monazite inclusions in the garnet. After leaching of contaminants, the garnets gave ages ranging from 635 to 555 Ma. (In this paper we present zircon data for what appears to be the same generation of leucogneiss.) A nearby two-pyroxene granulite gave an age of ca 630 Ma by the same method.

Finally, Phanerozoic K–Ar ages have been obtained for a

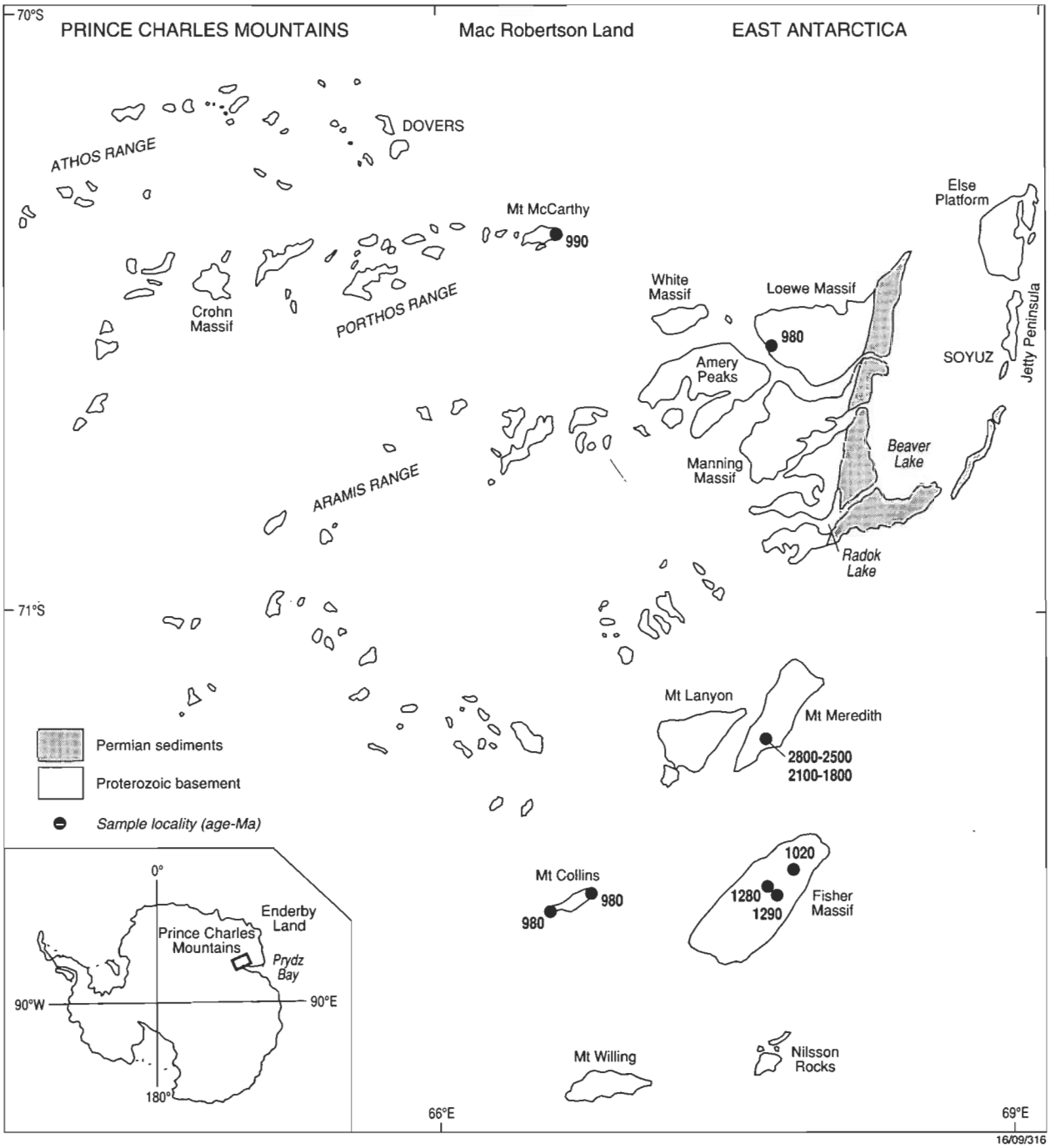

Figure 1. Sketch map of the northern PCM showing outcrops, sample localities (filled circles), and corresponding SHRIMP U–Pb zircon ages (Ma).

Table 1. Chemical analyses of dated samples.

Sample no.	*91286403*	*91286407*	*91286412*	*91286413*	*91286415*	*91286416*	*91286417*	*91286419*	*91286420*	*91286421*
Field no.	*MAC3*	*LOE7*	*MEM12*	*MEM13*	*FIR15*	*FIR16*	*FIR17*	*COL19*	*COL20*	*COL21*
Locality	*Mount McCarthy*	*Loewe Massif*	*Mount Meredith*	*Mount Meredith*	*Fisher Massif*	*Fisher Massif*	*Fisher Massif*	*Mount Collins*	*Mount Collins*	*Mount Collins*
Lithology	*Gt leuco-granite–gneiss*	*Bt-Hb-Op quartz monzonite*	*Bt-Kf-Qz-Pl gneiss*	*Bt-Pl psammite*	*Bt granite*	*Bt grano-diorite*	*Bt-Hb meta-dacite*	*Hb-Bt granite (foliated)*	*Hb-Bt granite*	*Cp quartz syenite*
SiO_2	76.28	58.92	70.27	86.23	67.11	72.60	64.75	64.44	74.55	58.66
TiO_2	0.02	1.57	0.53	0.26	0.51	0.27	0.53	0.59	0.21	0.81
Al_2O_3	12.41	15.11	13.86	6.25	15.04	13.43	13.02	15.72	12.45	17.80
Fe_2O_3	0.22	2.28	2.07	0.53	1.56	1.23	1.83	1.41	0.86	2.28
FeO	0.77	5.44	2.19	1.06	1.74	1.59	3.10	3.27	1.31	4.07
MnO	0.03	0.13	0.06	0.02	0.07	0.07	0.08	0.08	0.05	0.16
MgO	0.18	2.32	0.98	0.53	1.11	0.55	3.17	1.15	0.12	0.64
CaO	0.58	4.98	3.64	1.05	2.75	2.46	6.15	2.91	0.79	3.40
Na_2O	2.24	3.13	3.09	1.78	3.80	4.26	3.73	3.84	3.36	4.31
K_2O	6.19	3.71	1.36	0.72	3.85	1.72	0.37	4.37	5.44	5.89
P_2O_5	0.06	0.92	0.14	0.06	0.16	0.07	0.08	0.19	0.03	0.24
LOI	0.30	0.85	0.93	0.53	1.57	0.93	2.46	0.77	0.51	1.25
Rest	0.06	0.58	0.19	0.08	0.26	0.15	0.16	0.41	0.18	0.52
Total	**99.34**	**99.93**	**99.31**	**99.10**	**99.53**	**99.33**	**99.42**	**99.15**	**99.86**	**100.03**
	CIPW norms									
Q	37.65	12.90	37.52	69.74	22.63	34.62	25.05	16.24	31.94	2.17
C	1.11	–	1.02	0.78	–	0.26	–	–	–	–
Or	36.58	21.92	8.04	4.25	22.75	10.16	2.19	25.82	32.15	34.81
Ab	18.95	26.49	26.15	15.06	32.15	36.05	31.56	32.49	28.43	36.47
An	2.49	16.22	17.14	4.82	12.60	11.75	17.69	12.75	2.82	11.83
Di	–	2.05	–	–	–	–	9.92	0.37	0.78	2.97
Hy	1.70	10.51	3.99	2.43	3.96	2.96	6.55	6.69	1.33	4.62
Mt	0.32	3.31	3.00	0.77	2.26	1.78	2.65	2.04	1.25	3.31
Il	0.04	2.98	1.01	0.49	0.97	0.51	1.01	1.12	0.40	1.54
Ap	0.14	2.18	0.33	0.14	0.38	0.17	0.19	0.45	0.07	0.57
mg	29.4	43.2	44.4	47.1	53.2	38.1	64.6	38.5	14.0	21.9
	Trace elements in parts per million									
Ba	103	2185	590	70	1182	587	156	1754	278	2441
Li	9	22	17	12	21	7	11	12	4	6
Rb	138	124	88	47	135	34	8	80	98	83
Sr	22	640	162	87	407	232	312	414	57	411
Pb	77	39	18	15	8	3	7	15	22	18
Th	5	8	13	5	9	3	<2	15	16	3
U	<0.5	<0.5	3.5	4.0	1.0	0.5	0.5	1.0	<0.5	<0.5
Zr	56	519	219	175	206	129	134	477	377	916
Nb	<2	48	14	5	9	10	6	38	30	11
Y	23	80	44	16	21	30	24	39	53	19
La	21	177	36	10	25	22	11	104	107	25
Ce	28	350	65	25	48	45	19	175	216	48
Pr	<2	36	8	3	6	5	<2	16	23	6
Nd	7	170	27	12	22	21	12	69	86	24
Sc	3	26	15	4	10	11	23	10	2	18
V	2	110	51	27	51	14	127	42	<2	9
Cr	2	40	15	25	6	2	120	8	1	3
Ni	3	16	12	8	5	3	29	8	3	6
Cu	1	24	13	8	2	2	66	14	1	10
Zn	7	121	49	27	32	45	43	79	59	69
Sn	<2	2	5	2	2	2	3	3	3	<2
Ga	11	25	15	6	16	15	13	19	21	22
As	1.5	2.0	0.5	<0.5	0.5	<0.5	0.5	0.5	4.0	1.0
S	<100	90	100	<100	<100	<100	100	100	20	250

mg = atomic 100 Mg/(Mg + Fe2+)

number of alkaline dykes, sills, and flows whose occurrence has been associated with development of the Lambert rift (e.g., Sheraton & England 1980; Sheraton 1983; Hofmann 1991).

Quartz monzonite ('charnockite') at Loewe Massif

In the northern half of Loewe Massif, a batholith of compositionally varied orthopyroxene-bearing ('charnockitic') granitic rocks intrudes prominently layered felsic orthogneiss and leucogneiss. Occupying an outcrop of 150 km^2, this batholith may be represented by similar rocks at nearby White Massif and Amery Peaks, which would increase its outcrop area to over 300 km^2. Near a sharp, cross-cutting, clearly intrusive contact exposed at the base of the southwest flank of Loewe Massif adjacent to the McKinnon glacier, the batholith contains remnants of assimilated blocks of the leucocratic country rock. Sample 91286407 (lat. 70°35.62′S, long. 67°37′E), from 3 km inside the contact, is a medium to coarse, slightly porphyritic biotite–hornblende–orthopyroxene–quartz monzonite with a hypidiomorphic inequigranular texture cut by microshears. It comprises reddish brown biotite (4%), greenish brown hornblende (4%), orthopyroxene (partly replaced by iddingsite, 4%), quartz (12%), perthite (30%), zoned sodic andesine (45%), and minor ilmenite, magnetite, apatite, and zircon.

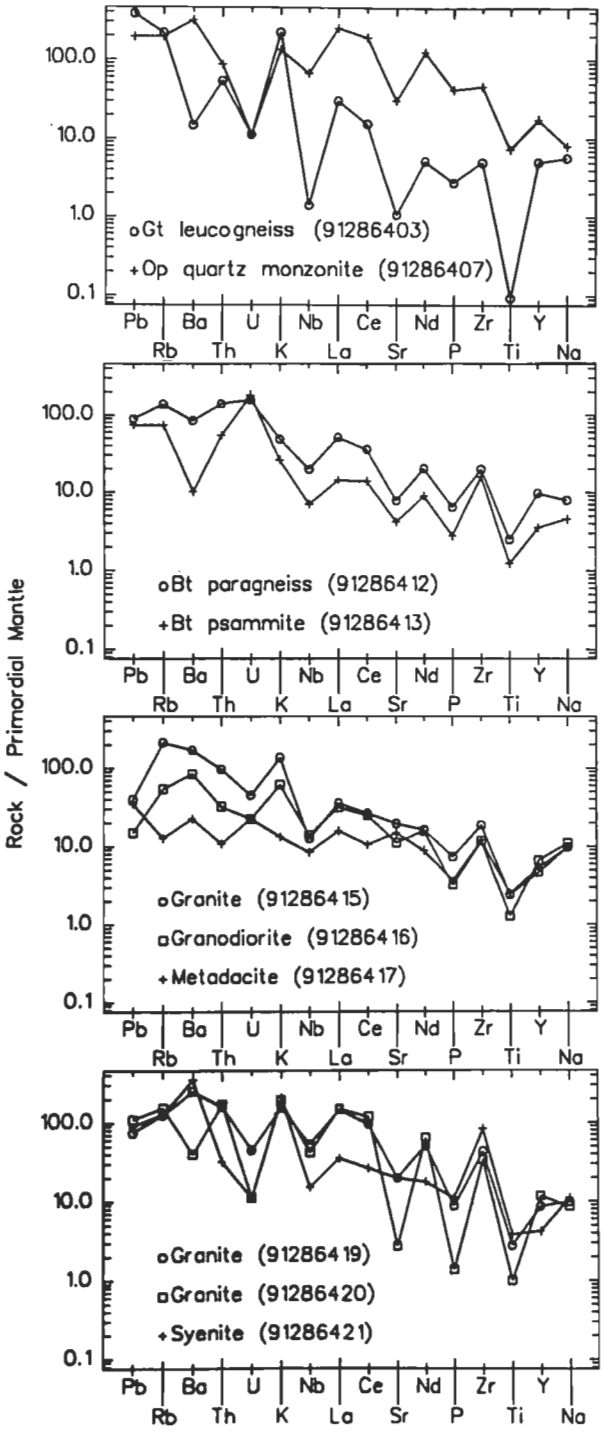

Figure 2. Primordial mantle-normalised incompatible-element-abundance patterns (spidergrams) for the PCM geochronology samples. The normalising values are from Sun & McDonough (1989).

The analysed rock (58.9% SiO_2) belongs to a low-SiO_2 group within the batholith. Its intermediate composition suggests that it originated from a mantle-derived mafic to intermediate magma, possibly through AFC (assimilation–fractional-crystallisation) processes (DePaolo 1981), implying that the rock has a crustal component. Alternatively, it might have originated from the dry partial melting of mafic to intermediate lower-crustal rocks, but this would have required an unusually large heat input. The lack of Y depletion (Fig. 2) precludes both hydrous (and thus lower-temperature) melting with significant residual amphibole, and high-pressure melting with residual garnet. High TiO_2, P_2O_5, Zr, Nb, Y, La, and Ce can be explained by the increased solubilities of minor phases in high-temperature melts (e.g., Watson & Harrison 1983), whether mantle- or crust-derived. Either model would be consistent with the moderate degree of Sr depletion (Fig. 2), implying plagioclase fractionation and/or residual plagioclase during melting. Other samples from the batholith are more siliceous (granite s.s.), and probably represent a distinct magma type formed by the dry melting of lower-crustal granulites (Sheraton et al. 1996).

Zircon grains in the monzonite are up to 600 m long, and have average elongation ratios of 3:1. Most appear to be rounded owing to dominant first-order prismatic faces with multifaceted terminations. Neither optical zoning nor cores are evident. A simple igneous origin befits the zircons, whose terminations were slightly modified later.

Isotopic data for the zircons (Table 2) plotted on a U–Pb concordia diagram (Fig. 3a) largely fall within the limits of analytical uncertainty of a mean $^{207}Pb/^{206}Pb$ age of 980 ± 21 Ma, which is taken as the crystallisation age of the charnockitic quartz monzonite. One discrepant analysis (2.1, shaded in Fig. 3a) has a marginally higher $^{207}Pb/^{206}Pb$ ratio than the mean. The mean $^{206}Pb/^{238}U$ age of the population is 944 ± 41 Ma, which overlaps with the $^{207}Pb/^{206}Pb$ age; the data are concordant to within error. If this analysis is included, the chi-square value (a statistic which compares the population statistics of the unknown with those of the interspersed analyses of the standard) of the entire group is 1.96, and the age 992 ± 28 Ma. For all samples discussed in this paper, the more precise $^{207}Pb/^{206}Pb$ age is preferred.

Leucogneiss at Mount McCarthy

The eastern end of Mount McCarthy is composed of intensely deformed (D_6 L-fabric; Fitzsimons & Thost 1992) garnet-bearing leucogneiss and 'charnockitic' rocks, whose main contact is tectonic. However, at one locality several sheets and irregular pods of leucogneiss clearly intrude the 'charnockitic' rock (Fitzsimons & Thost 1992, fig. 3d). Sample 91286403 (lat. 70°24.25′S, long. 66°36′E), from the largest of these intrusive leucogneiss bodies, is an inequigranular garnet leucogranite–gneiss consisting of ribbon quartz, sericitised perthite and subordinate sericitised plagioclase, together with garnet (1%) and minor muscovite and zircon. The rock is markedly

peraluminous (ASI 1.10), although not to the extent that an S-type origin is certain. It probably resulted from the local partial melting of either metasedimentary or a mixture of metasedimentary and meta-igneous country rocks when they were intruded by the 'charnockitic' magma. It is intensely fractionated (low TiO_2, MgO, CaO, Ba, Sr, Zr, Nb, La, Ce, V, Cr, and Ni), and has a highly irregular spidergram with a large negative Sr anomaly (Fig. 2), typical of partial melts of plagioclase-rich felsic crustal rocks (Tarney et al. 1987).

Zircon in the leucogneiss forms mostly elongate grains up to 450 μm long with length:breadth ratios as much as 6:1. Other grains are more equant. Many have overgrowths and distinct cores. Although the cores are mostly anhedral, some are internally zoned and have inclusions, imparting an igneous appearance. The overgrowths, in contrast, are mostly irregular in shape, unzoned, devoid of inclusions, and less clearly of igneous origin.

Twenty-four zircon grains from this sample were analysed. Among two old, ca 1850-Ma cores (15.2 and 27.1), one is enclosed by a ca 1650-Ma overgrowth (15.1, discordant analysis). The remaining analyses gave a mean $^{207}Pb/^{206}Pb$ age of 997 ± 21 Ma. However, the chi-square value of 4.3 for this group indicates more scatter in the data than for a single age population. Some of the scatter might be the result of Pb loss associated with the high U contents (>800 ppm) of some grains, but the behaviour is non-systematic. Even separating the data for core and rim populations (Figs. 3b, c) does not eliminate the scatter: the rims (3.1, 6.1, 7.2, 10.2, 13.1, 17.1, and 25.2) yield a mean $^{207}Pb/^{206}Pb$ age of 994 ± 39 Ma and a chi-square value of 5.4, and the cores (3.2, 6.2, 7.1, 10.1, 13.2, and 25.1) 1005 ± 57 Ma and 3.9. The chi-square value of the cores can be reduced to unity by deleting analysis 13.2 (perhaps a slightly older core), resulting in a revised age of 990 ± 30 Ma, but the ages yielded by the two morphological subgroups remain indistinguishable. There are several possible interpretations: the cores might be inherited from the source while the rims formed during the melting; both cores and rims might have formed during the same melting event; or the cores might have formed during the melting, and the rims were added later. Regardless, the bulk of the isotopic data suggest that partial melting to form the leucogneiss occurred about 990 Ma ago.

Granite and volcanics at Fisher Massif

Fisher Massif (300 km^2) is composed of thick-layered meta-volcanic, pyroclastic, and minor metasedimentary rocks, and intrusive igneous rocks ranging in composition from gabbro to granite (Fedorov et al. 1987; Crowe 1994; Kamenev et al. 1993; Mikhalsky et al. 1996). The metavolcanics, mainly mafic, include amygdaloidal basalt and ultramafic and intermediate to felsic varieties. Associated metasediments include banded ironstone, calcarenite, and conglomerate with clasts of siliceous rock and ironstone in a sandy matrix. Mineral assemblages in these rocks reflect lower-amphibolite-facies metamorphism with estimated P–T peaks of 0.1–0.3 GPa and 450–550°C, and subsequent retrogression to the greenschist facies (Crowe 1994). The volcanics have an early steeply dipping S1 fabric folded into tight F2 structures and later broken up by mylonitic faults. Granodioritic intrusions are cut by undeformed but metamorphosed mafic dykes which do not appear to cut a later granite in the north. One sample of each from the granite, granodiorite, and felsic volcanics were selected for study.

Sample 91286415 (lat. 71°26.73′S, long. 67°51′E) is an undeformed medium-grained biotite granite from Blustery Cliffs, at the northeast end of Fisher Massif. The sharply intrusive but locally sheared contact between this granite and mafic volcanic country rocks is exposed on the side of an

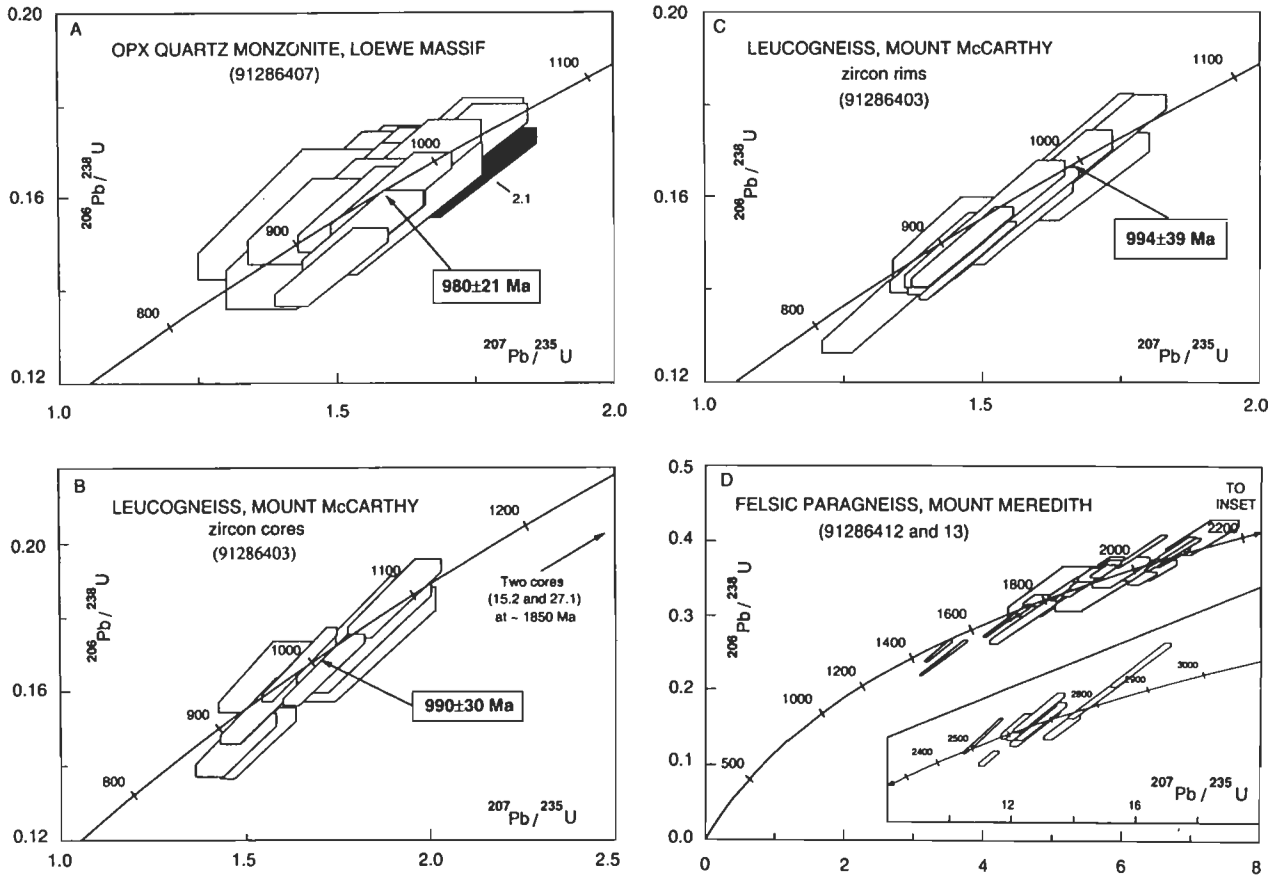

Figure 3. U–Pb concordia diagrams showing SHRIMP data for samples from the Loewe Massif, Mount McCarthy, and Mount Meredith. Error boxes reflect 95% confidence limits.

Table 2. U–Th–Pb isotopic compositions of zircons from the northern Prince Charles Mountains.

Grain area	*U (μg/g)*	*Th (μg/g)*	*Th/U*	$^{206}Pb/^{204}Pb$	f_{206} %	$^{206}Pb/^{238}U$ *±1σ error*	$^{207}Pb/^{235}U$ *±1σ error*	$^{207}Pb/^{206}Pb$ *±1σ error*	$^{207}Pb/^{206}Pb$ *Age (Ma)±1σ*	*% conc*
					91286407 (orthopyroxene–quartz monzonite, Loewe Massif)					
1.1	299	173	0.580	4471	0.382	0.1457±0.0069	1.398±0.078	0.0696±0.0017	917±51	96
2.1	209	273	1.309	53100	0.032	0.1515±0.0072	1.595±0.082	0.0764±0.0012	1105±31	82
4.1	164	231	1.407	110000	0.016	0.1398±0.0066	1.419±0.074	0.0736±0.0012	1031±33	82
5.1	145	180	1.246	37600	0.045	0.1504±0.0071	1.530±0.083	0.0738±0.0016	1036±44	87
8.1	405	433	1.070	15500	0.110	0.1591±0.0075	1.587±0.081	0.0723±0.0011	996±31	96
9.1	291	333	1.145	5070	0.337	0.1704±0.0080	1.695±0.092	0.0721±0.0016	990±44	102
11.1	182	101	0.557	7307	0.234	0.1596±0.0075	1.579±0.091	0.0717±0.0020	979±57	98
12.1	233	236	1.011	8157	0.209	0.1468±0.0069	1.431±0.080	0.0707±0.0018	949±52	93
14.1	154	123	0.798	2025	0.843	0.1537±0.0073	1.489±0.099	0.0703±0.0029	936±87	98
16.1	375	171	0.455	13100	0.130	0.1562±0.0074	1.532±0.081	0.0711±0.0014	961±40	97
19.1	193	279	1.441	6492	0.263	0.1481±0.0070	1.435±0.081	0.0703±0.0018	936±54	95
20.1	406	551	1.359	16300	0.105	0.1439±0.0068	1.479±0.076	0.0746±0.0011	1057±31	82
22.1	177	135	0.761	1607	1.062	0.1576±0.0074	1.482±0.098	0.0682±0.0028	874±87	108
24.1	151	151	1.004	4810	0.355	0.1647±0.0078	1.579±0.092	0.0695±0.0020	914±60	108
26.1	226	272	1.205	23700	0.072	0.1692±0.0080	1.705±0.091	0.0731±0.0014	1017±40	99
29.1	242	186	0.766	4701	0.363	0.1744±0.0082	1.715±0.093	0.0713±0.0015	966±43	107
30.1	172	112	0.647	6272	0.272	0.1727±0.0082	1.696±0.101	0.0712±0.0022	964±65	106
33.1	189	189	1.000	3617	0.472	0.1719±0.0081	1.624±0.096	0.0685±0.0021	884±64	116
34.1	157	99	0.632	2291	0.745	0.1680±0.0079	1.531±0.096	0.0661±0.0024	809±77	124
37.1	191	121	0.632	12500	0.137	0.1606±0.0076	1.566±0.088	0.0707±0.0018	950±53	101
38.1	177	191	1.080	10500	0.162	0.1692±0.0080	1.686±0.108	0.0723±0.0027	994±78	101
					91286403 (garnet leucogneiss, Mount McCarthy)					
3.1	2010	73	0.036	8402	0.203	0.1579±0.0074	1.534±0.074	0.0704±0.0004	941±13	100
3.2	1120	79	0.070	47100	0.036	0.1533±0.0072	1.510±0.073	0.0714±0.0005	970±14	95
6.1	634	233	0.367	10900	0.157	0.1531±0.0072	1.552±0.077	0.0736±0.0007	1029±21	89
6.2	116	93	0.803	7142	0.239	0.1626±0.0077	1.591±0.100	0.0709±0.0025	956±75	102
7.1	598	264	0.442	8198	0.208	0.1533±0.0072	1.522±0.077	0.0720±0.0009	987±27	93
7.2	1839	155	0.084	1731	0.986	0.1629±0.0077	1.667±0.088	0.0742±0.0014	1048±37	93
10.1	858	284	0.331	8438	0.202	0.1837±0.0087	1.889±0.096	0.0746±0.0010	1058±27	103
10.2	2795	236	0.085	96600	0.018	0.1449±0.0068	1.464±0.070	0.0733±0.0003	1022±8	85
13.1	884	150	0.169	1887	0.904	0.1498±0.0071	1.451±0.083	0.0703±0.0019	936±57	96
13.2	700	324	0.462	7804	0.219	0.1449±0.0068	1.520±0.077	0.0761±0.0010	1098±26	79
15.1	1282	40	0.031	42100	0.038	0.2506±0.0118	3.501±0.169	0.1013±0.0006	1648±12	87
15.2	801	104	0.130	390000	0.004	0.3018±0.0142	4.661±0.223	0.1120±0.0005	1832±8	93
17.1	939	129	0.138	11300	0.151	0.1330±0.0063	1.291±0.067	0.0704±0.0011	940±32	86
18.1	569	115	0.201	8257	0.207	0.1707±0.0080	1.706±0.086	0.0725±0.0009	999±25	102
21.1	711	151	0.213	11500	0.149	0.1467±0.0069	1.416±0.070	0.0700±0.0008	928±23	95
23.1	569	469	0.825	15300	0.112	0.1644±0.0077	1.698±0.084	0.0749±0.0008	1066±21	92
25.1	377	205	0.544	32600	0.052	0.1443±0.0068	1.461±0.077	0.0734±0.0014	1026±39	85

Table 2. cont.

Grain area	*U (µg/g)*	*Th (µg/g)*	*Th/U*	$^{206}Pb/^{204}Pb$	f_{206} %	$^{206}Pb/^{238}U$ *±1σ error*	$^{207}Pb/^{235}U$ *±1σ error*	$^{207}Pb/^{206}Pb$ *±1σ error*	$^{207}Pb/^{206}Pb$ *Age (Ma)±1σ*	*% conc*
25.2	1027	102	0.100	270000	0.006	0.1478±0.0069	1.454±0.071	0.0714±0.0006	967±18	92
27.1	863	159	0.184	55600	0.028	0.3430±0.0161	5.378±0.257	0.1137±0.0005	1859±7	102
28.1	150	146	0.969	22600	0.075	0.1856±0.0088	1.950±0.112	0.0762±0.0021	1100±56	100
31.1	670	153	0.228	4355	0.392	0.1719±0.0081	1.710±0.086	0.0722±0.0009	990±26	103
32.1	445	153	0.343	3331	0.512	0.1638±0.0077	1.634±0.086	0.0723±0.0013	995±37	98
35.1	262	182	0.695	4185	0.408	0.1885±0.0089	1.951±0.106	0.0751±0.0016	1070±43	104
36.1	486	108	0.222	13000	0.132	0.1654±0.0078	1.618±0.081	0.0709±0.0009	955±26	103
					91286415 (biotite granite, Fisher Massif)					
18.1	129	79	0.609	1101	1.533	0.1772±0.0054	1.693±0.135	0.0693±0.0048	907±151	116
19.1	108	81	0.750	1913	0.883	0.1717±0.0052	1.783±0.122	0.0753±0.0044	1077±121	95
22.1	111	66	0.592	1923	0.878	0.1818±0.0054	1.853±0.113	0.0739±0.0037	1040±103	104
23.1	138	103	0.742	2757	0.612	0.1796±0.0053	1.857±0.086	0.0750±0.0024	1067±65	100
26.1	223	227	1.021	2992	0.564	0.1769±0.0052	1.843±0.080	0.0756±0.0021	1083±58	97
27.1	74	58	0.777	500	3.376	0.1697±0.0053	1.396±0.179	0.0597±0.0072	591±286	171
30.1	63	47	0.749	536	3.152	0.1782±0.0056	1.494±0.231	0.0608±0.0090	632±354	167
31.1	143	128	0.896	1963	0.860	0.1868±0.0056	1.908±0.107	0.0741±0.0032	1044±91	106
34.1	100	70	0.700	1455	1.160	0.1790±0.0054	1.726±0.106	0.0699±0.0035	926±107	115
35.1	72	45	0.626	805	2.097	0.1796±0.0055	1.727±0.148	0.0698±0.0053	921±166	116
38.1	134	90	0.670	2550	0.662	0.1832±0.0054	1.935±0.105	0.0766±0.0032	1111±86	98
39.1	166	101	0.608	4170	0.405	0.1865±0.0055	1.856±0.075	0.0722±0.0017	991±49	111
42.1	104	65	0.620	1250	1.350	0.1791±0.0054	1.721±0.126	0.0697±0.0044	920±135	115
43.1	135	117	0.866	979	1.724	0.1564±0.0047	1.591±0.115	0.0738±0.0046	1036±132	90
46.1	153	99	0.642	1891	0.893	0.1848±0.0055	1.907±0.109	0.0748±0.0034	1064±94	103
47.1	81	54	0.660	1211	1.539	0.1888±0.0057	1.868±0.139	0.0717±0.0046	979±137	114
					91286416 (biotite ± hornblende granodiorite, Fisher Massif)					
20.1	113	82	0.725	5072	0.325	0.2231±0.0067	2.580±0.134	0.0839±0.0033	1290±8	101
21.1	106	59	0.553	4694	0.352	0.2245±0.0067	2.613±0.113	0.0844±0.0024	1302±55	100
24.1	210	192	0.916	40300	0.041	0.2208±0.0065	2.649±0.101	0.0870±0.0018	1361±41	95
25.1	107	55	0.513	1854	0.890	0.2220±0.0067	2.527±0.143	0.0826±0.0037	1259±90	103
28.1	132	138	1.044	2742	0.602	0.2122±0.0063	2.417±0.109	0.0826±0.0025	1260±61	98
29.1	172	80	0.466	5159	0.320	0.2219±0.0066	2.613±0.107	0.0854±0.0021	1325±49	97
32.1	61	23	0.376	851	1.939	0.2200±0.0068	2.221±0.199	0.0732±0.0059	1020±172	126
33.1	106	58	0.541	10500	0.158	0.2309±0.0069	2.747±0.124	0.0863±0.0026	1345±60	100
36.1	100	65	0.648	11700	0.141	0.2254±0.0069	2.645±0.219	0.0851±0.0062	1318±149	99
37.1	330	336	1.019	18900	0.087	0.2221±0.0065	2.581±0.086	0.0843±0.0011	1299±25	100
40.1	108	55	0.505	2583	0.639	0.2278±0.0068	2.613±0.126	0.0832±0.0029	1274±69	104
41.1	134	99	0.735	3510	0.470	0.2313±0.0069	2.729±0.111	0.0856±0.0021	1329±47	101
44.1	91	56	0.614	10800	0.152	0.2252±0.0068	2.678±0.133	0.0862±0.0031	1343±71	97
45.1	87	49	0.563	1161	1.421	0.2346±0.0071	2.337±0.146	0.0722±0.0037	993±107	137

Table 2. cont.

Grain area	*U (μg/g)*	*Th (μg/g)*	*Th/U*	$^{206}Pb/^{204}Pb$	f_{206} %	$^{206}Pb/^{238}U$ *±1σ error*	$^{207}Pb/^{235}U$ *±1σ error*	$^{207}Pb/^{206}Pb$ *±1σ error*	$^{207}Pb/^{206}Pb$ *Age (Ma)±1σ*	*% conc*
48.1	96	58	0.604	2420	0.682	0.2328±0.0070	2.673±0.137	0.0833±0.0032	1276±76	106
49.1	165	120	0.725	2400	0.688	0.2298±0.0068	2.589±0.112	0.0817±0.0023	1238±56	108
50.1	85	33	0.394	1916	0.861	0.2262±0.0068	2.507±0.134	0.0804±0.0033	1206±82	109
					91286417 (metadacite, Fisher Massif)					
2.1	316	383	1.213	9571	0.173	0.2249±0.0048	2.704±0.066	0.0872±0.0008	1365±18	96
3.1	141	113	0.799	4331	0.381	0.2272±0.0049	2.644±0.076	0.0844±0.0014	1302±33	101
4.1	119	82	0.686	1000000	0.002	0.1808±0.0039	1.975±0.051	0.0792±0.0009	1178±23	91
5.1	87	59	0.680	1194	1.384	0.2065±0.0046	2.163±0.123	0.0760±0.0038	1094±103	111
6.1	126	106	0.844	4749	0.348	0.2193±0.0048	2.474±0.082	0.0818±0.0018	1241±45	103
5.2	143	116	0.810	2975	0.555	0.2139±0.0046	2.436±0.085	0.0826±0.0021	1260±50	99
6.2	160	151	0.940	3220	0.513	0.2186±0.0047	2.510±0.079	0.0833±0.0017	1276±40	100
7.1	136	107	0.783	4226	0.391	0.2112±0.0046	2.391±0.079	0.0821±0.0018	1248±45	99
8.1	645	871	1.351	3972	0.416	0.2203±0.0047	2.531±0.061	0.0833±0.0008	1277±19	100
9.1	139	112	0.804	3768	0.439	0.2233±0.0048	2.558±0.079	0.0831±0.0016	1271±38	102
10.1	77	58	0.749	5257	0.314	0.2246±0.0050	2.592±0.105	0.0837±0.0026	1286±62	102
2.2	205	190	0.929	4168	0.396	0.2301±0.0049	2.685±0.081	0.0846±0.0016	1307±37	102
11.1	80	68	0.849	1000000	0.002	0.1805±0.0039	1.875±0.053	0.0753±0.0012	1077±32	99
12.1	185	99	0.535	1486	1.112	0.1607±0.0034	1.667±0.068	0.0752±0.0024	1074±66	89
13.1	693	1047	1.512	2744	0.602	0.2242±0.0047	2.506±0.061	0.0811±0.0008	1223±20	107
14.1	148	83	0.563	3357	0.492	0.2121±0.0046	2.548±0.083	0.0871±0.0019	1363±43	91
15.1	336	153	0.455	11400	0.145	0.3393±0.0072	5.515±0.125	0.1179±0.0007	1924±10	98
16.1	380	457	1.204	4444	0.372	0.2251±0.0048	2.615±0.066	0.0842±0.0010	1298±22	101
17.1	91	61	0.674	1016	1.625	0.2319±0.0051	2.351±0.127	0.0735±0.0034	1029±97	131
8.2	652	908	1.392	2020	0.818	0.2234±0.0047	2.468±0.065	0.0801±0.0011	1200±27	108
					91286419 (grey granite, Mount Collins)					
1.1	21	12	0.600	4470	0.382	0.1663±0.0045	1.868±0.266	0.0815±0.0111	1232±294	80
2.1	135	67	0.497	4060	0.420	0.1623±0.0034	1.534±0.070	0.0686±0.0026	886±80	109
3.1	331	254	0.768	56800	0.030	0.1656±0.0034	1.684±0.047	0.0738±0.0013	1035±35	95
4.1	141	99	0.702	1828	0.934	0.1613±0.0034	1.459±0.075	0.0656±0.0029	793±95	122
5.1	111	66	0.593	19900	0.086	0.1647±0.0035	1.650±0.066	0.0726±0.0023	1004±65	98
6.1	63	42	0.660	11800	0.145	0.1759±0.0039	1.762±0.109	0.0726±0.0040	1004±116	104
6.2	113	52	0.458	2152	0.793	0.1608±0.0034	1.510±0.080	0.0681±0.0031	871±98	110
8.1	45	23	0.504	1117	1.527	0.1664±0.0039	1.480±0.159	0.0645±0.0066	758±230	131
9.1	46	24	0.531	1473	1.158	0.1764±0.0041	1.602±0.157	0.0659±0.0061	803±207	130
11.1	183	81	0.445	3471	0.492	0.1649±0.0034	1.576±0.058	0.0693±0.0019	908±59	108
12.1	441	189	0.429	50300	0.034	0.1662±0.0034	1.685±0.041	0.0735±0.0008	1028±22	96
13.1	47	22	0.464	1721	0.991	0.1582±0.0036	1.536±0.142	0.0704±0.0061	939±189	101
14.1	883	455	0.515	43600	0.039	0.1781±0.0036	1.743±0.039	0.0710±0.0006	957±16	110

Table 2. cont.

Grain area	*U (μg/g)*	*Th (μg/g)*	*Th/U*	$^{206}Pb/^{204}Pb$	f_{206} %	$^{206}Pb/^{238}U$ ±1σ *error*	$^{207}Pb/^{235}U$ ±1σ *error*	$^{207}Pb/^{206}Pb$ ±1σ *error*	$^{207}Pb/^{206}Pb$ *Age (Ma)*±1σ	% *conc*
					91286420 (pink granite, Mount Collins)					
3.1	449	209	0.466	220000	0.008	0.1673±0.0032	1.679±0.035	0.0728±0.0005	1009±15	99
4.1	405	160	0.394	9925	0.172	0.1578±0.0030	1.533±0.036	0.0705±0.0008	942±24	100
7.1	319	195	0.609	37900	0.045	0.1639±0.0031	1.618±0.037	0.0716±0.0008	974±22	100
8.1	623	338	0.542	130000	0.014	0.1578±0.0030	1.572±0.033	0.0723±0.0005	994±15	95
11.1	460	137	0.297	92400	0.018	0.1584±0.0030	1.597±0.035	0.0731±0.0006	1017±18	93
12.1	394	78	0.197	140000	0.012	0.1584±0.0030	1.584±0.034	0.0725±0.0006	1000±17	95
16.1	1223	585	0.478	3000000	0.001	0.1684±0.0031	1.670±0.033	0.0719±0.0003	984±9	102
17.1	680	443	0.651	150000	0.012	0.1667±0.0031	1.645±0.034	0.0716±0.0005	973±14	102
20.1	682	322	0.472	156000	0.011	0.1679±0.0031	1.665±0.034	0.0719±0.0004	984±12	102
21.1	422	155	0.368	13300	0.128	0.1668±0.0031	1.637±0.038	0.0712±0.0008	963±23	103
24.1	318	41	0.130	61700	0.028	0.1728±0.0033	1.702±0.038	0.0714±0.0007	970±19	106
25.1	379	152	0.402	13900	0.123	0.1665±0.0031	1.617±0.040	0.0704±0.0010	940±28	106
28.1	490	134	0.273	13100	0.130	0.1639±0.0031	1.618±0.036	0.0716±0.0007	974±21	100
29.1	583	427	0.733	27500	0.062	0.1604±0.0030	1.582±0.035	0.0715±0.0007	972±19	99
32.1	501	206	0.412	72900	0.023	0.1621±0.0031	1.629±0.037	0.0729±0.0007	1011±21	96
34.1	493	197	0.400	82100	0.021	0.1641±0.0031	1.632±0.035	0.0721±0.0006	990±17	99
35.1	444	177	0.398	18000	0.095	0.1674±0.0032	1.629±0.040	0.0706±0.0010	946±28	105
38.1	343	122	0.356	16600	0.103	0.1664±0.0032	1.630±0.040	0.0711±0.0010	959±28	103
39.1	501	264	0.526	24700	0.069	0.1720±0.0033	1.690±0.040	0.0713±0.0008	965±24	106
42.1	370	403	1.092	23000	0.074	0.1645±0.0031	1.644±0.044	0.0725±0.0012	999±33	98
43.1	303	274	0.904	8011	0.213	0.1640±0.0032	1.610±0.043	0.0712±0.0012	964±34	102
44.1	438	181	0.415	22000	0.077	0.1708±0.0033	1.684±0.040	0.0715±0.0009	971±24	105
45.1	462	203	0.440	17000	0.100	0.1679±0.0032	1.651±0.037	0.0713±0.0007	966±21	104
48.1	451	219	0.485	27400	0.062	0.1612±0.0030	1.612±0.036	0.0725±0.0007	1001±20	96
49.1	595	63	0.105	850000	0.002	0.1516±0.0028	1.514±0.032	0.072±0.0005	998±15	91
52.1	555	170	0.307	38600	0.044	0.1674±0.0031	1.669±0.036	0.0723±0.0006	994±18	100
53.1	421	211	0.501	100000	0.017	0.1628±0.0031	1.605±0.035	0.0715±0.0006	972±18	100
					91286421 (pyroxene–quartz syenite, Mount Collins)					
1.1	108	31	0.290	5247	0.325	0.1679±0.0034	1.628±0.066	0.0703±0.0023	938±70	107
2.1	153	118	0.770	15000	0.114	0.1635±0.0032	1.596±0.047	0.0708±0.0014	951±42	103
5.1	229	124	0.543	17100	0.100	0.1601±0.0030	1.620±0.042	0.0734±0.0011	1025±32	93
6.1	205	152	0.741	6211	0.275	0.1595±0.0031	1.551±0.045	0.0706±0.0014	944±41	101
9.1	155	45	0.289	3968	0.430	0.1725±0.0034	1.636±0.058	0.0688±0.0019	893±58	115
10.1	148	90	0.606	29400	0.058	0.1554±0.0030	1.560±0.047	0.0728±0.0015	1009±42	92
13.1	103	48	0.461	24300	0.070	0.1643±0.0032	1.623±0.054	0.0716±0.0017	976±50	100
14.1	224	105	0.471	51400	0.033	0.1648±0.0031	1.649±0.042	0.0726±0.0011	1002±30	98
18.1	349	163	0.467	550000	0.003	0.1667±0.0032	1.674±0.036	0.0728±0.0006	1009±16	99
19.1	713	517	0.724	24200	0.071	0.1667±0.0031	1.657±0.035	0.0720±0.0005	987±15	101

Table 2. cont.

Grain area	U (μg/g)	Th (μg/g)	Th/U	$^{206}Pb/^{204}Pb$	f_{206} %	$^{206}Pb/^{238}U$ ±1σ error	$^{207}Pb/^{235}U$ ±1σ error	$^{207}Pb/^{206}Pb$ ±1σ error	$^{207}Pb/^{206}Pb$ Age (Ma)±1σ	% conc
22.1	93	38	0.405	30500	0.056	0.1690±0.0033	1.654±0.058	0.0710±0.0019	958±55	105
23.1	131	62	0.472	78500	0.022	0.1651±0.0032	1.699±0.043	0.0746±0.0010	1058±28	93
26.1	160	71	0.443	1627	1.049	0.1653±0.0032	1.616±0.063	0.0709±0.0023	954±66	103
27.1	251	144	0.573	56900	0.030	0.1644±0.0031	1.643±0.040	0.0725±0.0010	999±27	98
30.1	140	84	0.600	10300	0.166	0.1706±0.0033	1.690±0.053	0.0718±0.0016	981±46	103
31.1	269	153	0.571	14200	0.120	0.1708±0.0033	1.661±0.041	0.0705±0.0010	944±29	108
33.1	167	123	0.735	20900	0.082	0.1586±0.0031	1.602±0.057	0.0732±0.0020	1021±56	93
36.1	259	149	0.576	45100	0.038	0.1560±0.0030	1.554±0.045	0.0723±0.0014	993±41	94
37.1	91	43	0.473	44300	0.039	0.1682±0.0034	1.658±0.053	0.0715±0.0016	971±46	103
40.1	180	115	0.637	15500	0.110	0.1672±0.0033	1.640±0.047	0.0712±0.0014	962±39	104
41.1	329	184	0.559	32800	0.052	0.1666±0.0032	1.627±0.039	0.0708±0.0009	952±26	104
19.2	246	141	0.576	14200	0.121	0.1594±0.0030	1.559±0.042	0.0709±0.0012	955±35	100
33.2	223	163	0.731	2762	0.618	0.1678±0.0033	1.569±0.060	0.0678±0.0021	862±65	116
46.1	188	65	0.345	8648	0.197	0.1629±0.0031	1.635±0.048	0.0728±0.0014	1009±40	96
47.1	160	64	0.399	5640	0.303	0.1654±0.0032	1.643±0.056	0.0721±0.0018	988±53	100
50.1	217	89	0.413	11300	0.151	0.1681±0.0033	1.636±0.043	0.0706±0.0011	946±32	106
51.1	128	46	0.358	23100	0.074	0.1621±0.0032	1.595±0.054	0.0714±0.0018	968±53	100
54.1	191	102	0.534	37500	0.046	0.1653±0.0032	1.644±0.042	0.0721±0.0011	989±30	100
55.1	283	178	0.631	21600	0.079	0.1619±0.0031	1.612±0.044	0.0722±0.0012	991±35	98
						91286413 (felsic layer, paragneiss, Mount Meredith)				
1.1	500	175	0.350	3281	0.458	0.3923±0.0074	6.792±0.138	0.1256±0.0007	2037±10	105
2.1	458	274	0.599	2513	0.597	0.3910±0.0074	6.801±0.140	0.1262±0.0008	2045±12	104
4.1	100	40	0.400	806	1.719	0.5090±0.0100	12.294±0.308	0.1752±0.0023	2608±22	102
5.1	238	178	0.749	1444	1.054	0.3667±0.0070	5.753±0.135	0.1138±0.0013	1861±21	108
5.2	379	320	0.844	1984	0.767	0.3622±0.0068	5.712±0.124	0.1144±0.0010	1870±16	107
7.1	141	90	0.634	4303	0.313	0.5081±0.0098	13.641±0.293	0.1947±0.0015	2782±12	95
9.1	74	47	0.636	1355	1.108	0.3623±0.0072	6.406±0.191	0.1282±0.0026	2074±36	96
10.1	414	142	0.342	12400	0.126	0.3351±0.0063	5.145±0.107	0.1113±0.0007	1821±12	102
10.2	566	160	0.283	5909	0.264	0.3043±0.0057	4.529±0.092	0.1079±0.0006	1765±11	97
12.1	340	228	0.671	3688	0.417	0.3393±0.0064	5.378±0.114	0.1150±0.0009	1879±14	100
13.1	235	132	0.559	2365	0.635	0.3806±0.0072	6.674±0.148	0.1272±0.0012	2059±16	101
14.1	149	86	0.578	3227	0.426	0.5305±0.0156	12.901±0.399	0.1764±0.0012	2619±11	105
15.1	146	89	0.610	2106	0.653	0.5177±0.0152	12.668±0.394	0.1775±0.0013	2629±12	102
16.1	89	28	0.315	783	1.890	0.4066±0.0120	7.150±0.265	0.1276±0.0024	2065±34	107
16.2	1028	5	0.005	6521	0.244	0.2526±0.0073	3.358±0.101	0.0964±0.0005	1556±9	93
17.1	714	478	0.669	8953	0.157	0.4942±0.0144	11.099±0.328	0.1629±0.0004	2486±5	104
18.1	270	133	0.493	1827	0.839	0.3561±0.0104	5.624±0.181	0.1146±0.0012	1873±19	105
20.1	628	251	0.399	11200	0.132	0.3833±0.0111	6.724±0.200	0.1272±0.0005	2060±7	102
24.1	233	126	0.539	2558	0.526	0.5531±0.0162	14.737±0.448	0.1932±0.0010	2770±9	102
24.2	1292	6	0.005	10800	0.145	0.2878±0.0083	4.256±0.126	0.1073±0.0004	1753±6	93

Table 2. cont.

Grain area	*U (μg/g)*	*Th (μg/g)*	*Th/U*	$^{206}Pb/^{204}Pb$	f_{206} %	$^{206}Pb/^{238}U$ ±1σ *error*	$^{207}Pb/^{235}U$ ±1σ *error*	$^{207}Pb/^{206}Pb$ ±1σ *error*	$^{207}Pb/^{206}Pb$ *Age (Ma)*±1σ	% *conc*
25.1	139	38	0.273	1878	0.732	0.5171±0.0152	12.956±0.407	0.1817±0.0014	2669±13	101
26.1	116	43	0.374	2679	0.511	0.5075±0.0150	12.795±0.403	0.1829±0.0014	2679±13	99
27.1	122	65	0.536	1630	0.932	0.3597±0.0106	5.988±0.210	0.1207±0.0019	1967±28	101
28.2	1049	321	0.306	4789	0.316	0.3879±0.0113	6.272±0.187	0.1173±0.0005	1915±8	110
29.1	298	103	0.344	5499	0.246	0.6081±0.0178	16.155±0.488	0.1927±0.0009	2765±8	111
30.1	86	72	0.835	964	1.525	0.3410±0.0172	5.716±0.337	0.1216±0.0030	1979±45	96
30.2	1536	14	0.009	5259	0.299	0.2433±0.0122	3.423±0.174	0.1020±0.0004	1662±8	84
						91286412 (paragneiss, Mount Meredith)				
32.1	81	37	0.464	577	2.586	0.3334±0.0169	5.034±0.326	0.1095±0.0038	1792±64	104
32.2	353	49	0.139	1922	0.787	0.2920±0.0146	4.582±0.242	0.1138±0.0013	1861±21	89
33.1	284	134	0.474	6750	0.229	0.3457±0.0044	5.350±0.092	0.1122±0.0011	1836±18	104
34.1	257	149	0.580	5103	0.292	0.3514±0.0045	6.292±0.103	0.1299±0.0012	2096±16	93
35.1	260	67	0.257	7101	0.194	0.4586±0.0058	11.277±0.167	0.1784±0.0011	2638±10	92
37.1	205	105	0.512	13900	0.110	0.3609±0.0046	5.740±0.096	0.1153±0.0011	1885±17	105
38.1	156	82	0.524	3987	0.387	0.3558±0.0047	5.579±0.110	0.1137±0.0015	1859±24	106
40.1	109	76	0.693	1368	1.135	0.3212±0.0043	4.868±0.138	0.1099+0.0026	1798±43	100

f_{206} is the proportion, expressed as a percentage, of common ^{206}Pb to total ^{206}Pb. The reported ages are derived from radiogenic $^{207}Pb/^{206}Pb$ ratios. % conc is the relative concordance of the isotopic ages; values less than 100% plot below concordia, and values above 100% plot above concordia. The grain area values represent sequentional analytical order. Gaps in the order do not indicate that data have been omitted; some reflect the abortion of a partial analysis owing to technical considerations, whereas others are due to the intermingling of analyses from different samples (as for samples 91286403 and 91286407).

arête between two alpine glaciers. At this locality the somewhat altered granite contains abundant mafic xenoliths, biotite aggregates (~4%) which might be partly of secondary origin, and sericitised oligoclase. Accessory minerals are allanite, titanite, zircon, apatite, and magnetite, plus secondary muscovite, chlorite, carbonate, and ?prehnite. Offshoots of the granite cut the volcanics.

Sample 91286416 (lat. 71°28.75′S, long. 67°45′E) was collected from a medium-grained, foliated biotite ± hornblende granodiorite in the central part of Fisher Massif. A major mylonite zone forms the boundary between the granodiorite and volcanics here, whereas other contacts are poorly exposed (moraine-covered). Unlike the biotite granite, the granodiorite is cut by numerous undeformed mafic dykes, suggesting that it is the older of the two intrusions. Its texture is hypidiomorphic inequigranular, but the rock is considerably recrystallised and altered; plagioclase (zoned oligoclase), in particular, is sericitised, and near the mylonite zone the granodiorite is highly sheared. Dark brown biotite (5%) occurs both as large grains and fine-grained aggregates. Minor phases are allanite, titanite, zircon, apatite, ilmenite, magnetite, epidote, muscovite, chlorite, and carbonate. Hornblende is absent from the sample, but occurs in other parts of the granodiorite.

Neither of the Fisher Massif intrusives clearly represents juvenile felsic crust, because Ce/Y ratios — and, by implication, rare-earth-element (REE) fractionation — are too low to be consistent with the melting of a garnet-bearing mafic source in the mantle; however, an amphibolite source (e.g., subducted, hydrated oceanic crust) could have produced the melt from which these intrusives were derived. Both samples have irregular spidergrams (depleted in P and Ti relative to light REE and Zr) typical of intracrustal melts, yet neither shows the marked Sr depletion consistent with major plagioclase control (Fig. 2). The moderately high Y (30 ppm), low Ce/Y_n (3.8, chondrite-normalised), and Sr depletion of the granodiorite (91286416) indicate that either residual plagioclase or plagioclase fractionation, or both, were of some significance, and that an intracrustal origin is more likely for this sample than for 91286415. The younger granite (91286415) — with 21 ppm Y, Ce/Y_n of 5.7, and, more significantly, little or no Sr depletion — may represent new crust, although isotopic data would be necessary to confirm this. Melting of intermediate to felsic lower-crustal rocks cannot be discounted, but the lack of an Sr anomaly requires very high degrees of melting (Champion & Sheraton 1993).

Zircon grains in sample 91286415 are moderately uniform, averaging about 180 × 90 μm. They are euhedral to subhedral, clear and unzoned, and evidently of igneous origin. Perfectly preserved terminations composed of both primary and secondary pyramids are common, as are primary and secondary prisms. All 16 analyses define a statistically simple concordant population with $^{206}Pb/^{238}U$, $^{207}Pb/^{235}U$, and $^{207}Pb/^{206}Pb$ ages of 1056 ± 24, 1048 ± 25, and 1020 ± 48 Ma respectively (Fig. 4a). The last is preferred as the crystallisation age of the granite.

The slightly larger zircons in 91286416 (averaging 220 × 90 μm) are mostly subhedral, not visibly zoned, and cloudy, presumably because they contain tiny inclusions. However, they include some clear grains, and others with a faint zoning. Both primary and secondary prisms and pyramids are common. All 17 analyses form a statistically simple concordant population with $^{206}Pb/^{238}U$, $^{207}Pb/^{235}U$, and $^{207}Pb/^{206}Pb$ ages of 1309 ± 29, 1297 ± 23, and 1293 ± 28 Ma respectively (Fig. 4b). The last best dates the crystallisation of this granodiorite.

Sample 91286417 (lat. 71°28′S, long. 67°41′E), very fine-grained hornblende metadacite, consists of relict altered plagioclase and quartz phenocrysts and has a relict ?flow foliation. It contains green hornblende (~12%), which forms fine-grained aggregates with carbonate, accompanied by minor biotite, chlorite, apatite, and opaque minerals.

Compared with the nearby granitic rocks the metadacite has lower Al_2O_3, K_2O, Rb, and Ba, and higher MgO, CaO, Cr, and Ni. It is markedly Di-normative and has an unfractionated REE pattern (Ce/Y_n = 2.0). A small positive Sr anomaly on its spidergram (Fig. 2) may result from plagioclase accumulation. Associated rocks such as low-K island-arc tholeiites and andesitic to rhyolitic calc-alkaline volcanics are interpreted by Mikhalsky et al. (1996) as evidence of generation at an active continental margin (?Andean type) with an associated island arc.

Zircon grains in the metadacite have diverse morphologies. A few have straight edges, but most are subhedral to anhedral. Their average grainsize is 180 × 110 μm. Most are broken; some have totally ragged margins, yet others are only slightly embayed. Second-order pyramids are present on some terminations. Zoning is uncommon, and there are no obvious cores.

The isotopic data for 91286417 are more scattered than for the other Fisher Massif samples (Fig. 4c). Although this might be partly due to analytical problems (discussed in the Appendix), a geological component of scatter is evident. There is little, if any, correlation of morphology with either isotopic or chemical (U, Th, Th/U) composition of the grains (Table 2) to assist in an interpretation. The most obvious analysis to be discarded from the age calculations is that of grain 15.1, which has an age of about 1900 Ma and must have a xenocrystic origin. Analyses 4.1, 11.1, and 12.1 (shaded in Fig. 4c) plot well below the other analyses, either because they experienced post-crystallisation Pb loss, or because they grew during a subsequent event. The chi-square value of the remaining 16 analyses is 3.4, which indicates a non-ideal grouping. Deletion of four more analyses (2.1, 8.2, 14.1, and 17.1; shaded in Fig. 4c) reduces the value to unity. The removal of these points does not significantly alter the resultant mean age. The remaining 12 analyses yield a concordant data set with pooled $^{206}Pb/^{238}U$, $^{207}Pb/^{235}U$, and $^{207}Pb/^{206}Pb$ ages of 1277 ± 24, 1281 ± 18, and 1283 ± 21 Ma respectively. The spread of both Pb/U ages may signify minor recent Pb loss. Because all the well-preserved grains of igneous appearance are included in the final grouping, the igneous crystallisation of the metadacite is deduced to have occurred at 1283 ± 21 Ma.

Granitic rocks at Mount Collins

Mount Collins, a narrow ridge 13 km long 20 km west of Fisher Massif, is dominated by granitic rocks cut by abundant undeformed tholeiitic dykes. Its principal rock types are pink syenitic granite and quartz monzonite which both grade into darker rocks of charnockitic appearance (though lacking orthopyroxene) and form veins and migmatite in older grey granite. Mafic dykes of at least two generations intrude the granites, and all but the youngest dykes are cut by an association of minor granite sheets, pegmatites, and brittle shear zones.

Sample 91286419, from the eastern end of Mount Collins (lat. 71°29.75′S, long. 66°45′E), is an unfoliated, slightly recrystallised fine to medium-grained grey hornblende–biotite granite (almost a quartz monzonite) that consists of quartz, slightly perthitic microcline (as sparse phenocrysts), oligoclase–andesine, dark brownish green hornblende (4%), dark brown biotite (6%), and minor allanite, zircon, apatite, ilmenite, and magnetite. Sample 91286420, from the same locality, is a medium-grained pink equigranular hornblende–biotite granite which veins and intrudes the grey granite. It is petrographically similar to sample 91286419, but contains more quartz and microcline, and less plagioclase (albite–oligoclase), hornblende (2%), and biotite (2%). Microcline is markedly perthitic, some grains approaching mesoperthite.

Both samples have fractionated spidergrams that evince marked negative Sr anomalies (Fig. 2), typical of granites derived by the melting of an intracrustal source with residual

plagioclase but not garnet. Moderately fractionated Ce/Y_n ratios (11.2 in 91286419, and 10.2 in 91286420) are due to high Ce rather than low Y contents. 91286420 is much more evolved (low MgO, CaO, Ba, and Sr, and high SiO_2), and could have been derived from a less siliceous melt (compositionally resembling 91286419) by the fractionation of plagioclase, apatite, an Fe–Ti oxide, and a ferromagnesian phase. Both are enriched in Zr, Nb, Y, La, and Ce compared with the Fisher Massif granitic rocks, consistent with the high-temperature melting of near-anhydrous granulite-facies source rocks (Sheraton & Black 1988), and both are less visibly altered.

Zircon grains in 91286419 are moderately coarse (averaging 400 × 150 μm) and of igneous morphology, albeit with rounded terminations. About half of them are euhedrally zoned. Cores (not analysed) are rare. All of the 13 analyses form a statistically simple concordant population with $^{206}Pb/^{238}U$, $^{207}Pb/^{235}U$, and $^{207}Pb/^{206}Pb$ ages of 992 ± 22, 989 ± 20, and 976 ± 25 Ma respectively (Fig. 4d). The intrusion age is considered to be 976 ± 25 Ma.

The moderately coarse elongate zircon grains (averaging 300 × 130 μm) in 91286420 consist mostly of perfectly euhedral first-order prisms and pyramids. About half of them are clear and homogeneous; the rest display euhedral igneous-type zoning. A few have small, roughly equant cores (not analysed). All 27 isotopic analyses form a statistically simple concordant population with pooled $^{206}Pb/^{238}U$, $^{207}Pb/^{235}U$, and $^{207}Pb/^{206}Pb$ ages of 980 ± 11, 980 ± 8, and 984 ± 7 Ma (Fig. 4e); the last is assumed to be the crystallisation age of this granite.

Sample 91286421 (lat. 71°30.62′S, long. 66°31′E), from the western end of Mount Collins, is a dark medium to coarse-grained, lightly recrystallised, slightly K-feldspar-phyric pyroxene–quartz syenite containing locally sericitised plagioclase (calcic oligoclase). Pyroxene (~7%) in the sample is extensively altered to colourless to pale green clinoamphibole and iddingsite; though the fresher grains are clinopyroxene,

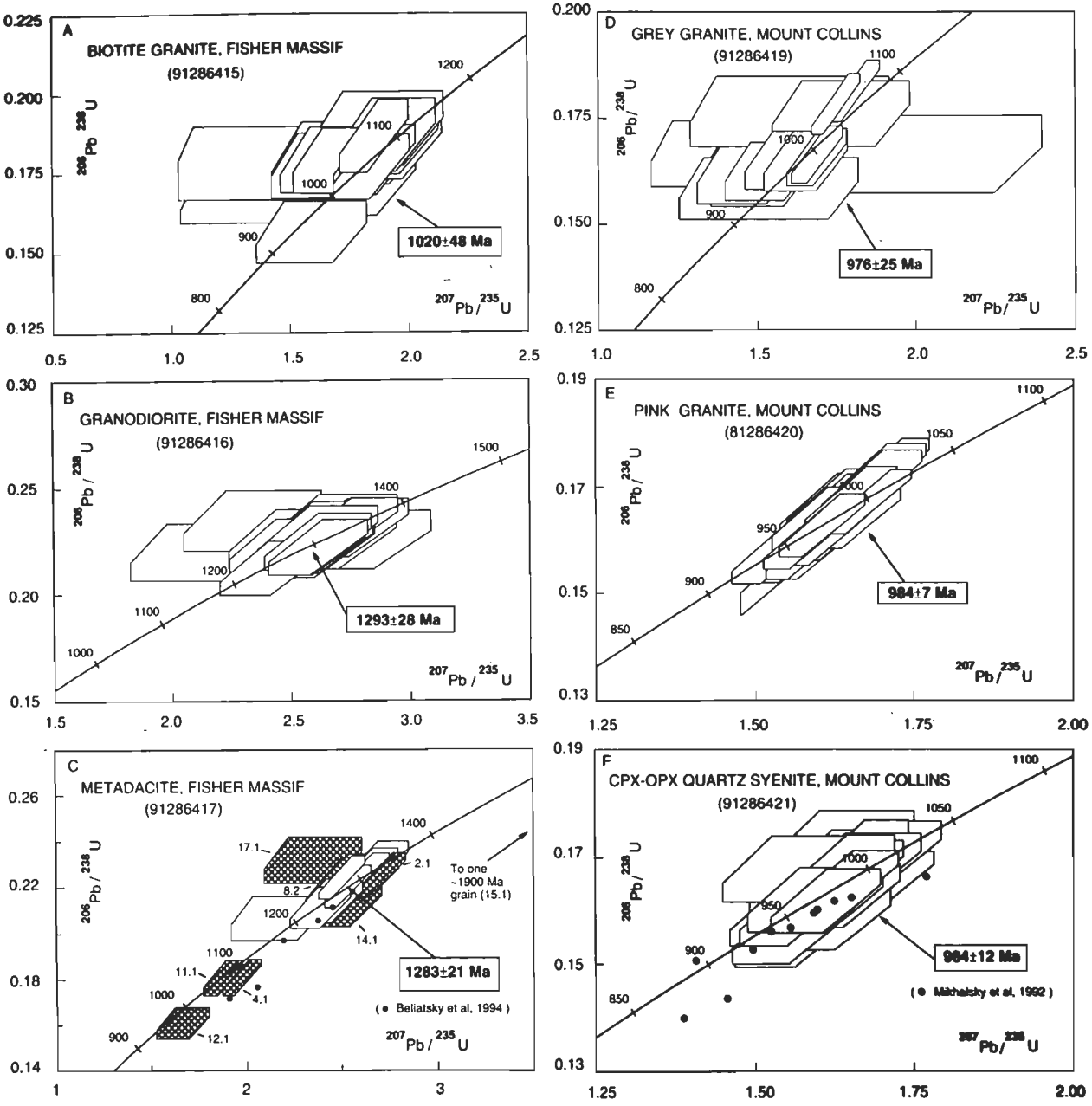

Figure 4. U–Pb concordia diagrams showing SHRIMP data for samples from the Fisher Massif and Mount Collins. Diagram C includes orthodox multigrain data of Beliatsky et al. (1994; filled circles, errors not supplied). Diagram F includes multigrain data of Mikhalsky et al. (1992; filled circles, errors in Pb/U ratios not supplied). SHRIMP error boxes reflect 95% confidence limits.

some of the intensely altered ones might have been orthopyroxene. Zircon is unusually abundant in the rock, which also contains small amounts of biotite, hornblende, ilmenite, magnetite, apatite, and carbonate. Other rocks from the same area grade into monzonite and quartz monzonite, which generally contain more hornblende and, to a lesser extent, biotite. Some of the hornblende forms sieve-like aggregates with quartz, possibly replacing pyroxene. Partly altered clinopyroxene locally exhibits exsolution textures. Allanite is a significant accessory mineral in some of these rocks, and all have abundant zircon.

The quartz syenite (91286421) is unrelated to the granites analysed from the eastern end of Mount Collins; it has lower MgO, Th, Cr and Ni, and higher Ba and Zr (allowing for different SiO_2 contents). Its spidergram is unusual in showing a pronounced positive Zr anomaly, as well as Ba and K anomalies, but there are no corresponding enrichments in REE, Nb, Y, or Ga (Fig. 2). The rock does not, therefore, have the compositional features (other than high Zr) of A-type ('anorogenic') intrusions (Collins et al. 1982). This is not surprising, as the intrusion is evidently syn- to late metamorphic in age. Fractionation of an alkali basalt magma, probably with some degree of crustal assimilation, was suggested by Zhao et al. (1995) for the Cambrian Yamato syenite of Dronning Maud Land. However, the high Zr and lack of a negative Sr anomaly (as well as a large positive Eu anomaly) in an otherwise highly evolved (low *mg*, Ni and Cr) rock suggest that the Mount Collins syenite is a feldspar- (and zircon-) rich cumulate.

Zircons in this rock are moderately fine-grained (averaging 100×50 μm), optically clear, unzoned, and of obvious original igneous morphology, though no sharp terminations remain. All 29 isotopic analyses define a simple statistical population with concordant $^{206}Pb/^{238}U$, $^{207}Pb/^{235}U$, and $^{207}Pb/^{206}Pb$ ages of 982 ± 11, 981 ± 9, and 984 ± 12 Ma, of which the last defines the crystallisation age (Fig. 4f). The ages of all three analysed samples from Mount Collins are thus indistinguishable.

Paragneiss at Mount Meredith

The southeastern side of Mount Meredith is composed principally of coarse-grained, pegmatite-banded biotite–quartz–feldspar gneiss. Though non-diagnostic, assemblages and textures suggest this rock was metamorphosed to the amphibolite facies. Sample 91286412 (lat. 71°15.5′S, long. 67°42′E), a granoblastic inequigranular interlobate-textured fine to medium-grained gneiss, has a prominent foliation defined by oriented biotite grains. Rich in quartz (~37%) and sodic andesine (~53%), it contains only minor, slightly perthitic orthoclase (~2%), dark brown biotite (6%, partly altered to bright green pleochroic chlorite), muscovite (1%), and minor apatite, zircon, monazite, and opaque minerals. Retrograde patches contain chlorite, sericite, and a little epidote. Sample 91286413, from a more quartzofeldspathic layer twenty metres up-section from and petrographically similar to 91286412, contains much more quartz (~70%), less plagioclase (sericitised oligoclase, 25%) and biotite (4%), but little or no K-feldspar.

The Mount Meredith samples are probably of sedimentary origin. The normative Q/(Q+Ab+Or) ratio (52%) of sample 91286412 is much higher than in typical felsic igneous rocks, and quartz-rich 91286413 presumably represents a metamorphosed impure sandstone or quartzite (i.e. a psammite). Both samples have fractionated spidergrams that show marked Nb, Sr, P, and Ti depletion (Fig. 2), typical of clastic sedimentary rocks (Tarney et al. 1987). 91286413 is more depleted in most incompatible elements, particularly Ba, consistent with its very low K-feldspar content. Moderately high Zr in both rocks suggests the presence of detrital zircon. Somewhat surprisingly, neither sample is very peraluminous, implying derivation from immature sedimentary rocks. Their K/Na ratios suggest the rocks were derived from a K-poor source, like some Archaean hornblende–biotite gneisses of the southern PCM (J.W. Sheraton, unpublished data).

Most zircon grains in 91286412 are about 200 μm long, and have elongation ratios between 2:1 and 3:1. The morphology of the more euhedral grains indicates a magmatic origin, although most have been rounded, and some pitted by subsequent sedimentary processes. Some grains are zoned; others are optically homogeneous. Some have cores, but the enclosing rims are too narrow (just a few microns) to be analysed.

Zircon grains in 91286413 are on average slightly larger than those in 91286412, and appear to constitute two morphological types: one comprises grains resembling but somewhat more rounded than those in 91286412; in the other type, the grains are more equant (elongation ratios 1:1 to 2:1), multifaceted, and invariably homogeneous.

Similar populations of Archaean and Proterozoic zircons occur in both samples (Fig. 3d). The Archaean grains range in $^{207}Pb/^{206}Pb$ age from about 2800 Ma to 2500 Ma. A distinct hiatus separates that group from the Proterozoic zircons, which range from 2100 Ma to 1800 Ma old. There is a suggestion that the Archaean group might represent three discrete populations at about 2500, 2650–2700, and ca 2800 Ma, but differentiating age groups among the Proterozoic grains requires a higher degree of speculation. Both morphological types of zircon in the more leucocratic sample exhibit a similar range of ages.

Overgrowths on three zircons from the more quartzofeldspathic sample were found to have much higher U contents (>1000 ppm) than the cores (<200 ppm) they enclose. Two rims (24.2 and 30.2) yielded similar ages of about 1670 Ma, despite their contrasting core ages (24.1 Archaean, 30.1 Proterozoic), and the other analysed rim (16.2) was about 100 Ma younger; all three are somewhat discordant. The overgrowths are similarly structured: each has inner and outer growth zones separated by a thin, more brightly cathodoluminescent layer, from which one might infer that they were generated by the same event — although it is not clear whether that event produced the present banded gneiss or an antecedent.

Discussion

Orthopyroxene-bearing quartz monzonite from Loewe Massif and quartz syenite from Mount Collins have yielded identical ages of 980 ± 21 and 984 ± 12 Ma (Table 3), implying that they formed during widespread magmatism that accompanied regional high-grade metamorphism. Mount Collins is the southernmost pyroxene-bearing intrusion, and Loewe Massif the largest. Intrusive charnockitic rocks are common in this part of East Antarctica; they also occur at several places in the Porthos Range (Munksgaard et al. 1992), in the Reinbolt Hills area (140 km east of Jetty Peninsula; Nichols & Berry 1991), around Mawson Station on the Mac.Robertson Land coast (Young & Black 1991), and at many other localities. Previously reported dates are similar to those reported here. For example, zircons from the Mawson charnockite dated by Young & Black (1991) using SHRIMP yielded indistinguishable crystallisation ages of 985 ± 29 and 954 ± 2 Ma.

The charnockitic intrusives postdate the dominant flat-lying structures of the northern PCM (D_3 of Fitzsimons & Thost 1992). D_3 most likely developed during the earlier stages of the ca 1000-Ma metamorphic episode. Later upright fold and shear structures (D_{5-8} of Fitzsimons & Thost 1992) postdate the intrusions and leucogneiss bodies, but the interval may be short. An imprecise Rb–Sr isochron age of 880 ± 140 Ma for the Porthos Range charnockites (Hensen et al. 1992) suggests that no younger (e.g., 500-Ma) high-grade tectonothermal events have affected these rocks.

Having zircon populations that are simple and isotopically concordant to within error, the three analysed granitic rocks

Table 3. Summary of SHRIMP zircon ages from the northern Prince Charles Mountains.

Sample (prefix 912864)	*Locality*	*Lithology*	$^{207}Pb/^{206}Pb$ *age* ± *ts*	$^{206}Pb/^{238}U$ *age* ± *ts*	± *Inheritance*
07	Loewe Massif	Quartz monzonite	980 ± 21	944 ± 41	
19	Mount Collins	Granite	976 ± 25	992 ± 22	
20	Mount Collins	Granite	984 ± 7	980 ± 11	
21	Mount Collins	Quartz syenite	984 ± 12	982 ± 11	
03	Mount McCarthy	Leucogneiss	990 ± 30	963 ± 100*	~1850 Ma
15	Fisher Massif	Granite	1020 ± 48	1056 ± 24	
16	Fisher Massif	Granodiorite	1293 ± 28	1309 ± 29	
17	Fisher Massif	Metadacite	1283 ± 21	1277 ± 24	~1900 Ma
12/13	Mount Meredith	Felsic gneiss	2800–2500, 2100–1800 Ma detrital populations		

* Error multiplication by 2.8 to account for residual scatter.

from Mount Collins are essentially coeval at ca 980 Ma. Our data, therefore, contrast with the conventional bulk-zircon data of Mikhalsky et al. (1992) for three syenitic granites from Mount Collins. Mikhalsky et al. (1992) obtained a cluster of near-concordant points between 900 and 1000 Ma, plus a number of more discordant points with younger ages, and two discordant points from one sample (34341) with older $^{207}Pb/^{206}Pb$ ages (cf. Fig. 4f). By extrapolating to concordia through these exceptional discordant points, Mikhalsky et al. (1992) deduced a crystallisation age of 1400 ± 80 Ma for all three samples and later disturbances between 700 and 900 Ma. Our results, however, suggest that crystallisation at ca 980 Ma was much more likely. Sample 34341, which gave the older apparent ages probably contains some inherited zircon, while the more highly discordant points in the other samples might reflect partial Pb loss in recent times. We can see no evidence for a disturbance at ca 700 Ma (cf. Mikhalsky et al. 1992).

Our results from Fisher Massif support the conclusions of Beliatsky et al. (1994), based on bulk zircon data, regarding the age of the metavolcanic sequence there. Our metadacite sample contained zircons of diverse morphology: a concordant ca 1280 Ma population with some excess scatter in age suggesting a non-ideal grouping; one clearly inherited grain with a minimum age of ca 1900 Ma; and three analyses with younger apparent ages of ca 1100 Ma, which might reflect lost Pb (? at 1000 Ma). From these data, we have interpreted the volcanic eruption age to be 1283 ± 21 Ma, which also coincides with our age estimate for the nearby granodiorite (1293 ± 28 Ma). Beliatsky et al.'s (1994) pooled fractions (shown in Fig. 4c for comparison) form a similar array of points indicating intrusion ca 1300 Ma, plus one sample with a major inherited component (offscale). The extrapolated lower intercept ages of these bulk discordia (364 ± 16 and –63 ± 68 Ma) probably are not geologically significant.

The new data for Fisher Massif and Mount Collins also provide important age constraints on the mafic dykes in the area. These had been previously correlated with metadolerite dyke swarms in the southern PCM (Tingey 1982), believed to be of Mesoproterozoic age on the basis of their geochemical similarity to dated dyke suites in the Vestfold Hills and Enderby Land (Sheraton & Black 1981). However, the geochemistry of the northern PCM dyke suites is not consistent with such a correlation (J.W. Sheraton, unpublished data), and indicates different origins for the Mount Collins dykes and the Fisher Massif–Mt Willing group (e.g., much lower Nb/Zr in the Fisher Massif dykes). Our isotopic results support this distinction and show that the Fisher Massif dykes are between 1290 and 1020 Ma old (i.e. bracketed by the ages of the two analysed granites), whereas the Mount Collins dykes are younger than 980 Ma. In comparison, the tholeiitic suites in the Vestfold Hills, which have been correlated with the southern PCM metadolerites, are now known to have been emplaced in separate events at ca 1380 and 1240 Ma (Lanyon et al. 1993). Such local and regional differences may assist with terrane reconstructions.

The isotopic ages presented in this paper do not address directly the question of the original protolith ages of the northern PCM basement orthogneisses affected by the ca 1000-Ma tectonothermal episode. However, some indication of basement ages is recorded in the minor inherited zircon in two of the samples: one ca 1900-Ma grain in the Fisher Massif metadacite, and the two ca 1850-Ma cores in the locally derived Mount McCarthy leucogneiss. A felsic xenolith from the Mawson charnockite studied by Young & Black (1991) contains many zircons in this age range, which is well represented also in the detrital zircon population analysed from the Mount Meredith paragneiss. The Mount Meredith suite also includes a late Archaean population (2500 to 2800 Ma), perhaps derived from the southern PCM terranes. Additionally, analyses of zircon rims from the Mount Meredith suite and also from the Mount McCarthy inherited zircons, suggest a possible metamorphic event at ca 1650 Ma. The absence of zircons in the age range 1300 to 1000 Ma from the paragneiss implies that its sedimentary precursor accumulated before the other rocks dated in this study were emplaced.

Model ages (1070–1320 Ma) derived from previously compiled initial Sr ratios for northern PCM orthogneisses (Tingey 1991) imply relatively short crustal residence times for their precursors, but could also reflect the effects of disturbance at ca 1000 Ma. Nd-depleted-mantle (DM) model ages, which may be more reliable, extend as far back as 2000 Ma (S.-s. Sun, unpublished data).

These results will also influence the current debate on the nature and extent of the 500-Ma metamorphic episode in East Antarctica. At present, the only rock in the northern PCM known to have formed 500 Ma ago is the Jetty Peninsula pegmatite analysed by Manton et al. (1992). None of the zircon populations analysed in this study includes a 500-Ma component either in the form of younger rims, as separate zircon populations, or as the lower intercept of Pb-loss discordia. Most of our data are concordant to within error, and the few exceptions show no clear discordance trends — like the zircon populations of the basement gneisses of the Vestfold Hills on the Prydz Bay coast (Black et al. 1991), but in marked contrast to those of the nearby Rauer Islands (Kinny et al. 1993) and Larsemann Hills (Zhao et al. in press), which show major effects of 500-Ma events on the zircon isotopic systematics. Furthermore, large (>1 km) granite bodies were emplaced in the Mawson Escarpment (southern PCM) and eastern Amery Ice Shelf areas at about this time (Sheraton & Black 1988; Tingey 1991).

Tingey (1982, 1991) interpreted the 500-Ma event in the northern PCM as the time of a low-grade 'pervasive heating event' which reset Rb–Sr mineral systems (biotite, muscovite). Hand et al. (1994), by contrast, assigned this event to probable upper-amphibolite-facies metamorphism on Else Platform. Zhou & Hensen (1995) obtained ca 500-Ma Sm–Nd ages from garnets in rocks from Mount McCarthy (including the leucogneiss, which yielded 990-Ma zircons in our study). The regional significance of these results is not yet clear. Certainly on Fisher Massif, there is no indication of metamorphic grade ever having advanced beyond the lower amphibolite facies, and textures of the <980 Ma tholeiitic dykes on Mount Collins are intergranular to gabbroic (i.e., igneous).

Conclusion

Two important episodes of magmatism in the northern PCM occurred at 1300–1280 Ma (Fisher Massif–Mount Willing area) and at 1020–980 Ma. The ca 1300-Ma episode involved multiple intrusions of mafic to felsic magmas in the southern part of the region, and extrusion of a major volcanic pile on Fisher Massif. The ca 1000-Ma episode involved the widespread intrusion of granitic magmas (orthopyroxene-bearing quartz monzonite, granite, and syenitic granite) representing a combination of both mantle-derived and intracrustal melts. These intrusions were accompanied by granulite-facies metamorphism, local partial melting of the country rock gneisses, and the formation of minor leucogneiss bodies, except on Fisher Massif, where a biotite granite pluton was emplaced at this time under lower-amphibolite-facies conditions. The Fisher Massif volcanics have never been metamorphosed beyond the lower amphibolite facies and appear to represent a remnant of originally higher-level crust than the rocks now exposed to the north and west (e.g., Mount Collins), or even a distinct microplate.

Later additions to the northern PCM crust are few. They include: the intrusion on Jetty Peninsula of minor granitic stocks and dykes at ca 940 Ma and of pegmatites at ca 500 Ma (Manton et al. 1992); emplacement of tholeiitic dykes at Mount Collins (<980 Ma) and alkaline dykes of various ages (Sheraton 1983); and deposition of Permian sediments in the Beaver Lake area (Fig. 1) associated with the development of the Lambert Rift. Overall, the 500-Ma metamorphic episode, which is prominent elsewhere in East Antarctica, appears to have been of relatively minor importance in the northern PCM because it affected only some mineral systems.

Acknowledgments

Fieldwork by PDK was funded by a grant from the Antarctic Science Advisory Council. Our thanks to all members of the ANARE 1990–91 PCM expedition, particularly W. Crowe, I. Scrimgeour, N. Williams, and P. Colpo for assistance in sample collection; to AGSO technicians C. Foudoulis, J. Pyke, K. Armstrong, L. Keast, W. Pappas, and E. Webber; and to R.J. Tingey and C.M. Fanning for helpful reviews of the paper.

References

Arriens, P., 1975. The Precambrian geochronology of Antarctica. In: First Australian Geological Convention, Adelaide. Geological Society of Australia, Abstracts, 97–98.

Beliatsky, B.V., Laiba, A.A. & Mikhalsky, E.V., 1994. U–Pb zircon age of the metavolcanic rocks of Fisher Massif (Prince Charles Mountains, East Antarctica). Antarctic Science, 6, 355–358.

Black, L.P., Kinny, P.D., Sheraton, J.W. & Delor, C.P., 1991. Rapid production and evolution of late Archaean felsic crust in the Vestfold Block of East Antarctica. Precambrian Research, 50, 283–310.

Champion, D.C. & Sheraton, J.W., 1993. Geochemistry of granitoids of the Leonora–Laverton region, Eastern Goldfields Province. In: Williams, P.R. & Haldane, J.A. (editors), An international conference on crustal evolution, metallogeny and exploration of the Eastern Goldfields. Extended abstracts. Australian Geological Survey Organisation, Record 1993/94, 39–46.

Chappell, B.W. & White, A.J.R., 1974. Two contrasting granite types. Pacific Geology, 8, 173–174.

Compston, W., Williams, I.S. & Meyer, C., 1984. U–Pb geochronology of zircons from lunar breccia 73217 using a sensitive high mass-resolution ion microprobe. Journal of Geophysical Research, 89, B525–534.

Compston, W., Williams, I.S., Kirschvink, J.L., Zichao, Z. & Guogan, M., 1992. Zircon U–Pb ages for the Early Cambrian time-scale. Journal of the Geological Society, London, 149, 171–184.

Collins, W.J., Beams, S.D., White, A.J.R. & Chappell, B.W., 1982. Nature and origin of A-type granites with particular reference to southeastern Australia. Contributions to Mineralogy and Petrology, 80, 189–200.

Crowe, W., 1994. Geology, metamorphism, and petrogenesis of the Fisher Terrane, Prince Charles Mountains, East Antarctica. MSc thesis, Australian National University, Canberra (unpublished).

Cruikshank, B.I. & Pyke, J.G., 1993. Analytical methods used in Mineral and Land Use Program's geochemical laboratory. Australian Geological Survey Organisation, Record 1993/26.

Cumming, G.L. & Richards, J.R., 1975. Ore lead isotopes in a continuously changing Earth. Earth and Planetary Science Letters, 28, 155–171.

DePaolo, D.J., 1981. Trace element and isotopic effects of combined wallrock assimilation and fractional crystallisation. Earth and Planetary Science Letters, 53, 189–202.

Fedorov, L.V., Zatsepin, E.N. & Leichenkov, G.L., 1987. Geology of the Fisher Massif. Abstract, International Symposium on Antarctic Earth Sciences, Cambridge, UK, 42.

Fitzsimons, I.C.W. & Thost, D.E., 1992. Geological relationships in high-grade basement gneiss of the northern Prince Charles Mountains, East Antarctica. Australian Journal of Earth Sciences, 39, 173–193.

Hand, M., Scrimgeour, I., Stüwe, K., Arne, D. & Wilson, C.J.L., 1994. Geological observations in high-grade mid-Proterozoic rocks from Else Platform, northern Prince Charles Mountains region, East Antarctica. Australian Journal of Earth Sciences, 41, 311–329.

Hensen, B.J., Munksgaard, N.C. & Thost, D.E., 1992. Geochemistry and geochronology of Proterozoic granulites from the northern Prince Charles Mountains, East Antarctica. ANARE Research Notes, 85, 9.

Hofmann, J., 1991. Fault tectonics and magmatic ages in the Jetty Oasis area, Mac.Robertson Land: a contribution to the Lambert rift development. In: Thomson, M.R.A. et al. (editors), Geological evolution of Antarctica. Cambridge University Press, UK, 107–112.

Kamenev, E., Andronikov, A.V., Mikhalsky, E.V., Krasnikov, N.N. & Stüwe, K., 1993. Soviet geological maps of the Prince Charles Mountains, East Antarctic Shield. Australian Journal of Earth Sciences, 40, 501–517.

Kinny, P.D., Black, L.P. & Sheraton, J.W., 1993. Zircon ages and the distribution of Archaean and Proterozoic rocks in the Rauer Islands. Antarctic Science, 5, 193–206.

Lanyon, R., Black, L.P. & Seitz, H.-M., 1993. U–Pb zircon dating of mafic dykes and its application to the Proterozoic geological history of the Vestfold Hills, East Antarctica. Contributions to Mineralogy and Petrology, 115, 184–203.

McKelvey, B.C. & Stephenson, N.C.N., 1990. A geological reconnaissance of the Radok Lake area, Amery Oasis, Prince Charles Mountains. Antarctic Science, 2, 53–66.

Manton, W.I., Grew, E.S., Hofmann, J. & Sheraton, J.W., 1992. Granitic rocks of the Jetty Peninsula, Amery Ice Shelf area, East Antarctica. In: Yoshida, Y. (editor), Recent progress in Antarctic Earth science. Terra Scientific Publishing Co., Tokyo, 179–189.

Mikhalsky, E.V., Andronikov, A.V. & Beliatsky, B.V., 1992. Mafic igneous suites in the Lambert Rift Zone. In: Yoshida, Y. (editor), Recent progress in Antarctic Earth science. Terra Scientific Publishing Co., Tokyo, 173–178.

Mikhalsky, E.V., Sheraton, J.W., Laiba, A.A. & Beliatsky, B.V., 1996. Geochemistry and origin of Mesoproterozoic metavolcanic rocks of Fisher Massif, Prince Charles Mountains, East Antarctica. Antarctic Science, 8, 85–104.

Munksgaard, N.C., Thost, D.E. & Hensen, B.J., 1992. Geochemistry of Proterozoic granulites from northern Prince Charles Mountains, East Antarctica. Antarctic Science, 4, 59–69.

Nichols, G.T. & Berry, R.F., 1991. A decompressional P–T path, Reinbolt Hills, East Antarctica. Journal of Metamorphic Geology, 9, 257–266.

Norrish, K. & Chappell, B.W., 1977. X-ray fluorescence spectrometry. In: Zussman, J. (editor), Physical methods in determinative mineralogy. Academic Press, London, 201–272.

Norrish, K. & Hutton, J.T., 1969. An accurate X-ray spectrographic method for the analysis of a wide range of geological samples. Geochimica et Cosmochimica Acta, 33, 431–453.

Sheraton, J.W., 1983. Geochemistry of mafic igneous rocks of the northern Prince Charles Mountains, Antarctica. Journal of the Geological Society of Australia, 30, 295–304.

Sheraton, J.W. & Black, L.P., 1981. Geochemistry and geochronology of Proterozoic dykes of East Antarctica: evidence for mantle metasomatism. Contributions to Mineralogy and Petrology, 78, 305–317.

Sheraton, J.W. & Black, L.P., 1988. Chemical evolution of granitic rocks in the East Antarctic Shield, with particular reference to post-orogenic granites. Lithos, 21, 37–52.

Sheraton, J.W. & England, R.N., 1980. Highly potassic mafic dykes from Antarctica. Journal of the Geological Society of Australia, 27, 129–135.

Sheraton, J.W., Tindle, A.G. & Tingey, R.J., 1996. Geochemistry, origin and tectonic setting of granitic rocks of the Prince Charles Mountains, Antarctica. AGSO Journal of Australian Geology & Geophysics, 16(3), 345–370.

Steiger, R.H. & Jäger, E., 1977. Subcommission on geochronology: convention on the use of decay constants in geo- and cosmochronology. Earth and Planetary Science Letters, 36, 359–362.

Sun, S.-s. & McDonough, W.F., 1989. Chemical and isotopic systematics of oceanic basalts: implications for mantle composition and processes. In: Saunders, A.D. & Norry, M.J. (editors), Magmatism in the ocean basins. Geological Society, Special Publication, 42, 313–345.

Tarney, J., Wyborn, L.E.A., Sheraton, J.W. & Wyborn, D., 1987. Trace element differences between Archaean, Proterozoic and Phanerozoic crustal components — implications for crustal growth processes. In: Ashwal, L.D. (editor), Workshop on the growth of continental crust. Lunar and Planetary Institute, Technical Report 88.02, 139–140.

Tingey, R.J., 1982. The geologic evolution of the Prince Charles Mountains — an Antarctic Archean cratonic block. In: Craddock, C. (editor), Antarctic geoscience. University of Wisconsin Press, Madison, 455–464.

Tingey, R.J., 1991. The regional geology of Archaean and Proterozoic rocks in Antarctica. In: Tingey, R.J. (editor), The geology of Antarctica. Oxford University Press, UK, 1–73.

Watson, E.B. & Harrison, T.M., 1983. Zircon saturation revisited: temperature and composition effects in a variety of crustal magma types. Earth and Planetary Science Letters, 64, 295–304.

Yakovlev, B.G., Ol'khovik, Yu.A., Litvin, A.L., Lavrov, P.I. & Semenov, V.S., 1986. Physico-chemical conditions of metamorphic development in the enderbite–gneiss complex of Mac.Robertson Land (East Antarctica). Mineralogicheskiy Zhurnal, 8(6), 20–34 (in Russian).

Young, D.N. & Black, L.P., 1991. U–Pb zircon dating of Proterozoic igneous charnockites from the Mawson Coast, East Antarctica. Antarctic Science, 3, 205–216.

Zhao, J.-X., Shiraishi, K., Ellis, D.J. & Sheraton, J.W., 1995. Geochemical and isotopic studies of syenites from the Yamato Mountains, East Antarctica: implications for the origin of syenitic magmas. Geochimica et Cosmochimica Acta, 59, 1363–1382.

Zhao, Y., Song, B., Zhang, Z., Fu, Y., Chen, T., Wang, Y., Ren, L., Yao, Y., Li, J. & Liu, X., in press. Early Paleozoic ("Pan-African") thermal event of the Larsemann Hills and its neighbours, Prydz Bay, East Antarctica. Precambrian Research.

Zhou, B. & Hensen, B.J., 1995. Inherited Sm/Nd isotope components preserved in monazite inclusions within garnets in leucogneiss from East Antarctica. Chemical Geology, 121, 317–326.

Appendix

Analytical notes

All samples were chemically analysed (Table 1) in the AGSO laboratory. FeO was determined volumetrically, LOI (loss on ignition) gravimetrically, and Li by atomic absorption spectrophotometry. All the remaining elements were determined by X-ray fluorescence spectrometry according to the methods of Norrish & Hutton (1969) and Norrish & Chappell (1977). Further details of methods and accuracy are presented by Cruikshank & Pyke (1993).

Zircons were separated by standard heavy liquid and magnetic procedures, and then by hand-picking. They were then mounted in epoxy resin discs along with fragments of the SL13 standard zircon. The discs were polished and Au-coated before they were analysed on the SHRIMP I ion-microprobe at the Research School of Earth Sciences, Australian National University, Canberra. (Samples 91286412 and 13 were analysed under similar conditions on the SHRIMP II at the Western Australia Isotope Science Research Centre, Perth.) A primary beam of singly, negatively charged oxygen was used to sputter positive secondary ions from areas of ca 25-μm diameter in individual sectioned zircons. Zr_2O^+, $^{204}Pb^+$, background (baseline) near $^{204}Pb^+$, $^{206}Pb^+$, $^{207}Pb^+$, $^{208}Pb^+$, $^{238}U^+$, ThO^+ and UO^+ were measured in cycles by magnetic-field switching, seven cycles per data set. Operating at a mass resolution >6500 facilitated the removal of significant spectral interferences (Compston et al. 1984). Discrimination between the Pb isotopes was negligible. Differential fractionation between U and Pb was monitored by reference to a $^{206}Pb/^{238}U$ ratio of 0.0928 (equivalent to an age of 572 Ma) for the SL13 zircon standard during interspersed analyses based on a power-law ($^{206}Pb^+/^{238}U^+ = a[^{238}UO^+/^{238}U^+]^2$) relationship. The precision of the Pb/U ratios of the unknowns is augmented

by the precision of $^{206}Pb/^{238}U$ for the standard (these ranged from 1.8% to 3.0%) during each relevent session. The factor 'f' for converting the measured $^{232}ThO^+/^{238}U^+$ ratios to $^{232}Th/^{238}U$ is derived from the linear relationship $f = 0.03446.^{238}UO^+/^{238}U^+ + 0.8680$. Radiogenic Pb compositions were determined after subtracting contemporaneous common Pb (Cumming & Richards 1975).

All reported ages represent $^{207}Pb/^{206}Pb$ data that have been corrected by the ^{204}Pb technique (Compston et al. 1984). However, this procedure had to be modified for deriving the composition (and age) of sample 91286417, because a slight offset from the normal magnetic-field settings for the 207 and 208 peaks had occurred during the analysis of this sample. On the basis of an atypical composition of the standard zircon fragment, this bias was estimated to be 2.7 per cent, and was added to both the 207 and 208 count rates. The same fragment of the standard showed no such bias during the analysis of samples 91286415 and 91286416, confirming that it could be meaningfully used to assess non-ideal instrument conditions.

Ages have been calculated from the U and Th decay constants recommended by Steiger & Jäger (1977). Their uncertainties are expressed at the 95% ($t\delta$) confidence level, and so are the precision fields for each analysis in the concordia diagrams. In contrast, 1-σ precision limits are cited in Table 2.

AGSO Journal of Australian Geology & Geophysics, 16(5), 655–676

Fossil woods from the Upper Permian Bainmedart Coal Measures, northern Prince Charles Mountains, East Antarctica

Lydia Weaver[1], Stephen McLoughlin[1], & Andrew N. Drinnan[1,2]

Upper Permian silicified gymnosperm woods from the Bainmedart Coal Measures (Amery Group) near Beaver Lake, East Antarctica, are described as two new species, *Australoxylon bainii* and *A. mondii*, on the basis of morphometric and qualitative characters — including ray anatomy, tracheid shape, and cross-field pit structure. *Australoxylon mondii* has two forms, one of which is characterised by a distinctive ray architecture comprising semidetached rows of ray cells with intervening gaps bridged by sporadic joins. Wood of *Vertebraria* could not be distinguished from *Australoxylon mondii* on microanatomical characters, which suggests that these two organ taxa may represent different parts of the same glossopterid plant. Many characters used traditionally in wood taxonomy could not be applied owing to substantial variation or preservational differences both within and between specimens.

Three types of presumed biogenic cavities occur in the woods. Coprolite-containing cavities distributed in seasonal bands represent rare evidence for Permian wood-boring arthropods. Other, irregularly distributed cavities and appositions were probably formed by pathogenic fungi.

Growth-ring analysis indicates a markedly seasonal climate with low to moderate interseasonal variation in wood production. Significant intraseasonal influences on growth are also evidenced by numerous false rings.

Introduction

During the Permian (290–245 Ma), Antarctica was centrally placed within the Gondwanan supercontinent. It occupied a high latitude position similar to its present location, and presumably experienced a pronounced seasonal variation in photoperiod. However, the Late Permian climate was very different from current Antarctic conditions. Although current palaeoclimatic models are rudimentary, the large geographical area and latitudinal extent of Gondwana probably prevented the development of south-circumpolar wind and ocean currents, and resulted in a more equable global climate (Parrish 1990). Some indication of the palaeoclimate can be gained from fossil evidence of organisms that were living at the time, such as the growth rings of fossil trees, and congruence with sedimentological data.

Permian strata in East Antarctica and the Transantarctic Mountains preserve a macrofossil and palynological record of *Glossopteris*-dominated plant communities similar to coeval rocks of other Gondwanan continents. In the Beaver Lake area of the northern Prince Charles Mountains, the Bainmedart Coal Measures include about 80 coal seams up to 10.5 m thick. Cropping out over an area of about 280 km^2, these seams are the legacy of once vast and long-lived expanses of forested swamps. Associated macrofossils are mainly glossopterid (*Glossopteris* and *Vertebraria*), but dispersed palynological assemblages reveal a more diverse plant community containing other gymnosperms, lycopods, ferns, and sphenophytes.

The upper 10–40 cm of a coal seam immediately below the base of the Dragon's Teeth Member of the Bainmedart Coal Measures is preserved as a discontinuous nodular chalcedony/chert layer. This layer represents crystallisation of dissolved silica in the uppermost portion of the swamp leaf litter. The chalcedony layer entombed a remarkably well-preserved in situ assemblage of petrified plant organs that were either decaying or growing in the swamp, and prevented this layer of peat from turning to coal during subsequent burial. Leaves of *Glossopteris* lie in layers suggestive of deciduous leaf mats; roots of *Vertebraria* remain in life position; and large fragments of wood represent trunks and branches of substantial trees.

Secondary wood is the only plant tissue not periodically shed. It is produced internally by the vascular cambium, and accumulates in the stems and roots for the life span of the tree. Wood structure is known to reflect the climatic conditions that a plant experienced during growth, but it can also reflect other influences on the tree. Before determining the possible palaeoclimatic signature of fossil woods, it is necessary to identify other factors that might have caused anatomical variation, such as taxonomic diversity, and damage by arthropods, fungi, and other microbial parasites and saprobes. It is also important to distinguish between wood derived from aerial axes and wood from subterranean roots. Root growth partly reflects the productivity of the plant, but is strongly influenced by substrate conditions. Inadvertently mixing data from both stems and roots could lead to spurious interpretations of palaeoenvironmental conditions. These factors need to be identified before palaeoclimatic implications can be assessed.

This paper investigates several aspects of gymnosperm woods from the Bainmedart Coal Measures of the Beaver Lake area, East Antarctica, in order to:

- determine the taxonomic diversity of the woods in the coal measures;
- assess the utility of morphological and anatomical characters traditionally used to differentiate fossil wood taxa;
- compare the Beaver Lake woods with woods described previously from elsewhere in Antarctica and other Gondwanan continents;
- describe and interpret trace fossils associated with the woods; and
- assess the utility of growth rings for local palaeoclimatic interpretation.

Geological setting

The Amery Group is the only substantial Palaeozoic–Mesozoic sedimentary succession known from the eastern half of Antarctica. This gently tilted succession is preserved in a downfaulted block on the western margin of the Lambert Graben, now largely occupied by the Lambert Glacier (Ravich & Fedorov 1982; Tingey 1982; Stagg 1985). It is exposed around the shores of Beaver and Radok Lakes near the western edge of the Lambert Glacier in the northern Prince Charles Mountains (Fig. 1), and correlative rocks may extend subsurficially to parts of the southern Prince Charles Mountains (Tingey 1982; Truswell 1991) and beneath Prydz Bay to the north (Turner 1991; Turner & Padley 1991). The Lambert Graben may represent a pre-break-up extension of the Mahanadi Graben of eastern India, where coeval sedimentary rocks are preserved (Fedorov et al. 1982).

The Amery Group comprises three formations: Radok Conglomerate, Bainmedart Coal Measures, and Flagstone Bench Formation, in ascending order (Fig. 1). The Radok

[1] School of Botany, The University of Melbourne, Parkville, Victoria 3052, Australia.
[2] Author for correspondence.

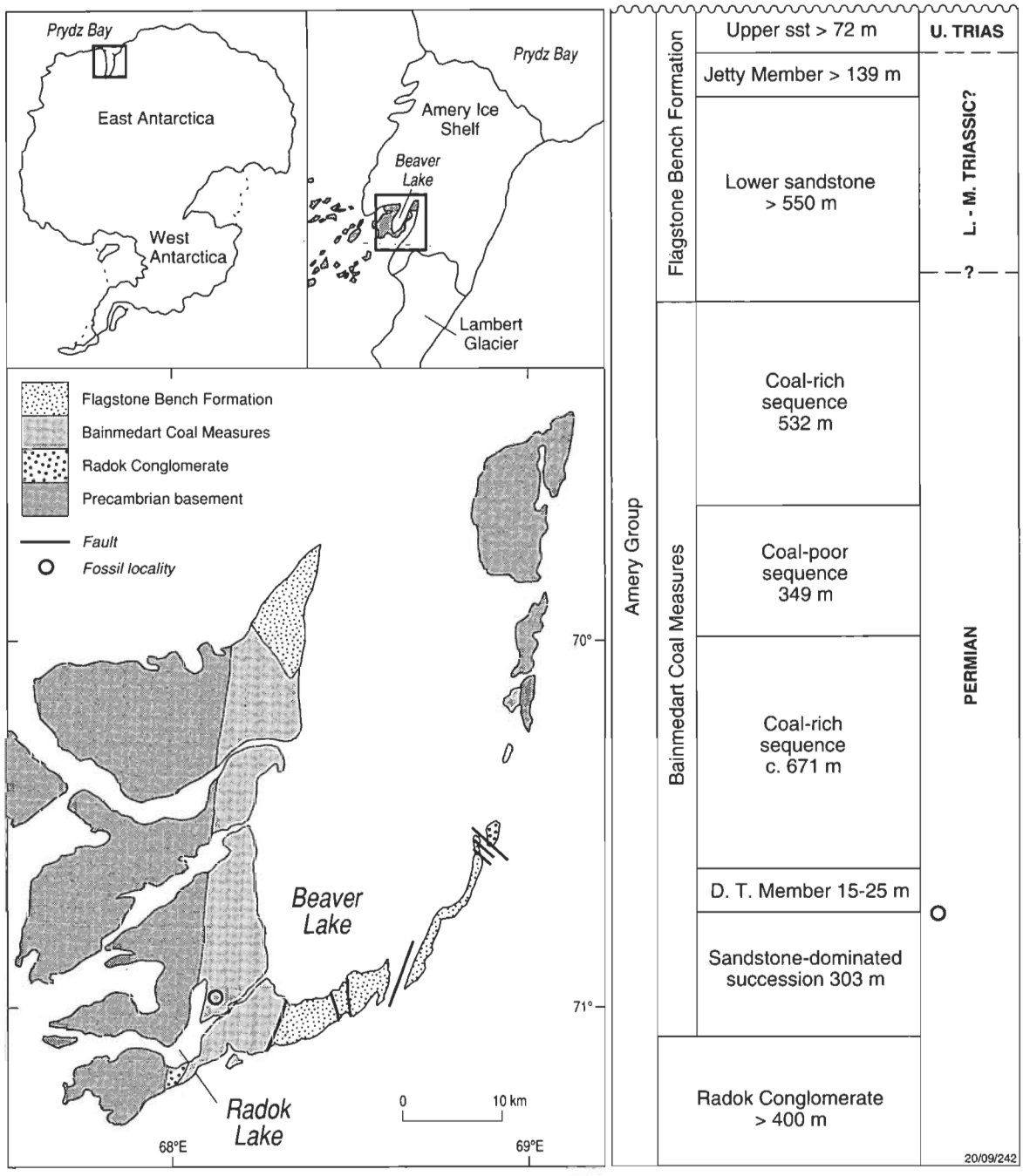

Figure 1. Geological map of the Beaver Lake area showing the fossil locality and a stratigraphic column indicating the sampled horizon.

Conglomerate represents a coarse-grained alluvial apron, up to 400 m thick, that was deposited by easterly directed stream, sheet, and debris flows and abuts a faulted basement contact (Fielding & Webb 1995). The succeeding Bainmedart Coal Measures — 1870 m of interbedded coal, sandstone, siltstone, and shale — were deposited by northerly flowing braided rivers within a broad alluvial plain (Webb & Fielding 1993; McLoughlin & Drinnan in press a). A distinctive 15–25-m package of ferruginous sandstone and shale about 300 m above the base of the coal measures has been designated the Dragon's Teeth Member (Fielding & Webb 1996). The fossil woods described here are from a silicified peat layer (representing a drowned glossopterid-dominated forest-mire depositional environment) immediately underlying the Dragon's Teeth Member. The Flagstone Bench Formation is greater than 700 m thick and consists of a lower sandstone-dominated unit, a middle unit of interbedded sandstone and ferruginous siltstone (Jetty Member), and an upper sandstone-dominated unit (Webb & Fielding 1993; McLoughlin & Drinnan in press b).

Limited palynological data indicate a late Early to Late Permian age (stage 5 palynoflora) for the Radok Conglomerate and Bainmedart Coal Measures (Balme & Playford 1967; Kemp 1973; Playford 1990). The lower Flagstone Bench Formation may also be of Late Permian age (Dibner 1978), but palynofloras and macrofloras from the upper part of the unit indicate a Late Triassic (Norian) age (Foster et al. 1994; Cantrill & Drinnan 1994; Cantrill et al. 1995).

Materials and methods

The fossils described here were collected from the Beaver Lake area of the northern Prince Charles Mountains (lat. 70°49′45″, long. 68°03′07″E; Fig. 1) as part of an Australian National Antarctic Research Expedition in January and February

of 1992. The fossils (prefixed NMVP: lodged with the National Museum of Victoria, Melbourne) consist of gymnospermous wood occurring as either isolated fragments or pieces embedded in siliceous, permineralised peat.

Acetate peels were prepared from the specimens according to a method similar to that of Joy et al. (1956). Transverse, radial, and tangential faces were ground flat on a lap wheel, and then etched in 50 per cent hydrofluoric acid for 50 to 70 seconds. Cellulose acetate film (50 μm thick) was dissolved in acetone onto the etched surface, and left to dry for a minimum of 60 hours before it was removed to reduce subsequent shrinkage. Acetate peels were mounted on a ground glass slide in histomount (National Diagnostics) and sealed under a coverslip. Petrographic thin sections were made from all three faces of several of the best preserved specimens.

Morphometric measurements of anatomical features were made on an Olympus BH–2 light microscope with a graticule eyepiece. For each specimen, at least 10 measurements were made for ray height, number of ray cells, tracheid length in tangential section, and radial pit diameter. The slide was moved randomly between measurements, and only complete rays and tracheids were assessed. Pit diameters were measured [a] transverse to and [b] parallel to the tracheid axis.

Morphometric data were analysed using PATN (Belbin 1987). The data were range-standardised, and equal weight was assigned to characters. Manhattan distances were calculated to create an association matrix of dissimilarity measurements between specimens. Both flexible UPGMA (unweighted pair group arithmetic averages) and flexible WPGMA (weighted pair group arithmetic averages) were used as fusion strategies for cluster analysis. The data were ordinated in three dimensions from the multidimensional scaling KYSP algorithm with the hybrid option (see Belbin 1987). For this, twenty different random starting points all returned the same result, indicating that the global minimum had been obtained. The lowest stress of 0.0417 was used. The PCC function was used to obtain character correlations with the ordination vectors.

Results and discussion

Forty-four wood specimens were examined, but only 34 were sufficiently well preserved to be included in the morphometric analyses. One of these had central wedge-shaped air-spaces, and was definitely a piece of *Vertebraria* root (identified by Neish et al. 1993), but the other 33 were of unknown position within the plant body. Most specimens were isolated fragments of wood up to 24 cm in largest dimension, but a few were smaller axes embedded in blocks of permineralised peat. Only seven specimens contained tissues preserved in the centre of the axes, but in all of these the primary wood structure was damaged. Preservation of anatomical details varied between specimens. Some specimens had areas of crushed tissues, identified in cross-section by distortion of the tracheids. Many specimens had areas of either damaged cells or hollow cavities of apparent biogenic origin.

Taxonomic diversity

Ordination

Mean values and standard deviations of morphometric data are presented in Table 1. The MDS ordination (Fig. 2A, B) distinguished two groups of specimens discriminated by the WPGMA classification at 0.56 dissimilarity (the results of the WPGMA and UPGMA analyses were similar). The first group contained three specimens (here described as *Australoxylon bainii* sp. nov.), and the second group contained 30 specimens (*Australoxylon mondii* sp. nov.). The single specimen of *Vertebraria* plotted within the field of the second group (Fig. 2A, B). The most highly correlated characters were ray height (correlation of –0.9254 to axis two), ray cell number (–0.8929, axis two), and tracheid length (–0.8719, axis three).

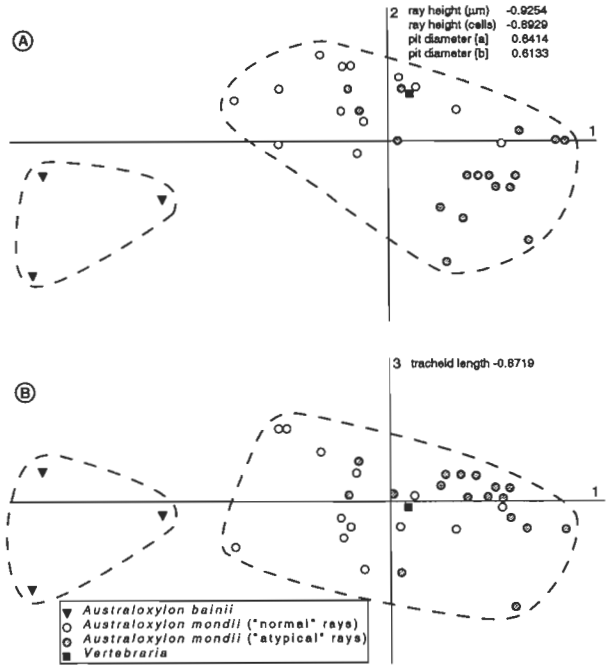

Figure 2. Ordinations of Beaver Lake woods based on ray height and cell number, tracheid length, and radial pit diameters. A, first and second axes. B, second and third axes.

Wood description

The taxonomy of Gondwanan Permian woods is complicated by the multitude of taxa and numerous nomenclatural changes and diagnostic emendations. Several authors have attempted to review the field, but have stopped short of a comprehensive revision at the species level (e.g., Maheshwari 1972; Prasad 1982; Pant & Singh 1987). Pant & Singh (1987) listed what they regarded as every Permian wood genus occurring in the southern hemisphere. They separated the genera on tracheid pit arrangement (i.e., araucarioid only, araucarioid and abietoid, or grouped pits in combination with others), the presence of taxinean tertiary spirals, and the structure of the primary wood where known. They list 122 species of fossil wood from the Permian of Gondwana, not including *Vertebraria*. These are assigned to 37 genera, of which 16 are monotypic. Eighteen genera (eight monotypic) comprising 69 species represent woods with only secondary tissue preservation. Because these are form-genera and species of uncertain relationship to other plant organs, a higher-order taxonomy is not available. The establishment of separate genera to encompass woods with primary tissues preserved and those with only secondary tissues has probably resulted in considerable duplication of taxa (Prasad 1982).

The Beaver Lake woods have no taxinean tertiary spirals, and the pith and primary vasculature are not preserved, so they can be compared to wood taxa based only on secondary tissues. *Australoxylon* Marguerier appears best to incorporate most of the characteristic features and the variation in both groups of Beaver Lake woods, and they are ascribed to that genus accordingly. Marguerier (1973) erected the genus for two species of wood from the Permian of Africa. She noted that the variation in pit arrangement is considerable, and that the generic delimitation could incorporate a number of species inappropriately attributed to *Dadoxylon* Endlicher and *Trigonomyelon* Walton. *Australoxylon* has radial pits arranged alternately (araucarioid), oppositely (abietoid), or in groups of up to five pits. The bordered radial pits are less than 15 m in diameter, and some of them are separated by bars of Sanio. The tracheids are quadrangular in transverse section, some with tangential pits.

Genus *Australoxylon* Marguerier 1973

Type species. *A. teixeirae* Marguerier 1973

Australoxylon bainii sp. nov.

Figs. 3; 8A–D, G; 9

Holotype. NMVP200011.

Etymology. After geologist J.H.C. Bain, for whom Bainmedart Cove (and the Bainmedart Coal Measures) was partly named by Mond (1972).

Diagnosis. Gymnospermous secondary wood with tall uniseriate rays up to 91 cells high; two to seven round, contiguous pits with oblique elliptical pores per tracheid-ray cross-field; tracheids circular to oval in cross-section, with bi- to quadriseriate bordered pits on radial walls; regular clusters of pits separated by bars of Sanio.

Description and remarks. This species is represented by the three best preserved specimens in the assemblage. The rings show only slight curvature in transverse section, indicating that these specimens all come from the outer part of one or more large axes. One specimen measures over 10 cm radially, and appears to be derived from an axis much greater than 30 cm in diameter.

Tracheids are moderately straight, and range from 4050 to 6795 μm long (Fig. 3B). The lumens are circular to oval in

Table 1. Variation (based on 10 measurements per specimen) in selected microanatomical characters within the Beaver Lake woods. Specimens marked by an asterisk were used in morphometric data ordinations (Fig. 2A, B).

Specimen number (NMVP)	*Tangential ray height (μm)*			*Ray height (number of cells)*			*Tangential tracheid length (μm)*			*Radial pit diameter [a] (μm)*			*Radial pit diameter [b] (μm)*		
	range	av.	SD	range	av.	SD	range	av.	SD	range	av.	SD	range	av.	SD
A. bainii															
200011 *	330–1590	625	340	8–38	19	9	4050–6440	5115	770	12–17	13	2	10–14	12	1
200012 *	505–2665	1090	520	19–91	39	18	5885–6795	6280	420	11–17	13	2	11–15	12	2
200013 *	150–1350	765	445	4–49	27	17	5320–6540	6055	425	13–17	15	2	11–14	13	1
***A. mondii* (normal)**															
200014										9–14	11	2	9–11	10	1
200015	30–155	65	40	1–6	3	2	1040–1695	1390	225						
200016 *	60–165	90	45	1–6	3	2	1730–2875	2445	460	10–13	11	1	9–11	10	1
200017				1–3											
200018 *	35–260	120	70	1–8	3	12	1340–2275	1570	340	9–12	11	1	9–11	10	1
200019 *	25–185	105	50	1–5	3	2	1090–2110	1580	320	6–9	8	1	6–10	8	2
200020 *	50–240	135	40	1–9	4	2	1290–3670	2245	605	10–16	14	2	10–14	12	2
200021										8–10	9	1	7–10	9	1
200022	95–310	160	75	3–13	7	3				12–15	14	2	10–15	12	2
200023 *	105–280	210	60	6–11	9	2	4695–6650	5630	610	13–16	14	9	10–12	11	1
200024	60–340	180	95	2–9	6	3	2490–4295	3155	530						
200025 *	120–280	195	60	3–10	6	3	1765–3715	2840	595	10–15	12	2	9–13	11	2
200026	45–215	120	55	1–6	4	2	1260–2710	1990	450						
200027 *	150–320	230	60	4–12	9	3	1320–2140	1665	285	10–15	12	2	10–12	11	1
200028 *	55–170	110	40	2–6	4	2	2085–3975	2720	640	10–14	12	2	9–13	11	1
200029 *	200–580	390	130	6–18	11	4	1265–3465	2315	690	12–16	14	2	11–13	12	1
200030 *	75–470	165	115	2–18	6	5	2865–4755	3660	530	10–13	11	2	8–11	10	1
200031 *	85–375	215	85	3–15	8	4	1925–3675	2615	630	12–17	14	2	11–15	13	2
200032 *	75–155	115	35	2–5	4	2	1675–5040	3100	1010	11–14	12	1	9–14	11	2
200033 *	35–245	100	70	1–7	3	2	1580–2790	2255	406	8–11	10	1	7–9	8	1
200034										8–10	9	1	8–10	9	1
200035	70–355	135	90	2–10	4	3	2645–4075	3070	495						
***A. mondii* (atypical)**															
200036 *	110–380	185	70	3–8	5	2	1600–4365	2685	570	9–12	13	2	9–11	10	1
200037 *	70–685	240	165	2–18	7	5	750–1810	1340	275	7–12	8	1	6–9	8	1
200038 *	60–480	455	150	2–21	8	5	810–3620	1630	730	5–10	8	1	4–8	7	2
200039 *	75–420	215	75	2–11	6	2	980–2170	1440	295	6–9	8	1	6–8	7	1
200040 *	90–345	195	90	3–12	6	3	1525–2445	2020	330	10–16	13	2	10–11	10	1
200041 *	80–285	135	60	2–7	3	2	1015–1715	1375	215	7–9	8	1	6–9	8	1
200042 *	100–450	195	125	2–18	8	5	1280–2225	1845	290	10–13	11	1	9–11	10	1
200043 *	80–325	165	75	3–10	5	2	1030–1795	1375	240	6–8	8	1	6–7	7	1
200044 *	135–360	215	75	4–10	6	2	1265–1870	1520	215	7–10	8	2	7–17	8	1
200045 *	265–805	470	165	8–23	13	5	1255–2610	1880	395	8–10	9	1	7–9	8	1
200046 *	35–155	90	45	1–6	3	2	2005–4065	3330	660	10–12	11	1	8–10	9	1
200047 *	155–630	315	155	5–21	10	5	1330–1895	1580	185	8–12	9	1	7–10	8	1
200048 *	90–370	215	105	2–10	6	3	1020–2195	1675	360	8–10	9	1	7–8	8	1
200049 *	70–555	290	145	2–18	9	5	1295–2165	1780	310	8–11	10	1	7–8	8	1
200050										5–9	7	1	6–8	7	1
200051 *	40–145	100	40	1–4	2	1	2280–3695	3065	450	8–10	8	1	6–8	7	1
200052 *	20–100	55	30	1–4	2	1	470–1395	980	280	6–9	8	1	5–8	6	1
200053 *	110–300	215	85	3–10	6	2	1045–1460	1185	135	7–10	9	1	6–10	8	2
Vertebraria															
200054 *	35–330	105	70	1–10	3	2	760–3060	1940	735	9–12	11	1	9–11	10	1

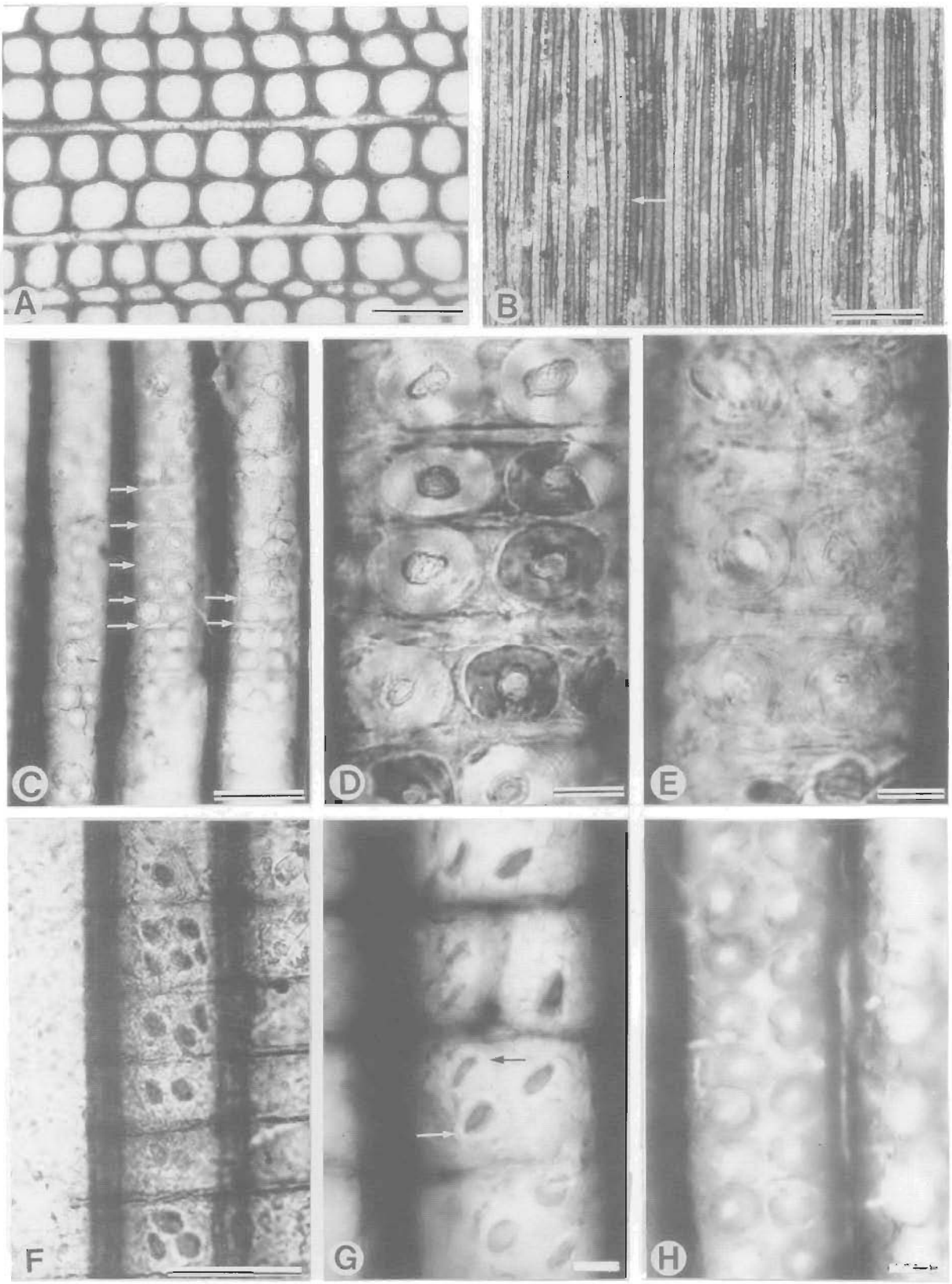

Figure 3. *Australoxylon bainii* sp. nov. A, transverse section of secondary wood showing unevenly thickened tracheids with circular lumens (NMVP200012A). B, tangential section showing tall uniseriate rays; arrowed ray is 91 cells high (NMVP200012B). C, radial section showing bars of Sanio (arrowed; NMVP200011B). D, radial section showing bars of Sanio separating paired pits, pores circular (NMVP200013A). E, radial section showing bars of Sanio and a border around each pair of pits, pores elliptical (cupressoid; NMVP200011B). F, radial section showing cross-field pits with prominent elliptical pores (NMVP200011B). G, enlargement of cross-field pits; indistinct border arrowed (NMVP200011B). H, opposite radial pits (NMVP200011C). Scale bars: B = 0.5 mm; A = 0.1 mm, C. F = 0.05 mm; D, E, G, H = 0.01 mm.

transverse section, and the walls are thickened at the corner junctions with neighbouring cells (Fig. 3A). Rays are uniseriate (never biseriate), and up to 2665 μm (91 cells) high (Fig. 3B). Rays extend radially for only a few growth rings before lensing out; they are shorter at their beginnings and ends, which accounts for the variation in cell number and total height measured in tangential section. Two to seven pits occur per cross-field. Cross-field pits are round, contiguous, and contain a prominent elliptical-oblique pore. Often only the pore is evident (Fig. 3F, G). Pits on tracheid radial walls are either opposite and square to slightly distorted (Fig. 3H) or alternate and hexagonal (Fig. 8A–C). The pit diameters for [a] are 11–17 μm and for [b] 10–15 μm. Tracheid radial pits are generally bi- to quadriseriate, and laterally contiguous. Uniseriate pits uncommonly are tightly packed and distorted to an oval shape. Many pits occur in short horizontal rows separated by bars of Sanio (thickenings between the upper and lower margins of pit-pairs; Figs. 3C–E; 8D). Bars of Sanio form

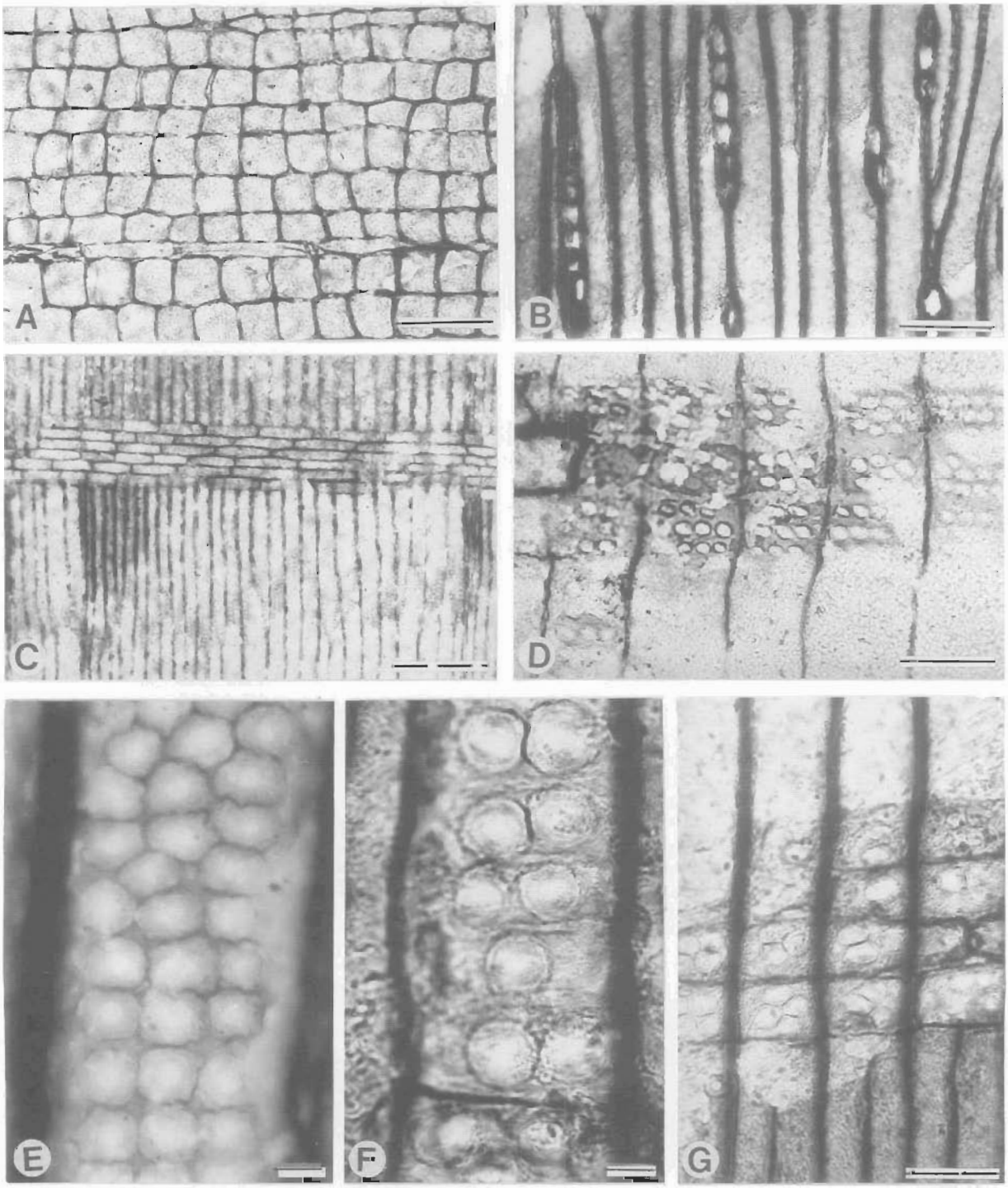

Figure 4. *Australoxylon mondii* sp. nov. with 'normal' ray anatomy. A, transverse section showing square/rectangular tracheids with uniform wall thickness (NMVP200024). B, tangential section showing short rays with all ray cells contiguous (NMVP200020C). C, radial section showing ray with contiguous cells forming a brickwork pattern (NMVP200030). D, radial section showing cross-field pits that appear simple owing to poor preservation (NMVP200034). E, radial section showing opposite pits with circular pores (NMVP200022). F, radial wall of tracheid showing bars of Sanio between pits (NMVP200020A). G, bordered cross-field pits (NMVP200020A). Scale bars: A, B, C = 0.1 mm; D, G = 0.05 mm; E, F = 0.01 mm.

either scalariform-like borders between adjacent rows of pits (Fig. 3C, D), or rings that encircle groups of two or three pits (Fig. 3E); both styles may occur within a single specimen. Pores of radial pits are circular or oblique.

Prominent growth rings 1 to 4 mm wide are present, and false rings occur intermittently in the earlywood of each growth increment. There can be up to 90 cells of earlywood, but the latewood (distinguished by smaller cells with slightly thicker walls) is usually only a few cells thick.

No biseriate rays are apparent in *A. bainii*, but some other species of this genus have a very low proportion (around 1%) of biseriate rays (Marguerier 1973). No *Australoxylon* species has rays of similar height to *A. bainii*, but sporadic rays up to 60 cells high occur in *A. teixeirae* Marguerier 1973 from Mozambique.

Australoxylon mondii sp. nov.

Figs 4–7; 8E, F, H–O; 10–12

Holotype. NMVP200020.

Etymology. After geologist A. Mond (formerly Medvecky), for whom Bainmedart Cove was partly named.

Diagnosis. Gymnospermous secondary wood with rays up to 23 cells high with 3–10 contiguous pits per cross-field. Rays consist of either compact, closely joined cells, or partly detached files of cells separated by cavities and bridged by sporadic extensions of adjacent ray cells. Tracheids are square or rectangular in cross-section, and have variably arranged bordered pits with circular to diagonally elliptical pores on radial and tangential walls.

Description and remarks. *Australoxylon mondii* is represented by 40 variably preserved specimens. Tracheids are 1040 to 6650 μm long, and are square in cross-section (Figs. 4A; 5A). Rays are up to 800 μm (or 23 cells) high (Figs. 4B; 5B). They extend radially for only a few growth rings before lensing out; they are shorter at their beginnings and ends, which accounts for the variation in cell number and total height measured in tangential section. Ray cells are roughly square in tangential section (Fig. 4B). Two forms with different ray anatomy are present. In the 'normal' form, ray cells adjoin their neighbours in the overlying and underlying files along the entire length of the ray (Fig. 4C). In the 'atypical' form, ray cells are separated from those above and below by a prominent gap, and are connected only rarely by narrow bridges (Figs. 5B–E; 6). Uncommonly, two joins may occur between adjacent cells (Fig. 6G). Not all joins are of the same dimensions (Figs. 5; 6). They appear hollow, generally with a horizontal (Fig. 6D) or diagonal (Fig. 6C) wall separating the two cells. Some broken joins were observed, but these are probably preservational features (Fig. 6E). Joins are less obvious in tangential sections (Fig. 6H). The ray is locally biseriate for a distance of a few cells, and the files of cells are joined along their radial walls as in a normal biseriate ray, but are separated from the files above and below by a gap. It is uncertain whether the gaps between the ray cells in 'atypical' *A. mondii* were air-filled or fluid-filled.

A thin-sectioned specimen of 'atypical' *A. mondii* has numerous hollow dark structures that appear to 'bud' from the ray cell walls (Fig. 7D, F). There are also hollow bridges between some cells that are probably more fully developed 'bud' structures (Fig. 7D, E). Some of the rays also contain circular thin-walled balloon-shaped structures that connect adjacent cells (Fig. 7A–C). Some of the smaller dark 'buds' may represent the bases of broken or undeveloped 'balloons' (Fig. 7E).

The balloon-shaped structures are possibly tyloses formed in the gaps between ray cells. If so, the gaps between the ray cells are not post-mortem features. In modern plants, tyloses are normally formed by ray parenchyma protruding into air-filled vessels, so it is feasible that they would be able to grow out into the spaces between the ray cells. Tyloses are formed as a result of either injury (including parasite damage) or ageing. The 'buds' may be unexpanded tyloses, although a complete sequence showing the progression was not found. As these tyloses were observed only in the one thin-sectioned specimen, it is not possible to generalise about their cause.

Cross-field pits of both ray types are identical, although they are generally poorly preserved (Fig. 4D). There are between three and ten bordered pits per cross-field; some individuals show a broad range of variation, whereas others are more consistent. The pores of the cross-field pits are either diagonally elliptical (cupressoid) or round. Normally, the pits fill the cross-field, and are contiguous but not very distorted. The pits are tightly packed in a more or less alternate (araucarioid) arrangement (Figs. 4D, G; 5F; 8L–N).

Tracheids have numerous radial pits, but these are poorly preserved in many specimens. They can be uniseriate (Fig. 5G) or multiseriate (Fig. 8F), and opposite or alternate. Some specimens tend to have only one arrangement, others have several. Pits are commonly contiguous, but may be found individually or in groups of 2 to 5 (Fig. 8E, F). Horizontal rows in places are separated by bars of Sanio (Fig. 4F). The pores are round or either transversely (taxodioid) or obliquely (cupressoid) elliptical (Figs. 4E; 8H, I). Radial pit diameters are [a] 6 to 17 μm and [b] 6 to 15 μm. Some of the specimens show sparse tangential bordered pits (Figs. 5E; 8J, K); these are more apparent in thin sections than in peels. These pits are similar in size to radial pits, contiguous, and uniseriate or spaced irregularly along a tracheid. In some places, up to three rows of tangential pits are present in both opposite and alternate arrangements. One specimen has pits on tracheid end walls (Fig. 8O).

Australoxylon mondii appears to fit securely within the circumscription of *Australoxylon*. Although neither of the species assigned to *Australoxylon* by Marguerier (1973) possess both tangential pits and bars of Sanio, it is only the lack of one or the other, or both, of this combination that renders *Australoxylon teixeirae*, *A. natalense* Marguerier, *Dadoxylon barakarense* Surange & Saxena, and *D. kharkhariense* Maithy substantially different. As discussed below, the intra-specimen variation in the Beaver Lake woods suggests that the ability to discern tangential pits and bars of Sanio is mainly a feature of preservation and preparation, and is probably an unreliable means of separating species. Apart from the presence or absence of tangential pits and the bars of Sanio, these species of *Australoxylon* and *Dadoxylon* are very similar, and are separated mainly on subtle quantitative rather than structural characters.

Genus *Vertebraria* Royle emend Schopf 1982

Type species. *Vertebraria indica* Royle 1836

Vertebraria sp.

One specimen analysed in this study clearly showed the central wedge-shaped air cavities typical of the genus *Vertebraria*. The tracheids are square to rectangular in transverse section. The rays are uniseriate, or rarely biseriate, and are up to 330 μm (10 cells) high. Tracheids are 7690 to 3060 μm long. Cross-fields contain from four to eight araucarioid pits. Adjacent files of ray cells are contiguous. Pits are common on tracheid radial walls. They are variously arranged; they can be opposite, alternate, or in groups of 4 to 6 (rarely 2 or 3). Groups of pits in places are separated by horizontal spaces, but no bars of Sanio were observed. Pit diameters are [a] 9 to 12 μm and [b] 9 to 11 μm.

Comparison between Beaver Lake wood types

Australoxylon. The two species of *Australoxylon* are differentiated principally by ray height, both in total dimensions and in number of cells. The rays of *A. bainii* clearly contain more cells (av. height of 30 cells, max. 91) compared to *A. mondii*

(max. 23 cells). Tracheid lengths reinforce the difference between *A. bainii* (with average tracheid length of 5630 μm) and *A. mondii* (average tracheid length 2207 μm), although the tracheid dimensions of specimens assigned to either species may overlap.

Australoxylon bainii has tracheids that are quite rounded in transverse section and the walls are thickened unevenly (Figs. 3A; 9A, F). Pit borders are very faint, perhaps not as thick as in *A. mondii*, and no tangential pits are evident. In most modern woods, tangential pits are much more common in the latewood than the earlywood (Barefoot & Hankins 1982), but *A. bainii* has very little latewood. In *A. mondii*, tangential pits are not restricted to the latewood, but are found throughout the rings.

Character ordinations (Fig. 2) based on ray height, ray cell number, tracheid length, and pit diameter did not unequivocally distinguish the two forms of *A. mondii* that can be recognised on the presence or absence of 'separated' files of ray cells.

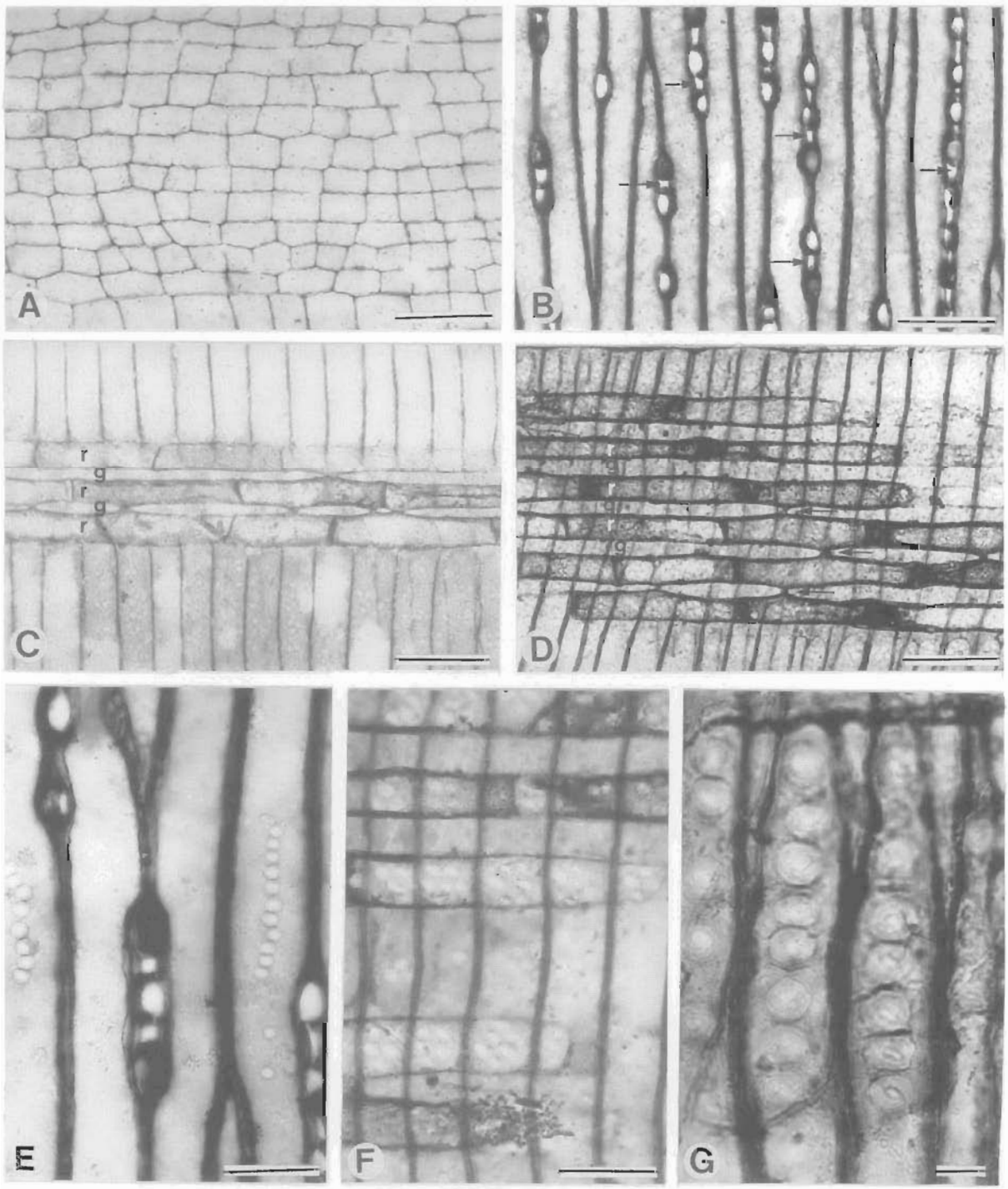

Figure 5. *Australoxylon mondii* sp. nov. with 'atypical' ray anatomy. A, transverse section showing square/rectangular tracheids with uniform wall thickness (NMVP200040C). B, tangential section showing short rays. Note gaps between the ray cells (arrowed; NVMP200041B). C, radial section showing three rows of ray cells (r) and two lines of gaps (g) with joins across them (NMVP200053B). D, radial section with rays (r), gaps (g) and joins (arrowed; NMVP200041A). E, tangential bordered pits (NMVP200041B). F, bordered cross-field pits (NMVP200041A). G, uniseriate radial pits with oblique pores (cupressoid; NMVP200041A). Scale bars: A, B, C, D = 0.5 mm; E, F = 0.05 mm; G = 0.05 mm.

However, specimens with the different ray characteristics did tend to dominate different parts of the ordination field. The single *Vertebraria* specimen included in the analysis plotted close to representatives with 'normal' ray anatomy.

Australoxylon mondii tracheids are square to rectangular in transverse section, and are evenly thickened around the cell

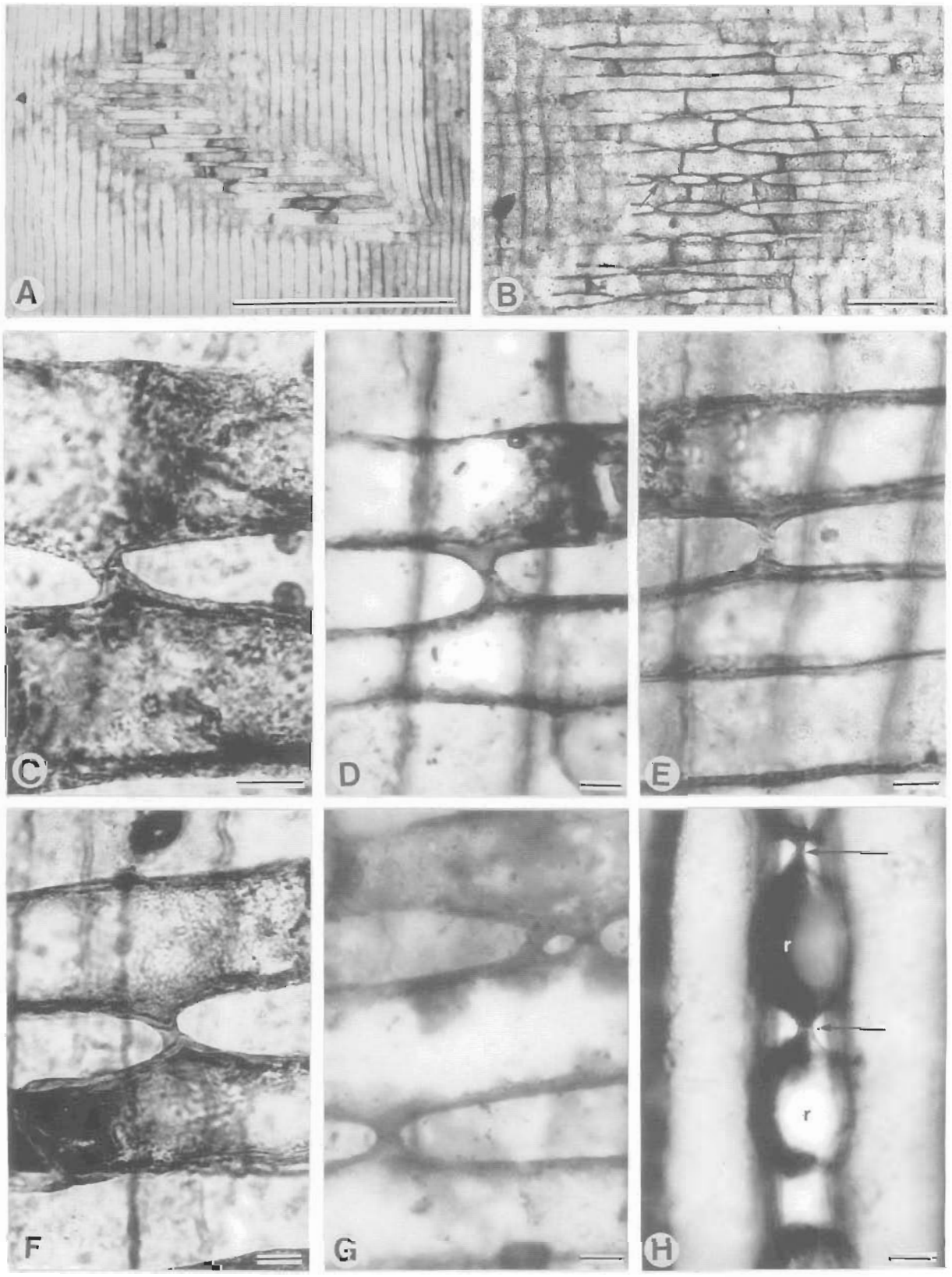

Figure 6. Joins between ray cells in 'atypical' *Australoxylon mondii*. A, radial section showing ray cells with various joins (NMVP200047). B, radial section showing frequency of ray cell joins, and double joins (arrowed; NMVP200047). C–G, joins between ray cells of adjacent files (NMVP200041A). H, tangential section showing ray cells (r) and the joins between them (arrowed; NMVP200041B). Scale bars: A = 0.5 mm; B = 0.1 mm; C–H = 0.01 mm.

circumference. Their rays are shorter than in *A. bainii*, although they are quite variable. The separated files of ray cells characteristic of about half the *A. mondii* specimens examined do not appear to be found in any extant plants, and have previously been reported only twice (White 1973; Pant & Singh 1987).

From the same locality at Beaver Lake, White (1973) described specimens that undoubtedly belong to *A. mondii*. She stated that 'The cells of the rays are in the form of filaments with cross connections to each other, not a solid plate of cells', but gave no additional details. White (1973: pl. 4, fig. 3) figured the rays, but cell details are difficult to discern in the illustrations. She assigned the wood to *Taeniopitys scottii* Kräusel. This species, however, is defined on primary wood and pith characters, which are generally lacking in the Beaver Lake specimens. Kräusel's (1962) original description of *T. scottii* does not mention the unusual rays or tangential pits that are found in *A. mondii*.

Two specimens that Pant & Singh (1987) described as two new species (*Paracatervoxylon raniganjensis* and *P. biseriatum*) from the Raniganj Formation in the Raniganj Coalfield of India have a ray anatomy similar to 'atypical' *A. mondii*. They illustrated the rays in radial and tangential section, and referred to the gaps between the ray cells as air spaces. Despite the similarity in ray anatomy between the Indian specimens and 'atypical' *A. mondii*, the latter is distinguished here by the possession of tangential pits, bars of Sanio, and the absence of taxoid cross-field pits.

The presence of structures interpreted here as tyloses that have intruded into the intercellular spaces from adjacent ray cells indicates that the spaces were present in the living wood, and are not decay or post-fossilisation features. A pathogenic cause for the ray anatomy is unlikely, as the intercellular gaps are very regular, consistent in width, and are bridged by semiregular joins between cells. The ray structure may characterise a specialised structural/functional feature of a particular region of the plant body; for example, the air spaces may represent aeration passages to the living parenchyma cells within semisubmerged portions of the plant growing in swampy, anaerobic environments. Air spaces formed by schizogeny in the medullary rays of *Vertebraria*, which was the root form of at least some glossopterids, are generally considered to be adaptations for facilitating aerobic respiration in an anaerobic growth-environment (Neish et al. 1993).

Anatomical characters of *Vertebraria* in these deposits are virtually identical with those of 'normal' *A. mondii*, suggesting that these two organ taxa are probably root and trunk of the same plant; 'atypical' *A. mondii* might represent intermediate regions of transition from subaquatic roots to subaerial axes. However, the 'normal' and 'atypical' variants might represent two different species, but until the significance of the semidetached ray cell structure is understood they are best regarded as a single taxon.

***Vertebraria* sp.** Wood of the root *Vertebraria* is identical with 'normal' *A. mondii* in all quantitative and qualitative microanatomical features examined here, but has radiating wedges of secondary wood rather than a solid axis. Readers are referred to Neish et al. (1993) for a more complete discussion of the structure, ontogeny, and affinities of the Amery Group permineralised *Vertebraria* axes. At least some of the 'normal' *A. mondii* axes have a thick central pith but no radiating secondary wood wedges or air spaces, indicating that they are clearly stems; however, other specimens may be outer portions of *Vertebraria* roots.

Gould (1975) noted that permineralised Upper Permian *Vertebraria* wood from the Bowen Basin, Australia, is microanatomically indistinguishable from the wood of associated non-septate axes assigned to *Araucarioxylon arberi* (Seward) Maheshwari by Beeston (1972). *Araucarioxylon* is characterised by multiseriate, contiguous, hexagonal, alternate, bordered pits, but both Beeston (1972) and Gould (1975) identified at least some tracheids with opposite pitting in their specimens, suggesting closer affinities with *Australoxylon*. Pant & Singh (1968) and Gould (1975) also identified pit clusters on radial walls of *Vertebraria* tracheids similar to those found in Antarctic *Australoxylon* specimens (Fig. 8E). Circular to oblique cross-field pits with circular, elliptical, or slit-like pores characterise Australian *Araucarioxylon arberi* specimens (Beeston 1972) and Indian, Australian, and Antarctic *Vertebraria* and *Australoxylon* woods (Pant & Singh 1968; Gould 1975; this study). The consistency of alternate versus opposite pitting and the shape of cross-field pits as taxonomic discriminators between *Vertebraria*, *Araucarioxylon*, and *Australoxylon* requires reassessment.

Vertebraria roots would be expected to account for a significant fraction of the peat biomass, so, unless an axis is sufficiently preserved to determine whether its central part was either solid or contained wedge-shaped air spaces, it is not possible to distinguish between stem and root wood. This has implications for palaeoclimatic interpretation based on growth rings and other anatomical characters, as it is unclear whether stem and root wood both respond in the same way to environmental conditions. All previous application of growth-ring features to climatic history, both extant and fossil woods, have invoked trunk or stem woods; the reliability of root wood as an environmental record is unknown. Growth-ring analysis in this study chiefly uses woods that have complete rings which are more likely to be from subaerial parts of a plant.

Variability in anatomical characters. Both *A. bainii* and *A. mondii* show considerable intra-specimen variation in pit arrangement and type. Tracheids exhibiting the full range from alternate pits, through subalternate and subopposite, to opposite pits are interspersed in the same specimen. Although it is tempting to categorise a specimen as having mostly one or the other type of pit arrangement, a significant proportion of the pits elsewhere in the specimen may represent an alternative character state. Both species have some specimens with both circular and oblique pores in their radial pits, and other specimens with only one type. In *A. mondii*, the orientation can be either diagonal (Fig. 8I, cupressoid) or horizontal (Fig. 8H, taxodioid).

Pits are variably arranged into continuous zones or small groups, or are individually isolated. Most specimens of *A. mondii* exhibit at least two of these states, and many have all three (Fig. 8E, F, H, I). Some specimens of *A. bainii* have areas where pits are separated by bars of Sanio, or arranged in horizontal rows suggesting ill-preserved bars of Sanio (Fig. 8D, G), but in other areas the pits are in continuous zones (Fig. 8B, C). In some specimens, continuous fields tend to be nearer the ends of tracheids, and small groups nearer the centre, but most specimens appear to have a completely random distribution of the different pit clusters. The smaller fragments appear to have a more uniform pit arrangement, but this is probably due to an insufficiently large sample of wood to reveal the full range of real variation.

The presence/absence of pits on tracheid tangential walls, and bars of Sanio, are characters that require special caution, as their recognition seems to be partly determined by preservation and preparation, rather than wood type. Both characters are more readily apparent in well-preserved specimens and woods prepared by thin-sectioning.

Clearly, large sections of wood need to be examined to gain an accurate representation of pit characters and other microanatomical features. If the variation exhibited by the Beaver Lake woods is at all typical of Permian woods, then previous fossil wood studies that have used pit morphology and arrangement as discriminate and exclusive identifying

characters may have suffered from inadequate examination of insufficient material.

Ichnofossils

Many of the specimens show local tissue damage of presumed biogenic origin that appears to have occurred before fossilisation. Three forms of damage are categorised; no specimen was observed with more than one type.

Irregular cavities

All three specimens of A. *bainii* show a type of damage not seen in any of the *A. mondii* specimens. The damage consists of numerous small irregular cavities (0.4 mm in diameter, 2.5 mm long) that lack sharp margins (Fig. 9A, B). The cavity margins show a gradational decay pattern extending into the surrounding xylem tissue (Fig. 9C). The cell walls in degraded areas are thinner than normal, and have commonly separated into two or more layers (Fig. 9E, H). Tracheids in these degraded areas have small holes in the wall (Fig. 9D). These wall disruptions are larger and more numerous the nearer they are to the edge of the cavity. Appositions are present in some specimens (Fig. 9F, G). No cause for this type of decay was established. The decay may have been caused by bacterial or fungal agents that were too delicate to be preserved.

Spindle-shaped cavities within latewood

Five specimens of *A. mondii* have cavities that are elongate–elliptical in longitudinal section and circular or slit-like in transverse section. The cavities are completely enclosed within the wood, and have no obvious connection to the exterior of the axis. They are generally separated from one another, but locally merge to form an interconnected system (Fig. 10A, C). They range from 0.45–3.0 mm in radial diameter and 3.5–13.5 mm in height. Cells at the edges of the cavities are not deformed, but show a sharp truncation of their walls (Fig. 10D, E). Adjacent tracheids are undamaged. The cavities typically start in the outer part of the earlywood, extend through the latewood, then end within a few cells of the

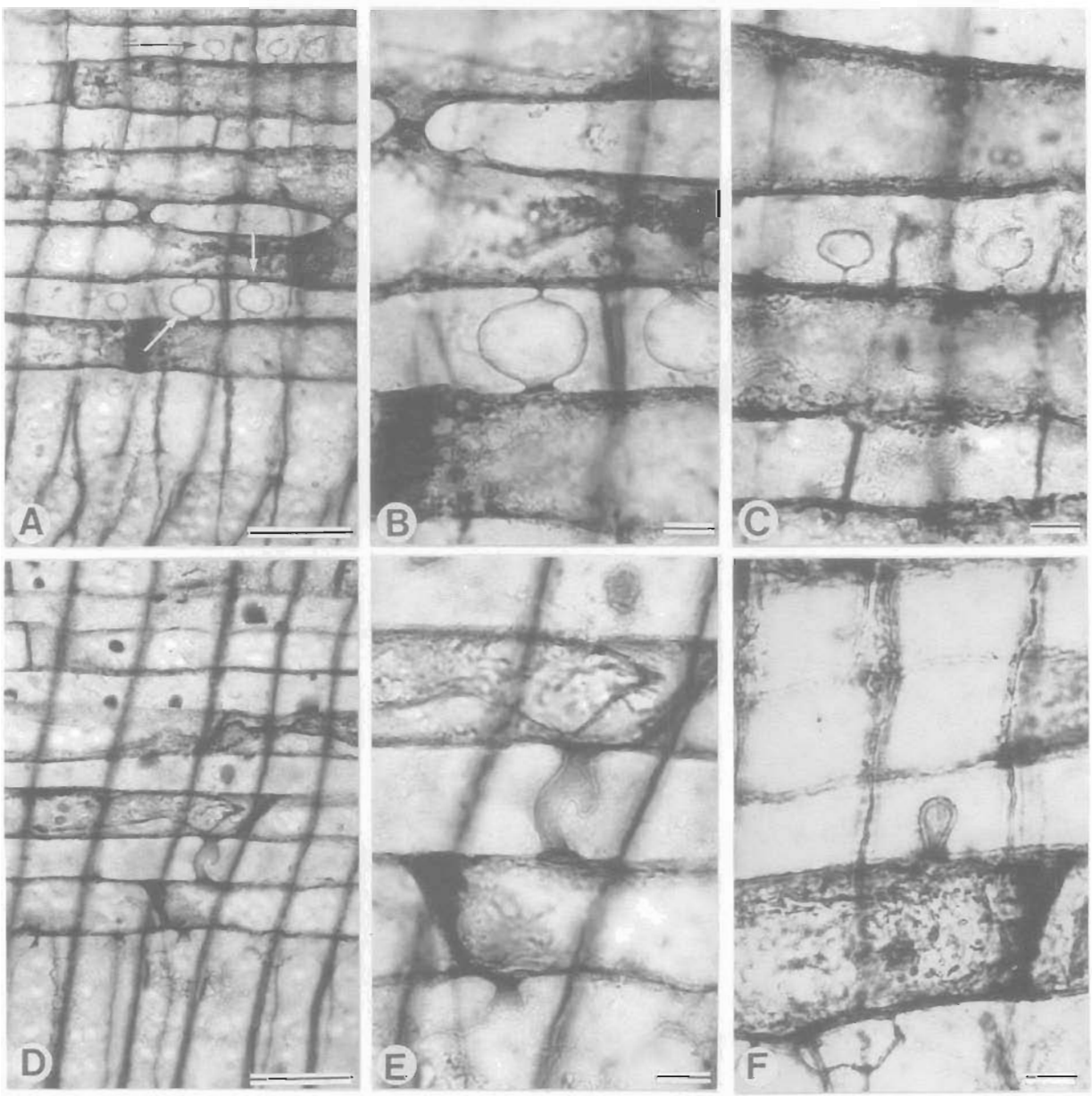

Figure 7. Tyloses in 'atypical' *Australoxylon mondii* (all illustrations of NMVP200043A). A, ray cells with balloon-shaped tyloses (arrowed) between cells. B, enlargement of the balloon-shaped tyloses and a join. C, magnification of the balloon-shaped tyloses. D, radial section, showing unusual join and dark, bud-like structures. E, higher magnification of unusual join. F, higher magnification of a bud-like protuberance. Scale bars: A, D = 0.05 mm; B, C, E, F = 0.01 mm.

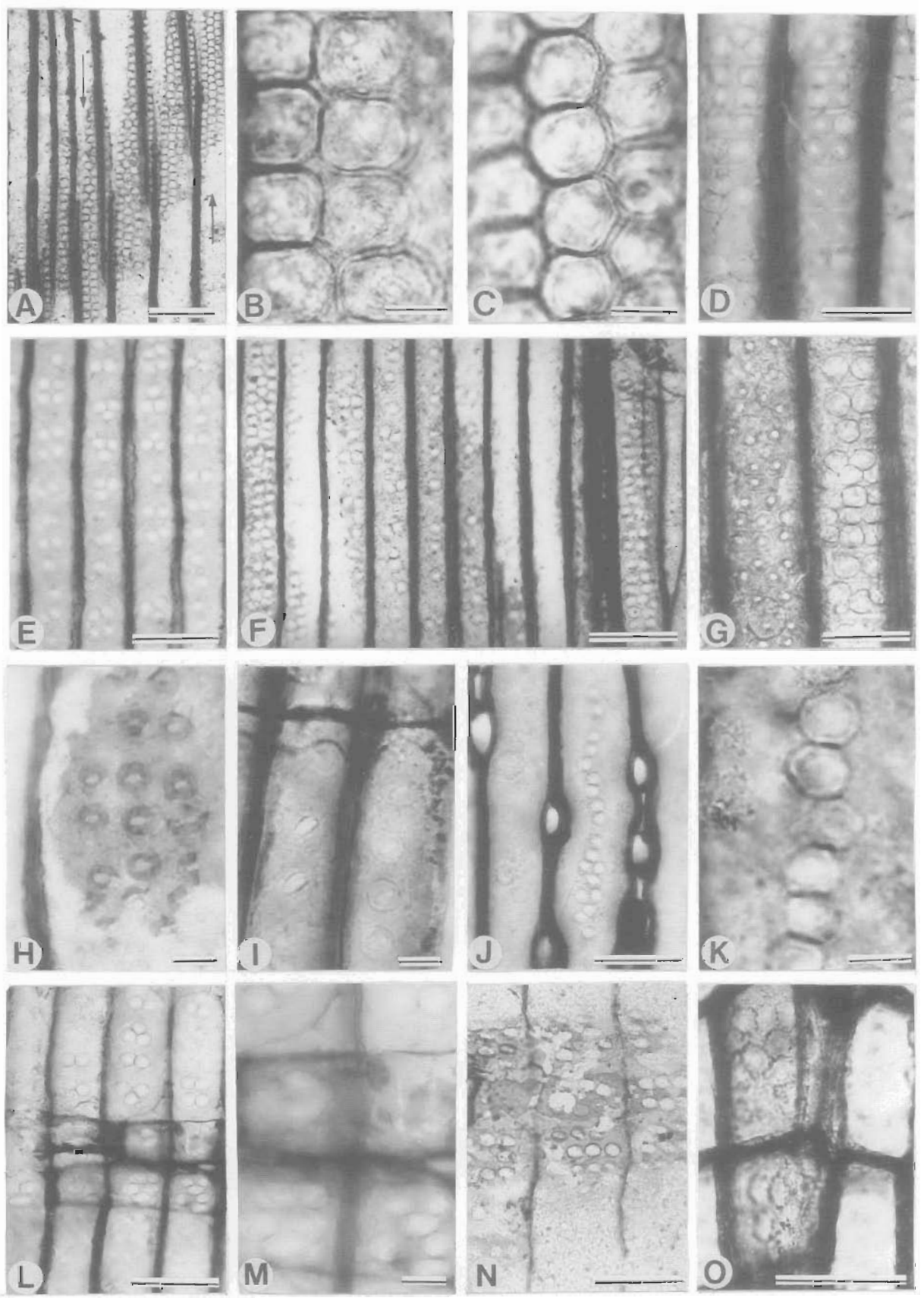

Figure 8. Pit structure and arrangement. A-D, G, *Australoxylon bainii*; E, F, H–O, *A. mondii*. A, radial section of tracheids with both opposite and alternate pit arrangement. Tracheids illustrated in Figure 8B and 8C are arrowed (NMVP200013B). B, magnification of part of Figure 8A showing square pits (opposite arrangement; NMVP200013B). C, magnification of part of Figure 8A showing partly hexagonal, alternate pits (araucarioid arrangement; NMVP200013B). D, radial pits with oblique pores (cupressoid) and bars of Sanio (NMVP200013B). E, groups of up to 5 pits (NMVP200041A). F, specimen showing contiguous areas of pits, and pits in small groups or isolated (NMVP200020A). G, bars of Sanio and pits with circular pores (NMVP200013B). H, taxodioid pits (horizontally oriented, elliptical pores; NMVP200034).

(continued on facing page)

succeeding earlywood (Fig. 10A, B). Within these cavities are numerous small fragments of indeterminate tissue, and abundant larger spherical to oblong organic masses 40 to 120 μm in diameter (Fig. 10D–G). These pelletal structures vary in size within each cavity.

Similar cavities containing pelletal material of plant origin (frass) are reasonably common and widespread in wood from the Late Carboniferous and Early Cretaceous, and there are a few examples recorded from the Triassic and Jurassic, but Permian records are rare (Chaloner et al. 1991; Scott & Taylor 1983; Scott 1992; Scott et al. 1985; Zavada & Mentis 1992). Pellet-filled cavities of this type in other fossil woods have been interpreted as the action of arthropod borers leaving behind coprolites and powdered frass. Numerous similar cavity types filled with pelletal dung and powdery frass are found in modern trees.

There are about 78 extant species of arthropods from 20 families in 8 orders capable of digesting wood (Martin 1991). Modern isopterid borings differ from the simple spindle-shaped cavities in the Antarctic woods by their meandroid and branching arrangement. Frass produced by modern hymenopterid and dipterid borers differs from the Antarctic coprolites by its typical powdery nature, and coprolites of modern lepidopteran borers are commonly bound by silken threads (Duffy 1953). Hymenoptera, Lepidoptera, Diptera, and Isoptera do not have a documented pre-Mesozoic fossil record (Carpenter & Burnham 1985).

Among modern invertebrates, beetles and mites are the most common wood-borers, and produce the most similar excavations and coprolites to those in the Antarctic woods. Both have a pre-Permian fossil record (Savory 1977; Carpenter & Burnham 1985), and wood borings ascribed to these groups are known in woods as old as the Carboniferous (Brzyski 1969; Chichan & Taylor 1982). However, mites typically produce excavations less than 1 mm in diameter (Wallwork 1976), which is considerably narrower than many of the Antarctic wood cavities. Coprolite and excavation size suggest that beetles (or beetle larvae) were the most probable agent of attack, but no evidence of insect pupae was found in any of the Antarctic woods. In some specimens, only certain rings show evidence of attack, indicating that in some years there was a greater degree of infestation, at least for individual trees.

Many modern cerambycid beetles overwinter in wood excavations as larvae or pupae (Duffy 1953). The restriction of cavities largely to the latewood in Antarctic woods might be explained by a similar life cycle among the Permian arthropods. If eggs were laid during the polar summer, larvae may have spent the polar winter living within and feeding on the xylem tissue of the tree. With the onset of spring, they may have emerged through the bark, and the cavities thereafter would have closed up as cambial activity resumed in the following season. Because the tree would have been essentially dormant while the larvae were feeding, there would be no extensive wound reactions. Coprolite-filled cavities in a specimen of *Dadoxylon* wood from the Permian of South Africa also appear to occur near growth ring boundaries (Zavada & Mentis 1992: fig. 5B), and similar sharply bounded cavities in latewood are known from Indian Permian woods (Pant & Singh 1987: pl. 10, fig. 93).

Several examples of Permian and Triassic wood from the Transantarctic Mountains (Stubblefield & Taylor 1985, 1986) and the Bowen Basin, Australia (McLoughlin 1992), show cavities arranged around growth rings. They commonly show the clean-cut walls characteristic of arthropod attack, but they lack coprolites and have been attributed to fungal saprophytism. In some of the Transantarctic Mountains and Bowen Basin examples, the woods do exhibit decayed cells and host responses, as well as having fungal hyphae within associated tissues, so it is likely that these were caused directly by fungal attack or by fungi utilising sites of damage caused by arthropods to gain access to the plant tissues. Significantly, some modern wood-boring beetles and fungi show mutualistic relationships, whereby the beetles actively or passively disperse fungi between plants, and the insect larvae feed (at least in part) on the fungi invading the plant tissues around the larval excavation chamber (Francke-Grosman 1963; Matthews 1976).

Other studies of modern cerambycid borers have shown that, in some species, larvae preferentially attack wood only near the cambium. This suggests that, apart from holocellulose, the larvae are preferentially utilising minor nutrients such as starch (Iwata & Yamada 1990).

One or a combination of these factors (seasonal larval activity, fungal–insect association, or selective nutrient utilisation) may account for the regular positioning of the wood excavations in the Beaver Lake specimens.

Diffuse spindle-shaped cavities

Sixteen specimens of *A. mondii* have decay pockets that are superficially similar to the previously described cavities. They are round to oval in transverse section, up to 5 mm in diameter, elongate–elliptical in longitudinal section, and up to 41 mm long. They can occur within a single growth ring, or intersect several growth rings (Fig. 11A, B). The cavities are randomly distributed throughout the wood, or restricted to local areas. In a few specimens they appear to occur in bands parallel to the growth rings, but are generally not confined to one part of the ring. The cavities lack organic contents, except for cell fragments locally, and are typically filled with chalcedony. The cells along the edges of the cavities are partly decayed, and have thin walls with thickened corners (Fig. 11C). Fungal hyphae were not observed, but some cell lumens contain unidentified filamentous structures (Fig. 11G, H). These cells are always filled with a light brown substance surrounding the filaments. The filaments are most evident in petrographic thin sections. They usually occur only in isolated cells (Fig. 11H), but some fill several adjacent cells when the cell walls are partly or wholly missing (Fig. 11G). In some regions, numerous cells containing these filaments are scattered among normal cells. The filaments also occur in specimens of *A. mondii* that lack cavities, so it is uncertain whether filaments and cavities are in any way causally related. Appositions are apparent in some cells, and indicate a host response to pathogen attack (Fig. 11D–F). Woods showing this type of damage generally have thinner cell walls than normal, and the corners of adjacent cells remain conspicuous. This is in contrast to the sharply cut margins of the arthropod-bored cavities.

Similar spindle-shaped cavities have been recorded in Permian and Triassic wood from the Transantarctic Mountains (Stubblefield & Taylor 1986; Taylor 1993) and Cretaceous wood from Western Australia (McLoughlin et al. 1994). These authors attributed the cavities to the actions of fungi, as they found preserved fungal hyphae, degraded cell walls, and appositions in the same specimens. These cavities were thought to be caused by basidiomycetes similar to modern white-pocket rot fungi, such as that described by Blanchette (1980). Stubblefield & Taylor (1986) discounted insects as the cause

Figure 8 *(continued from facing page).*
I, cupressoid pits (obliquely oriented, elliptical pores; NMVP200046A). J, partially biseriate tangential pits (NMVP200041B). K, magnification of tangential pits showing borders (NMVP200041B). L, bordered cross-field pits and groups of two and three radial pits (NMVP200048). M, Figure 8L magnified to show cross-field pits (NMVP200048). N, cross-field pits that appear simple owing to poor preservation (NMVP200034). O, transverse section showing pits on the end of tracheids (NMVP200020B). Scale bars: A = 0.1 mm; D, E, F, G, J, L, N, O = 0.05 mm; B, C, H, I, K, M = 0.01 mm.

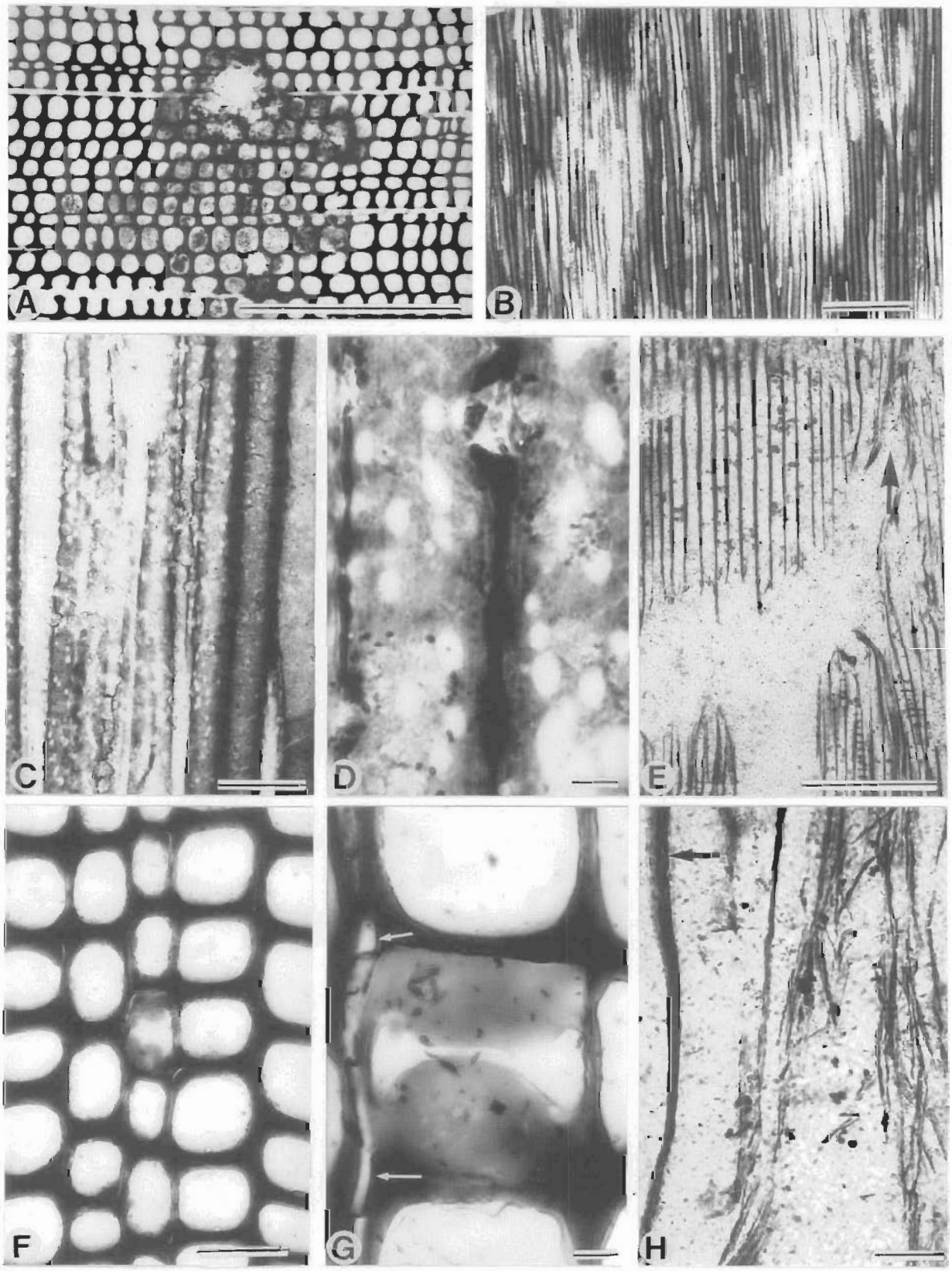

Figure 9. Irregular decay in *Australoxylon bainii* wood. A, transverse section showing cavity surrounded by damaged tracheids (NMVP200011A). B, damage holes in tangential section (NMVP200011D). C, portion of Figure 9B enlarged (NMVP200011D). D, portion of Figure 9B highly enlarged showing that the damaged area is formed by coalescence of numerous small holes in the tracheid walls (NMVP200011D). E, damage hole in radial section; the part magnified in Figure 9H is arrowed (NMVP200011B). F, apposition intruding into the lumen of a cell (NMVP200011A). G, apposition nearly blocking a tracheid, and separation of the cell walls (arrowed; NMVP200011A). H, higher magnification of Figure 9E; arrow shows normal-thickness tracheid wall; extensive damage to the cell walls evident (NMVP200011B). Scale bars: A, B, E = 0.5 mm; C = 0.1 mm; F, H = 0.05 mm; D, G = 0.01 mm.

of these cavities because they are very variable in size, contain no coprolites or frass, do not show joining galleries, and have degraded peripheral cells. Similarly, diffuse cavities in Beaver Lake woods do not seem to have been caused by arthropods.

Growth rings

All the Beaver Lake woods possess distinct growth rings that indicate marked seasonality in the environment. Each season's growth consists mostly of uniform-size earlywood cells with just two to four smaller cells comprising the latewood. The small amount of latewood is a common feature in woods from high latitudes, and is interpreted to be a function of the plant's sharply reduced wood production in response to the rapid change in photoperiod at the end of the growing season (Parrish & Spicer 1988).

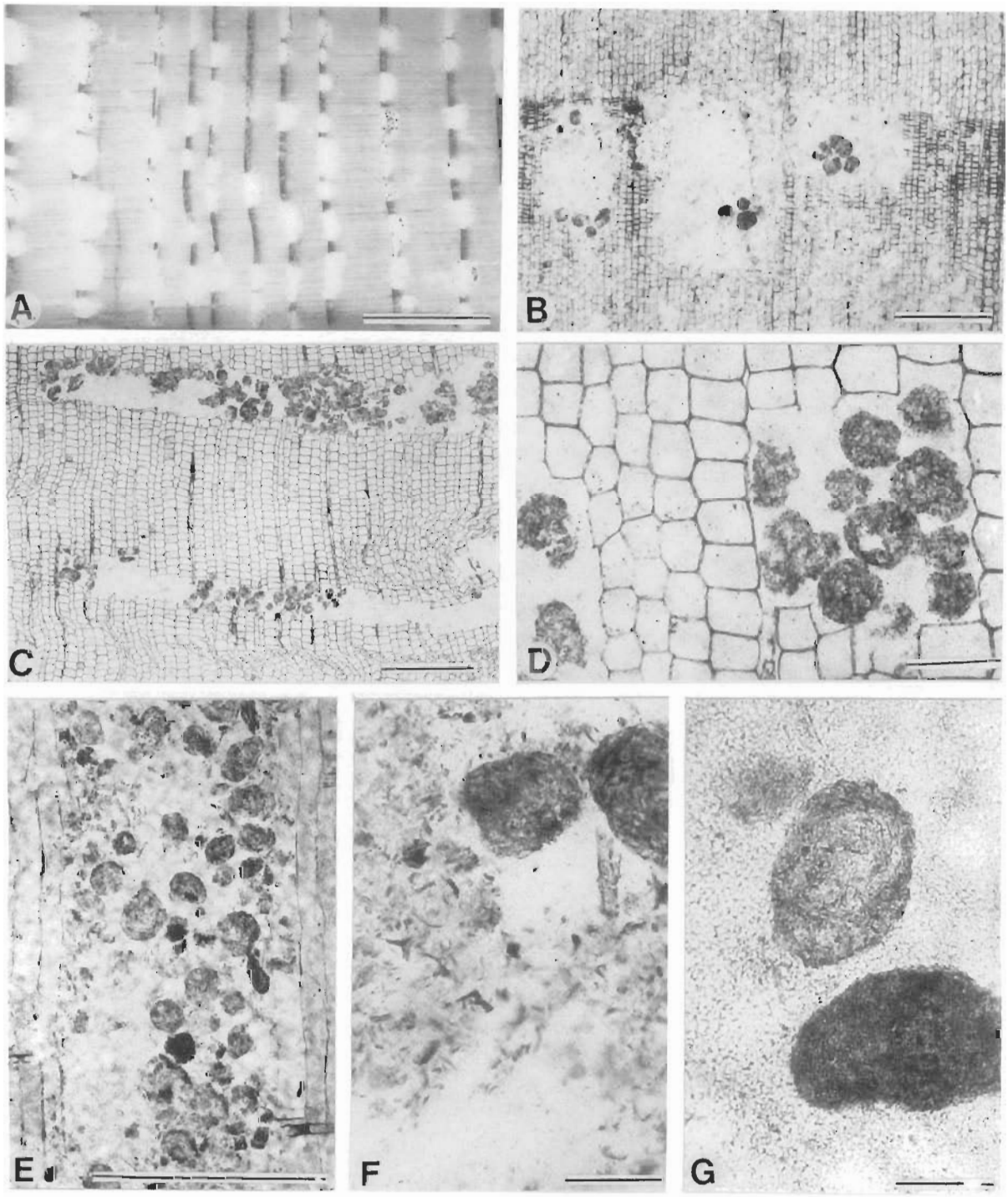

Figure 10. Arthropod borings in *Australoxylon mondii*. A, cavities mainly in latewood; some contain visible coprolites (NMVP200040D). B, cavities confined mainly to the latewood, not extending into the next season's growth (NMVP200040C). C, coprolites in slit-like holes in latewood (NMVP200051). D, coprolites in holes showing minimal damage to surrounding tissue (NMVP200051). E, cavities in radial section showing range of coprolite sizes (NMVP200040B). F, coprolites and powdered frass (NMVP200040A). G, magnification of coprolites showing granular-fibrous texture (NMVP200040A). Scale bars: A = 5 mm; B, C, E = 0.5 mm; D = 0.1 mm; F, G = 0.05 mm.

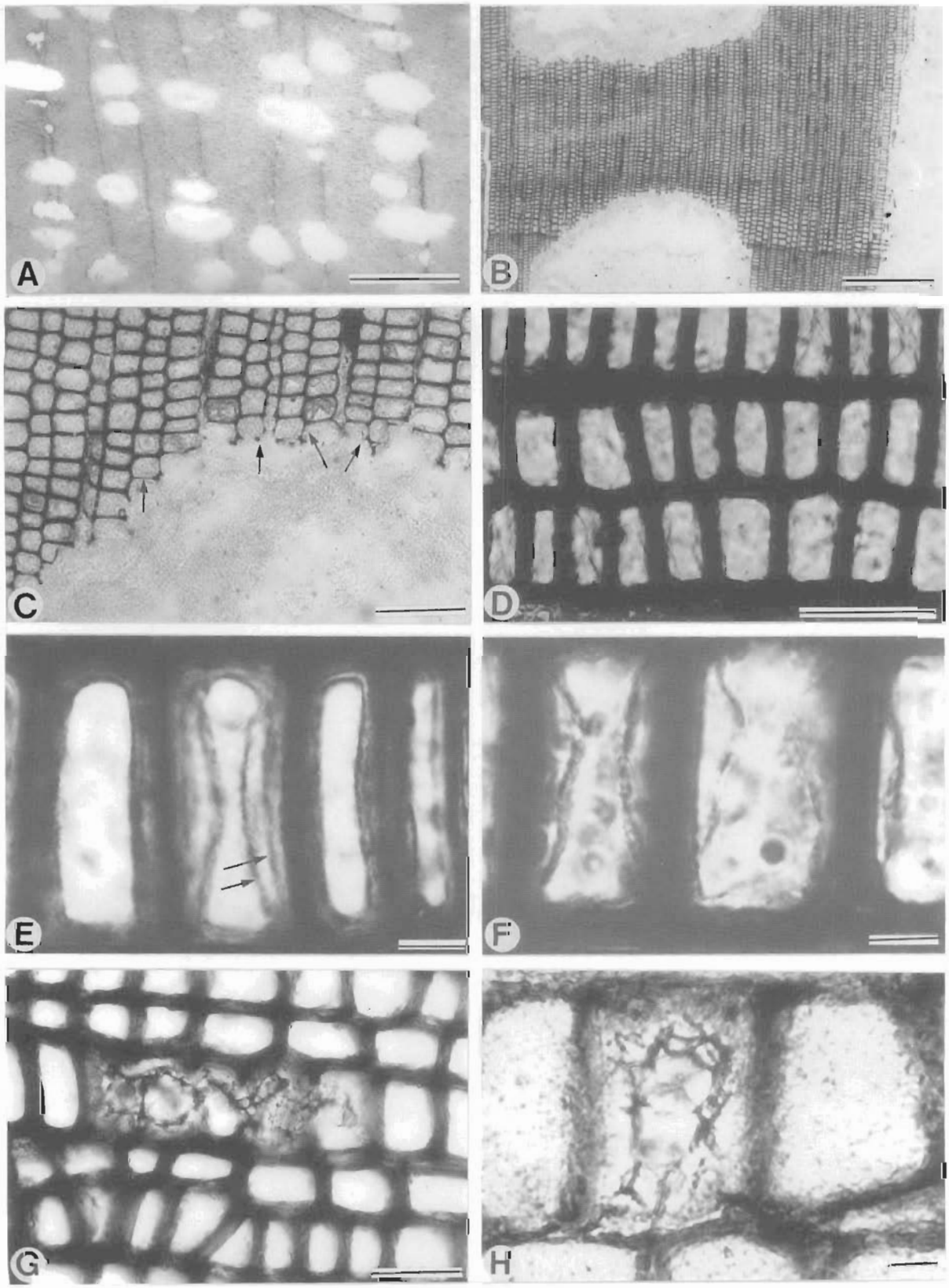

Figure 11. Diffuse cavities in *Australoxylon mondii*. A, specimen showing many cavities, not confined to latewood (NMVP200023). B, holes intersecting ring boundary, with chalcedony infillings (NMVP200037). C, cavity showing limited damage to surrounding cells; cell corners appear to have suffered less decay than the straight walls (arrowed; NMVP200037). D, section of latewood showing numerous appositions caused by splitting walls (NMVP200041C). E, apposition showing two layers arrowed (NMVP200041C). F, apposition caused by the detachment of a layer of the cell wall (NMVP200041C). G, filamentous structures filling several damaged cells (NMVP200020B). H, enlargement of filamentous structures (NMVP200020D). Scale bars: A = 5 mm; B = 0.5 mm; C = 0.1 mm; D, G = 0.05 mm; E, F, H = 0.01 mm.

Many specimens, especially smaller axes, show asymmetry in their rings (Fig. 12G, H), which could have been caused by uneven growth due to loss of crown, tree lean or shading, or increase in incident sunlight on one side of the tree producing different growth conditions. One specimen (Fig. 12H) has extreme ring-width variation on the same radii, as well as

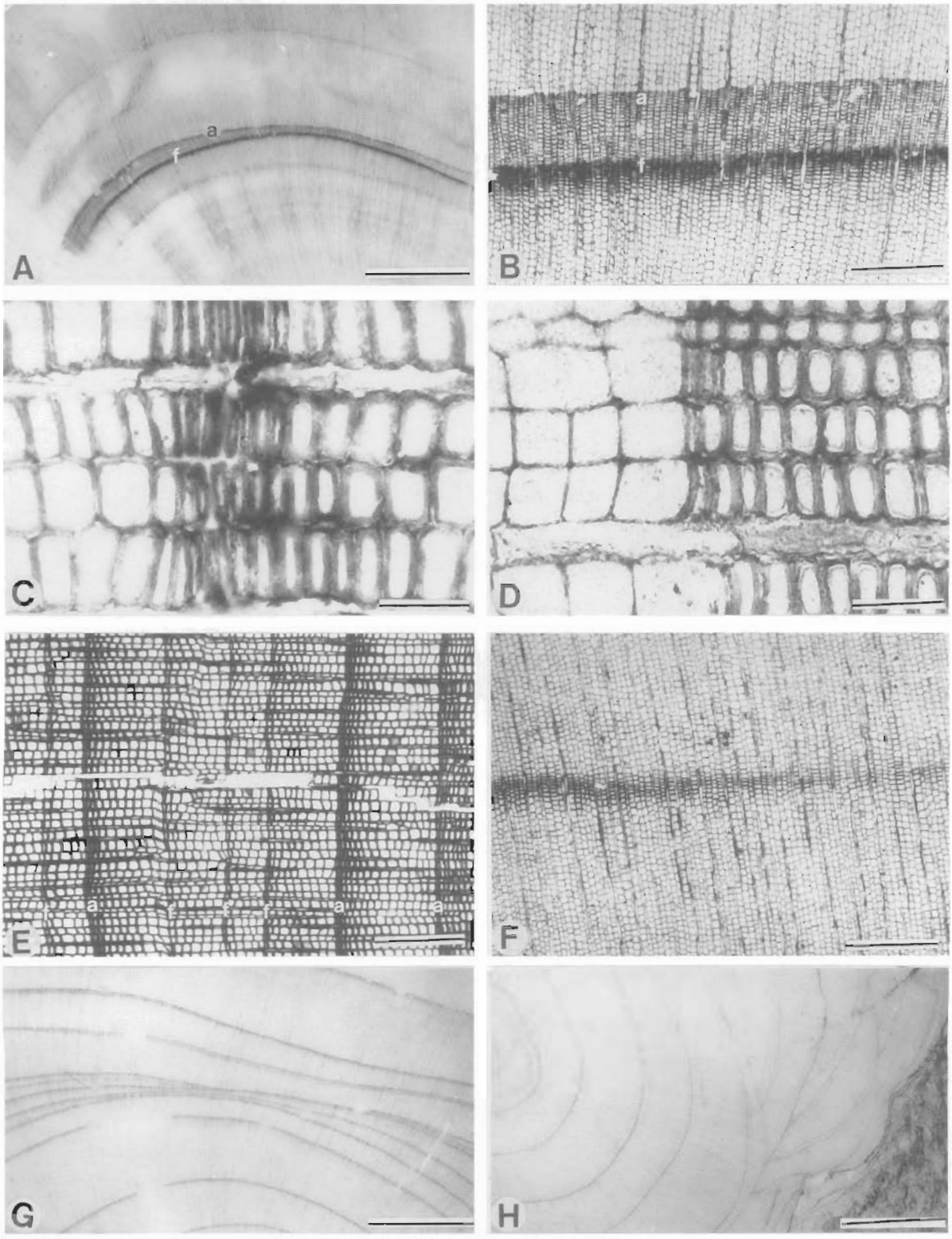

Figure 12. Growth rings in *Australoxylon mondii*. A, false (f) and annual (a) rings (NMVP200053C). B, portion of Figure 12A magnified to show the false (f) and annual (a) rings (NMVP200053A). C, high magnification of false ring in Figure 12A showing the gradual change in cell wall thickness and cell size from earlywood (left) to latewood (right) in transverse section (NMVP200053A). D, high magnification of annual ring in Figure 12A showing sharp change in cell wall thickness and cell size from latewood (right) to earlywood (left) in transverse section (NMVP200053A). E, three annual rings (a) and four false rings (f; NMVP200020B). F, false ring which varies in prominence around the stem (NMVP200049). G, transverse section showing strong variation in ring widths around the axis (NMVP200046B). H, unusual pattern of ring distribution in a specimen (embedded in peat) with discontinuous and merging rings (NMVP200014). Scale bars: A, G, H = 5 mm; B, E, F = 0.5 mm; C, D = 0.05 mm.

Table 2. Growth-ring data recorded for 19 fossil wood specimens from Beaver Lake.

Specimen (NMVP)	*Species*	*Number of rings*	*Range of ring widths (mm)*	*Mean ring width (mm)*	*Mean sensitivity*	*False rings*
200011	*A. bainii*	40	0.8–4.0	2.31	0.226	0
200014	*A. mondii* (normal)	13	0.8–2.8	1.81	0.367	0
200015	*A. mondii* (normal)	14	0.4–3.9	1.14	0.368	8
200019	*A. mondii* (normal)	26	0.7–3.7	1.53	0.428	0
200020	*A. mondii* (normal)	82	0.2–2.3	0.77	0.439	0
200024	*A. mondii* (normal)	21	1.1–3.3	2.02	0.190	1
200025	*A. mondii* (normal)	29	0.5–3.0	1.69	0.249	0
200026	*A. mondii* (normal)	24	0.5–3.0	1.51	0.371	6
200028	*A. mondii* (normal)	26	0.9–2.4	1.57	0.258	0
200029	*A. mondii* (normal)	12	1.8–6.2	3.40	0.252	0
200035	*A. mondii* (normal)	27	0.5–3.1	1.29	0.303	1
200037	*A. mondii* (atypical)	28	1.2–5.0	2.62	0.475	5
200038	*A. mondii* (atypical)	29	0.7–7.1	2.67	0.472	3
200040	*A. mondii* (atypical)	22	1.0–4.5	2.28	0.375	0
200044	*A. mondii* (atypical)	16	0.3–5.8	2.52	0.421	7
200045	*A. mondii* (atypical)	13	1.7–4.8	2.88	0.270	2
200046	*A. mondii* (atypical)	15	1.4–6.0	3.03	0.259	11
200047	*A. mondii* (atypical)	18	1.4–6.6	3.87	0.398	8
200049	*A. mondii* (atypical)	14	0.7–5.0	2.24	0.287	3

around the circumference. Its rings decrease in thickness laterally and disappear in a mesh of overlapping lenses. There is no wound response tissue to suggest that this was caused by a traumatic event, such as fire or frost, so it is presumably a normal growth feature of the wood. The variable rings may indicate that this wood is from a root that has been distorted by obstacles in the substrate. This specimen, however, does not possess the xylem wedges of *Vertebraria*, the typical glossopterid root form. Nevertheless, it is possible that not all glossopterids possessed *Vertebraria*-type roots, or that this wood belongs to some other plant (cf. Neish et al. 1993). The grouping of roots and stems together for palaeoclimatic analyses must be avoided, but this is difficult for the Beaver Lake woods, which appear to be indistinguishable for most anatomical characters. Larger specimens with continuous rings were chiefly used in the growth-ring analysis.

Nineteen wood samples (comprising eighteen *A. mondii* and one *A. bainii* specimens) with good cellular preservation were selected for growth-ring analysis (Table 2). The broadest ring measured within the Beaver Lake specimens selected for detailed analysis was 7.1 mm wide (Table 2), but other specimens in the collection have rings up to 9.9 mm wide. Mean ring widths for individual axes are in the range 0.77–3.87 mm (average 2.17 mm).

The variation in width of rings is principally a function of different cell numbers (Fig. 13) rather than of cell diameters, and indicates that the rate of cell division in the cambium varied from year to year and/or that the length of the growing season was variable. Annual sensitivity is a measure of the similarity between adjacent pairs of growth rings, and mean sensitivity is the average of these values for each wood specimen (Fritts 1976; Creber 1977). Annual sensitivity values for the Beaver Lake woods generally fall into the 'complacent' field (<0.3). Some specimens, however, show several highly variable ring couplets, for which high annual sensitivity values result in mean sensitivities skewed towards the 'sensitive' field (Fig. 14). Mean sensitivities are in the range 0.190–0.475 (average 0.337), and roughly equal numbers of specimens fall into the complacent and sensitive fields (Fig. 15).

Several authors have analysed growth-ring data from fossil woods of Tertiary to Permian age (Table 3), particularly for the purposes of understanding past forest growth in polar latitudes. Although some features of the Beaver Lake woods (e.g., ring widths, mean sensitivity, presence of false rings)

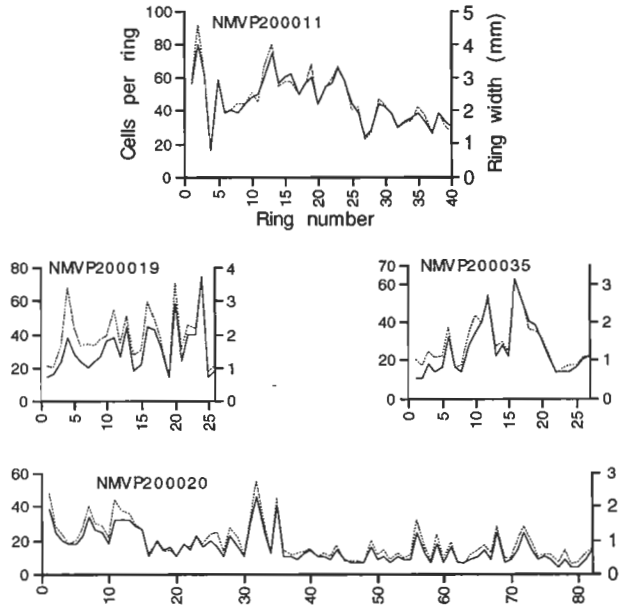

Figure 13. Plots of selected growth ring sequences in the Beaver Lake woods. Solid line = ring width in mm; dashed line = number of cells per ring.

are similar to woods from other sites and ages, no other assemblage of fossil woods closely matches the gross suite of growth measurements (Table 3). Average ring widths are most similar to high-latitude Cretaceous and early Tertiary conifer and angiosperm woods, but the Beaver Lake specimens typically have higher mean sensitivities. The low mean sensitivities of the Antarctic Peninsula floras (Francis 1986) may have been a function of growth in a more equable maritime climate than other studied assemblages derived chiefly from continental interiors. Local factors may also significantly influence sensitivity values in tree wood. Trees growing at the margins of forests tend to have higher mean sensitivity values than those growing in forest centres (Fritts 1976). Differences in growth characters between the Beaver Lake and other taxonomically different fossil woods may also reflect, in part, a genetic control on wood production (Jefferson 1982).

However, despite the abundance of Gondwanan Permian woods, no detailed growth analyses have previously been conducted on them. This deficiency precludes ready comparison of glossopterid/cordaite-versus-conifer-versus-angiosperm climate responses. Among the Beaver Lake woods, the single *A. bainii* specimen analysed for ring dimensions shows the second lowest mean sensitivity, but additional material would be required to determine whether *A. bainii* and *A. mondii* showed significant differences in their growth characteristics.

The woods show many false rings. These are generally only a few cells wide, but some are of considerable thickness. False rings can usually be distinguished from the annual rings by the gradual-versus-abrupt change in the cell diameters and cell wall thicknesses (Fig. 12C, D, F). They can be either very dark and more prominent than the annual rings (Fig. 12A, B), or much fainter (Fig. 12E). False rings may have been caused by factors affecting the individual tree, such as enhanced herbivory, or by general climatic conditions affecting all trees. In extant trees, false rings can result from drought, flood, herbivory, pathogen attacks, and many other intraseasonal environmental fluctuations (Creber & Chaloner 1984a, b). The number of false rings in a season varies considerably: some seasons have no false rings, while others have up to four (Fig. 12E).

Although false rings are common in trees from ancient and modern semiarid and Mediterranean climates (Francis 1984), they also appear to be common in some (but not all) ancient high-latitude forest trees of wet environments (Table 3). In semiarid climates, false rings typically form in response to water shortage during the growing season, but in high latitudes, especially Permian glossopterid mire-forests (sensu Retallack 1980), false rings were probably induced by other factors — perhaps light availability, temperature fluctuations, or insect/parasite attack. Numerous false rings within distinctive broad annual rings were also reported from Late Permian fossil woods from the Transantarctic Mountains (Taylor et al. 1992), suggesting that intraseasonal environmental fluctuations may have been a common phenomenon affecting growth in high-latitude glossopterid forests.

Plots of ring widths and annual sensitivity (Figs. 13; 14) suggest that the trees generally showed a complacent response to interseasonal environmental conditions, but that sporadic seasons of high or low growth rates strongly skew mean sensitivity values towards the sensitive field. Although there appear to be strong seasonal controls and intraseasonal influences on the trees, the variation between and within specimens, the number and variation in false rings, the difficulty in differentiating root and stem wood, and the scarcity of studies of coeval fossil woods hamper a quantitative palaeoclimatic analysis. It is, nevertheless, clear that high seasonal productivity was a feature of glossopterid mire-forests at the high palaeolatitudes of the Prince Charles Mountains (ca 60°S: Smith et al. 1981) and at even higher palaeolatitudes (80–85°S: Taylor et al. 1992) in other parts of Antarctica during the

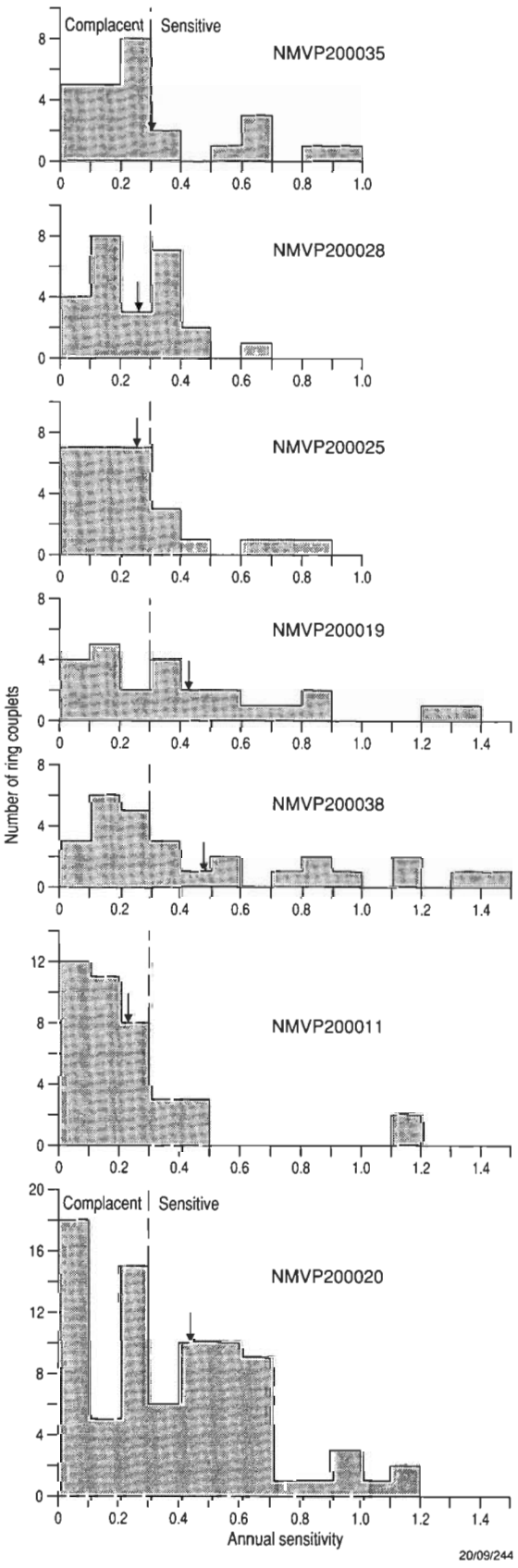

Figure 14. Histograms of annual sensitivity values for selected Beaver Lake woods. Arrows indicate mean sensitivity for each specimen.

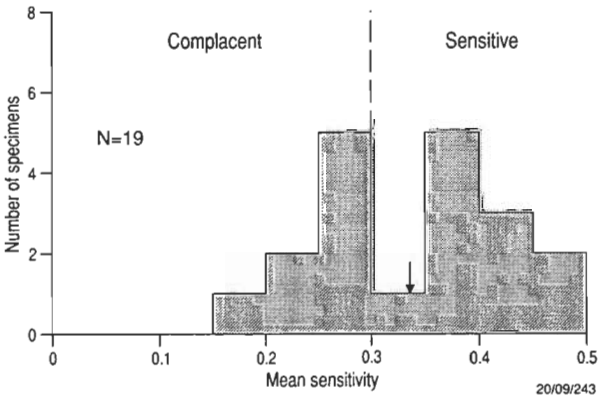

Figure 15. Histogram of mean sensitivity values for 19 wood specimens from Beaver Lake. Arrow indicates average mean sensitivity.

Table 3. Comparison of tree-ring data among various assemblages of fossil wood of Permian to early Tertiary age. Numbers in parentheses represent average values. Wood types: A = angiosperms; C = conifers; G = glossopterids; Cord. = cordaites.

Authors	*Age*	*Locality*	*Palaeo-latitude*	*Wood type*	*Mean ring widths (mm)*	*Mean sensitivity*	*False rings*
Francis (1986)	early Tertiary	Seymour Island, Antarctica	ca 60°S	A,C	0.52–5.70 (2.25)	0.139–0.371 (0.228)	Not observed
Taylor et al. (1990)	Paleocene	Bombala, SE Australia (>400 m altitude)	60–65°S	C,A	0.28–3.83 (0.97)	0.185–0.491 (0.284)	Not observed
Francis (1986)	Early–Late Cretaceous	Antarctic Peninsula	ca 60°S	C,A	0.61–7.50 (2.35)	0.123–0.357 (0.184)	Not observed
Parrish & Spicer (1988)	mid-Cretaceous	Central North Slope, Alaska	74–85°N	C	1.1–4.6 (2.74)	0.28–0.76 (0.427)	Scarce
Jefferson (1982, 1983)	Early–mid-Cretaceous	Alexander Island, Antarctica	ca 65–75°S	C	up to 2.5 (1.397)	0.4–0.5 (0.424)	Common
Frakes & Francis (1990)	Early–mid-Cretaceous	Eromanga Basin, S Australia	ca 70°S (65–75°S)	C	popn A 0.34–0.92 (0.63) popn B 1.17–4.53 (2.23)	popn A (0.157) popn B (0.202)	Not observed Not observed
McLoughlin et al. (1994)	Early Cretaceous	Carnarvon Basin, W Australia	45–50°S	C	0.305–9.390 (1.598)	0.148–0.673 (0.348)	Uncommon
Francis (1984)	Late Jurassic	Purbeck, England	36°N	C	0.52–2.28 (1.13)	0.290–0.769 (0.527)	Common
Taylor et al. (1992)	Late Permian	Mt Achernar, Transantarctic Mtns	80–85°S	G	(4.5)	?	Common
This study	Late Permian	Prince Charles Mtns	60°S	G/Cord.	0.77–3.87 (2.17)	0.190–0.475 (0.337)	Common
Francis et al. (1993)	late Early–Late Permian	Allan Hills, Victoria Land, Antarctica	ca 70–80°S	G	rings up to 8mm	?	?

Late Permian. High gymnosperm growth rates and closely spaced in-situ tree trunks imply that it was probably the seasonal availability of light rather than low temperatures that chiefly regulated wood productivity in Antarctica at that time (Taylor et al. 1992).

Conclusions

Two types of wood from the Beaver Lake area are assigned to new species of the genus *Australoxylon*. *Australoxylon mondii* is similar to several other Gondwanan woods, but some of the problematic characters are not consistent with established diagnoses; the species is distinguished on ray and tracheid dimensions, shape of tracheids in transverse section, cross-field pits, and ray structure. *Australoxylon mondii* has two forms that are identical in all respects except ray structure. Unusual rays of semidetached files of cells are found in 'atypical' *A. mondii*. They have been previously observed only in woods from Beaver Lake and the Raniganj Coalfield of India. The cause and function of this anatomical arrangement is not known, but it appears not to be a post-mortem artefact. The gaps between the files of ray cells may have been air spaces used to aerate roots. Secondary wood of *Vertebraria* is very similar to 'normal' *A. mondii*, and could be distinguished only on the gross shape of the xylem cylinder. This suggests that *A. mondii* is of glossopterid origin. The absence of attached foliage or other organs does not allow determination of the botanical affinities of *A. bainii*, but the abundantly associated leaves and fructifications at the site of fossilisation (McLoughlin & Drinnan 1996) suggest that it might have glossopterid or cordaitalean affinities.

Radial pit arrangement, pore shape, size, and groupings were not useful in taxonomic differentiation of the Beaver Lake woods. Neither were the presence of tangential pits and bars of Sanio, which proved to be preservationally controlled. These characters have been widely used in past studies to separate wood taxa; hence a thorough review of past fossil wood determinations is required to assess their validity. The degree of intraspecific variation in these characters, and the effects of the preservation and preparation on discerning these characters, need to be reassessed.

Three types of cavities are evident in the woods. Irregular cavities occur in all *A. bainii* specimens. Their cause was not identified, but the presence of appositions in some cells and the lack of detectable deterioration of the surrounding wood before it was fossilised suggest that they formed while the plant was alive. Sharp-walled cavities caused by wood-boring arthropods occur in *A. mondii*. They contain coprolites and powdered frass, probably from mites or beetle larvae, and occur mainly in the latewood of the growth rings. If eggs were laid within the bark of the tree, the larvae might have lived in the cavities during the trees' seasonal dormant period; the plant has not responded to the attack, and the cavities do not extend into the next season's growth.

Other cavities, similar to examples recorded from the Transantarctic Mountains and the Bowen Basin, have been attributed to white-pocket rot fungi. Cells surrounding these cavities have suffered wall degradation; fungal hyphae have not been identified, but there are some filamentous structures in cells of the specimens containing these cavities, as well as in specimens without cavities. Appositions and tyloses found in several specimens indicate that the trees had expressed some response to pathogens.

Quantifying palaeoclimatic parameters from the Beaver Lake woods is hindered by the lack of previous studies of glossopterid growth rings, the difficulties in differentiating stem and root wood, and potentially multiple causes for the development of false growth rings. Nevertheless, distinct growth rings in all of the woods indicate that the trees underwent an annual period of dormancy, probably during the polar winter. The deciduous character of high-latitude Permian

Gondwanan glossopterids and cordaites was probably also an adaptation for survival during the extended period of polar-winter darkness, when evergreen trees would have been subjected to severe energy loss through continued high levels of respiration. Broad rings (up to 9.9 mm wide) indicate that high wood productivity was sustainable in palaeolatitudes of 60°S during the Late Permian, but the presence of numerous false rings reflects frequent intraseasonal disturbances to plant growth. Growth was often uneven around the circumference of individual axes, and the stems and root organs of the trees could not be confidently differentiated. Nevertheless, analysis of tree rings shows roughly equal numbers of specimens with slightly sensitive and slightly complacent mean sensitivities, suggesting low to moderate interseasonal variation in growth conditions.

Acknowledgments

Material for this study was collected as part of the 1991–92 Australian National Antarctic Research Expedition (Antarctic Science Advisory Committee project number 509). Additional funding was provided by Australian Research Council Grant A39331444 to AND. Dr E.M. Truswell and J.F. Rigby provided valuable comments on the manuscript.

References

Balme, B.E. & Playford, G., 1967. Late Permian plant microfossils from the Prince Charles Mountains, Antarctica. Revue de Micropalontologie, 10, 179–192.

Barefoot, A.C. & Hankins, F.W., 1982. Identification of modern and Tertiary woods. Clarendon Press, Oxford.

Beeston, J.W., 1972. A specimen of *Araucarioxylon arberi* (Seward) Beeston comb. nov. from Queensland. Geological Survey of Queensland Publication, 352, 17–20.

Belbin, L., 1987. PATN pattern analysis package. Users, example, command and reference manuals. CSIRO Division of Wildlife and Ecology, Canberra.

Blanchette, R.A., 1980. Wood decomposition by *Phellinus (Fomes) pini*: a scanning electron microscopy study. Canadian Journal of Botany, 58, 1496–1503.

Brzyski, B., 1969. Tissue structures of petrified plant remains from the Carboniferous (Namurian A) of the Upper Silesian Coal Basin. Acta Palaeobotanica, 10, 1–98.

Cantrill, D.J. & Drinnan, A.N., 1994. Late Triassic megaspores from the Amery Group, Prince Charles Mountains, East Antarctica. Alcheringa, 18, 71–78.

Cantrill, D.J., Drinnan, A.N. & Webb, J.A., 1995. Late Triassic plant fossils from the Prince Charles Mountains, East Antarctica. Antarctic Science, 7, 51–62.

Carpenter, F.M. & Burnham, L., 1985. The geological record of insects. Annual Review of Earth and Planetary Science, 13, 297–314.

Chaloner, W.G., Scott, A.C. & Stephenson, J., 1991. Fossil evidence for plant–arthropod interactions in the Palaeozoic and Mesozoic. Philosophical Transactions of the Royal Society of London, 333B, 123–177.

Chichan, M.A. & Taylor, T.N., 1982. Wood-borings in *Premnoxylon*: plant–animal interactions in the Carboniferous. Palaeogeography, Palaeoclimatology, Palaeoecology, 39, 123–127.

Creber, G.T., 1977. Tree rings: a natural data-storage system. Biological Review, 52, 349–383.

Creber, G.T. & Chaloner, W.G., 1984a. Climatic indications from growth rings in fossil woods. In: Brenchley P.J. (editor), Fossils and climate. John Wiley, Chichester, 49–77.

Creber, G.T. & Chaloner, W.G., 1984b. Influence of environmental factors on the wood structure of living and fossil trees. Botanical Review, 50, 357–448.

Dibner, A.F., 1978. Palynocomplexes and age of the Amery Formation deposits, East Antarctica. Pollen et Spores, 20, 405–422.

Duffy, E.A.J., 1953. A monograph of the immature stages of British and imported timber beetles (Cerambycidae). British Museum (Natural History), London.

Fedorov, L.V., Ravich, M.G. & Hofman, J., 1982. Geologic comparison of southeastern peninsular India and Sri Lanka with a part of East Antarctica (Enderby Land, MacRobertson Land, and Princess Elizabeth Land). In: Craddock, C. (editor), Antarctic geoscience. University of Wisconsin Press, Madison, 73–78.

Fielding, C.R. & Webb, J.A., 1995. Sedimentology of the Permian Radok Conglomerate in the Beaver Lake area of MacRobertson Land, East Antarctica. Geological Magazine, 132, 51–63.

Fielding, C.R. & Webb, J.A., 1996. Facies and cyclicity of the Late Permian Bainmedart Coal Measures in the northern Prince Charles Mountains, MacRoberston Land, Antarctica. Sedimentology, 43, 295–322.

Foster, C.B., Balme, B.E. & Helby, R., 1994. First record of Tethyan palynomorphs from the Late Triassic of East Antarctica. AGSO Journal of Australian Geology & Geophysics, 15, 239–246.

Frakes, L.A. & Francis, J.E., 1990. Cretaceous palaeoclimates. In: Ginsburg, R.N. & Beaudoin, B. (editors), Cretaceous resources, events and rhythms. Kluwer Academic Publishers, Dordrecht, 273–287.

Francis, J.E., 1984. The seasonal environment of the Purbeck (Upper Jurassic) fossil forests. Palaeogeography, Palaeoclimatology, Palaeoecology, 48, 285–307.

Francis, J.E., 1986. Growth rings in Cretaceous and Tertiary wood from Antarctica and their palaeoclimatic implications. Palaeontology, 29, 665–684.

Francis, J.E., Woolfe, K.J., Arnot, M.J. & Barrett, P.J., 1993. Permian forests of Allan Hills, Antarctica: the palaeoclimate of Gondwanan high latitudes. Special Papers in Palaeontology, 49, 75–83.

Francke-Grosman, H., 1963. Some new aspects in forest entomology. Annual Review of Entomology, 8, 415–438.

Fritts, H.C., 1976. Tree rings and climate. Academic Press, London.

Gould, R.E., 1975. A preliminary report on petrified axes of *Vertebraria* from the Permian of eastern Australia. In: Campbell, K.S.W. (editor), Gondwana geology. Australian National University Press, Canberra, 109–115.

Iwata, R. & Yamada, F., 1990. Notes on the biology of *Hesperophanes campestris* (Faldermann) (Coleoptera, Cerambycidae), a drywood borer in Japan. Material un Organismen, 25, 305–314.

Jefferson, T.H., 1982. Fossil forests from the Lower Cretaceous of Alexander Island, Antarctica. Palaeontology, 25, 681–708.

Jefferson, T.H., 1983. Palaeoclimatic significance of some Mesozoic Antarctic fossil floras. In: Oliver, R.L., James, P.R. & Jago, J.B. (editors), Antarctic Earth science. Australian Academy of Science, Canberra, 593–598.

Joy, K.W., Willis, A.J. & Lacey, W.S., 1956. A rapid cellulose peel technique in palaeobotany. Annals of Botany, 20, 635–637.

Kemp, E.M., 1973. Permian flora from the Beaver Lake area, Prince Charles Mountains, Antarctica, 1: Palynological examination of samples. Bureau of Mineral Resources, Australia, Bulletin 126, 7–12.

Kräusel, R., 1962. Antarctic fossil wood. Appendix in: Plumstead, E.P., Fossil floras of Antarctica. Transantarctic Expedition (1955–1958), Scientific Report 9, 133–140.

McLoughlin, S., 1992. Late Permian plant megafossils

from the Bowen Basin, Queensland, Australia, part 1. Palaeontographica, 228B, 105–149.

McLoughlin, S. & Drinnan, A.N., in press a. Revised stratigraphy of the Permian Bainmedart Coal Measures, northern Prince Charles Mountains, East Antarctica. Geological Magazine.

McLoughlin, S. & Drinnan, A.N., in press b. Sedimentology and revised stratigraphy of the Permian–Triassic Flagstone Bench Formation, northern Prince Charles Mountains, East Antarctica. Geological Magazine.

McLoughlin, S. & Drinnan, A.N., 1996. Anatomically preserved Permian *Noeggerathiopsis* Feistmantel leaves from East Antarctica. Review of Palaeobotany and Palynology, 92.

McLoughlin, S., Haig, D.W., Backhouse, J., Holmes, M.A., Ellis, G., Long, J.A. & McNamara, K.J., 1994. Oldest Cretaceous sequence, Giralia Anticline, Carnarvon Basin, Western Australia: late Hauterivian–Barremian. AGSO Journal of Australian Geology & Geophysics, 15, 445–468.

Maheshwari, H.K., 1972. Permian wood from Antarctica and revision of some lower Gondwana wood taxa. Palaeontographica, 138B, 1–43.

Marguerier, J., 1973. Palaeoxylologie du Gondwana African: Études et affinities du genre *Australoxylon*. Palaeontologia Africana, 16, 37–58.

Martin, M.M., 1991. The evolution of cellulose digestion in insects. Philosophical Transactions of the Royal Society of London, 333B, 281–288.

Matthews, E.G., 1976. Insect ecology. University of Queensland Press, St Lucia.

Mond, A., 1972. Permian sediments of the Beaver Lake area, Prince Charles Mountains. In: Adie, R.J. (editor), Antarctic geology and geophysics. Universitetsforlaget, Oslo, 585–589.

Neish, P.G., Drinnan, A.N. & Cantrill, D.J., 1993. Structure and ontogeny of *Vertebraria* from silicified Permian sediments in East Antarctica. Review of Palaeobotany and Palynology, 79, 221–244.

Pant, D.D. & Singh, R.S., 1968. The structure of *Vertebraria indica* Royle. Palaeontology, 11, 643–653.

Pant, D.D. & Singh, V.K., 1987. Xylotomy of some woods from Raniganj Formation (Permian), Raniganj Coalfield, India. Palaeontographica, 203B, 1–82.

Parrish, J.T., 1990. Gondwanan paleogeography and paleoclimatology. In: Taylor, T.N. & Taylor, E.L. (editors), Antarctic paleobiology. Its role in the reconstruction of Gondwana. Springer-Verlag, New York, 15–25.

Parrish, J.T. & Spicer, R.A., 1988. Middle Cretaceous wood from the Nanushuk Group, central North Slope, Alaska. Palaeontology, 31, 19–34.

Playford, G., 1990. Proterozoic and Paleozoic palynology of Antarctica: a review. In: Taylor, T.N. & Taylor, E.L. (editors), Antarctic paleobiology. Its role in the reconstruction of Gondwana. Springer-Verlag, New York, 55–70.

Prasad, M.N.V., 1982. An annotated synopsis of Indian Palaeozoic gymnospermous woods. Review of Palaeobotany and Palynology, 38, 119–156.

Ravich, M.G. & Fedorov, L.V., 1982. Geologic structure of MacRobertson Land and Princess Elizabeth Land, East Antarctica. In: Craddock, C. (editor), Antarctic geoscience. University of Wisconsin Press, Madison, 499–504.

Retallack, G., 1980. Late Carboniferous to Middle Triassic megafossil floras from the Sydney Basin. New South Wales Geological Survey, Bulletin 26, 384–430.

Savory, T., 1977. Arachnida (2nd edition). Academic Press, London.

Scott, A.C., 1992. Trace fossils of plant–arthropod interactions. In: Maples, C.G. & West, R.R. (editors), Trace fossils. Short courses in paleontology. Palaeontological Society, University of Tennessee, Knoxville, 197–222.

Scott, A.C. & Taylor, T.N., 1983. Plant animal interactions during the Upper Carboniferous. Botanical Review, 49, 259–307.

Scott, A.C., Stephenson, J. & Chaloner, W.G., 1985. Evidence of pteridophyte–arthropod interactions in the fossil record. Proceedings of the Royal Society of Edinburgh, 86B, 133–140.

Smith, A.G., Hurley, A.M. & Briden, J.C., 1981. Phanerozoic paleocontinental world maps. Cambridge University Press, Cambridge.

Stagg, H.M.J., 1985. The structure of Prydz Bay and MacRobertson Shelf, East Antarctica. Tectonophysics, 114, 315–340.

Stubblefield, S.P. & Taylor, T.N., 1985. Fossil fungi in Antarctic wood. Antarctic Journal of the United States, 20, 7–8.

Stubblefield, S.P. & Taylor, T.N., 1986. Wood decay in silicified gymnosperms from Antarctica. Botanical Gazette, 147, 116–125.

Taylor, E.L., Taylor, T.N. & Cúneo, N.R., 1992. The present is not the key to the past: a polar forest from the Permian of Antarctica. Science, 257, 1675–1677.

Taylor, G., Truswell, E.M., McQueen, K.G. & Brown, M.C., 1990. Early Tertiary palaeogeography, landform evolution, and palaeoclimates of the southern Monaro, N.S.W., Australia. Palaeogeography, Palaeoclimatology, Palaeoecology, 78, 109–134.

Taylor, T.N., 1993. The role of late Paleozoic fungi in understanding the terrestrial paleoecosystem. Comptes Rendus XII ICCP, 2, 147–154.

Tingey, R.J., 1982. The geologic evolution of the Prince Charles Mountains – an Antarctic Archaean cratonic block. In: Craddock, C. (editor), Antarctic geoscience. University of Wisconsin Press, Madison, 455–464.

Truswell, E.M., 1991. Antarctica: a history of terrestrial vegetation. In: Tingey, R.J. (editor), The geology of Antarctica. Oxford Monographs in Geology and Geophysics, 17, Clarendon Press, Oxford, 499–537.

Turner, B.R., 1991. Depositional environment and petrography of preglacial continental sediments from hole 740A, Prydz Bay, East Antarctica. In: Barron, J., Larsen, B. et al. (editors), Proceedings of the Ocean Drilling Program, scientific results. Ocean Drilling Program, Texas, 119, 45–56.

Turner, B.R. & Padley, D., 1991. Lower Cretaceous coal-bearing sediments from Prydz Bay, East Antarctica. In, Barron, J., Larsen, B. et al. (editors), Proceedings of the Ocean Drilling Program, scientific results. Ocean Drilling Program, Texas, 119, 57–60.

Wallwork, J.A., 1976. The distribution and diversity of soil fauna. Academic Press, London.

Webb, J.A. & Fielding, C.R., 1993. Permo-Triassic sedimentation within the Lambert Graben, northern Prince Charles Mountains, East Antarctica. In: Findlay, R.H., Unrug, R.J., Banks, M.R. & Veevers, J.J. (editors), Gondwana 8: assembly, evolution and dispersal. A.A. Balkema, Rotterdam, 357–369.

White, M.E., 1973. Permian flora from the Beaver Lake area, Prince Charles Mountains, Antarctica, 2: plant fossils. Bureau of Mineral Resources, Australia, Bulletin 126, 13–18.

Zavada, M.S. & Mentis, M.T., 1992. Plant–animal interaction: the effect of Permian megaherbivores on the glossopterid flora. American Midland Naturalist, 127, 1–12.

AGSO Journal of Australian Geology & Geophysics. 16(5). 677–699

Biostratigraphy of *Rig Seismic* samples from Vening Meinesz seamounts, Christmas Island area, northeastern Indian Ocean

G.C. Chaproniere[1], Samir Shafik[1], & P.J. Coleman[2]

Samples from eight dredge hauls collected during BMR cruise 107 from several seamounts in the Vening Meinesz chain, south of Christmas Island, yielded calcareous nannofossils, foraminiferids, and fragmentary macrofossils with ages ranging from Late Cretaceous to Holocene. Many samples are mixtures, suggestive of debris flows, and some contain lithologies of various ages.

The Late Cretaceous assemblages suggest shallow-water to upper bathyal depths. The seamounts were built up rapidly by volcanism, probably commencing during the Albian or Santonian, continuing through the Campanian, by which time they had shoaled, and ceasing during the Maastrichtian. Atolls comprising mounds of shelly algal biostromes dominated by rudists and *Inoceramus* had formed by the Maastrichtian. The sea was warm at this time, when the area was at latitudes far south of those of today.

The Palaeogene assemblages suggest increasingly deeper depositional environments. The Paleocene is indirectly indicated by the presence of nannofloras of this age reworked into younger assemblages, but Eocene calcareous microfossils are well represented. Shallow-water assemblages (including large neritic benthic foraminiferids) are widespread in the late Early to early Middle Eocene samples, suggesting subtropical or tropical water temperatures. The fresh volcanic content in some samples hints at the possibility of renewed volcanism during the Eocene. The Oligocene is marked by pelagites containing nannofossils.

Most of the Neogene assemblages are Late Miocene or younger, although some Middle Miocene nannofloras were recovered. Depositional depths appear to have been bathyal during this time, an accompaniment to seamount sinking and crustal and subcrustal cooling. Volcanism had ceased. Debris flows, however, continued to transport shallow-water sediments downslope. Holocene and present-day oozes mantle all previous deposits.

Introduction

In early 1992, the Australian Geological Survey Organisation (formerly BMR) conducted a survey (BMR cruise 107) of seabed morphology and offshore resources aboard RV *Rig Seismic* in the area around Christmas Island, northeastern Indian Ocean. As part of the survey, a number of seamounts were dredged and samples taken from the Vening Meinesz Seamount Chain, west-southwest of Christmas Island (Fig. 1, Table 1). This paper presents the results of a study of calcareous nannofossils and foraminiferids in 70 preparations of 50 samples from eight of the dredge hauls.

In the main body of the text, we use nannofossil, foraminiferal, and macrofossil evidence to describe the biostratigraphy of the samples; we present the essential features in a stratigraphic summary; and we assess the significance of the sample ages, along with aspects of their lithology, to gain an understanding of the evolution of the parent seamounts. The fossil assemblages are consistent with shoaling of the seamounts in the Late Cretaceous (Shafik 1992, 1993a) and the formation of flat-topped platforms, some of which may have been of atoll form. The seamounts appear to have continued to be high-standing, probably through the Paleocene. The water temperatures were moderately high when the seamounts were at latitudes of about 35°S (Eocene/Oligocene).

Magnetic lineations around Christmas Island reflect trends in two groups separated roughly by a line striking 105°E (Shafik et al. 1996). The sea-floor of the south-southwesterly group, which includes the Vening Meinesz seamounts, has lineations trending E–W and ages at least as old as Santonian (minimum age of Chron 34); sea-floor of the north-northeasterly group has lineations trending NE–SW, and represents older crust — as old as Barremian. The fossil evidence supports the results derived from the study of these lineations.

Material and methods of study

The sample nomenclature reflects the number of the cruise (107) and the dredge (DR01 to DR10) from which it originated. The lithological group to which samples were assigned during shipboard sorting is described by a second number (for example, -02). Some of these groups were later divided according to shore-based studies, and letters (A, B, C) added to their nomenclature. As well, lower-case Roman symbols (i, ii) were added to some to distinguish subsamples. In the text, we refer to dredges (e.g., 107DR06), groups (e.g., 107DR06-08), samples (e.g., 107DR06-08A), and, in figure captions, subsamples (e.g., 107DR05-01Bii).

Dredged hauls are commonly made up of different rock types. Within each haul, the samples for palaeontological study were selected on the basis of promising lithology and subjective estimate of fossil promise. Lithological variation in the palaeontological samples is high; only part of it is due to the dredging action. Some samples are a mixture of shallow-water debris-flow material and deep-water pelagites; others are made up of lithic fragments in a chalky matrix; yet others are clearly mixtures of pelagite oozes cemented together, the result of reworking and bioturbation. Different lithologies have also resulted from the infilling of voids resulting from boring or solution processes during brief subaerial exposure of the host sediment.

Such composite samples may include sediment of diverse ages. For example, a nannofossil smear from a soft chalky portion of a sample might give an age estimate different from that of the indurated sediment of an adjacent clast which is suitable for foraminiferal study (an effective nannofossil study can be done on quite small amounts of sediment); another smear might give yet another age. A few of the samples yielded mixed nannofossil assemblages with species representing all ages from Campanian through to Pliocene.

The nannofossils were studied by conventional techniques for optical microscopy. All soft lithologies, and some of the hard carbonate samples which were thin-sectioned for their foraminiferids, were found to contain identifiable nannofossils. Slides were generally prepared from more than one spot of the same hard sample.

For the foraminiferids, most samples were lithified and of a size that allowed study by random thin section; only three (107DR05-01A, 107DR05-03B, and 107DR10-04A) could be disaggregated. The main study by thin section explains why many of the foraminiferal identifications, especially the planktics, are queried or referred to by open nomenclature. A query implies that the identification is reasonably certain but hedged because no critically diagnostic foraminiferal cross-section was distinguishable. Open nomenclature has the usual connotations. Despite these qualifications, we feel confident that there are no misleading identifications.

[1] Petroleum & Marine Division, Australian Geological Survey Organisation, GPO Box 378, Canberra, ACT 2601, Australia.
[2] Department of Geology, University of Western Australia, Nedlands, Western Australia.

Bulk samples, preparations, and thin sections are stored in the collections of the Australian Geological Survey Organisation. All illustrated specimens (Figs. 2–9) are housed in the Commonwealth Palaeontological Collection, and their catalogue numbers are prefixed by CPC.

Previous studies

The few biostratigraphic and palaeontological studies of the Christmas Island region were carried out in relation to the island's phosphate deposits, and discuss only the benthic foraminiferids in detail; planktic foraminiferids and nannofossils have not been previously studied.

Late Eocene, possibly Oligocene, and Miocene foraminiferal faunas were recognised first by Jones & Chapman (1900), who described a number of new species of Miocene larger neritic forms. Nuttall (1926), re-examined these neritic forms, and revised the nomenclature of some of them. In a study of limestone samples from Christmas Island, Ludbrook (1965) recognised both Late Eocene (T*b* stage) and Early Miocene (T*e* and T*f* stage) larger neritic foraminiferids. In a detailed study of the Oligocene to Miocene larger foraminiferal faunas from the island, Adams & Belford (1974) clarified both the taxonomy and biostratigraphy.

No samples from Christmas Island were included in our study, which is based solely on material collected from a number of nearby seamounts. As the results show, the only larger neritic foraminiferids found are Late Cretaceous and Middle Eocene (Ta_3 stage).

Biostratigraphy

Fossil assemblages in the samples range from Late Cretaceous to Holocene (Tables 2 and 3). The oldest fossil assemblage is late Campanian, but a few still-older derived species were found in a younger Late Cretaceous assemblage. Paleocene sediment is conspicuous in its rarity; reworked calcareous nannofossils of this age were found in one younger assemblage. This rarity may simply reflect the inherently random nature

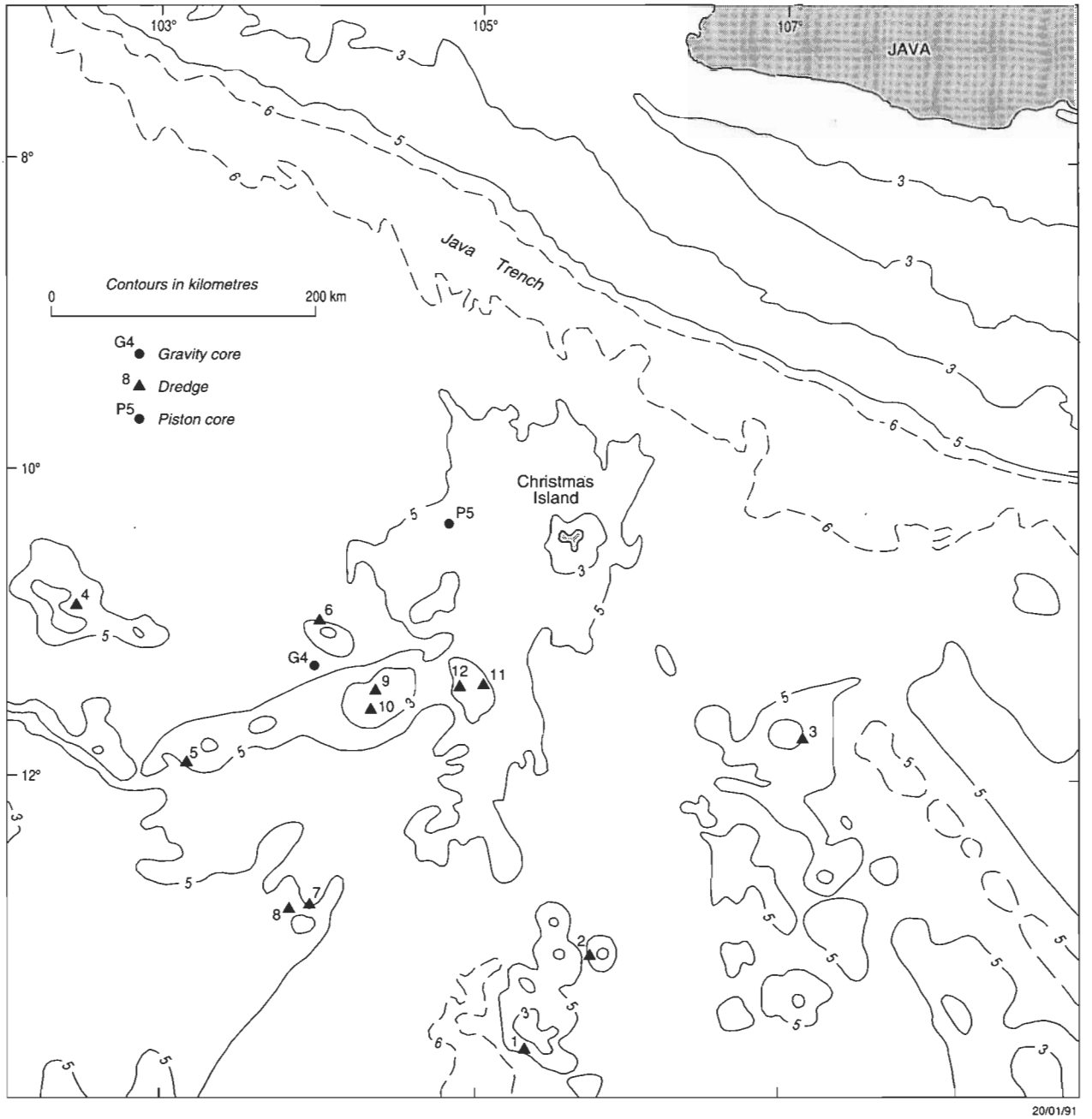

Figure 1. Locality map of the Christmas Island region showing location of samples collected during cruise 107 (after Exon et al. 1993).

Table 1. Cruise 107 dredge and core locations, water depths, and lithologies (after Exon et al. 1993).

Dredge/core	*Latitude, longitude*	*Seamount top/ dredge depth (m)*	*Rock types recovered/comments*
DR01	13°43.2′S, 105°24.1′E to 13°42.8′S, 105°23.5′E	2300/3273–2800	Basalt; hyaloclastite; volcanic breccia; Maastrichtian, Late Paleocene, and Early Eocene shallow-water limestone; pelagic limestone; pelagic ooze
DR03	11°46.4′S, 107°05.0′E to 11°46.2′S, 107°04.6′E	1950/2699–2234	Volcaniclastic rock; Late Cretaceous shallow-water limestone; pelagic ooze
DR04	10°58.5′S, 102°25.8′E to 10°58.8′S, 102°25.3′E	1800/3030–2300	Basalt; trachyte; hyaloclastite; volcaniclastic rock; Maastrichtian shallow-water limestone; pelagic ooze
DR05	11°48.0′S, 103°14.8′E to 11°46.6′S, 103°15.2′E	1500/2938–1812	Basalt; trachyte; Early, Middle, and Late Eocene shallow-water limestone; Late Paleocene, Early Eocene pelagic limestone; pelagic ooze
DR06	11°02.0′S, 103°58.1′E to 11°02.2′S, 103°56.7′E	2500/3346–2830	Basalt; trachyte; claystone; late Campanian, middle Maastrichtian, Late Eocene, and Late Miocene pelagic limestone and phosphorite
DR08	12°50.2′S, 103°53.4′E to 12°50.7′S, 103°53.4′E	1750/3750–3000	Basalt; trachyte; hyaloclastite; volcaniclastic rock; Late Cretaceous shallow-water limestone
DR09	11°27.4′S, 104°24.6′E to 11°27.3′S, 104°24.5′E	1200/1925–1800	Basalt; Late Miocene pelagic limestone; pelagic ooze
DR10	11°27.3′S, 104°24.6′E to 11°26.8′S, 104°24.4′E	1200/2050–1445	Basalt; volcaniclastic rock; Maastrichtian, Late Paleocene, Middle Eocene, Early and Late Oligocene, and Pliocene pelagic limestone; pelagic ooze
GC04	11°17.9′S, 103°58.6′E	1423	Foram–nanno ooze (south of DR06)
PC05	10°26.5′S, 104°48.3′E	4559	Nanno–foram ooze (west of Christmas I.)

of the dredge hauls. The planktic foraminiferid assemblages have been assigned wherever possible to biostratigraphic zones (Table 3) according to the schemes of Caron (1985) for the Cretaceous, and Blow (1969, 1979) for the Tertiary. Similarly, calcareous nannofossil assemblages have been assigned wherever possible to biozones according to the zonations of Sissingh (1977) for the Cretaceous, and Martini (1971) and Okada & Bukry (1980) for the Tertiary.

Cretaceous

Early Campanian. Although we have no *in situ* lower Campanian sediment, the presence of the nannofossil *Bukryaster hayii* in sample 107DR06-13 (middle and late Maastrichtian) suggests reworking from lower Campanian sources; this species is restricted to the early Campanian (Perch-Nielsen 1985). The presence of *Gartnerago obliquum* in the same sample, as well as in sample 107DR06-08A (late Campanian to early Maastrichtian), may also suggest reworking from pre-Maastrichtian Upper Cretaceous rocks.

Late Campanian–Early Maastrichtian. Sample 107DR06-08A, obtained from water depths of 3346–2830 m, contains assemblages of both planktic foraminiferids (Table 4) and calcareous nannofossils. The sample is an example of a common sample type — a mix of moderately lithified manganiferous chalky pelagites. Although the nannofossils are rare and poorly preserved in the several preparations examined, two assemblages could be differentiated by the presence of the key mid-Maastrichtian species, *Lithraphidites quadratus*, in one but not the other. The bulk of either assemblages comprises *Arkhangelskiella cymbiformis* (small form), *A. specillata, Broinsonia parca, ?Calculites obscurus, Chiastozygus litterarius, Ceratolithoides aculeus, Cretarhabdus surirellus, Cribrosphaerella ehrenbergii, Eiffellithus eximius, Gartnerago obliquum, Heterorhabdus sinuosus, Lithraphidites carniolensis, ?Lucianorhabdus cayeuxii, Microrhabdulus decoratus, M. helicoideus, Micula staurophora, Parhabdolithus embergeri, Placozygus sigmoides, Prediscosphaera cretacea, P. grandis, P. majungae, Quadrum gothicum, Q. trifidum, Reinhardtites levis, Tetrapodorhabdus decorus, Tranolithus exiguus, T. orionatus, Watznaueria barnesae,* and *Zygodiscus bicrescenticus.*

In the older assemblage of sample 107DR06-08A (i.e., the one without *Lithraphidites quadratus*), the co-occurrence of *Broinsonia parca, Quadrum trifidum, Reinhardtites levis,* and *Tranolithus orionatus*, in the absence of *Reinhardtites anthophorus,* suggests Subzone CC23a of late Campanian age. However, because of evidence for reworking in the Cretaceous assemblages examined in this study (see below), the late Campanian age is regarded as being a maximum age: the stratigraphic ranges of both *Q. trifidum* and *Reinhardtites levis* are known to straddle the Campanian–Maastrichtian boundary (Bukry & Bramlette 1970; Sissingh 1977), and the assemblage could be as young as the early Maastrichtian Subzone CC23b. If so, then both *B. parca* and *E. eximius*, whose highest occurrences have been used to indicate the top of the Campanian (Thierstein 1976; Shafik 1990), must have been reworked. A third alternative is that the assemblage comprises a mix of nannofloras from both Subzones CC23a and CC23b. Most of the Cretaceous rock samples (including 107DR06-08) are composed of a mix of lithic fragments which may contain assemblages of different ages. For this reason, the broader age assignment of late Campanian to early Maastrichtian is preferred.

Rare planktic foraminiferids in sample 107DR06-08 include *Globotruncana ?arca, G. ?lapparenti,* and *G. ?ventricosa,* suggesting a late Campanian to early Maastrichtian age

(*Globotruncana ventricosa* to *Globotruncana aegyptica* zonal interval). A thin section of this sample reveals micrite and chalky pelagite, almost brecciated, coated, and penetrated with manganese oxides.

Sample 107DR06-08A, in its composite character, is typical of many of the Vening Meinesz samples. Its lithology and nannofossil and foraminiferal assemblages imply that it accumulated at shallow depths, possibly upper bathyal, in a shelf or bank environment (suggested by ?*Calculites obscurus* and *Lucianorhabdus cayeuxii*); the surface of the water was warm (indicated by *Quadrum gothicum* and *Q. trifidum*, and the absence of cool-water species; Shafik 1992).

Several other samples — 107DR03-01A, 107DR03-01B, 107DR03-01C, 107DR03-06A, 107DR06-05A, 107DR06-07A, 107DR08-01A, and 107DR08-07 (Table 4) — lack age-diagnostic foraminiferids and nannofossils, but contain other taxa which range from Campanian to Maastrichtian. These samples include dominant molluscan bivalve grainstones with small basaltic volcanic clasts, prisms of *Inoceramus* sp., and micritic carbonate grainstones and wackestones. Such a mix of lithologies and fossil remains might reflect shallow-water sediments, probably transported down slope. *Inoceramus* sp. is the diagnostic fossil. Samples from 107DR08, 107DR03-06A, and 107DR06-07A contain likely rudist fragments. The samples from 107DR08 also include hyaloclastite, suggesting a debris-flow deposit.

Mid-Maastrichtian. Rare specimens of *Lithraphidites quadratus*, suggesting assignment to the lower part of Subzone CC25c of middle (or early late) Maastrichtian age, were recorded in a nannofossil assemblage identified among several preparations examined from sample 107DR06-08A. The bulk of this assemblage is similar to that listed above for the same sample. The presence of several species (*Broinsonia parca, Eiffellithus eximius, Quadrum gothicum, Q. trifidum, Reinhardtites levis,* and *Tranolithus orionatus*) which are not known above Subzone CC25c suggests massive reworking and/or an admixture from different lithic fragments forming the sample.

Two poorly preserved nannofossil assemblages were identified from sample 107DR06-13. These are differentiated mainly by the presence of the key late Maastrichtian species *Micula murus* in one but not the other. The bulk of either assemblage includes a few species whose presence could have resulted from reworking and/or mixing of lithologies. The main elements in either assemblage are *Actinozygus regularis, Arkhangelskiella cymbiformis* (small form), *A. specillata,* small *Biscutum constans, Broinsonia parca, Bukryaster hayii, Cal-*

Table 2. The spread of assemblage ages and samples. Nannofossil samples are in *italics*, *emboldened* if sample provided critical nannofossil evidence. Foraminiferal samples are in an upright font: all foraminiferid samples are thin sections, except the few that could be disaggregated, which are annotated in a bold face. Reworked assemblages are indicated by underlining. An asterisk (*) indicates the maximum age of a sample which may be as young as Quaternary.

Age	*Sample*
Quaternary	107DR01–07A, *107DR01–10*, ***107DR04–18A***, ***107DR04–19A***, *107DR05–08, 107DR06–11, 107DR09–05, 107DR10–07, 107DR11–01, 107DR12–01*
Pliocene	107DR06-05*, *107DR06–10*, 107DR10–06*
Miocene — Late	*107DR06–05*, ***107DR06–12A***, ***107DR09–03***, ***107DR09–04***, *107DR10–02*
Miocene	*107DR10–02*, 107DR10–02A*, *107GC04*
Oligocene — undifferentiated	*107DR05–08*, *107DR10–02*, 107DR10–02A, *107PC05*
Oligocene — Late	***107DR10–06A***, *107DR10–07*, *107GC04*
Oligocene — Early	107DR10–03, *107GC04*
	Late *107DR05–08*, 107DR06–04A, 107DR06–05, **107DR10–04A**, *107DR10–04A*, *107DR10–07?*
Eocene	Early to Middle 107DR01–06A, 107DR01–06B, 107DR01–08B, 107DR05–01A, *107DR05–01A*, **107DR05–01B**, *107DR05–01B*, 107DR05–02A, 107DR05–03A, **107DR05–03B**, *107DR05–03B*, 107DR05–03C, 107DR05–04A, *107DR05–04A*, 107DR05–04B, *107DR05–04B*, 107DR06–04A, 107DR06–05, 107DR10–04, *107DR10–07*, *107GC04*
	Early *107DR05–08*
Paleocene	***107DR05–08***
Cretaceous — undifferentiated	107DR03–08?, 107DR06–07A?, 107DR05–08, 107DR08–01A, 107DR08–07, *107GC04*, *107PC05*
Cretaceous — Maastrichtian	107DR01–08B, 107DR03-03A?, 107DR04-01, 107DR04-01A, 107DR04-02A, *107DR06-04*, ***107DR06-08A***, ***107DR06-13***, 107DR10–02A, 107DR10–02B?
Cretaceous — Campanian to Maastrichtian	107DR03–01A, 107DR03–01B?, 107DR03–01C?, 107DR03–06A?, *107DR05–08*, 107DR06–05A, 107DR06–07A, 107DR06–08, *107DR06–08A*, 107DR06–13, 107DR08–01A, 107DR08–07
Cretaceous — ?Campanian	*107DR06–08A, 107DR06–13*

culites obscurus, Chiastozygus litterarius, Ceratolithoides aculeus, Corollithion signum, Cretarhabdus surirellus, Cribrosphaerella ehrenbergii, Cyclindralithus serratus, Eiffellithus eximius, E. gorkae, E. turriseiffeli, ?Gartnerago obliquum, Heterorhabdus sinuosus, Lithraphidites carniolensis, L. quadratus, ?Lucianorhabdus cayeuxii, Manivitella pemmatoidea, Microrhabdulus decoratus, M. helicoideus, Micula concava, M. quadrata, M. staurophora, Placozygus fibuliformis, P. sigmoides, Prediscosphaera cretacea, P. spinosa, P. stoveri, Quadrum gothicum, Tranolithus sp., *Watznaueria barnesae,* and *Zygodiscus bicrescenticus.* The presence of *Lithraphidites quadratus* suggests that the assemblage should be assigned to the lower part of Subzone CC25c of middle (early late) Maastrichtian age, but the presence of *?Gartnerago obliquum, Bukryaster hayii, Broinsonia parca,* and *Eiffellithus eximius* is not compatible with this age assignment because their highest occurrences are known to be well below the lowest occurrence of *Lithraphidites quadratus* in *in situ* material.

Planktic foraminiferids are rare in sample 107DR06-13, but are similar to those recorded in 107DR06-08 (see above; Table 4). They suggest the *Globotruncana ventricosa–Globotruncana aegyptica* zonal interval of late Campanian to early Maastrichtian age, consistent with the occurrence of nannofloras older than the mid-Maastrichtian Subzone CC25b (e.g., *Broinsonia parca* and *Eiffellithus eximius*) in the sample.

Fairly shallow-water (neritic to upper bathyal conditions) are again suggested by the presence of *Calculites obscurus* and *?Lucianorhabdus cayeuxii.*

Late Maastrichtian. Rare specimens of *Micula murus,* a late Maastrichtian species indicative of the upper part of

Table 3. Biostratigraphic summary of studied samples.

Samples	Biostratigraphic Assignment	Lithology
107DR01-01A	Not determinable	Volcanic breccia with micrite cement., with shallow water bioclasts.
107DR01-01B	Not determinable	Volcantic grit with shallow water bioclasts.
107DR01-03A	Not determinable	Volcanic breccia with micrite cement., with shallow water bioclasts.
107DR01-06A	P.9 to P.10	Volcanic breccia with micrite cement, with pelagic bioclasts.
107DR01-06B	P.9 to P.10	Volcanic breccia with micrite cement, with pelagic bioclasts.
107DR01-06C	Not determinable	Highly recrystallised limestone fragment.
107DR01-07A	N.19-20 to N.23	Recrystallised limestone with cavities infilled with pelagic ooze.
107DR01-08A	Not determinable	Igneous grit with rounded bioclasts.
107DR01-08B	P.8 to P.10; + reworked Coniacian-Maastrichtian	Algal bioclastic grit with volcanic clasts and limestone clasts.
107DR03-01A	Late Cretaceous	Recrystallised limestone with igneous clasts and neritic bioclasts.
107DR03-01B	Late Cretaceous	Molluscan grainstone with igneous clasts and neritic bioclasts.
107DR03-01C	Late Cretaceous	Molluscan grainstone with igneous clasts and neritic bioclasts.
107DR03-02	?Late Cretaceous	Recrystallised limestone with neritic bioclasts.
107DR03-03A	Late Maastrichtian	Coarse gritty limestone with igneous clasts, and micrite.
107DR03-05A	Barren	Recrystallised limestone with Mn-coated cavities.
107DR03-05B	Not determinable	Recrystalliised coarse bioclastic limestone.with micrite.
107DR03-06A	?Late Cretaceous	Bioclastic grainstone with igneous clasts.
107DR03-07	Barren	Recrystallised micritic limestone.
107DR03-08	?Late Cretaceous	Recrystallised micritic limestone, with molluscan fragments.
107DR03-09	Not determinable	Recrystallised coarse limestone with micrite and Mn-coated cavities.
107DR04-01	Maastrichtian	Volcanic calcarenite with neritic and pelagic bioclasts.
107DR04-01A	Maastrichtian	Volcanic calcarenite with neritic and pelagic bioclasts.
107DR04-02A	Maastrichtian, ?late	Volcanic grainstone with neritic and rare pelagic bioclasts.
107DR04-18A	CN13 to CN14a; NN19	Pelagic ooze.
107DR04-19A	CN13 to CN14a; NN19	Pelagic ooze.
107DR05-01A	P.9 to P.10; NP12 to NP14; CP10 to CP12	Micritic calcwacke with micrite and neritic and pelagic bioclasts.
107DR05-01B	P.8 to P.11	Micritic calcwacke with micrite and neritic and pelagic bioclasts.
107DR05-01B-i	P.8 to P.11	Micritic bioclastic calcwacke with oncoliths.
107DR05-01B-ii	P.8 to P.11	Micritic bioclastic calcwacke with oncoliths.
107DR05-02A	P.9 to P.10	Lithic volcanic algal wacke with micirite.
107DR05-03A	P.9 to P.10	Micritic bioclastic calcwacke with micrite.
107DR05-03B	P.9 to P.10; NP12 to NP14; CP10 to CP12	Micritic bioclastic calcwacke with micrite.
107DR05-03C	P.8 to P.10	Micritic bioclastic pelagic calcwacke with micrite and neritic forams.
107DR05-04A	P.8 to P.10	Micritic bioclastic pelagic calcwacke with micrite and neritic forams.
107DR05-04B	P.8 to P.11; NP 12; CP10	Micritic calcwacke with micrite and neritic and pelagic bioclasts.
107DR05-07	Not determinable	Micritic calcwacke with micrite and neritic bioclasts.
107DR05-08	Quaternary + reworked L.Cret.., Paleoc., Early Eoc., Late Eoc./Oligoc.	Pale brown ooze.
107DR06-01C	Barren	Igneous.
107DR06-04	Late Maastrichtian	Pelagite.
107DR06-04A-1	P.8 to P.10	Pelagite.
107DR06-04A-2	P.12 to P.17	Pelagite.
107DR06-05	P.8 to P.11; P.12 to P.17; N.18 to N.23. NN11; CN9	Brecciated micrite with different lithologies; altered in part & zeolitised.
107DR06-05A	Late Campanian to early Maastrichtian	Recrystallised micritic limestone with planktic bioclasts.
107DR06-07A	Late Cretaceous	Fractured, recrystallised fine-grained limestone with molluscan bioclasts.
107DR06-08	Late Campanian to early Maastrichtian	Mix of pelagite micrites.
107DR06-08A	Middle Maast. (CC25c) + reworked late Camp. to early Maast.. (CC23a to b)	Mix of pelagite micrites.
107DR06-10	NN15; CN11b	Pelagic ooze.
107DR06-12A	NN11; CN9a	Pelagite.
107DR06-13	Late Maastrichtian (CC25c) + reworked Campanian to mid-Maastrichtian	Pelagite with volcanic clasts.
107DR08-01A	Late Cretaceous	Debris flow wackestone with micrite, volcanic clasts and neritic bioclasts.
107DR08-02C	Barren	Igneous.
107DR08-07	Late Cretaceous	Debris flow wackestone with micrite, volcanic clasts and neritic bioclasts.
107DR09-02	Not determinable	Pelagite with some siliceous microfossils.
107DR09-03	NN11; CN9a	Pelagite.
107DR09-04	NN11; CN9a	Pelagite.
107DR10-02	Oligocene, Middle Miocene (CN4, CN7), Late Miocene (NN11; CN9a)	Turbiditic wacke, with volcanic clasts, pelagic and neritic bioclasts; cavity infilling
107DR10-02A	Late Maastrichtian; mid-Oligocene; mid-Miocene to Holocene	Turbiditic wacke, with volcanic clasts, pelagic and neritic bioclasts; cavity infilling
107DR10-02B	Maastrichtian, ?late	Turbiditic grainstone with volcanic clasts and neritic bioclasts.
107DR10-03	P.19-20	Planktic foraminiferal wackestone.
107DR10-04	P.8 to P.10	Planktic foraminiferal wackestone.
107DR10-04A	P.14 to P.16; NP18 to NP19/20; CP15	Planktic foraminiferal wackestone.
107DR10-06	N.19-20 to N.23	Chalky pelagite.
107DR10-06A	NP24; CP19a	Chalky pelagite.
107DR10-07	NN21; CN15; + reworked Eocene, Late Oligocene	Pelagic ooze.
107GC04	Quaternary + reworked Cret., mid. & Late Eoc., Late Oligo., Early-Middle Mioc.	Pelagic ooze.
107PC05	Quaternary + rew. Late Cretaceous, late Palaeogene, Neogene.	Pelagic ooze.

107tab3.cvs

Table 4. Distribution chart for recovered foraminiferids.

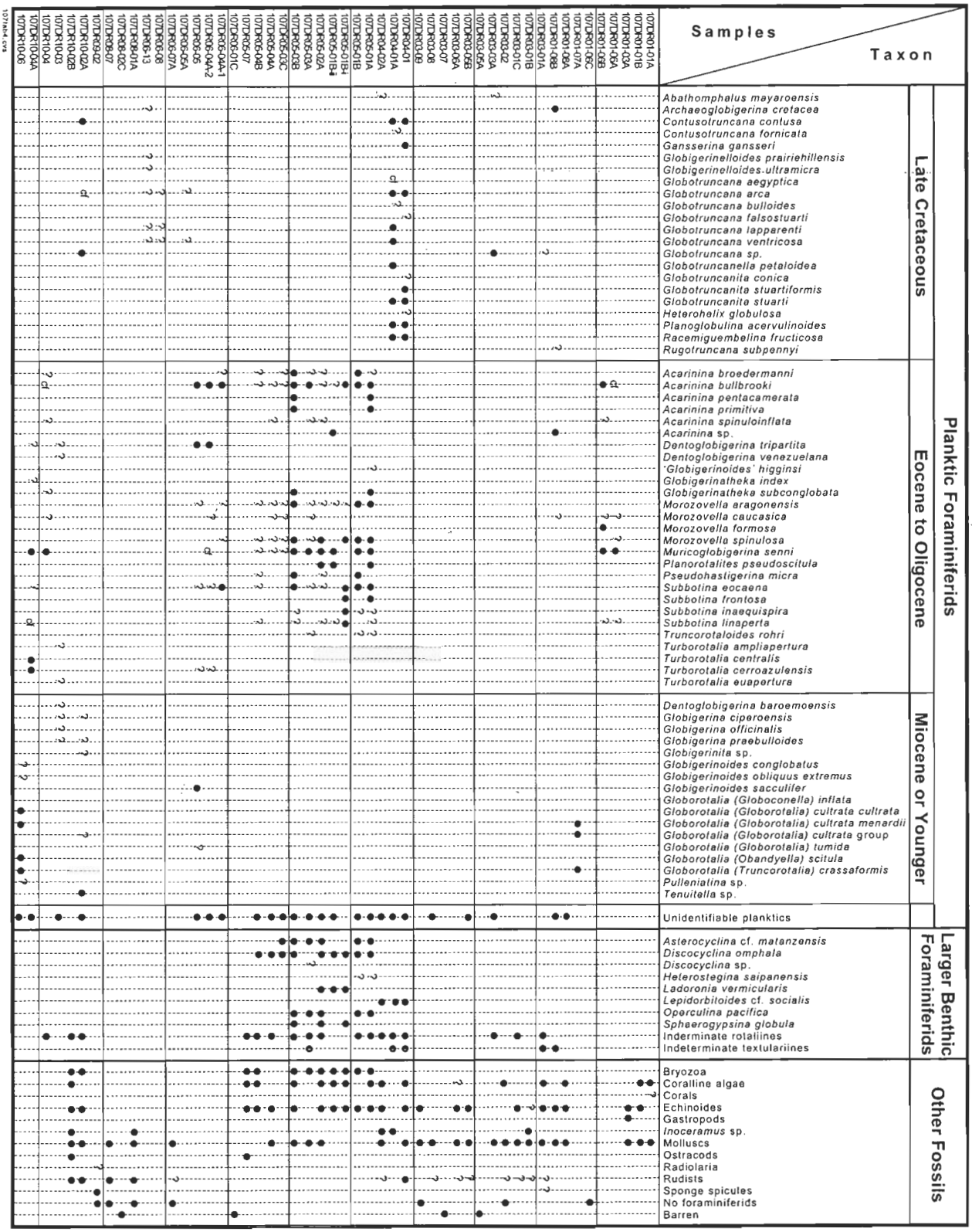

Subzone CC25c, were noted in a nannofossil assemblage identified from among several preparations examined from sample 107DR06-13. The bulk of the assemblage is similar to that listed above for the same sample. Reworking and/or mixing of lithologies bearing different nannofossil assemblages in sample 107DR06-13 is further confirmed by the association of *M. murus* and the older species — *?Gartnerago obliquum*, *Broinsonia parca*, and *Eiffellithus eximius*.

Micula murus was also recorded among a meagre, monogeneric nannofossil assemblage recovered from sample 107DR06-04, a phosphatised carbonate pelagite with vesicular basaltic clasts. Other species identified from the same sample include *Micula concava*, *M. quadrata*, *M. staurophora*, *M. swastica*, and *M.* sp. aff. *M. murus*.

The planktic foraminiferids *Globotruncana* sp. cf. *G. arca* and *Contusotruncana contusa*, which indicate a late Maastrichtian age (*Gansserina gansseri* to *Abathomphalus mayaroensis* Zones) were identified in a thin section of sample 107DR10-02A, which also contains mid-Tertiary (Oligocene and Miocene) planktic foraminiferids. This sample is complex: a turbiditic wacke layered with volcanic clasts and bioclasts set in micrite. Many of the bioclasts have been dissolved, and the resultant cavities filled with Tertiary fine-grained sediments. The original bioclasts are composed mainly of coralline algae, bivalve fragments, echinoids, and the Maastrichtian foraminiferids.

Faunas suggestive of late Maastrichtian age were also noted in thin sections of samples 107DR03-03A and 107DR04-02A. They include rare examples of *Abathomphalus ?mayaroensis*, indicative of the *A. mayaroensis* Zone. Sample 107DR04-02A also contains the larger neritic foraminiferid *Lepidorbitoides* sp. cf. *L. socialis*, coralline algae, and molluscan debris (altered aragonitic fragments); the bivalves include *Inoceramus* sp. and also likely rudist fragments.

Maastrichtian (general). Two more samples from dredge 107DR04 (107DR04-01 and 107DR04-01A) are dated as (undifferentiated) Maastrichtian. They comprise poorly sorted micrite-cemented lithic volcanic calcarenite/grainstone mixed with pelagite. The coarser clasts represent shallow-water, low-energy sedimentary debris carried into deeper water and mixed with pelagite. The samples contain well-preserved exotic specimens of orbitoidal larger foraminiferids and fragments of coralline algae, molluscs (especially prisms of *Inoceramus* sp. and pieces of rudist), red coralline algae, some echinoid material, and volcanic crystals and lithic grains. The exotic specimens of larger neritic foraminiferids are probably *Lepidorbitoides socialis*. In the finer-grained material of both samples, the planktic foraminiferids include typical Maastrichtian forms — *Globotruncana ?arca*, *G. ?falsostuarti*, *Globotruncanita ?conica*, *Gansserina ?gansseri*, *Planoglobulina acervulinoides*, *Contusotruncana contusa*, and *Racemiguembelina fructicosa*.

Reworked Coniacian to Maastrichtian planktic foraminiferal species — *Archaeoglobigerina cretacea* and *Rugotruncana ?subpennyi* — are present within an Early to Middle Eocene assemblage in sample 107DR01-08B.

Undifferentiated Cretaceous. Reworked Cretaceous nannofossils in Quaternary assemblages were recovered from sample 107DR05-08 and cores 107GC04 and 107PC05 (Shafik 1993a, b).

Paleocene

Sample 107DR05-08, a pale brown nannofossil–foraminiferid ooze, yielded a rich Quaternary assemblage which includes representative species of at least four older ages (discussed below). The Paleocene is indicated by the presence of *Fasciculithus tympaniformis*, *Chiasmolithus bidens*, and *Toweius eminens*.

Eocene

Early and Middle Eocene. The best assemblages of Early and Middle Eocene age are in samples from dredge 107DR05, which includes calc-wacke with micrite and sparry cement, lithic volcanic algal wacke with micritic cement, friable chalk, and bioturbated carbonate pelagite — a mix of shallow-water and deep-water lithologies. Other samples with Early and Middle Eocene forms include 107DR01-06A, 107DR01-06B, 107DR01-08B, 107DR06-04A, and 107DR06-05.

Preservation of nannofossils in three samples from dredge 107DR05 (107DR05-01A, 107DR05-03B, and 107DR05-04B — representing three lithofacies) is poor: recrystallisation of coccoliths and the presence of secondary calcite covering the discoasters seriously hampered identification of the rare nannofossils found. However, *Chiasmolithus grandis*, *Coccolithus formosus*, *C. pelagicus*, *Cyclicargolithus gammation*, *Discoaster lodoensis*, *Zygrhablithus bijugatus crassus*, and specimens of *Discoaster* and *Micrantholithus* could be identified in all three samples. Samples 107DR05-01A and 107DR05-03B were found also to contain *?Calcidiscus protoannulus*, *Campylosphaera dela*, unidentifiable species of *Chiasmolithus*, *Coccolithus magnicrassus*, *?Discoaster sublodoensis*, *Discoasteroides kuepperi*, *Pontosphaera plana*, *Sphenolithus moriformis*, and *S. radians*; in addition, sample 107DR05-03B contains *Braarudosphaera bigelowii*, *Discoaster barbadiensis*, *D. multiradiatus*, *?Pontosphaera plana*, and unidentifiable species of *Rhabdosphaera*.

The presence of pentaliths and holococcoliths suggests deposition in a shallow-water environment. Sphenoliths are abundant, and specimens of discoasters outnumber those of chiasmoliths; the presence of both suggests warm surface water. The co-occurrence of the key species *Chiasmolithus grandis*, *Cyclicargolithus gammation*, and *Discoaster lodoensis* in all three assemblages indicates an age not older than Early Eocene (Zone NP12 or CP10). The possible presence of *Discoaster sublodoensis* suggests a younger assignment (as young as Zone NP14 or CP12).

The planktic foraminiferids in the fine-grained material of samples 107DR05-01A, 107DR05-01B, 107DR05-02A, 107DR05-03A, and 107DR05-03B include *Acarinina broedermanni*, *A. bullbrooki*, *Muricoglobigerina senni*, *Morozovella aragonensis*, *M. ?caucasica*, *M. spinulosa*, *Pseudohastigerina micra*, *Subbotina eocaena*, *S. ?inaequispira*, and *S. ?linaperta*. The presence of *M. ?caucasica* and *Pseudohastigerina micra* indicates a level within the interval of Zones P.9 to P.10.

In the coarser wackes, larger neritic foraminiferids include *Asterocyclina* sp. cf. *A. matanzensis*, *Heterostegina ?saipanensis*, *Operculina pacifica*, *Discocyclina omphala*, *?Rotalia* sp., and *Sphaerogypsina globula*. This assemblage is typical of the Ta_3 letter stage (Adams 1984; Chaproniere 1994). Other benthic elements include coralline algae, commonly as balled bioclasts, echinoid spines and plates, bryozoa, ostracods, molluscan debris, and oncoliths containing the encrusting foraminiferid *Ladoronia vermicularis*, which is recorded for the first time below the Neogene (Chaproniere & Pigram 1993).

Sample 107DR05-08 yielded a mix of early Tertiary species among a rich Quaternary assemblage. In addition to the Paleocene species mentioned above, the Tertiary component of the 107DR05-08 assemblage includes *Cyclicargolithus gammation*, which suggests an Early Eocene age, and a younger group — *Bramletteius serraculoides*, *Cyclicargolithus floridanus*, *Pontosphaera multipora*, and *Reticulofenestra scissura* — which suggests a later Eocene (and/or Oligocene) age.

Dredge 107DR05 is clearly a mixture of warm shallow-water and deeper, bathyal sediments and biotas of different ages. The ages span the Early Eocene, and may extend into the Middle Eocene. The basaltic, trachytic, and volcanic content of dredge 107DR05 is noteworthy.

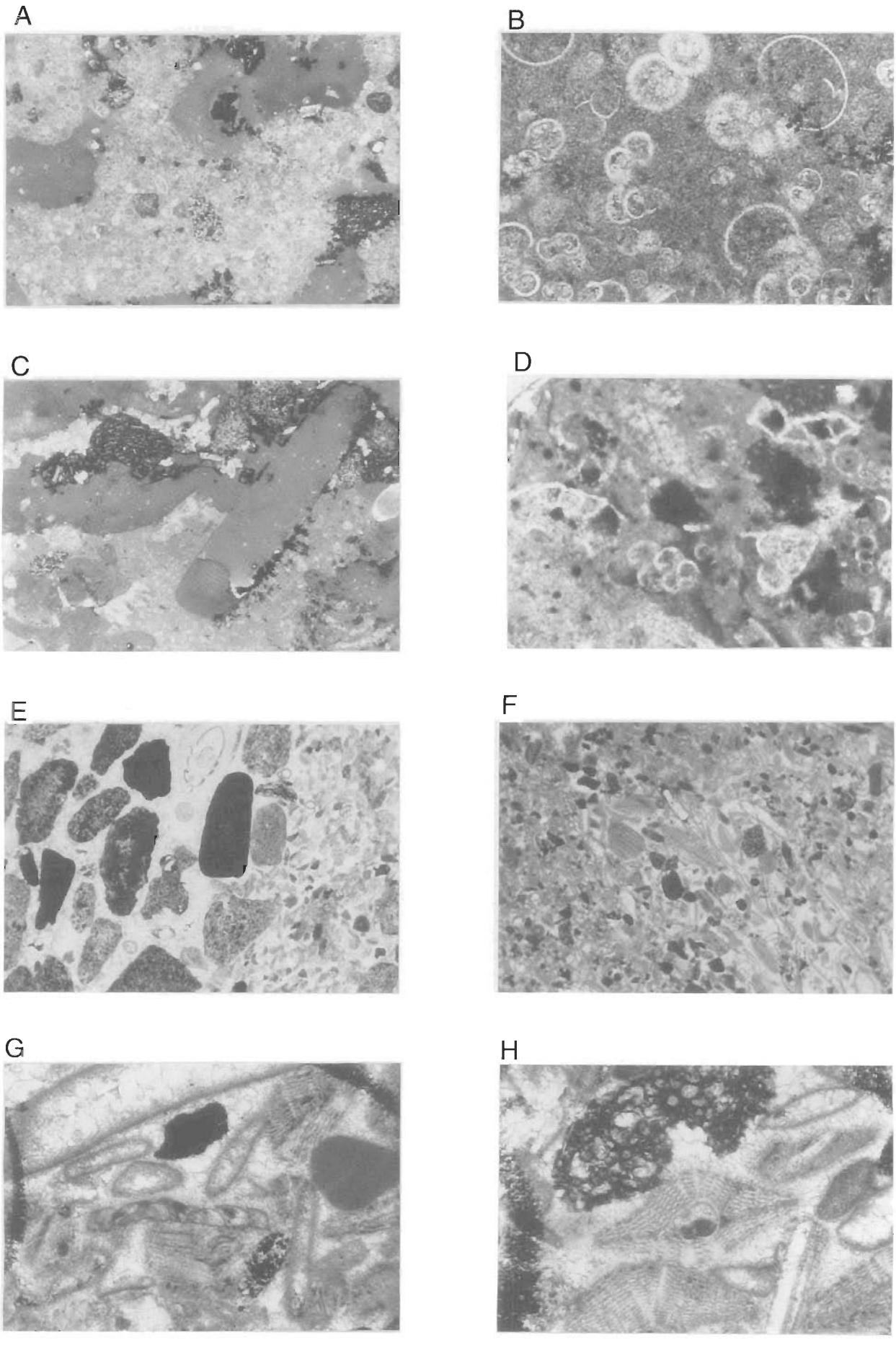
A
B
C
D
E
F
G
H

Dredge 107DR01 also yielded samples with foraminiferids of Early Eocene age (ranging into earliest Middle Eocene). They include 107DR01-06A, 107DR01-06B, and 107DR01-08B. Sample 107DR01-06A, a brecciated manganiferous volcanic arenite with micritic carbonate and glassy volcanic clasts, contains representatives of *Acarinina bullbrooki* group, *Muricoglobigerina senni, Morozovella ?caucasica, M. spinulosa* group, and *?Subbotina linaperta*. Sample 107DR01-08B has exotic specimens of *Rugotruncana ?subpennyi*. This sample is made up of shallow-water material washed down slope to deeper-water bathyal depths. The volcanic content suggests penecontemporaneous volcanism. Other samples from dredge 107DR01 did not yield diagnostic fossils, but are rich in volcanic clasts and shallow-water benthic fragments, especially bivalves.

Part of sample 107DR06-04A is a manganiferous pelagite with planktic foraminiferids, including *Acarinina ?broedermanni, A. bullbrooki* group, *Morozovella ?caucasica, M. ?spinulosa, Muricoglobigerina* cf. *M. senni*, and *?Subbotina eocaena* group. This is a latest Early to earliest Middle Eocene assemblage (Zones P.8–P.10). Another part of sample 107DR06-04A has similar lithology but has representatives of *Dentoglobigerina tripartita* group, *?Subbotina eocaena* group, and *?Turborotalia centralis*. This is a younger group — late Middle to Late Eocene (Zones P.12–P.17).

Sample 107DR06-05 also has mixed faunas that originate in different clasts within a micritic breccia. One fauna includes the species *Acarinina bullbrooki* group, *Morozovella ?aragonensis, ?Subbotina eocaena* group, *Dentoglobigerina tripartita* group, and *Turborotalia ?cerroazulensis*, reflecting an age of latest Early to earliest Middle Eocene (Zones P.8–P.11). Other younger faunas were found too (see below).

Sample 107DR10-04, a fine-grained wackestone, contains a poorer fauna with *Acarinina ?broedermanni, A. bullbrooki* group, *Globigerinatheka ?subconglobata, Morozovella ?caucasica*, and *Muricoglobigerina senni*, indicating a latest Early to earliest Middle Eocene (Zones P.8–P.10) assignment.

Late Eocene. Foraminiferids of possible Late Eocene age were identified in thin sections of sample 107DR06-04A (see above). Sample 107DR10-04A was disaggregated, and yielded Late Eocene nannofossils and foraminiferids.

The nannofossils in sample 107DR10-04A, a fine-grained white chalky wackestone, are abundant but poorly preserved. Those identified include *Bramletteius serraculoides, Coccolithus eopelagicus, C. formosus, Coronocyclus nitescens, Cyclicargolithus floridanus, ?C. reticulatus, ?C. abisectus, Discoaster barbadiensis, D. deflandrei, D. saipanensis, ?Helicosphaera compacta, Lanternithus minutus, Pedinocyclus larvalis, Reticulofenestra scissura, R. scrippsae, R. umbilicus, Sphenolithus moriformis, S. predistentus, S. radians, ?S. ciperoensis*, and *Zygrhablithus bijugatus bijugatus*.

The co-occurrence of *Bramletteius serraculoides, Sphenolithus predistenus, Discoaster barbadiensis*, and *D. saipanensis* — in the absence of *Chiasmolithus grandis* — suggests a minimum age of Late Eocene (Zone CP15); the presence of a contamination, in the form of questionable *Sphenolithus ciperoensis* and *Cyclicargolithus abisectus*, from the associated Oligocene sample 107DR10-06A is notwithstanding. The associated planktic foraminiferal assemblage of sample 107DR10-04A includes common *Turborotalia cerroazulensis, Subbotina eocaena* group, *S.* sp. cf. *S. linaperta, Muricoglobigerina senni,* and *Globigerinatheka ?index* of Late Eocene age (Zones P.14–P.16).

The presence of the holococcolith *Lanternithus minutus* suggests deposition in neritic depths; the other holococcolith present, *Zygrhablithus bijugatus bijugatus*, supports this conclusion. The frequency of discoasters and sphenoliths, and the absence of the cool-water chiasmoliths (e.g., *Chiasmolithus oamaruensis)* indicate warm surface water.

Late Eocene planktic foraminiferids (*Dentoglobigerina tripartita* group and *Turborotalia ?cerroazulensis* group) are present in sample 107DR06-05 (a complex rock with different lithoclasts), together with Early to Middle Eocene and Pliocene to Holocene elements.

Oligocene

Oligocene assemblages occur in samples from dredge 107DR10.

Planktic foraminiferids in a thin section of sample 107DR10-03, a planktic foraminiferal wackestone, include common *Turborotalia ?ampliapertura, ?T. euapertura, Dentoglobigerina tripartita* group, *D. ?venezuelana,* and small globigerines such as *Globigerina ?ciperoensis, G. ?praebulloides*, and *G. ?officinalis*. Typical Late Eocene forms such as *Turborotalia cerroazulensis* group are absent. This rock appears to be a bathyal turbiditic pelagite. Its age is probably Zone P.19/20 (Early Oligocene).

Calcareous nannofossils are abundant and moderately well preserved in sample 107DR10-06A, a chalky pelagite. The assemblage is dominated by *Cyclicargolithus abisectus, C. floridanus, Discoaster deflandrei*, and *S. predistentus*. Less abundant species (present in appreciable numbers, being frequent to common) include *Coccolithus eopelagicus, C. pelagicus, Coronocyclus nitescens, Sphenolithus ciperoensis, S. distentus, S. moroformis, S. pseudoradians, S. radians, ?Triquetrorhabdulus carinatus,* and *Zygrhablithus bijugatus bijugatus*. Species which are scarce include *Chiasmolithus altus, Discoaster tanii, Ericsonia subdisticha, Helicosphaera compacta, H. euphratis, H. recta, Pedinocyclus larvalis,* and *Reticulofenestra scissura*.

The co-occurrence of *Sphenolithus distentus* and *S. ciperoensis* indicates Zone NP24 or Subzone CP19a of Late Oligocene age. The presence of both *Reticulofenestra scissura* and *Helicosphaera recta* supports this assignment. The abundant occurrence of sphenoliths and the rarity of *Chiasmolithus altus* suggest warm surface water.

The make-up of the fine-grained sediments filling the solution cavities in sample 107DR10-02A includes planktic foraminiferids in the form of small globigerine and turborotaline morphology of different ages. The oldest of these foraminiferids, which evince low species diversity, have the appearance of typically mid-Oligocene species; they do not include Eocene or Neogene forms. Morphotypes typical of *Tenuitella* spp., *?Globigerinita* spp., *Globigerina ?praebulloides,* and *G. ?ciperoensis* are present, but *Globorotalia (Fohsella) kugleri* is not. The original bioclasts are much older — Maastrichtian (see above).

Oligocene species (such as *Helicosphaera recta*) occur in sample107DR10-02 in association with a Late Miocene nannoflora (see below).

Miocene

In sample 107DR10-02A, described above, some of the matrix contains specimens of the *Globorotalia (Gr.) ?cultrata* group, indicating an age range of Middle Miocene to Holocene.

Figure 2 (facing page). General lithologic features of Cretacous samples. A–D, turbiditic wacke, slide 107DR10-02Ai, showing A, dissolution cavity infilled with planktic ooze — x 10; B, detail of C, showing mid-Oligocene planktic foraminiferids — x 40; C, at least two generations of cavity formation, both with different infilling sediment — x 10; D, as for A, and Late Cretaceous planktic foraminiferids — x 25. E, volcanic calcarenite with both lithic and neritic bioclasts, slide 107DR04-01 — x 5. F, volcanic grainstone showing neritic and planktic bioclasts, slide 107DR04-02Aii — x 5. G–H, volcanic grainstone showing neritic bioclasts, slide 107DR04-02Ai — x 30: G, recrystallised bioclasts; H, the larger neritic foraminiferid *Lepidorbitoides* sp. cf *L. socialis*.

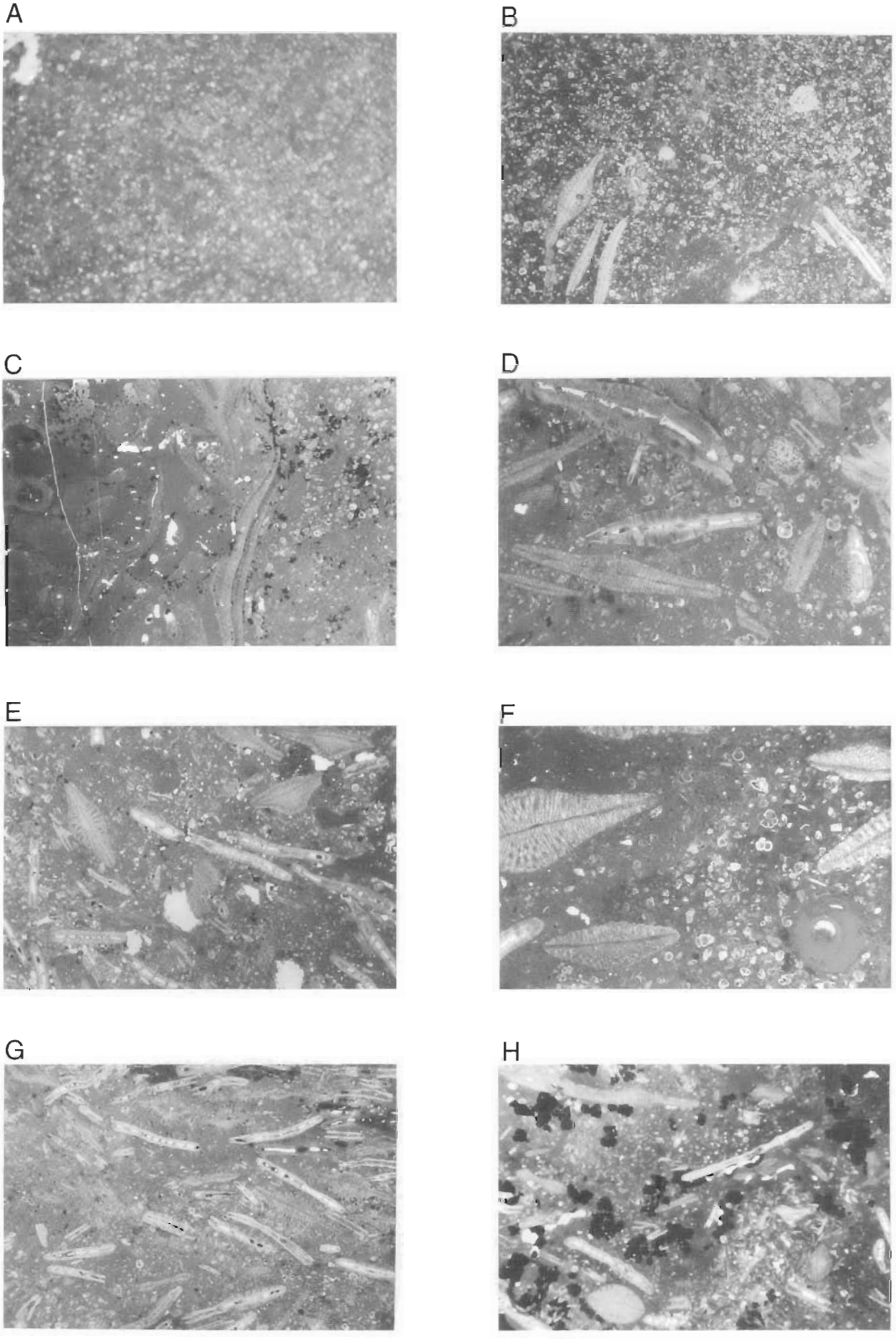
A
B
C
D
E
F
G
H

Abundant, poorly to moderately preserved nannofossils indicating a Miocene age were recovered from dredges 107DR06, 107DR09, and 107DR10. Samples 107DR06-12A, a moderately lithified foraminiferid–nannofossil chalk, 107DR09-03, a white well-lithified chalk, and 107DR09-04, a white soft chalky ooze, yielded similar assemblages. They include the key species *Amaurolithus amplificus, A. delicatus, A. primus, Calcidiscus leptoporus, Coccolithus pelagicus, Discoaster quinqueramus, D. surculus, Hayaster perplexus, Helicosphaera kamptneri, Reticulofenestra pseudoumbilicus, Sphenolithus abies,* and *Triquetrorhabdulus rugosus.*

The co-occurrence of species of *Amaurolithus* and *Discoaster quinqueramus* indicates an assignment to the upper part of Zone NN11 or its equivalent, Subzone CN9a. The age is latest Miocene. The abundance and diversity of species of *Amaurolithus* and *Discoaster* suggest warm surface water.

Sample 107DR10-02, a coarse carbonate with volcanic clasts in a fine-grained carbonate matrix, yielded a Late Miocene nannofossil assemblage, similar to those from sample 107DR06-12A and the two samples from dredge 107DR09 discussed above. The 107DR10-02 assemblage differs by having Oligocene and older Miocene elements. It contains the Late Miocene association of *Amaurolithus primus, Calcidiscus leptoporus, C. macintyrei, Discoaster brouweri, D. pentaradiatus, D. quinqueramus, D. variabilis, Hayaster perplexus, Helicosphaera kamptneri, Reticulofenestra pseudoumbilicus, Sphenolithus abies, S. neoabies,* and *Triquetrorhabdulus rugosus*, indicating assignment to the upper part of Zone NN11 or its equivalent — Subzone CN9a. The older Miocene is indicated by *Discoaster hamatus* (Zone CN7), *D. moorei* (Zones CN4 and CN5), and *Sphenolithus heteromorphus* (Zones CN3 and CN4). Another older nannoflora, with a few distinct Oligocene species, includes *Coccolithus formosus, Cyclicargolithus abisectus, C. floridanus, Discoaster deflandrei, Helicosphaera recta, Reticulofenestra scissura, Sphenolithus predistentus*, and *Triquetrorhabdulus carinatus*. The mixed assemblage is probably derived from carbonate clasts of different ages in the sample.

Sample 107DR06-05, a phosphatised carbonate breccia, contains a meagre nannofossil assemblage, which includes the key species *Discoaster quinqueramus* indicating Zone NN11 or Zone CN9.

Pliocene

In addition to the Eocene planktic foraminiferal assemblage recorded from a thin section of sample 107DR06-05 (a brecciated micritic mix of pelagites that are altered in part, zeolitised, and contain infilled solution cavities; see above), a younger fauna was also recorded from within the cavity-fill component. Thus, the interclast matrix, which is locally sparry, contains *Globorotalia (Gr.) ?tumida, Gr. (Globoconella) inflata,* and *Globigerinoides sacculifer*, indicating an age of Early Pliocene to Holocene (Zone N.18 or younger). The depositional history of this sample is complex, and may reflect transported Eocene material filling solution cavities in much younger (Late Miocene nannofossil-bearing) rock; alternatively, this rock might be a polymict breccia.

Sample 107DR10-06 is a chalky pelagite, a bathyal sediment, with many planktic foraminiferids — including *Globorotalia (Gr.) cultrata cultrata, Gr. (Gr.) cultrata menardii, Gr. (Obandyella) scitula, Gr. (Truncorotalia) crassaformis* group, *?Globigerinoides conglobatus,* and *?Globigerinoides obliquus extremus.* The age is Zone N.19–20 or younger (Pliocene or younger).

Sample 107DR06-10, a foraminiferid–nannofossil ooze, yielded abundant, poorly preserved nannofossils which include the association of *Ceratolithus rugosus, Reticulofenestra pseudoumbilicus, Discoaster asymmetricus, D. surculus,* and *D. tamalis.* In the absence of *Amaurolithus tricorniculatus*, this association suggests an Early Pliocene age, and assignment to the upper part of Zone NN15 or to its equivalent Subzone CP11b.

Quaternary

Dredge 107DR04 yielded abundant, moderately well-preserved Pleistocene nannofossils from two lithologies obtained from water depths of 3030 to 2300 m. The assemblages, from a cream nannofossil–foraminiferid ooze (sample 107DR04-18A) and a light olive grey nannofossil–foraminiferid ooze (sample 107DR04-19A), are similar, and of Early Pleistocene age. They include common to abundant *Calcidiscus leptoporus, C. macintyrei, Ceratolithus cristatus, Florisphaera profunda, Gephyrocapsa* sp., *Hayaster perplexus, Helicosphaera kamptneri, H. sellii, Pseudoemiliania lacunosa, Rhabdosphaera stylifer, Scapholithus fossilis,* and *Umbellosphaera irregularis.*

The absence of discoasters (particularly *Discoaster brouweri)* and the abundance of *Pseudoemiliania lacunosa* suggest an assignment to the lower part of Zone NN19 of Early Pleistocene age. An abundance of *Florisphaera profunda* is consistent with the present-day low-latitude position of the site of dredge 107DR04.

Sample 107DR05-08 yielded a rich Quaternary assemblage with *Ceratolithus cristatus, Florisphaera profunda*, and *Gephyrocapsa* sp., but, as mentioned above, includes older species.

Sample 107DR10-07, a pale brown nannofossil ooze, yielded abundant, moderately preserved nannofossils which are dominated by pre-Quaternary species. The association of *Calcidiscus leptoporus, Ceratolithus cristatus, Emiliania huxleyi, Gephyrocapsa* spp. (including *G. oceanica*), and *Florisphaera profunda* indicates Zone NN21 of Late Pleistocene to Holocene age. The older species suggest mixing of sediments from several levels, prominent among which are Lower and higher Eocene and Upper Oligocene (see below).

Undetermined

Preparations from samples 107DR01-1B, 107DR01-03A, 107DR01-06C, 107DR01-08A, 107DR03-05A, 107DR03-05B, 107DR03-07, 107DR03-09, 107DR05-07, 107DR06-01C, 107DR08-02C, and 107DR09-02 were checked, but contained neither diagnostic planktic foraminiferids nor calcareous nannofossils.

Sample 107DR01-07A is an altered limestone with solution cavities filled with ooze. The bulk of the rock is barren of foraminiferids and nannofossils, but a few planktic foraminiferids (*Globorotalia (Tr.) crassaformis* and specimens of *Globorotalia (Gr.) cultrata* group) were recorded only within the ooze cavity-fill, which is probably Holocene.

Displaced nannofossils in Quaternary sediments

A number of the Quaternary samples yielded nannofossil assemblages of different ages, some as old as Late Cretaceous

Figure 3 (facing page). Examples of general lithologic variation in Eocene bioclastic calc-wackes. A, sample containing only planktic foraminiferal bioclasts, slide 107DR05-03A — x 5. B, sample containing both planktic and neritic bioclasts (discocyclinids); slide 107DR05-04Bi — x 5. C, sample with oncolith (left) in a muddy matrix containing planktic foraminiferids, slide 107DR05-01B-2i — x 5. D, sample containing both planktic and neritic foraminiferal bioclasts (discocyclinids and operculines), slide 107DR05-01Aiv — x 10. E, sample showing poorly sorted planktic and neritic foraminiferal bioclasts (discocyclinids and operculines), slide 107DR05-03Biii — x 5. F, sample containing both planktic and neritic foraminiferal bioclasts (discocyclinids), slide 107DR05-04Biv — x 10. G, sample dominated by poorly sorted neritic foraminiferids (operculines and discocyclinids), slide 107DR05-02Aiii — x 5. H, sample dominated by poorly sorted neritic foraminiferids (operculines and discocyclinids), slide 107DR05-03B — x 5.

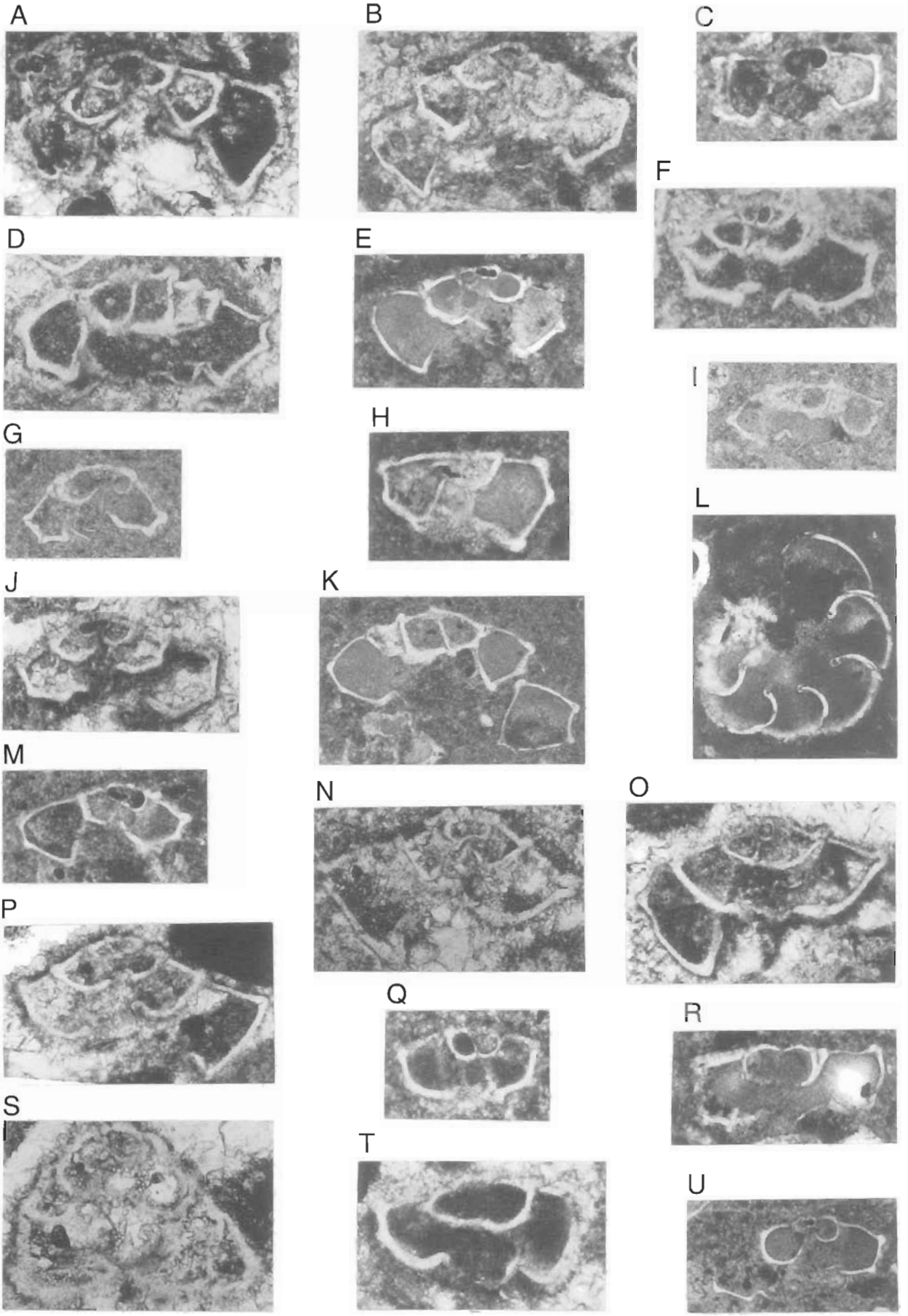
A
B
C
D
E
F
G
H
I
J
K
L
M
N
O
P
Q
R
S
T
U

(Shafik 1993a, b). For example, the Quaternary assemblage of sample 107DR10-07 includes reworked Eocene species (such as *Discoasteroides kuepperi, Discoaster sublodoensis,* and *D. saipanensis*), and other species suggestive of younger Eocene and/or Oligocene age (such as *Bramletteius serraculoides, Coccolithus eopelagicus, C. formosus, Cyclicargolithus floridanus, Sphenolithus predistentus, Reticulofenestra umbilicus, R. scissura,* and *Zygrhablithus bijugatus bijugatus*). Also present in the same sample is the Late Oligocene index species, *Sphenolithus ciperoensis*, in association with *Cyclicargolithus abisectus, Triquetrorhabdulus carinatus,* and younger (Neogene) species such as *Discoaster pentaradiatus* and *Helicosphaera kamptneri*. The reworked species provide important clues for piecing together the make-up of the pre-Quaternary sedimentary succession on the dredged seamount.

Sample 107DR05-08 is another example. As indicated above, it yielded a rich Quaternary assemblage and many older species indicative of different ages — the oldest being Late Cretaceous (based on the presence of *Calculites obscurus*). Other ages are Paleocene (on the presence of *Fasciculithus tympaniformis, Chiasmolithus bidens,* and *Toweius eminens*), Early Eocene (because of *Cyclicargolithus gammation*), and a younger age — Eocene and/or Oligocene (on account of *Bramletteius serraculoides, Cyclicargolithus floridanus, Pontosphaera multipora,* and *Reticulofenestra scissura*).

Quaternary nannofossil assemblages containing reworked species are not restricted to dredge samples. In two Quaternary cores (a gravity core, 107GC04, and a piston core, 107PC05; Table 1), Shafik (1993b) recorded older nannofossils. In core 107GC04 (Late Pleistocene–Holocene), the older nannofossils include: the long-ranging *Watznaueria barnesae* (which is known to disappear at the end of the Cretaceous); the Eocene *Chiasmolithus gigas* and *Discoaster barbadiensis*; the Eocene–Oligocene *Sphenolithus predistentus, S. pseudoradians, Reticulofenestra umbilicus,* and *R. scissura*; the Oligocene *Sphenolithus ciperoensis*; the Oligocene–Miocene *Cyclicargolithus abisectus*; and the Neogene *Sphenolithus heteromorphus, S. abies, Reticulofenestra pesudoumbilicus, Discoaster variabilis, D. surculus, D. pentaradiatus, D. brouweri, D. tamalis,* and *Calcidiscus macintyrei,* together with the long-ranging *Cyclicargolithus floridanus* (mid-Eocene–Early Miocene). In core 107PC05 (older Pleistocene), the reworked nannofossils include: the late Senonian *Ceratolithoides aculeus*; the late Palaeogene *Reticulofenestra scissura* and *Discoaster deflandrei*; and the Neogene *Reticulofenestra pseudoumbilicus, Discoaster variabilis, D. surculus, D. pentaradiatus, D. asymmetricus,* and *D. triradiatus*.

Stratigraphic summary

The spread of ages is consistent with the samples being dredge samples (Table 2), but has a few peculiarities. The oldest complete and diverse assemblage is late Campanian, but the samples yielding this age contained a few older species and some younger ones — that is, we have no samples, undoubtedly *in situ*, of late Campanian age. The features and biotas of the parent sediment suggest a warm shallow-water provenance for the late Campanian. This inference can be extended more definitely to Maastrichtian time. The undoubtedly Maastrichtian samples (in dredges 107DR04 and 107DR06) include basalt, trachyte, volcaniclastic rock, shallow-water limestone, and bathyal pelagite which accumulated in warm water.

The sole Paleocene assemblage is present in a sample from dredge 107DR05, but only as part of a mixed assemblage contained in a brown nannofossil–foraminiferid ooze. This scarcity is surprising considering the extensive vertical interval targeted by some dredges (Table 1) and the wide spread of ages in samples collected in a single dredge haul (e.g., dredge 107DR06; Table 3).

The Eocene is well represented in samples from four dredges (107DR01, 107DR05, 107DR06, and 107DR10). The lithologies echo those of the Maastrichtian: volcaniclastic rock, shallow-water limestone, and bathyal pelagite with indications that the water was warm. The evidence for renewed volcanism is persuasive but not conclusive (note the basalt, hyaloclastite, and volcanic breccia in dredge 107DR01). A few seamounts probably were elevated to sea level.

Oligocene foraminiferids are represented in three dredge samples (107DR10-02A, 107DR10-03, and 107DR10-07), and good Oligocene nannofloras are present in sample 107DR10-06A and in the two cores (107GC04 and 107PC05). Elements of these floras indicate deposition in warm shallow water.

The Miocene is represented as part of a mix of biotas in samples 107DR06-05, 107DR10-02A, and 107DR10-02, but is best shown in samples from dredges 107DR06 (sample 107DR06-12A) and 107DR09 (samples 107DR09-03 and 107DR09-04) of Late Miocene age. These samples are bathyal, foraminiferid–nannofossil chalks, and their nannofloras are suggestive of warm surface water. Evidence of the Middle Miocene is present in sample 107DR10-02, in which it is associated with the Late Miocene nannoflora.

The Pliocene sample 107DR06-10 is a pelagic ooze which yielded an Early Pliocene nannoflora.

The Quaternary is represented by a few deep-water pelagites (e.g., samples 107DR01-07A, 107DR04-18A, and 107DR04-19A).

The continuous records range over the late Campanian–Maastrichtian, Eocene–Early Oligocene, and mid-Miocene–Holocene. The most sparse record is for the Paleocene and the Oligocene–Miocene transition.

Conclusions

The ages and lithologies of the samples demonstrate that the large seamounts making up the Vening Meinesz chain had developed rapidly to produce extremely large edifices that had shoaled by the Campanian (if not earlier; Shafik 1992): volcanism had become, at the least, intermittent by the Maastrichtian. The initial outpourings must have begun before the Campanian — some time during the Albian–Santonian interval, the time span of the oldest magnetic lineations (Chron 34) identified in the area of the Vening Meinesz chain (Shafik et al. 1996). During the Campanian–Maastrichtian the seamounts achieved their present morphology as flattened guyots. Atoll-form with reef-wall perimeter is not demonstrated unambiguously, but suggestions of reef forms are present (Exon et al. 1993). These were probably shelly algal biostromes dominated by mounds of rudists and *Inoceramus* species.

This interpretation is similar to that projected for Resolution Guyot, Mid-Pacific Mountains, by the scientists of Ocean Drilling Program Leg 143 (ODP Leg 143 Scientific Party

Figure 4 (facing page). Cretaceous planktic foraminiferids, all axial sections except L, which is an oblique equatorial section. A, *Globotruncana ?falsostuarti,* sample 107DR04-01 — x 100. B, *Globotruncana ?falsostuarti,* sample 107DR04-01 — x 80. C, *Globotruncana ?lapparenti,* sample 107DR06-13 — x 90. D, *Contusotruncana ?fornicata,* sample 107DR04-01A — x 75. E, *Globotruncana ?aegyptica,* sample 107DR06-13 — x 75. F, *Globotruncana ?lapparenti,* sample 107DR04-01A — x 55. G, *Contusotruncana ?fornicata,* sample 107DR04-01 — x 80. H, *Globotruncana ?ventricosa,* sample 107DR06-13 — x 80. I, *Globotruncanita ?conica,* sample 107DR06-13 — x 75. J–M, *Globotruncana ?arca*: J, sample 107DR04-01 — x 75; K–M, sample 107DR06-13 — x 75. N–O, *Globotruncanita ?stuartiformis,* samples 107DR04-01A and 107DR04-01 — x 80. P, *Globotruncanita ?stuarti,* sample 107DR04-01 — x 80. Q, *Gansserina gansseri,* sample 107DR04-01 — x 80. R, *Abathomphalus mayaroensis,* sample 107DR06-13 — x 110. S, *Contusotruncana contusa,* sample 107DR04-01A — x 60. T, *Gansserina gansseri,* sample 107DR04-01 — x 80. U, *Globotruncana ?bulloides,* sample 107DR06-13 — x 80.

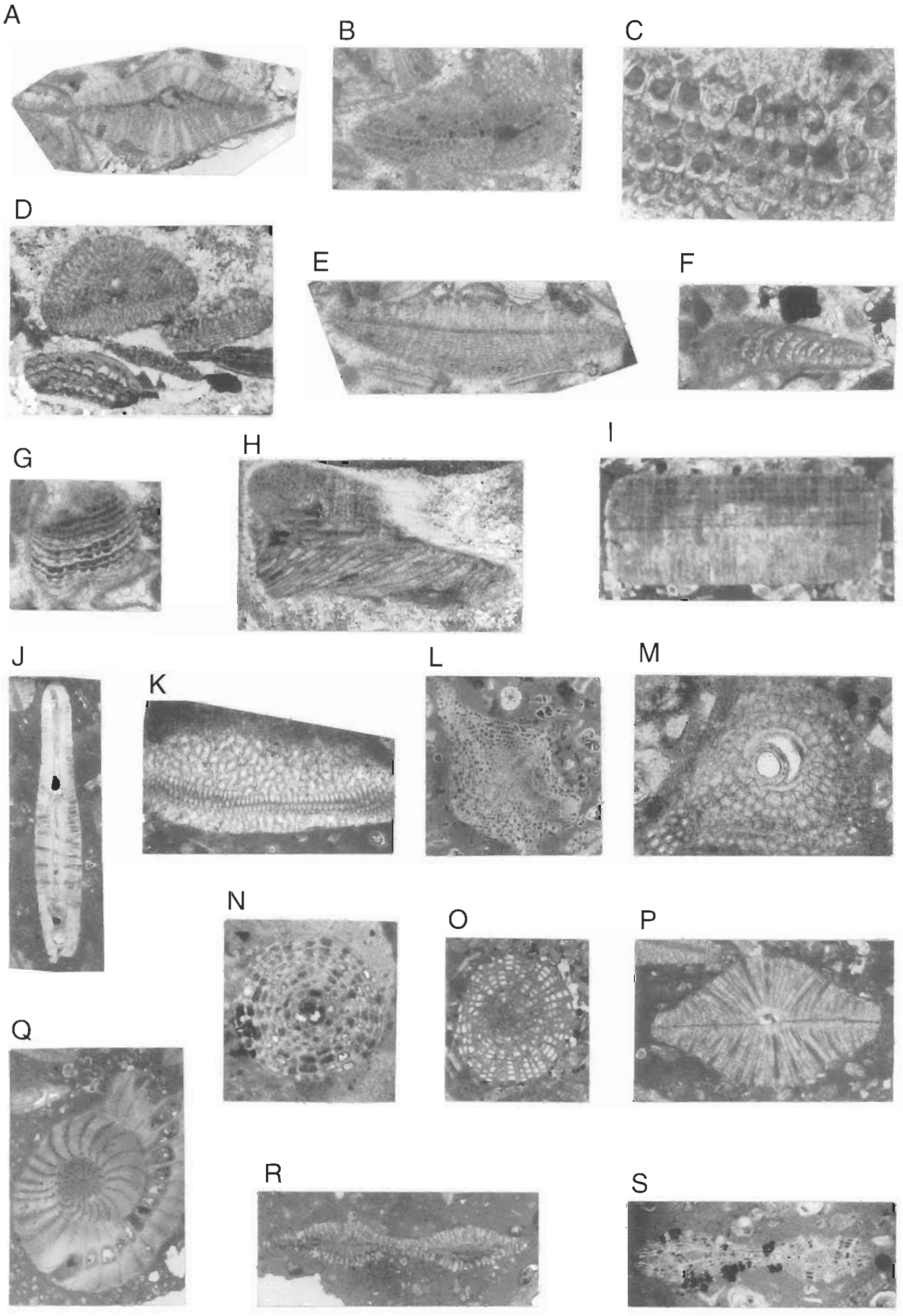
A
B
C
D
E
F
G
H
I
J
K
L
M
N
O
P
Q
R
S

1993). Parts of the large Vening Meinesz platforms had access to the open ocean during the late Senonian (Campanian and Maastrichtian) and were covered by water sufficiently deep to trap calcareous plankton, including planktic foraminiferids and nannoplankton. Some intermittent end-stage volcanism is suggested by the volcanic igneous content of some of the Upper Cretaceous (Maastrichtian) and the Lower Eocene samples.

Shallow (neritic to upper bathyal) warm-water event-markers are represented in the late Campanian and the Maastrichtian (Shafik 1992; this paper). This finding agrees with the worldwide occurrence of warm-water Late Cretaceous species over a wider range of latitudes than that of today. At times during the late Campanian–Maastrichtian, some of the seamounts may well have been very close to sea level.

If the tops of some seamounts had been above sea level during the Paleocene, then the apparent scarcity of Paleocene sediment in the dredge record would be explained.

Eocene samples range from Early through latest Early and earliest Middle to Late Eocene. Most of them indicate deposition at bathyal depths, and include admixtures of shallower sediments and biotas by way of turbidite and debris flows. The seamount crowns were probably close to or at sea level. The foraminiferids suggest Tethyan warm-water environments, at least subtropical (e.g., *Morozovella* spp.), and the nannofossils, of which abundant sphenoliths and discoasters outnumber chiasmoliths, suggest warm surface water. This result strengthens the proposal that Eocene oceanic temperatures were warmer at higher latitudes than they are today (Walker & Sloan 1992).

The fresh volcanic content in some of the Eocene samples indicates renewed volcanic or other igneous activity during the Early and perhaps the mid-Eocene.

The Oligocene is marked by pelagites containing nannofossils suggestive of warm shallow waters, but the foraminiferids suggest that at least the flanks of the seamount edifice were at upper or mid-bathyal depths.

The shallow-water features of the older biotas — Campanian, Maastrichtian, Eocene, and Oligocene — are in keeping with other shallow-water characteristics (e.g., phosphatisation, hyaloclastite, weathered lava clasts, and evidence of subaerial erosion) apparent in most Upper Cretaceous samples from dredges 107DR03, 107DR04, and 107DR06, and in samples 107DR05-07 (?mid-Eocene) and 107DR10-02A (Oligocene). These shallow-water features (which may include geopetal structures) are discussed by Williams & Exon (1993). Shallow-water features are also represented in samples from dredge 107DR01, which contains Eocene foraminiferids (e.g., samples 107DR01-06A and 107DR01-08B).

Fluctuations in relative height of the seamount crowns may reflect eustatic changes in sea level; elevation consequent on renewed volcanism (Shafik 1992), evidenced by the volcanic content of some of the samples discussed above; and, perhaps, the rise and fall of the Vening Meinesz platform as it moved north as part of the Indo-Australian plate (Menard 1973).

Depositional depths appear to have been bathyal during the Neogene, an accompaniment to seamount sinking and crustal and subcrustal cooling. Volcanism had ceased. Debris flows, however, continued to transport shallow-water sediments down slope. Holocene and present-day oozes mantle all previous deposits.

The magnetic lineations in the region of Christmas Island and the Vening Meinesz group have stratigraphic significance (Shafik et al. 1996). The ages of the magnetic lineations on the crust supporting the Vening Meinesz group in general agree with the ages derived from the fossil biotas. More importantly, the lineations are linked to those marking the passage northwards of the Australasian region, and probably indicate that the Vening Meinesz crust has been welded to the Australian plate since the Maastrichtian. This proposition is supported by the close links demonstrated by the Vening Meinesz microfossils with, for example, those from Papua New Guinea (especially the nannofossils; Shafik 1990, 1992). If the Vening Meinesz chain has been part of the Indo-Australian plate since that time, the Australian apparent polar-wander path demonstrates that it was at roughly latitudes 39°S at 60 Ma and 36°S at 40 Ma (M. Idnurm, AGSO, personal communication 1993; Idnurm 1985). This is a rough estimate, but it supports the concept that the Vening Meinesz group originated far south of its present position and that it maintained its relative geographic position to Australia since the latest Cretaceous (Shafik 1992; Shafik et al. 1996).

Acknowledgments

Drs David Haig and Greg Milner, Department of Geology, University of Western Australia, helped with the identification of many of the planktic foraminiferids and in the assessment of the age of the parent samples. We thank Dr Neville Exon and the scientific crew for the opportunity to work on the material collected during cruise 107, and the two referees, Drs Patrick Quilty and John Rexilius, for their comments and suggestions.

Figure 5 (facing page). Cretaceous and Eocene larger neritic foraminiferids and molluscs. A–E, *Lepidorbitoides* sp. cf. *L. socialis*: A–C, E, sample 107DR04-02A: A, vertical section — x 20; B, C, equatorial section of a fragment — x 20; C, detail of B — x 80; D, oblique sections, sample 107DR04-01 — x 20; E, vertical section — x 20. F, fragment of rudist shell, sample 107DR04-02A — x 20. G, *Lepidorbitoides* sp. cf. *L. socialis*, near equatorial section of fragment, sample 107DR04-02A — x 20. H, fragment of rudist shell, sample 107DR04-01 — x 20. I, fragment of *Inoceramus* shell, sample 107DR10-02A — x 20. J, *Operculina pacifica*, vertical section, sample 107DR05-04B — x 15. K, *Discocyclina omphala*, equatorial section, sample 107DR05-04B — x 15. L, *Asterocyclina matanzensis*, near equatorial section, sample 107DR05-02A — x 20. M, *Asterocyclina matanzensis*, near equatorial section, showing embryoconch, sample 107DR05-03B — x 65. N, *Sphaerogypsina globula*, near equatorial section, sample 107DR05-01B-2 — x 45. O, *Sphaerogypsina globula*, near equatorial section, sample 107DR05-03B — x 20. P, *Discocyclina omphala*, vertical section, sample 107DR05-04B — x 20. Q, *Operculina pacifica*, near equatorial section, sample 107DR05-01A — x 10. R, *Asterocyclina matanzensis*, vertical section, sample 107DR05-02A — x 20. S, *Asterocyclina matanzensis*, vertical section, sample 107DR05-03B — x 30.

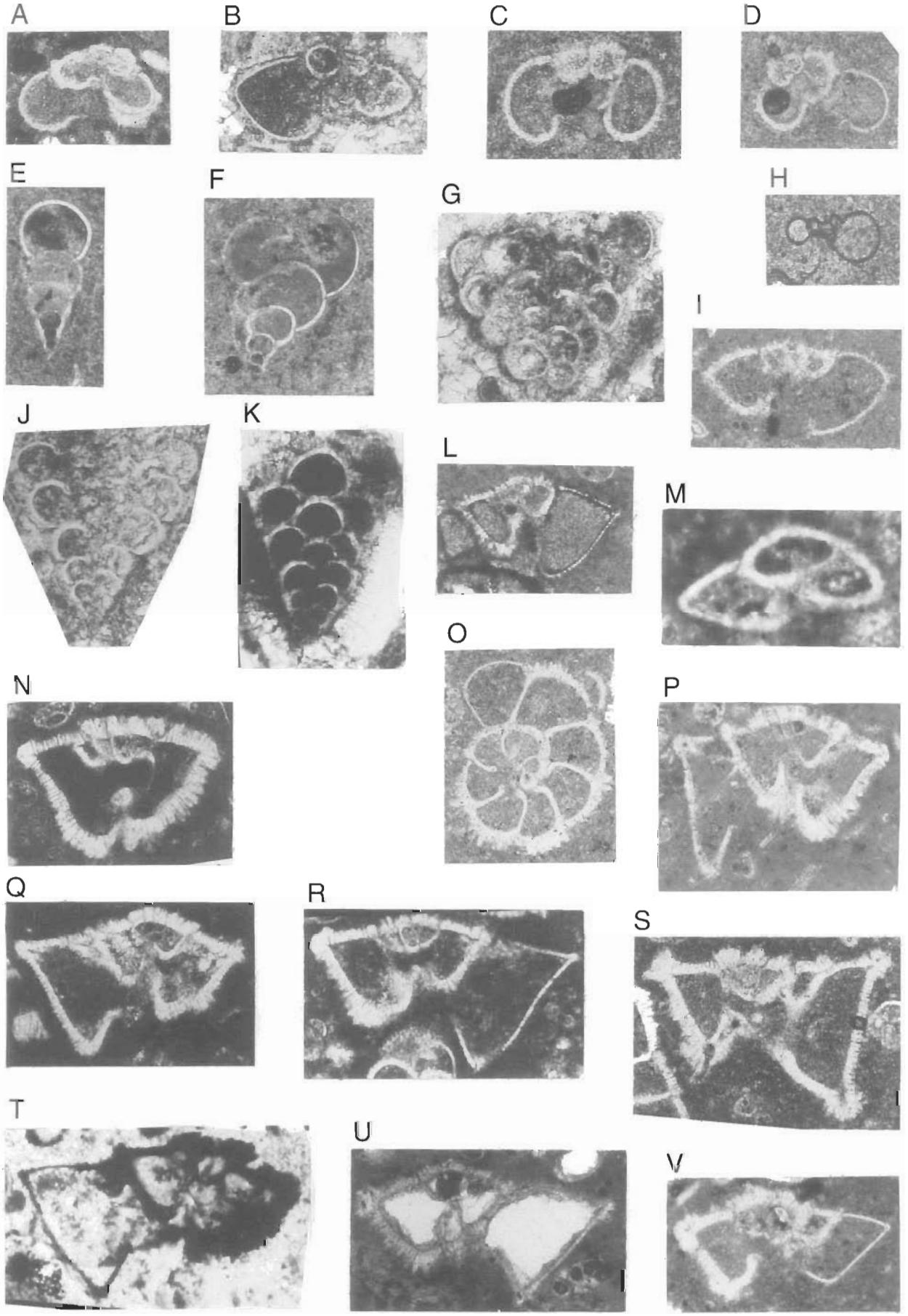
A
B
C
D
E
F
G
H
I
J
K
L
M
O
N
P
Q
R
S
T
U
V

References

Adams, C.G., 1984. Neogene larger foraminifera, evolutionary and geological events in the context of datum planes. In: Ikebe, N. & Tsuchi, R. (Editors), Pacific Neogene datum planes. Contributions to biostratigraphy and chronology. University of Tokyo Press, 47–67.

Adams, C.G. & Belford, D.J., 1974. Foraminiferal biostratigraphy of the Oligocene–Miocene limestones of Christmas Island (Indian Ocean). Palaeontology, 17, 475–506.

Blow, W.H., 1969. Late Middle Eocene to Recent planktonic foraminiferal biostratigraphy. In: Brönnimann, P. & Renz, H.H. (Editors), Proceedings of the First International Conference on Planktonic Microfossils, Geneva, 1967. E.J. Brill, Leiden, I, 199–421.

Blow, W.H., 1979. The Cainozoic Globigerinida, volumes 1–3. E.J. Brill, Leiden, 413 pp.

Bukry, D. & Bramlette, M.N., 1970. Coccolith age determinations Leg 3, Deep Sea Drilling Project. In: Maxwell, A.E., et al., Initial reports of the Deep Sea Drilling Project, 3, 589–611. U.S. Government Printing Office, Washington.

Chaproniere, G.C.H., 1994. Middle and Late Eocene larger foraminifers from Site 841, ODP Leg 135, Tonga Platform. In: Hawkins, J.W., Parson, L.M., Allan, J., et al., Proceedings of the Ocean Drilling Program, scientific results, 135, 231–243. College Station, Texas.

Chaproniere, G.C.H. & Pigram, C.J., 1993. Miocene to Pleistocene foraminiferal biostratigraphy of dredge samples from the Marion Plateau, offshore Queensland, Australia. AGSO Journal of Australian Geology and Geophysics, 14, 1–19.

Exon, N.F., Graham, T., Williams, S.M., Chaproniere, G.C.H., Chudyk, E., Coleman, P.J., Kalinisan, L., Moss, G., Shafik, S. & Technical Support Group, 1993. BMR cruise 107: Seabed morphology and offshore resources around Christmas Island, Indian Ocean. Australian Geological Survey Organisation, Record 1993/6.

Idnurm, M., 1985. Late Mesozoic and Cenozoic palaeomagnetism of Australia — I. A re-determined apparent polar wander path. Geophysical Journal of the Royal Astronomical Society, 83, 399–418.

Jones, T.R. & Chapman, F., 1900. On the foraminifera of the orbitoidal limestones and reef rocks of Christmas Island. In: Andrews, C.W., A monograph of Christmas Island (Indian Ocean). British Museum (Natural History), London, 226–264.

Ludbrook, N.H., 1965. Tertiary fossils from Christmas Island (Indian Ocean). Journal of the Geological Society of Australia, 12, 285–294.

Martini, E., 1971. Standard Tertiary and Quaternary calcareous nannoplankton zonation. In: Farinacci, A. (Editor), Proceedings of the Second Planktonic Conference, Roma 1970. Edizioni Tecnoscienza, Roma, 739–785.

Menard, H.W., 1973. Depth anomalies and the bobbing motion of drifting islands. Journal of Geophysical Research, 78, 5128–5137.

Nuttall, W.L.F., 1926. A revision of the orbitoides of Christmas Island. Quarterly Journal of the Geological Society of London, 82, 22–42.

ODP Leg 143 Scientific Party, 1993. History of Pacific guyots uncovered. Geotimes, 38, 18–19.

Okada, H. & Bukry, D., 1980. Supplementary modification and introduction of code numbers to the low-latitude coccolith biostratigraphic zonation (Bukry, 1973: 1975). Marine Micropaleontology, 5, 321–325.

Perch-Nielsen, K., 1985. Cenozoic calcareous nannofossils. In: Bolli, H.M., Saunders, J.B., & Perch–Nielsen, K. (Editors), Plankton stratigraphy. Cambridge University Press, Cambridge, 427–554.

Shafik, S., 1990. Late Cretaceous nannofossil biostratigraphy and biogeography of the Australian western margin. Bureau of Mineral Resources, Australia, Report 295, 164 pp.

Shafik, S., 1992. Nannofossil evidence for the age of the Vening-Meinesz Seamounts (Indian Ocean), and for periodic shallow-water carbonate deposition. In: First Australian Marine Geoscience Meeting, Abstracts, 9–11 July 1992. Australian National University, Canberra.

Shafik, S., 1993a. Calcareous nannofossil biostratigraphy of rocks dredged from seamounts near Christmas Island. In: Exon, N.F., et al., BMR cruise 107: Seabed morphology and offshore resources around Christmas Island, Indian Ocean. Australian Geological Survey Organisation, Record 1993/6, 60–70.

Shafik, S., 1993b. Calcareous nannofossil biostratigraphy of sediment cores from around Christmas Island. In: Exon, N.F., et al., BMR cruise 107: Seabed morphology and offshore resources around Christmas Island, Indian Ocean. Australian Geological Survey Organisation, Record 1993/6, 70–74.

Shafik, S., Chao-Shing Lee & Borissova, I., 1996. Calcareous nannofossils and magnetic lineations in the eastern Indian Ocean around Christmas Island: new evidence to the tectonic evolution of the northwest Australian region. In: 13th Australian Geological Convention, Canberra. Geological Society of Australia, Abstracts, 41, 385.

Sissingh, W., 1977. Biostratigraphy of Cretaceous calcareous nannoplankton. Geologie en Mijnbouw, 56, 433–440.

Thierstein, H.R., 1976. Mesozoic calcareous nannoplankton biostratigraphy of marine sediments. Marine Micropaleontology, 1, 325–362.

Walker, J.C.G. & Sloan, L.C., 1992. Something is wrong with climate theory. Geotimes, 37, 16–18.

Williams, S.M. & Exon, N.F., 1993. Rocks and sediments dredged from seamounts. In: Exon, N.F., et al., BMR cruise 107: Seabed morphology and offshore resources around Christmas Island, Indian Ocean. Australian Geological Survey Organisation, Record 1993/6, 29–38.

Figure 6 (facing page). Late Cretaceous and Eocene planktic foraminiferids, all axial sections. A, *Archaeglobigerina cretacea,* sample 107DR01-08B — x 80. B, *Globotruncanella petaloidea,* sample 107DR04-01A — x 80. C, *Hedbergella holmdelensis,* sample 107DR06-13 — x 75. D, *Rugoglobigerina rugosa,* sample 107DR06-13 — x 75. E, F, *Heterohelix globulosa,* sample 107DR06-13 — x 80. G, *Racemiguembelina fructosa,* sample 107DR04-01 — x 80. H, *Globigerinelloides prairiehillensis,* sample 107DR06-13 — x 80. I, *Planorotalites pseudoscitula,* sample 107DR05-01B — x 80. J, K, *Racemiguembelina fructosa,* samples 107DR04-01A, 107DR04-01 — x 70, x 115. L, *Morozovella subbotina/lensiformis,* sample 107DR05-01Bi — x 70. M, *Planorotalites pseudoscitula,* sample 107DR05-04B — x 320. N, O, *Morozovella aragonensis,* samples 107DR05-04B, 107DR05-04A — x 75, x 55. P, *Morozovella caucasica,* sample 107DR05-04B — x 60. Q, R, *Morozovella formosa,* sample 107DR05-04B — x 80. S, *Morozovella caucasica,* sample 107DR05-04A — x 80. T, *Morozovella formosa,* sample 107DR01-06B — x 85. U, *Morozovella ?spinulosa,* sample 107DR05-03A — x 75. V, *Morozovella spinulosa,* sample 107DR05-04A — x 80.

Appendix. List of cited foraminiferids and nannofossils

Planktic foraminiferids

Late Cretaceous

Abathomphalus mayaroensis (Bolli, 1951)
Archaeoglobigerina cretacea (Cushman, 1938)
Contusotruncana contusa (Cushman, 1926)
Contusotruncana fornicata (Plummer, 1931)
Gansserina gansseri (Bolli, 1951)
Globigerinelloides prairiehillensis Pessagno, 1967
Globigerinelloides ultramicra Subbotina, 1949
Globotruncana aegyptica Nakkady, 1950
Globotruncana arca (Cushman, 1926)
Globotruncana bulloides Volger, 1941
Globotruncana falsostuarti Sigal, 1952
Globotruncana lapparenti Brotzen, 1936
Globotruncana ventricosa White, 1928

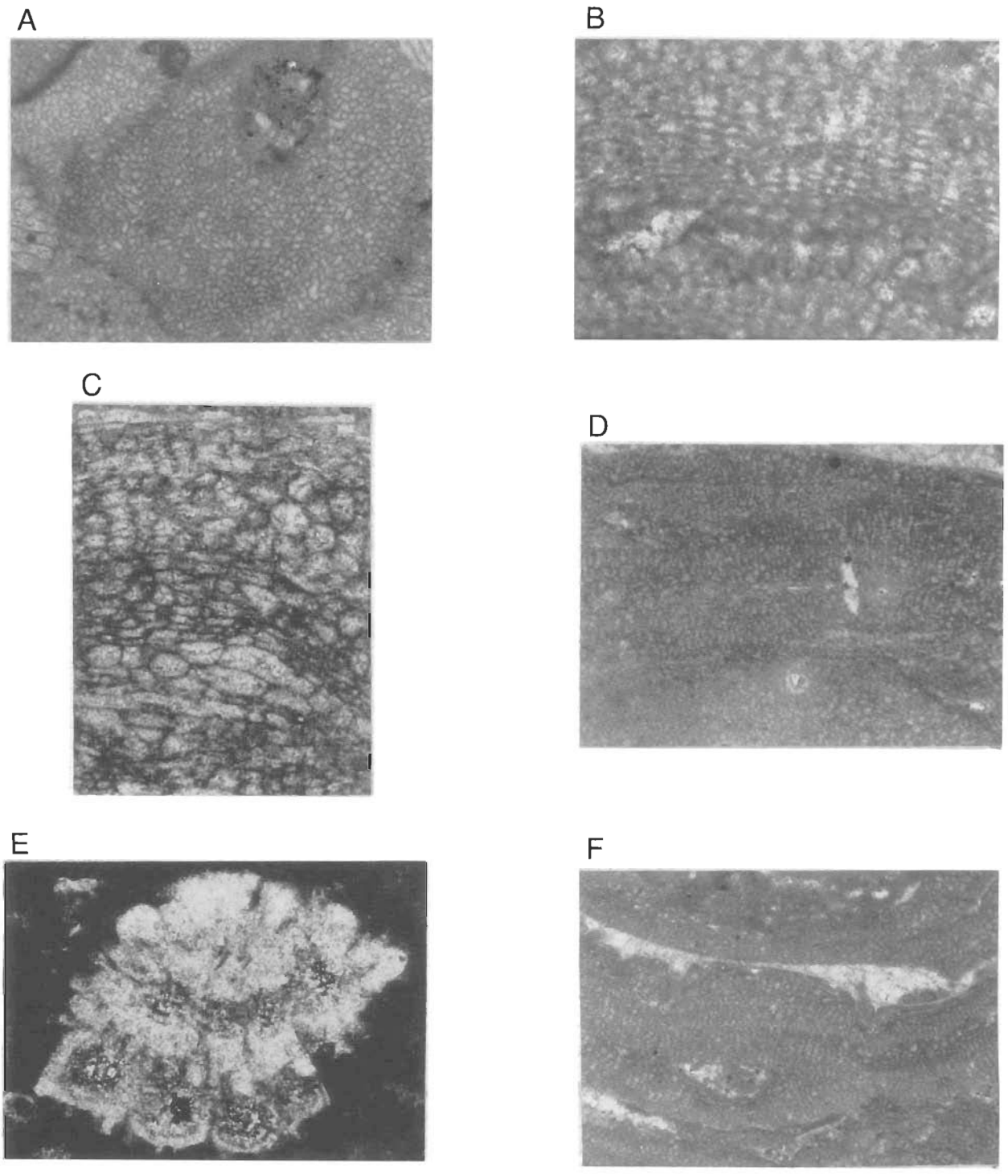

Figure 7. Eocene benthic foraminiferids. A–D, F, *Ladoronia vermicularis*, sample 107DR05-01B: A, near equatorial section — x 30; B, detail of F — x 110; C, detail of D — x 110; D, vertical section — x 30; F, vertical section — x 30. E, *Rotalia* sp., oblique section, sample 107DR05-04B — x 95.

Globotruncanella petaloidea (Longoria & Gamper, 1977)
Globotruncanita conica (White, 1928)
Globotruncanita stuartiformis (Dalbiez, 1955)
Globotruncanita stuarti (Lapparent, 1918)
Hedbergella holmdelensis Olsson, 1964
Heterohelix globulosa (Ehrenberg, 1840)
Planoglobulina acervulinoides (Egger, 1899)
Racemiguembelina fructicosa (Egger, 1899)
Rugoglobigerina rugosa (Eternod Olvera, 1959)
Rugotruncana subpennyi (Gandolfi, 1955)

Eocene

Acarinina broedermanni (Cushman & Bermudez, 1949)
Acarinina bullbrooki (Bolli, 1957)
Acarinina pentacamerata (Subbotina, 1947)
Acarinina primitiva (Finlay, 1947)
Acarinina spinuloinflata (Bandy, 1949)
Dentoglobigerina tripartita (Koch, 1926)
'Globigerinoides' higginsi (Bolli, 1957)
Globigerinatheka index (Finlay, 1939)
Globigerinatheka subconglobata (Shutskaya, 1958)
Morozovella aragonensis (Nuttall, 1930)
Morozovella caucasica (Glaessner, 1937)
Morozovella formosa (Bolli, 1957)
Morozovella lensiformis (Subbotina, 1953)
Morozovella spinulosa (Cushman, 1927)
Muricoglobigerina senni (Beckmann, 1953)
Planorotalites pseudoscitula (Glaessner, 1937)
Pseudohastigerina micra (Cole, 1927)
Subbotina eocaena (Gümbel, 1868)
Subbotina frontosa (Subbotina, 1953)
Subbotina inaequispira (Subbotina, 1953)
Subbotina linaperta (Finlay, 1939)
Truncorotaloides rohri (Brönnimann & Bermudez, 1953)
Turborotalia ampliapertura (Bolli, 1957)
Turborotalia centralis (Cushman & Bermudez, 1937)
Turborotalia cerroazulensis (Cole, 1928)
Turborotalia euapertura (Jenkins, 1960)

Oligocene and younger

Dentoglobigerina baroemoensis (LeRoy, 1939)
Dentoglobigerina venezuelana (Hedberg, 1937)
Dentoglobigerina tripartita (Koch, 1926)
Globigerina ciperoensis Bolli, 1954
Globigerina officinalis Subbotina, 1953
Globigerina praebulloides Blow, 1959
Globigerinoides conglobatus (Brady, 1879)
Globigerinoides obliquus extremus Bolli & Bermudez, 1965
Globigerinoides sacculifer (Brady, 1877)
Globorotalia (Fohsella) kugleri Bolli, 1957
Globorotalia (Globoconella) inflata d'Orbigny, 1839
Globorotalia (Globorotalia) cultrata cultrata (d'Orbigny, 1839)
Globorotalia (Globorotalia) cultrata menardii (Parker, Jones & Brady, 1865)
Globorotalia (Globorotalia) tumida (Brady, 1977)
Globorotalia (Obandyella) scitula (Brady, 1882)
Globorotalia (Truncorotalia) crassaformis (Galloway & Wissler, 1927)

Benthic foraminiferids

Asterocyclina matanzensis Cole, 1957
Discocyclina omphala (Fritsch, 1875)
Heterostegina saipanensis Cole, 1953
Ladoronia vermicularis Hanzawa, 1957
Lepidorbitoides socialis (Leymerie, 1851)
Operculina pacifica Whipple, 1932
Sphaerogypsina globula (Reuss, 1848)

Calcareous nannofossils

Cretaceous

Actinozygus regularis (Görka) Gartner, 1968
Arkhangelskiella cymbiformis Vekshina, 1959
Arkhangelskiella specillata Vekshina, 1959
Biscutum constans (Görka 1957) Black *in* Black & Barnes, 1959
Broinsonia parca (Stradner) Bukry, 1969 partim
Bukryaster hayii (Bukry 1969) Prins & Sissingh *in* Sissingh, 1977
Calculites obscurus (Deflandre 1959) Prins & Sissingh *in* Sissingh, 1977
Ceratolithoides aculeus (Stradner 1961) Prins & Sissingh *in* Sissingh, 1977
Chiastozygus litterarius (Görka 1957) Manivit, 1971
Corollithion signum Stradner, 1963
Cretarhabdus surirellus (Deflandre & Fert 1954) Reinhardt, 1970
Cribrosphaerella ehrenbergii (Arkhangelsky 1912) Deflandre *in* Piveteau, 1952
Cyclindralithus serratus Bramlette & Martini, 1964
Eiffellithus eximius (Stover 1966) Perch-Nielsen, 1968
Eiffellithus gorkae Reinhardt, 1965
Eiffellithus turriseiffeli (Deflandre *in* Deflandre & Fert 1954) Reinhardt, 1965
Gartnerago obliquum (Stradner 1963) Reinhardt, 1970
Heterorhabdus sinuosus Noël, 1970
Lithraphidites carniolensis Deflandre, 1963
Lithraphidites quadratus Bramlette & Martini, 1964
Lucianorhabdus cayeuxii Deflandre, 1959
Manivitella pemmatoidea (Deflandre in Manivit) Thierstein, 1971
Micrarhabdulus decoratus Deflandre, 1959
Micrarhabdulus helicoideus Deflandre, 1959
Micula concava (Stradner in Martini & Stradner 1960) Bukry, 1969
Micula murus (Martini 1961) Bukry, 1973
Micula staurophora (Gardet 1955) Stradner, 1963 (partim)
Micula swastica Stradner & Steinmetz 1984
Micula quadrata (Stradner 1961) Perch-Nielsen 1984
Parhabdolithus embergeri (Noël 1965) Stradner, 1963
Placozygus fibuliformis (Reinhardt 1964) Hoffmann, 1970
Placozygus sigmoides (Bramlette & Sullivan 1961) Romein, 1979

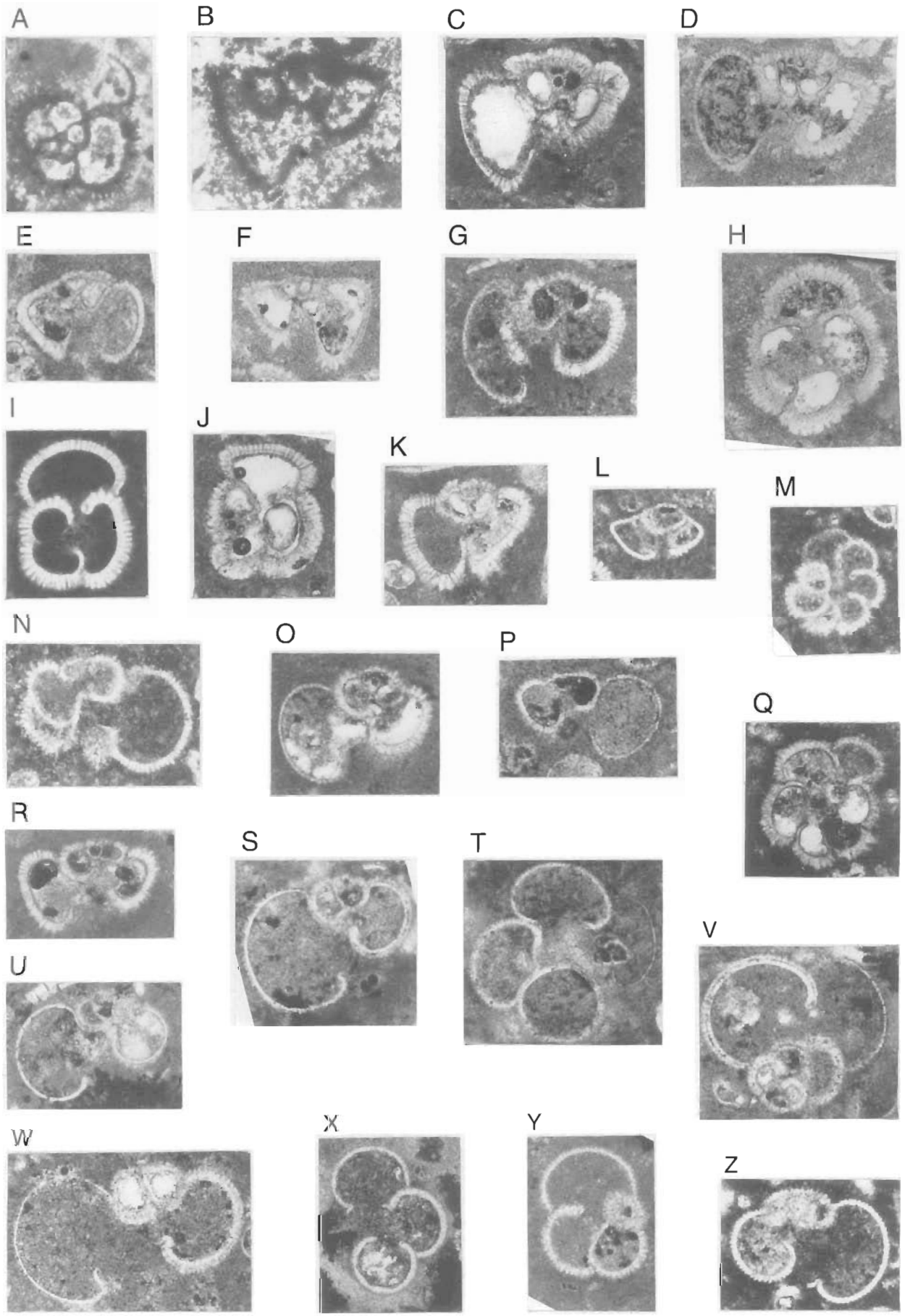
A
B
C
D
E
F
G
H
I
J
K
L
M
N
O
P
Q
R
S
T
U
V
W
X
Y
Z

Prediscosphaera cretacea (Arkhangelsky 1912) Gartner, 1968

Prediscosphaera grandis Perch-Nielsen, 1979

Prediscosphaera majungae Perch-Nielsen, 1973

Prediscosphaera spinosa (Bramlette & Martini 1964) Gartner, 1968

Prediscosphaera stoveri (Perch-Nielsen 1968) Shafik & Stradner, 1971

Quadrum gothicum (Deflandre 1959) Prins & Perch-Nielsen *in* Manivit et al., 1977

Quadrum trifidum (Stradner *in* Stradner & Papp 1961) Prins & Perch-Nielsen *in* Manivit et al., 1977

Reinhardtites anthophorus (Deflandre 1959) Perch-Nielsen, 1968

Reinhardtites levis Prins & Sissingh *in* Sissingh, 1977

Tetrapodorhabdus decorus (Deflandre *in* Deflandre & Fert 1954) Wise & Wind, 1983

Tranolithus exiguus Stover, 1966

Tranolithus orionatus (Reinhardt 1966a) Reinhardt, 1966b

Watznaueria barnesae (Black *in* Black & Barnes 1959) Perch-Nielsen, 1968

Zygodiscus bicrescenticus (Stover 1966) Wind & Wise *in* Wise & Wind, 1977

Cainozoic

Amaurolithus amplificus (Bukry & Percival 1971) Gartner & Bukry, 1975

Amaurolithus delicatus (Bukry 1973) Gartner & Bukry, 1975

Amaurolithus primus (Bukry & Percival 1971) Gartner & Bukry, 1975

Amaurolithus tricorniculatus (Gartner 1967) Gartner & Bukry, 1975

Braarudosphaera bigelowii (Gran & Braarud 1935) Deflandre, 1947

Bramletteius serraculoides Gartner, 1969

Calcidiscus leptoporus (Murray & Blackman 1898) Loeblich & Tappan, 1978

Calcidiscus macintyrei (Bukry & Bramlette 1969) Loeblich & Tappan, 1978

Calcidiscus protoannulus (Gartner 1971) Loeblich & Tappan, 1978

Campylosphaera dela (Bramlette & Sullivan 1961) Hay & Mohler, 1967

Ceratolithus cristatus Kamptner, 1950

Ceratolithus rugosus Bukry & Bramlette, 1968

Chiasmolithus altus Bukry & Percival, 1971

Chiasmolithus bidens (Bramlette & Sullivan 1961) Hay & Mohler, 1967

Chiasmolithus gigas (Bramlette & Sullivan 1961) Radomski, 1968

Chiasmolithus grandis (Bramlette & Riedel 1954) Radomski, 1968

Chiasmolithus oamaruensis (Deflandre 1954) Hay, Mohler & Wade, 1966

Coccolithus eopelagicus (Bramlette & Riedel 1954) Bramlette & Sullivan, 1961

Coccolithus formosus (Kamptner 1963) Wise, 1973

Coccolithus magnicrassus Bukry, 1971

Coccolithus miopelagicus Bukry, 1971

Coccolithus pelagicus (Wallich 1877) Schiller, 1930

Coronocyclus nitescens (Kamptner 1963) Bramlette & Wilcoxon, 1967

Cyclicargolithus abisectus (Müller 1970) Wise, 1973

Cyclicargolithus floridanus (Roth & Hay *in* Hay et al. 1967) Bukry, 1971

Cyclicargolithus gammation (Bramlette & Sullivan 1961) Shafik, 1990

Cyclicargolithus reticulatus (Gartner & Smith 1967) Bukry, 1971

Discoaster asymmetricus Gartner, 1969

Discoaster barbadiensis Tan, 1927

Discoaster brouweri Tan, 1927 emended Bramlette & Riedel, 1954

Discoaster deflandrei Bramlette & Riedel, 1954

Discoaster hamatus Martini & Bramlette, 1963

Discoaster lodoensis Bramlette & Riedel, 1954

Discoaster multiradiatus Bramlette & Riedel, 1954

Discoaster moorei Bukry, 1971

Discoaster pentaradiatus Tan, 1927 emended Bramlette & Riedel, 1954

Discoaster quinqueramus Gartner, 1969

Discoaster saipanensis Bramlette & Riedel, 1954

Discoaster sublodoensis Bramlette & Sullivan, 1961

Discoaster surculus Martini & Bramlette, 1963

Discoaster tamalis Kamptner, 1967

Discoaster tanii Bramlette & Riedel, 1954

Discoaster triradiatus Tan, 1927

Discoaster variabilis Martini & Bramlette, 1963

Discoasteroides kuepperi Stradner, 1959

Emiliania huxleyi (Lohmann 1902) Hay & Mohler *in* Hay et al. 1967

Ericsonia subdisticha (Roth & Hay *in* Hay et al. 1967) Roth *in* Baumann & Roth, 1969

Fasciculithus tympaniformis Hay & Mohler in Hay et al., 1967

Florisphaera profunda Okada & Honjo, 1973

Gephyrocapsa Kamptner, 1943

Gephyrocapsa oceanica Kamptner, 1943

Figure 8 (facing page). Eocene planktic foraminiferids, all axial sections except A, H, M, Q, T, X and Y, which are oblique equatorial sections. A, B, *Acarinina bullbrooki*, sample 107DR06-05 — x 85. C–E, *Acarinina spiroinflata*: C, D, sample 107DR10-04 — x 75; E, sample 107DR05-03B — x 80. F, *Acarinina bullbrooki*, sample 107DR10-04 — x 85. G, H, *Acarinina spiroinflata*: G, sample 107DR05-01Bii — x 80; H, sample 107DR10-04 — x 80. I, *Acarinina ?primitiva*, sample 107DR05-01A — x 75. J, K, *Acarinina primitiva*: J, sample 107DR05-03A — x 75; K, sample 107DR05-01A — x 80. L, M, *Acarinina broedermanni*, sample 107DR05-04B — x 80. N, O, *Acarinina ?pentacamerata*: N, sample 107DR05-04B — x 75; O, sample 107DR05-02A — x 75. P, Q, *Acarinina broedermanni*, sample 107DR05-02A — x 75. R, ?*Truncorotaloides rohri*, sample 107DR05-01A — x 70. S, *Subbotina frontosa*, sample 107DR05-01B — x 75. T, V, *Subbotina eocaena*, sample 107DR05-01B — x 70. U, X, *Subbotina ?inaequispira*: U, sample 107DR10-03 — x 80; X, sample 107DR05-01Bi — x 40. W, *Subbotina inaequispira*, sample 107DR05-01Bii — x 75. Y, *Subbotina frontosa*, sample 107DR05-01A — x 70. Z, *Subbotina eocaena*, sample 107DR05-04B — x 75.

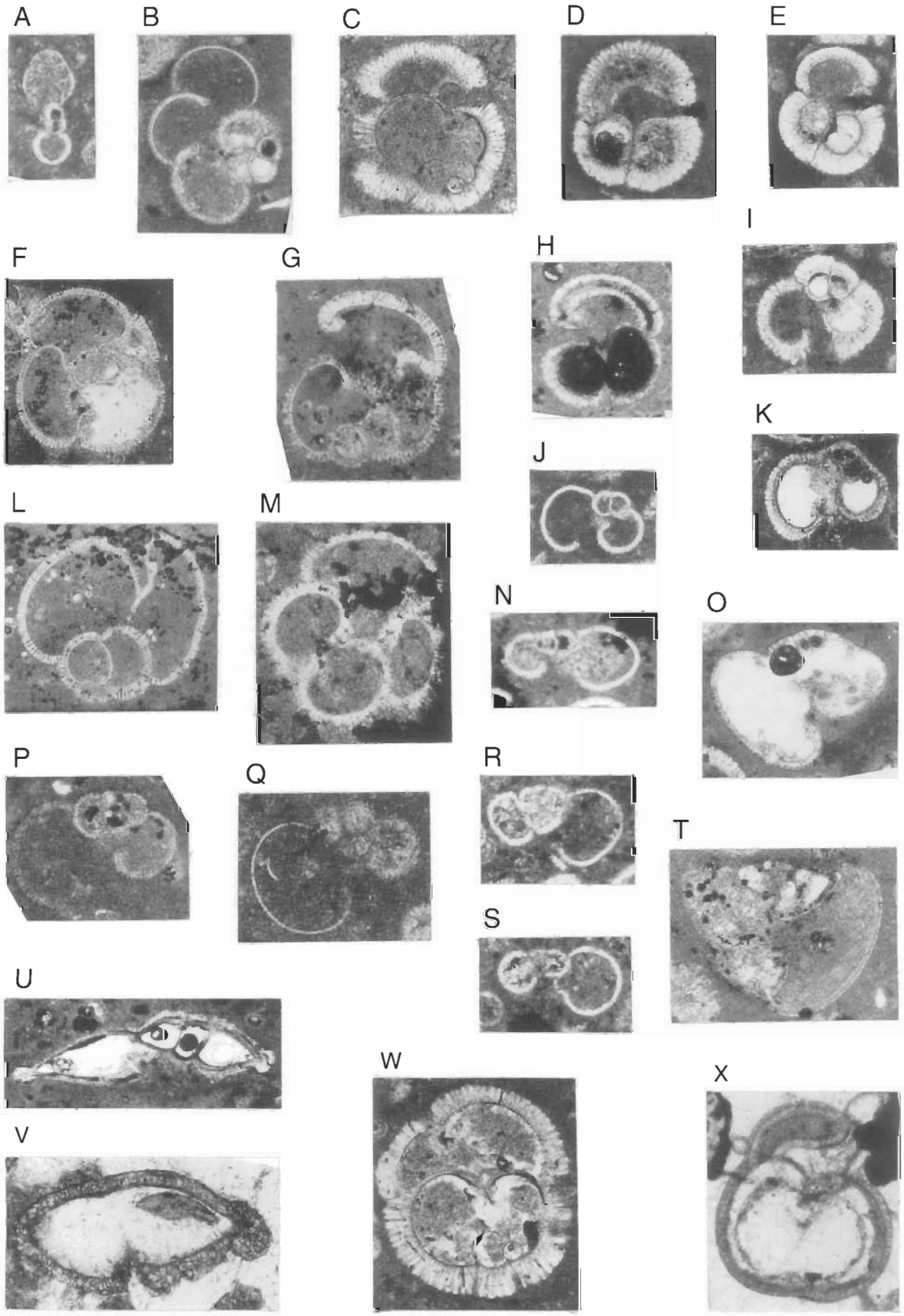
A
B
C
D
E
F
G
H
I
J
K
L
M
N
O
P
Q
R
S
T
U
V
W
X

Hayaster perplexus (Bramlette & Riedel 1954) Bukry, 1973

Helicosphaera compacta Bramlette & Wilcoxon, 1967

Helicosphaera euphratis Haq, 1966

Helicoshaera kamptneri Hay & Mohler *in* Hay et al., 1967

Helicosphaera recta Haq, 1966

Helicosphaera sellii Bukry & Bramlette, 1969

Lanternithus minutus Stradner, 1962

Micrantholithus Deflandre *in* Deflandre & Fert, 1954.

Pedinocyclus larvalis (Bukry & Bramlette 1969) Loeblich & Tappan, 1973

Pontosphaera multipora (Kamptner 1948) Roth, 1970

Pontosphaera plana (Bramlette & Sullivan 1961) Haq, 1971

Pseudoemiliania lacunosa (Kamptner 1963) Gartner, 1969

Reticulofenestra scissura Hay, Mohler & Wade, 1966

Reticulofenestra scrippsae (Bukry & Percival 1971) Shafik, 1981

Reticulofenestra pseudoumbilicus (Gartner 1967) Gartner, 1969

Reticulofenestra umbilicus (Levin 1965) Martini & Ritzkowski, 1968

Rhabdosphaera Haeckel, 1894

Rhabdosphaera stylifer Lohmann, 1902

Scapholithus fossilis Deflandre *in* Deflandre & Fert, 1954

Sphenolithus abies Deflandre *in* Deflandre & Fert, 1954

Sphenolithus ciperoensis Bramlette & Wilcoxon, 1967

Sphenolithus distentus (Martini 1965) Bramlette & Wilcoxon, 1967

Sphenolithus heteromorphus Deflandre, 1963

Sphenolithus moriformis (Brönnimann & Stradner 1960) Bramlette & Wilcoxon, 1967

Sphenolithus neoabies Bukry & Bramlette, 1969

Sphenolithus predistentus Bramlette & Wilcoxon, 1967

Sphenolithus pseudoradians Bramlette & Wilcoxon, 1967

Sphenolithus radians Deflandre *in* Grassé, 1952

Toweius eminens (Bramlette & Sullivan 1961) Perch-Nielsen, 1971

Triquetrorhabdulus carinatus Martini, 1965

Triquetrorhabdulus rugosus Bramlette & Wilcoxon, 1967

Umbellosphaera irregularis Paasche in Markali & Paasche, 1955

Zygrhablithus bijugatus bijugatus (Deflandre 1954) Deflandre, 1959

Zygrhablithus bijugatus crassus Locker, 1967

Figure 9 (facing page). Eocene and younger planktic foraminiferids. A, G–L, N–V, near axial sections; B–F, M, W, X, oblique equatorial sections. A, *Pseudohastigerina micra,* sample 107DR05-04B — x 90. B, ?*'Globigerinoides' higginsi,* sample 107DR05-01A — x 75. C, *Globigerinatheka ?index,* sample 107DR10-04A — x 60. D, *Globigerinatheka index,* sample 107DR10-04A — x 80. E, *Muricoglobigerina senni,* sample 107DR05-01A — x 75. F, G, *Dentoglobigerina tripartita,* sample 107DR10-03 — x 70, x 50. H, *Globigerinatheka ?subconglobata,* sample 107DR10-04A — x 80. I, *Muricoglobigerina senni,* sample 107DR05-02A — x 75. J, *Globigerina praebulloides,* sample 107DR05-04B — x 60. K, *Muricoglobigerina senni,* sample 107DR05-03A — x 75. L, *Dentoglobigerina tripartita,* sample 107DR10-03 — x 50. M, *Dentoglobigerina ?baroemoensis,* sample 107DR06-05 — x 70. N, R, S, *Tenuitella* sp., sample 107DR10-02A: N, R — x 140; S — x 170. O, *Turborotalia cerroazulensis,* sample 107DR10-04A — x 75. P, Q, *Globigerina praebulloides,* sample 107DR05-02A — x 75, x 110. T, *Turborotalia centralis,* sample 107DR10-04A — x 65. U, *Globorotalia (Globorotalia) cultrata,* sample 107DR10-06 — x 50. V, *Globorotalia (Globorotalia) tumida,* sample 107DR06-05 — x 40. W, *Globigerinoides conglobatus,* sample 107DR10-06 — x 70. X, *Globorotalia (Globoconella) ?inflata,* sample 107DR06-05 — x 80.

AGSO Journal of Australian Geology & Geophysics, 16(5), 701–716

Early Ordovician fauna of the Gap Creek Formation, Canning Basin, Western Australia

John R. Laurie[1]

The trilobite and brachiopod fauna of the Gap Creek Formation is revised. Recorded are the trilobites: *Geragnostus* aff. *splendens*, *Opipeuter angularis*, *O. ?inconnivus*, *Carolinites ?genacinaca*, *Canningella hardmani*, *Encrinurella ?reedi*, and several indeterminate forms. Brachiopods include *?Pseudomimella* sp., *?Oligorthis* sp., *Tritoechia* sp., *Spanodonta hoskingiae*, and *Tinopena shergoldi* gen. et sp. nov. Also recorded are the gastropods *Teiichispira* sp. and *Helicotoma* sp., and calcareous plates of uncertain affinities. Correlations based largely on the telephinid trilobites indicate this fauna is of late Bendigonian (Be3–Be4) age.

Introduction

The Canning Basin, situated between latitudes 17° and 24°S and longitudes 119° and 128°E (Fig. 1), is a large northwest–southeast-oriented Ordovician to Cretaceous pericratonic basin which covers an area of about 430 000 km^2 in northern Western Australia. It is bounded by the Early Proterozoic Halls Creek Province to the northeast, and by other Archaean and Proterozoic blocks and several Proterozoic to Palaeozoic basins to the east and south (Palfreyman 1984). The northeastern

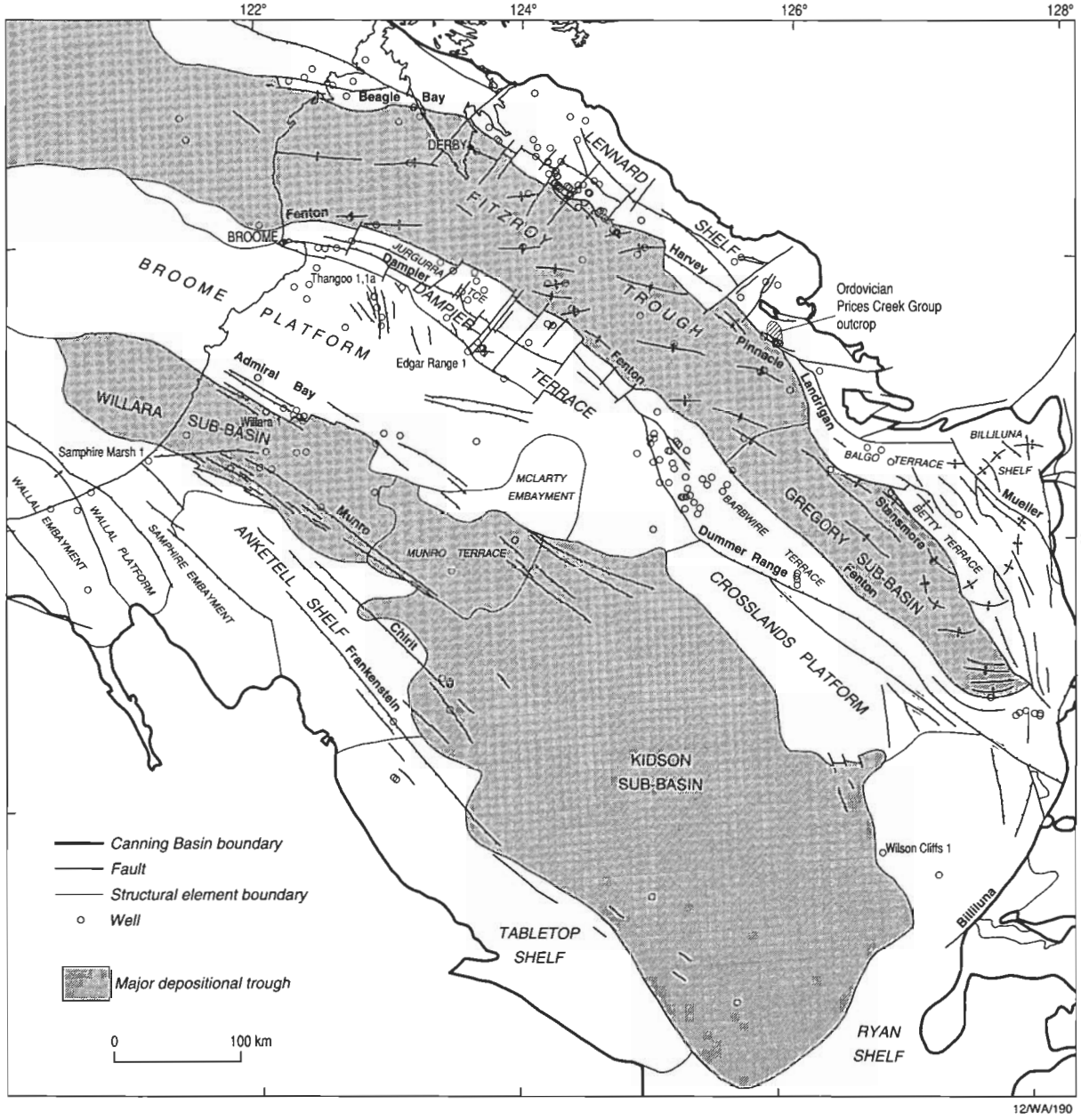

Figure 1. Major structural features of the Canning Basin. The Prices Creek Group outcrop is midway along the northeastern margin of the basin (modified from Kennard et al. 1994).

[1] Petroleum & Marine Division, Australian Geological Survey Organisation, GPO Box 378, Canberra, ACT 2601.

marginal portion of the basin is referred to as the Lennard Shelf, and it is here where most of the outcropping Ordovician rocks occur. The outcrops containing the fauna described herein are restricted to an area of about 20 km^2 between Prices Creek and Gap Creek (Fig. 2), south of the Emanuel Range, and about 60 km southeast of the township of Fitzroy Crossing.

The Ordovician age of rocks in the Prices Creek area on the northern margin of the Canning Basin was first recognised from fossils found in 1949 by D.J. Guppy and A.W. Lindner during the mapping of rocks previously considered Devonian in age. The discovery was reported by Guppy & Öpik (1950) establishing the Prices Creek Group, which they divided into a lower 'Emanuel Limestone' (509 m thick) and an upper 'Gap Creek Dolomite'.

Exposures near Gap Creek, north of the Emanuel Formation type section (705 in Fig. 2), and apparently overlying the Emanuel Formation were named the Gap Creek Formation by Guppy & Öpik (1950). The type section, comprising 186 m of dolomite, calcareous sandstone, and lesser limestone, was detailed by Guppy et al. (1958).

In a study of the prioniodontacean conodonts from the Emanuel Formation, McTavish (1973) referred to three stratigraphic sections. The longest of these was the type section of the unit (Guppy et al. 1958), whose base is attached to the section in BMR Noonkanbah No.3 (termed BMR 3 Prices Creek by McTavish). The third section, RM10 of McTavish (corresponding to section 707 in Fig. 2), was asserted to represent the top of the Emanuel Formation. However, this part of the sequence represents the lower part of the Gap Creek Formation as defined by Guppy et al. (1958). The

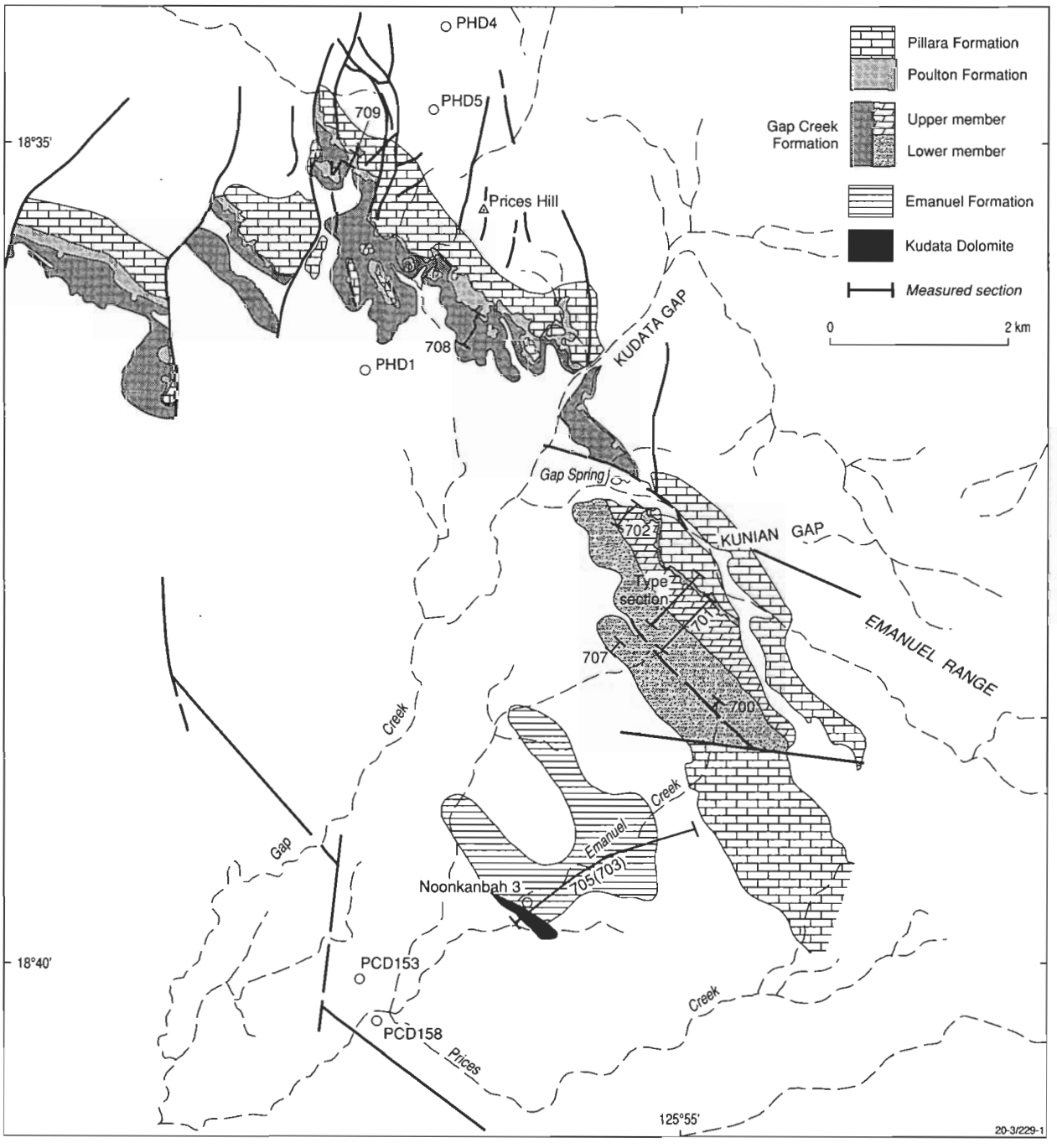

Figure 2. Geology of the Prices Creek outcrop area, showing location of measured sections. The type section of the Gap Creek Formation is near Kunian Gap and is labelled 'type section'. The other sections of the Gap Creek Formation discussed herein are 707 (southwest of the type section) and 708 (west of Kudata Gap). Localities with PHD and PCD prefixes are BHP–Utah coreholes.

recent lithological analysis by Nicoll et al. (1993) indicates that the boundary between the Emanuel and Gap Creek Formations lies well below the base of section RM10 of McTavish (1973). This is the concept of the Gap Creek Formation used herein; it includes McTavish's section RM10, which has been remeasured (as section WCB 707) and sampled for conodonts and macrofauna.

Biostratigraphy

Öpik (*in* Guppy & Öpik 1950) recognised four faunal stages within the Emanuel Formation in its type area, and one stage in the Gap Creek Formation. Öpik's trilobite biostratigraphy is readily recognised, and was essentially used as the basis of a revised scheme devised by Legg (1973, 1978). This author (1973) recognised in the Emanuel Formation three trilobite assemblages based on *Kayseraspis*, *Ogygiocaris*, and *Encrinurella*. The *Encrinurella* zone occurs in the uppermost beds, which Legg included in the Emanuel Formation. However, these beds are here regarded as Gap Creek Formation, since they are much more dolomitic than and faunally unlike the underlying Emanuel Formation and more like that of the remainder of the Gap Creek Formation. From this part of the sequence, Legg (1976, 1978) recorded the trilobites *Opipeuter emanuelensis*, *Carolinites bulbosa*, *Canningella hardmani*, *Encrinurella reedi*, *Gogoella wadei*, *Bumastus* sp., and *Geragnostus* sp., and the brachiopod *Spanodonta hoskingiae*.

The trilobite biostratigraphic scheme recognised in the Emanuel Formation has been revised by Laurie & Shergold (1996, in press). The trilobite and brachiopod fauna from the Gap Creek Formation, which Öpik referred to his stage V (characterised by the plectambonitacean brachiopod *Spanodonta*), is revised herein.

Although *Spanodonta hoskingiae* Prendergast is found throughout most of the unit (sections 707 and 708; Figs. 3 and 4), the lower part of the formation is characterised also by the presence of trilobites, and is here referred to as the *Encrinurella/Carolinites* assemblage zone. This assemblage contains the trilobites *Geragnostus* aff. *splendens* (Holub), *Opipeuter angularis* (Young), *Opipeuter ?inconnivus* Fortey, *Carolinites ?genacinaca* Ross, *Canningella hardmani* Legg, *Encrinurella ?reedi* Legg, and several indeterminate species of asaphids. Brachiopods include *?Oligorthis* sp., *Tritoechia* sp., *?Pseudomimella* sp., and *Spanodonta hoskingiae* Prendergast. The gastropods *Teiichispira* sp. and *Helicotoma* sp. are also present.

The upper part of the formation is mostly lacking in trilobites and is characterised by the plectambonitoidean brachiopods *Spanodonta hoskingiae* and *Tinopena shergoldi*. *T. shergoldi* is restricted to this assemblage, termed the

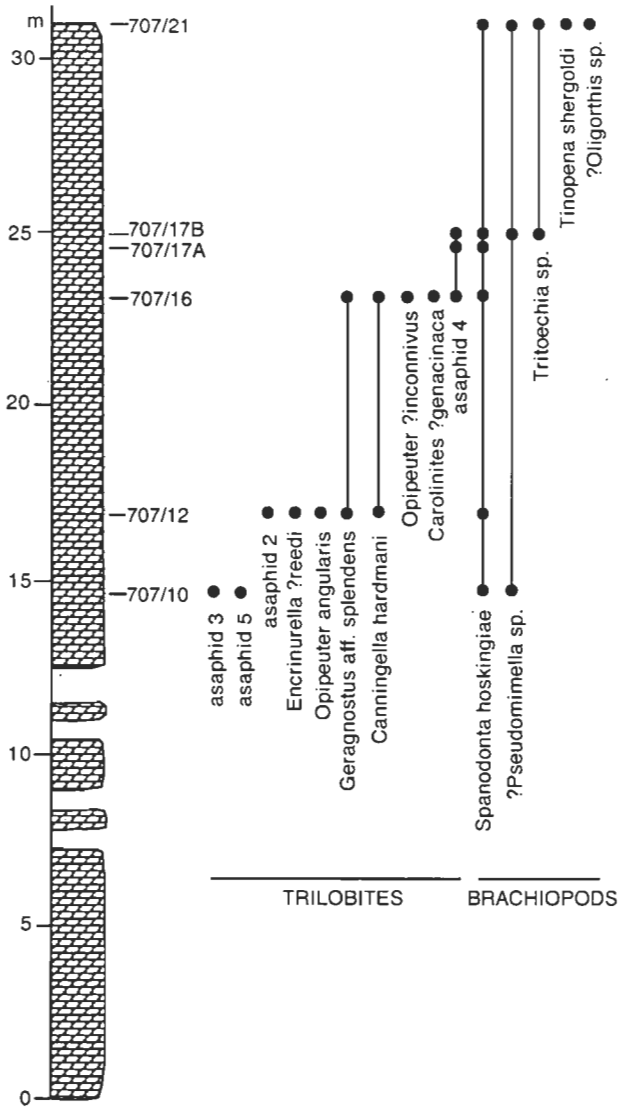

Figure 3. Graphic representations of section WCB 707 (SW of type section) of the Gap Creek Formation, and the stratigraphic ranges of selected trilobites and brachiopods.

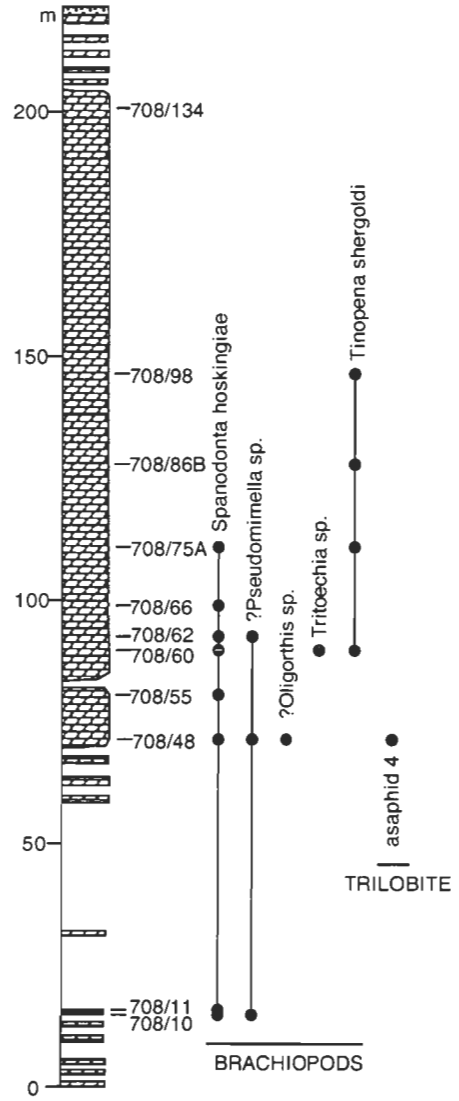

Figure 4. Graphic representations of section WCB 708 (W of Kudata Gap) of the Gap Creek Formation, and the stratigraphic ranges of selected trilobites and brachiopods.

Spanodonta/Tinopena assemblage, and its first appearance denotes the base of the assemblage zone. This assemblage also contains the brachiopods *?Oligorthis* sp., *Tritoechia* sp., and *?Pseudomimella* sp.

Correlations

Canning Basin

The Gap Creek Formation fauna was referred to as subfauna 3b by Legg (1978), who recorded it from cores in two petroleum exploration wells: core 13 in Willara No.1, and core 12 in Edgar Range No.1. However, in his taxonomic treatment of the faunas, he recorded neither of the characteristic pliomerids (*Encrinurella* and *Canningella*) from either of these cores. Legg's record of *Opipeuter emanuelensis* from his subfauna 3b is apparently in error, and so is his record of *Carolinites bulbosa* from subfauna 3a (Laurie & Shergold 1996, in press). Therefore there is some doubt as to the veracity of records of these species in the subsurface.

Amadeus Basin

The Gap Creek Formation probably correlates with the lower part of the Horn Valley Siltstone of the Amadeus Basin. The faunas of these two units show some similarities in that *Carolinites genacinaca,* tentatively recorded from the Gap Creek Formation, occurs throughout most of the Horn Valley Siltstone, whose lower part contains a species of *Encrinurella* (Laurie unpublished data).

One of the dominant asaphid genera from the Horn Valley Siltstone, *Lycophron,* has also been recorded as *?Aulacoparia* sp. by Legg (1976, p. 9) in his subfaunas 4 and 5 in the Canning Basin. Examination of Legg's specimens has shown that they are probably referable to the unnamed species of *Lycophron* characteristic of the upper part of the Horn Valley Siltstone, rather than to *L. howchini*, which characterises the lower part of the unit (Laurie unpublished data).

Georgina Basin

Correlation with the Georgina Basin is difficult because little is known of the faunal content of much of this part of the Ordovician sequence. The Gap Creek Formation probably correlates with the Coolibah Formation of the Georgina Basin insofar as the base of the overlying Nora Formation contains *Carolinites genacinaca* and a species of *Lycophron* similar to that from the upper Horn Valley Siltstone (Fortey & Shergold 1984; Laurie unpublished data), and is therefore probably younger than the Gap Creek Formation. Furthermore, like the Gap Creek Formation, the Coolibah Formation also contains the gastropod *Teiichispira* (Gilbert-Tomlinson 1973; Hill et al. 1969).

Northeastern Queensland

The fauna in the Rollston Range Formation in the Mount Windsor Subprovince near Charters Towers contains *Carolinites genacinaca* and *Opipeuter insignis* (Henderson 1983). The latter is most unlike *Opipeuter angularis*. Rather, having a very narrow glabella tongue, it more closely resembles both *O. inconnivus* Fortey and the unnamed species that succeeds *O. inconnivus* in the Spitsbergen sequences (Fortey 1974, 1980). As both *C. genacinaca* and *O. inconnivus* are tentatively recorded from the Gap Creek Formation, it is likely that the Rollston Range fauna is of similar age.

Northwestern New South Wales

Little detailed work has been done on the Gnalta Shelf and Mount Arrowsmith areas of northwestern New South Wales, where most of the information comes from the unpublished work of Warris (1967) updated by Shergold (1971) and Webby et al. (1981). On the Gnalta Shelf, the Rowena Formation contains *Carolinites* (probably *C. genacinaca*). In the Mount Arrowsmith area, the Tabita Formation also contains *Carolinites genacinaca*, as well as specimens of *Lycophron*, possibly conspecific with that from the upper part of the Horn Valley Siltstone of the Amadeus Basin. This indicates that they are probably slightly younger than the Gap Creek Formation.

Tasmania

The basal Karmberg Limestone of the Florentine Valley in southern Tasmania contains an unnamed species of *Canningella* and possibly representatives of *Carolinites*; a species of *Teiichispira* occurs higher in the formation (Laurie 1991, p. 21). Thus the Karmberg Limestone may well be of similar age to the Gap Creek Formation.

In the Caroline Creek Sandstone of northern Tasmania, both *Carolinites tasmaniensis* (Etheridge) and a species of pliomerid tentatively assigned to *Protoencrinurella* by Jell & Stait (1985) are recorded. This unit may thus correlate with the lower part of the Gap Creek Formation and upper part of the underlying Emanuel Formation insofar as *C. tasmaniensis* predates *C. genacinaca*, and *Protoencrinurella* is found in the upper part of the Emanuel Formation.

Intercontinental

Correlations outside Australia are largely accomplished through the cosmopolitan telephinids *Opipeuter* and *Carolinites*. These

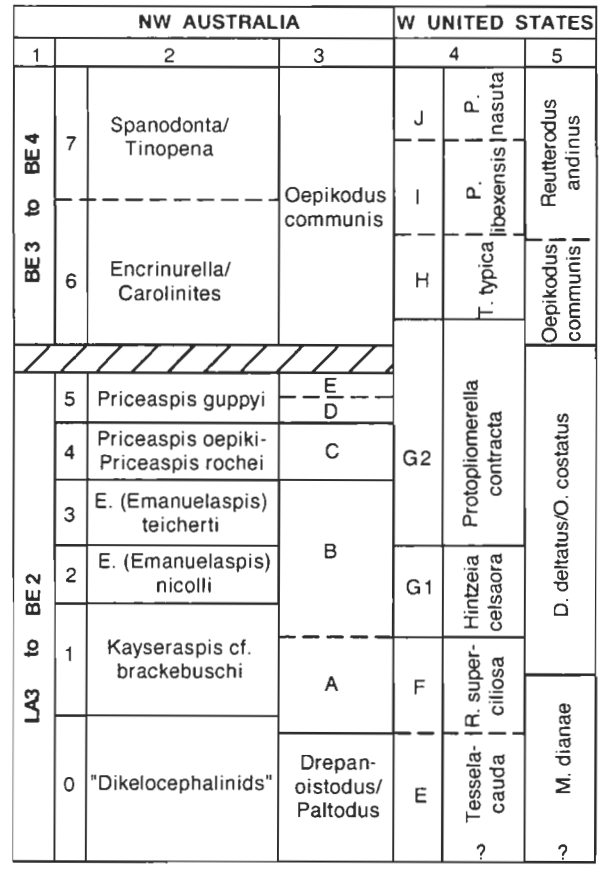

Figure 5. Correlation of the northern Canning Basin Early Ordovician biostratigraphic scheme with that from western North America. Column 1 is a tentative correlation with the Victorian graptolite standard. Column 2 is an amalgamation of the trilobite zonation of Laurie & Shergold (1996) and the trilobite–brachiopod zonation of this paper. Column 3 is the current state of conodont biostratigraphic analysis (R.S. Nicoll, Australian Geological Survey Organisation, personal communication 1996). Column 4 is the trilobite zonation from Nevada and Utah (Ross 1951; Hintze 1952, 1973; Ross et al. 1982). Column 5 is the conodont zonation of Ross et al. (1993). The hatched area represents the 100–200-metre-thick covered interval spanning the boundary of the Emanuel and Gap Creek Formations (from Shergold et al. 1995).

genera facilitate the correlation of the Gap Creek faunas with the trilobite zonations established by Ross (1951) and Hintze (1952, 1973) in Utah and Nevada. Laurie & Shergold (1996) have shown that the underlying Emanuel Formation probably correlates with zones F, G1, and G2 (Fig. 5). The presence of *Opipeuter angularis* in locality 707/12 (Fig. 3) of the Gap Creek Formation indicates a correlation with zone H of the Fillmore Formation, where this species has been recorded from a single cranidium as *Remopleuridiella angularis* by Young (1973). Additionally, the presence of *Carolinites genacinaca* in locality 707/16 of the Gap Creek Formation suggests a correlation with zones I or J of the Utah and Nevada scheme.

The presence of *O. angularis* in the lower part of the Gap Creek Formation allows a correlation with the lowermost Olenidsletta Member (V1a) of the Valhallfonna Formation in Spitsbergen (Fortey 1974, 1980). According to Cooper & Fortey (1982), the graptolite fauna at this level correlates with the late Bendigonian Be3, a correlation in accordance with the Be1–Be2 age assigned to the underlying Emanuel Formation by Laurie & Shergold (1996). The subsequent appearance of *Carolinites genacinaca* and *Opipeuter ?inconnivus* indicates a correlation of the upper parts of the Gap Creek Formation with perhaps the V1b or later assemblages in the middle Olenidsletta Member in Spitsbergen (Fortey 1980). Cooper & Fortey consider the graptolites in the V1b assemblage to indicate a correlation with Bendigonian Be3 to Chewtonian Ch1.

Although no telephinid trilobites have been described from the lower Setul Limestone of Pulau Langgun, off the west coast of Malaysia, the similarities of its fauna to the Gap Creek fauna are worthy of note, and suggest a close correlation. The Setul Limestone is the only other place from which the brachiopod genus *Spanodonta* has been recorded, as the species *S. floweri* (Cooper; see Laurie & Burrett 1992). In addition, the gastropods *Teiichispira* (Yochelson & Jones 1968) and *Helicotoma* (Kobayashi 1959) have also been recorded from the same locality within the lower Setul Limestone.

Systematic palaeontology

Phylum Arthropoda Siebold & Stannius, 1845

?Class Trilobita Walch, 1771

Order Agnostida Salter, 1864

Superfamily Agnostoidea M'Coy, 1849

Family Metagnostidae Jaekel, 1909

Genus *Geragnostus* Howell, 1935

Type species. *Geragnostus sidenbladhi* (Linnarsson, 1869).

Geragnostus aff. *splendens* (Holub, 1912)

Figures 6.1–6.3

Material. Three cephala from locality 707/16, one of which is illustrated (CPC 33223); one cephalon found in float (CPC 33224); and one pygidium from locality 707/12 (CPC 33225)

Comments. These specimens belong to the peculiar Early Ordovician group of agnostid species, currently assigned to *Geragnostus*, which have a short, generally unfurrowed glabella and a long, broad pygidial axis with a clearly defined, rounded, slightly bulbous posterior axial lobe. This morphological group may well represent one species, and several names are available, of which *G. splendens* (Holub) appears to have priority.

Geragnostus splendens (Holub) comes from the Arenig Klabava Formation of central Bohemia (Pek 1977). Specimens similar to it (*G.* cf. *splendens*) have been recorded from the *M. planilimbata* zone of the Hunnebergian to the *M. estonica* zone of the late Billingenian (Ahlberg 1992) of southern Sweden.

Class Trilobita Walch, 1771

Order Proetida Fortey & Owens, 1975

Superfamily Bathyuroidea Walcott, 1886

Family Telephinidae Marek, 1952

Comments. Fortey (1974) considered the genus *Opipeuter* to be related to the Remopleuridiidae, although he believed it to be sufficiently distinct to require the introduction of the new family Opipeuteridae. Laurie & Shergold (1996) have demonstrated that *Opipeuter* belongs to the Telephinidae and this systematic position is adopted herein.

Genus *Opipeuter* Fortey, 1974

Type species. *Opipeuter inconnivus* Fortey, 1974.

Opipeuter angularis (Young, 1973)

Figures 6.6, 6.10

1973 *Remopleuridiella angularis* n. sp.; Young, p. 112, pl. 1, figs. 21, 22, 26; not figs. 25, 27.

1980 *Opipeuter angularis* (Young); Fortey, p. 48, pl. 6, figs. 9, 13.

Material. One cranidium (CPC 33228) and one librigena (CPC 33229), both from locality 707/12; other fragmentary material, possibly conspecific, from locality 707/10.

Comments. Although represented by only a few poorly preserved specimens, they show features which are consistent with assignment to *O. angularis* (Young) rather than *O. inconnivus* Fortey. Compared with the latter, the Gap Creek specimens have a glabella which, in lateral profile, is of greater convexity relative to length, and has a broader, shorter tongue and a more forwardly placed anterolateral glabellar angle with consequent longer (exsag.) posterior portion of the fixigena.

The librigena has more in common with that illustrated by Fortey (1974, pl. 13, fig. 10) for *O. inconnivus* than any other assigned to the genus, apart from those referred to *O. emanuelensis translator* by Shergold (in Laurie & Shergold 1996). It has a small genal spine, and between the eye and the border furrow, at about the midlength level of the eye, there is a moderately short (exsag.), narrow (tr.) genal field. On the other hand, anterolaterally, the border of the librigena abruptly begins to narrow towards the front, such that in front of the eye it is extremely narrow (exsag.). At the same position, the border also abruptly bends ventrally through about 60°. This is unlike the librigenal border in all subspecies of *O. emanuelensis*, in which the border does not alter direction to anywhere near the same extent. It is unclear whether this feature is present in either *O. angularis* or *O. inconnivus*.

Opipeuter ?inconnivus Fortey, 1974

Figures 6.7–6.9

?1974 *Opipeuter inconnivus* sp. nov.; Fortey, p. 112, pl. 13, figs. 2–4, 9, 11, 12; pl. 14, figs. 1–3, 5, 8–10, 11–13.

?1980 *Opipeuter inconnivus* Fortey; Fortey, p. 47, pl. 6, figs. 12, 14, 15.

Material. Two cranidia, one of which is illustrated (CPC 33230); and two librigenae, both of which are illustrated (CPC 33231, CPC 33232). All from locality 707/16.

Comments. One very poorly preserved cranidium from locality 707/16 is probably pathological because it is asymmetrical, but it seems to have a glabellar tongue that is narrower than that of *O. angularis* from 707/12. A narrow glabellar tongue is characteristic of the type and subsequent species of *Opipeuter*; therefore this specimen is tentatively assigned to the type species, *O. inconnivus*.

Genus *Carolinites* Kobayashi, 1940

[= *Keidelia* Harrington & Leanza, 1957;
= *Dimastocephalus* Stubblefield, 1950]

Type species. *Ptychoparia? tasmaniensis* Etheridge, 1919 = *Carolinites bulbosus* Kobayashi, 1940 = *Carolinites genacinaca nevadensis* Hintze, 1953.

Remarks. Jell & Stait (1985, pp. 40–41) redescribed the originally designated type species of the genus, *Carolinites*

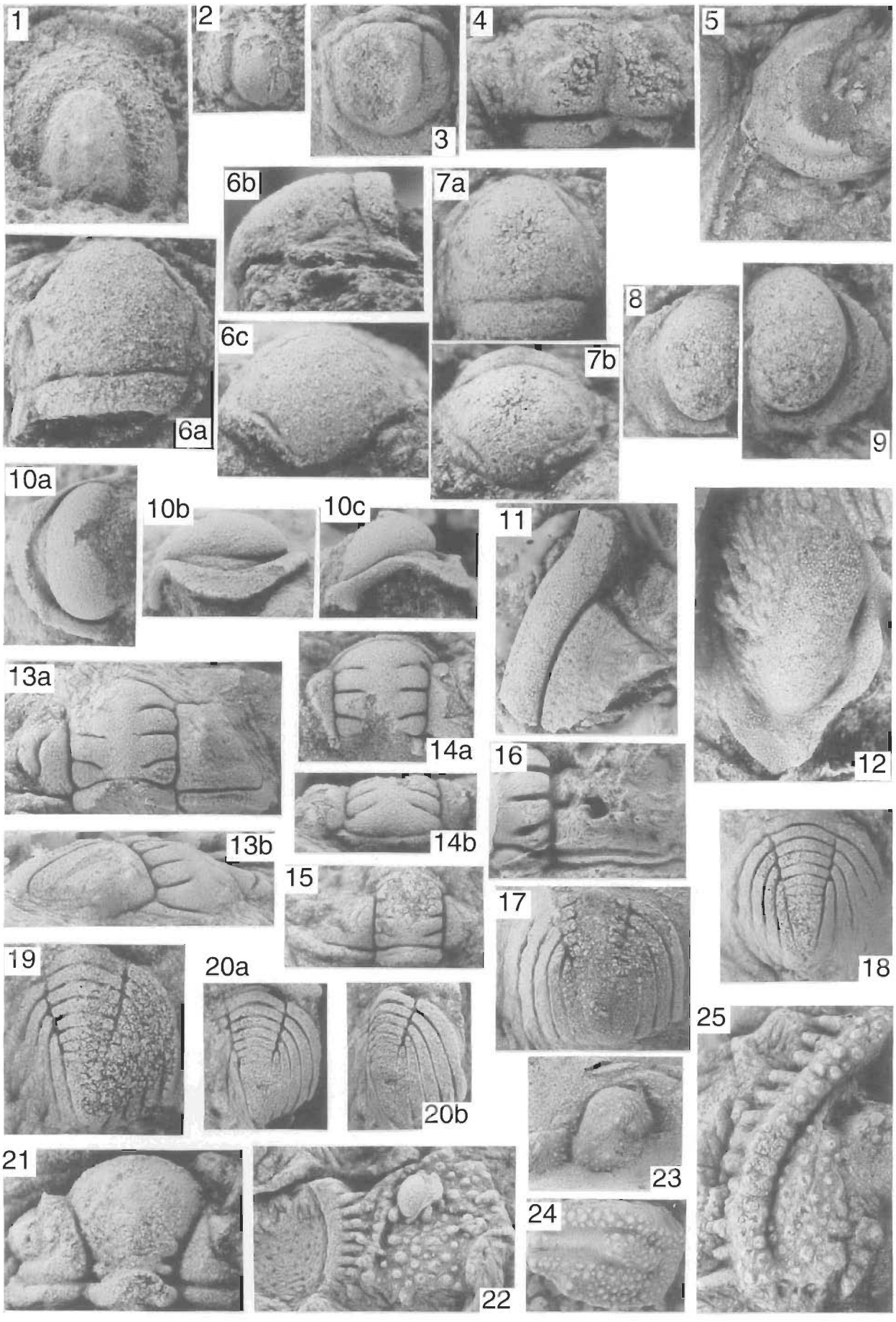
1
2
3
4
5
6b
7a
6c
6a
7b
8
9
10a
10b
10c
11
12
13a
14a
16
14b
13b
15
17
18
19
20a
20b
25
23
21
22
24

bulbosus, and concluded that it was a junior subjective synonym of *Ptychoparia*? *tasmaniensis* Etheridge. They also concluded that *Carolinites genacinaca nevadensis* Hintze was similarly synonymous. Therefore, under Article 61d of the International Code of Zoological Nomenclature (Ride et al. 1985), the species *C. tasmaniensis* is the genotype and if one wishes *C. genacinaca* to be conspecific but of a separate subspecies then it should be referred to as *C. tasmaniensis genacinaca*. In his extensive revision of species of *Carolinites,* Fortey (1975, p. 103) discusses only some of the diagnostic features, and does not illustrate intermediate specimens, despite stating that the gradation between the two 'sub-species appears to be perfect'. Therefore, my preference is for *C. genacinaca* to be retained as a separate species.

Carolinites ?genacinaca Ross, 1951

Figures 6.4–6.5

?1951 *Carolinites genacinaca* n. sp.; Ross, p. 84, pl. 18, figs. 25, 26, 28–36.

?1975 *Carolinites genacinaca genacinaca* Ross; Fortey, p. 112, pl. 37, figs. 1–15, pl. 38, figs. 1–3.

Material. One poorly preserved cranidium (CPC 33226) and one librigena (CPC 33227), both from locality 707/16.

Comments. Although very poorly preserved, these specimens clearly belong to *Carolinites*. This is because the glabella is stout, quadrate, expands slightly forward, and is flanked posteriorly by small bacculae; the anterior cranidial border is narrow (sag.) and immediately in front of the glabella. The fixigenae are difficult to discern anteriorly, but the posterior part of the right fixigena is preserved and indicates that these specimens belong to either *C. genacinaca* or *C. tasmaniensis*. Despite the poor preservation, the presence of an advanced genal spine and the lack of a subocular ridge indicate that an assignment to the former species is more likely.

Superfamily incertae sedis

?Family Hystricuridae Hupé, 1953

Indeterminate ?hystricurid 1

Figures 6.22-6.25

Material. One partial cranidium from float (CPC 33246); three librigenae from locality 707/12 (CPC 33244, CPC 33245, CPC 33248); one librigena from locality 707/16; one partial pygidium from locality 707/12 (CPC 33247); and one partial pygidium from float.

Comments. This species is known only from the few fragmentary specimens listed above, most of which are illustrated. The entire dorsal carapace appears to be spinose. The glabella appears to taper forwards, the fixigenae are wide, the preglabellar field narrow (sag.), about the same width as the anterior border. The librigena is wide (tr.), and has low convexity and a well-developed roll-like border which has a row of more-or-less radial spines extending outwards. The size of the eye socle indicates that the eye was fairly large. The fragment of the pygidium exhibits well developed pleural furrows and a narrow convex border. This species shows some resemblance to representatives of the spinose hystricurid *Amblycranium* Ross.

Indeterminate ?hystricurid 2

Figures 7.2–7.3

Material. Two librigenae, one each from locality 707/12 and 707/16 (CPC 33250 and CPC 33251 respectively).

Comments. This species is represented by only two librigenae. In these, the eye is large and reniform, similar in many respects to that of the Telephinidae. The librigenal field is small, and convex; the border moderately wide; and the genal spine long and posterolaterally directed.

Order Phacopida Salter, 1864

Suborder Cheirurina Harrington & Leanza, 1957

Family Pliomeridae Raymond, 1913

Genus *Canningella* Legg, 1976

Type species. *Canningella hardmani* Legg, 1976.

Revised diagnosis. Glabella nearly parallel-sided, evenly curved anteriorly, with S3 furrows arising immediately behind anterolateral angles of glabella. Pygidium has 7 or 8 axial rings and an elongate lanceolate terminal piece; pleurae have 5 ribs, the last pair of which run parallel to the axial furrow and posteriorly nearly envelop the terminal piece.

Comments. Legg (1976, p. 22) stated in his diagnosis of this genus that it had 10–11 pygidial axial rings in addition to the terminal piece. However, the specimens illustrated by him do not show that many rings. It seems that in his estimation of the number of axial rings, Legg included several of the incomplete transverse furrows in the terminal piece. Furthermore, he also stated that the 3p glabellar furrow (S3 herein) arose from the anterolateral glabellar angle. The furrow certainly is very close to that angle, but instead intersects the axial furrow a short distance behind it.

Canningella hardmani Legg, 1976

Figures 6.11–6.20

1976 *Canningella hardmani* sp. nov.; Legg, p. 23, pl. 7, figs. 1–10.

Material. Five cranidia from float, four of which are illustrated (CPC 33235, CPC 33236, CPC 33237, CPC 33238); one partial cranidium from locality 707/10; one cranidium from locality 707/16; two hypostomes from locality 707/16, one of which is illustrated (CPC 33234); one librigena from float (CPC 33233) and one from locality 707/16; one pygidium from float, two from locality 707/12, one of which is illustrated (CPC 33239), and five from locality 707/16, three of which are illustrated (CPC 33240, CPC 33241, CPC 33242).

Figure 6 (facing page). 1–3, *Geragnostus* aff. *splendens* (Holub, 1912): 1, partial cephalon, x12, CPC 33223, from loc.707/16; 2, posterior part of cephalon, x15, CPC 33224, from float; 3, damaged pygidium, x8, CPC 33225, from loc.707/12.
4–5, *Carolinites genacinaca* Ross, 1951: 4, damaged cranidium, x8, CPC 33226, from loc. 707/16; 5, left librigena, x6, CPC 33227, from loc.707/16. 6, 10, *Opipeuter angularis* (Young, 1973): 6a–c, cranidium, dorsal, lateral, and anterior views respectively, x10, CPC 33228, from loc.707/12; 10a–c, left librigena, dorsal, lateral, and anterior views respectively, x9, CPC 33229, from loc.707/12. 7–9, *Opipeuter ?inconnivus* Fortey, 1974: 7a–b, ?pathological cranidium, dorsal and anterior views respectively, x11, CPC 33230, from loc.707/16; 8, left librigena, x13, CPC 33231, from loc.707/16; 9, right librigena, x12, CPC 33232, loc.707/16. 11–20, *Canningella hardmani* Legg, 1976: 11, partial left librigena, x6, CPC 33233, float; 12, partial hypostome, x8, CPC 33234, from loc.707/16; 13a–b, partial cranidium, dorsal and anterolateral oblique views respectively, x4, CPC 33235, float; 14a–b, partial cranidium, dorsal and anterior view respectively, x8, CPC 33236, float; 15, small cranidium, x8, CPC 33237, float; 16, partial large cranidium, latex cast of internal mould, x3, CPC 33238, float; 17, poorly preserved pygidium, x4, CPC 33239, from loc.707/12; 18, pygidium, x4, CPC 33240, from loc.707/16; 19, pygidium, x8, CPC 33241, from loc.707/16; 20a–b, pygidium, dorsal and posterolateral oblique views respectively, x3, CPC 33242, from loc.707/16. 21, *Encrinurella ?reedi* Legg, 1976: poorly preserved cranidium, x9, CPC 33243, from loc.707/12. 22–25, indeterminate ?hystricurid 1: 22, two partial librigenae, specimen on the left in ventral view showing marginal spines, CPC 33244, specimen on the right in dorsal view showing spinose dorsal surface, CPC 33245, with associated *Opipeuter* librigena, x4, from loc.707/12; 23, latex cast of partial cranidium, showing anterior border, anterior part of glabella and portions of fixigenae, x4, CPC 33246, float; 24, anterolateral fragment of pygidium, x4, CPC 33247, from loc.707/12; 25, fragmentary librigena showing marginal spines, x4, CPC 33248, from loc.707/12.

Description. Cranidium much wider than long, of moderate convexity. Glabella with finely granular ornament, parallel-sided or expanding slightly forward. Occipital furrow deep, evenly bent forward. S1 furrows curving backwards toward occipital furrow, extending about two-thirds distance from axial furrow to glabellar midline. S2 furrows nearly straight, transverse, or directed slightly backwards. S3 furrows curved, arising from the axial furrow a very short distance behind the anterolateral glabellar angle, convex anteriorly with both extremities about level with one another. Anterior margin of

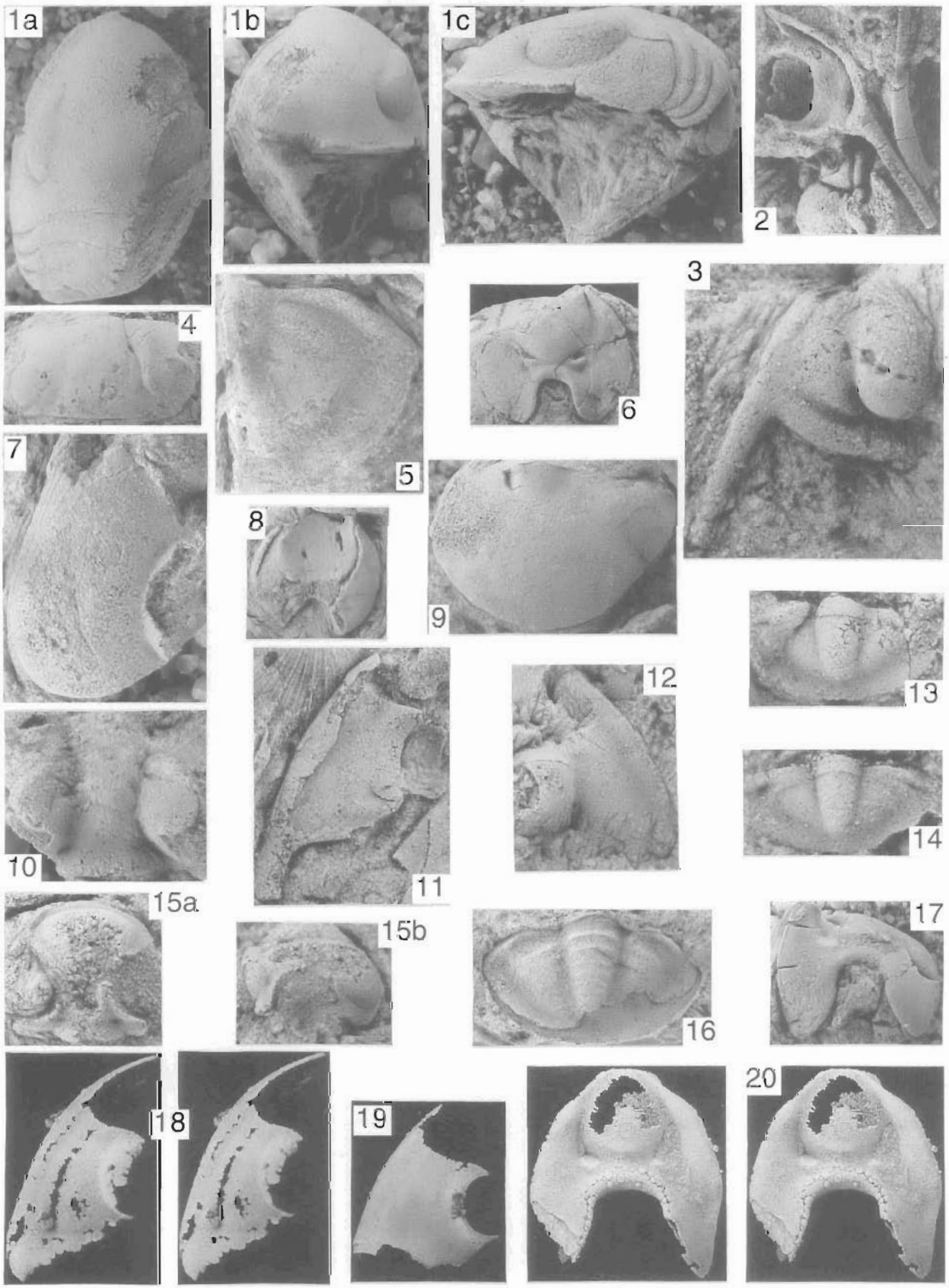

glabella broadly and evenly curved, separated from narrow border by a narrow, well-defined preglabellar axial furrow. Anterior limb of fixigena narrow (tr.). Palpebral lobe large, wide, long, evenly curved, separated from remainder of fixigena by a well-developed palpebral furrow. Posterior limb of fixigena very broad (tr.), with well-developed border widening laterally, anteriorly defined by deep narrow border furrow.

Librigena represented only by fragmentary specimens, most of which are poorly preserved. The illustrated specimen shows that the border has a finely granular ornament, similar to that of the glabella, while that of the librigenal field has superimposed on this a more coarsely pitted ornament.

Hypostome represented by usually poorly preserved fragmentary specimens. Illustrated specimen exhibits a finely granular ornament over entire surface. Middle body clearly defined by deep border furrow, elongate ovate, with oblique middle furrow very weakly developed. Border incompletely preserved, of moderate width, widening slightly posteriorly; posterior extremity probably pointed.

Pygidium subcircular to subquadrate. Axis consisting of 7 or 8 axial rings and an elongate lanceolate terminal piece, clearly separated from pleural lobes by deep narrow axial furrow. Pleural lobes consisting of 5 pleural ribs; only the anterior two are adjacent to their respective axial rings; the more posterior ribs are more offset; the posteriormost (fifth) arises level with the sixth axial ring, and extends alongside the remainder of the axis, widening posteriorly, and curving at the posterior extremity to nearly envelop the terminal piece of the axis.

Genus *Encrinurella* Reed, 1915

Type species. *Pliomera insangensis* Reed, 1906.

Encrinurella ?reedi Legg, 1976

Figure 6.21

?1976 *Encrinurella reedi* sp. nov.; Legg, p. 22, pl. 7, figs. 11–13, 15, 16, 18, 19.

Comments. Only one cranidium (CPC 33243) has been recovered (from locality 707/12) in the present collections. It is too poorly preserved to make any detailed comparison with the specimens described by Legg (1976, p. 22), but has a glabella that expands more strongly forward and has a more broadly curved anterior margin than the single enrolled specimen illustrated by Legg (1976, pl. 7 fig. 16). The assignment is therefore very tentative.

Order Asaphida Salter, 1864

Superfamily Asaphoidea Burmeister, 1843

?Family Asaphidae Burmeister, 1843

Indeterminate asaphid 1

Figure 7.1

Comments. This specimen is represented by a single incomplete enrolled individual (CPC 33249) found as float. It has been laterally compressed and is weathered, such that the right side of the cephalon and thorax are missing and the pygidium is also missing. The axial furrows are effaced; the eyes are large; the preglabellar area is short (sag., exsag.); the librigena is narrow (tr.) and steeply inclined; and the genal angle is broadly rounded. This species is similar in many respects to *Fitzroyaspis irritans* Fortey & Shergold (1984) from the Nora Formation of the Georgina Basin and to a similar species from the Horn Valley Siltstone of the Amadeus Basin (Laurie unpublished data). However, the present species lacks the well-defined cephalic border of these other two species.

Indeterminate asaphid 2

Figures 7.4–7.5, 7.7–7.8

Material. One partial cranidium (CPC 33252); a partial librigena (CPC 33254); a partial pygidium (CPC 33253) doubtfully associated; and a hypostome (CPC 33255). All from locality 707/12.

Comments. Several asaphid fragments were obtained from locality 707/12 and are here tentatively grouped together for no other reason than their co-occurrence. The partial cranidium and librigena probably come from the same species insofar as they have a characteristic extremely rearwardly located eye, and the cranidium has a very short (tr.) prong-like posterior limb of the fixigena. The occipital furrow is effaced, and the axial furrow seems to fade out anteriorly. The associated pygidium is unlike that expected for such an effaced cephalon, and may not belong to the same species.

Indeterminate asaphid 3

Figures 7.6, 7.9

Comments. This species is represented by a partial hypostome (CPC 33256) and a damaged and weathered pygidium (CPC 33257), both of which come from locality 707/10. These specimens may be conspecific with indeterminate asaphid 1, because they are also very similar to *Fitzroyaspis irritans* Fortey & Shergold (1984) and a similar species from the Amadeus Basin (Laurie unpublished data). The hypostome is very similar to that from the Amadeus form, from which it differs in having slightly longer posterior prolongations of the margin. The pygidium differs from that of the Amadeus Basin form in lacking a border, a feature which is always present if only weakly developed in the Amadeus form.

Indeterminate asaphid 4

Figures 7.10–7.15, 7.17–7.20

Material. Three cranidia from float, two of which are illustrated (CPC 33258, CPC 33263), one from locality 707/16 and one partly silicified from locality 707/17B; one hypostome (CPC 33264) from float and one silicified (CPC 33267) from locality 707/17A; three librigenae, two of which are illustrated (CPC 33259, CPC 33260), from locality 707/16 and two silicified librigenae from localities 707/17A (CPC 33266) and 707/17B (CPC 33265); two pygidia from locality 707/16 (CPC 33261, CPC 33262).

Comments. This is perhaps the best understood of the Gap Creek asaphids insofar as it is represented by the most specimens, some of which are partly silicified. The species is represented by several cranidia, many librigenae, two

Figure 7 (facing page). 1a–c, indeterminate asaphid 1: enrolled specimen with deeply weathered posterior thorax and pygidium; dorsal, anterior, and lateral views respectively, x4, CPC 33249, float. 2–3, indeterminate ?hystricurid 2: 2, ventral surface of librigena, x4, CPC 33250, from loc. 707/12; 3, dorsal surface of librigena, x7, CPC 33251, from loc. 707/16; 4–5, 7–8, indeterminate asaphid 2, all from loc. 707/12: 4, posterior part of cranidium, x1, CPC 33252; 5, fragmentary pygidium, x4, CPC 33253; 7, partial librigena, x4, CPC 33254; 8, hypostome, x1.5, CPC 33255. 6, 9, indeterminate asaphid 3, both from loc. 707/10: 6, partial hypostome, x1, CPC 33256; 9, damaged and weathered pygidium, x3, CPC 33257. 10–15, 17–20, indeterminate asaphid 4: 10, posterior part of cranidium, x6, CPC 33258, from float; 11, ventral surface of librigena, x4, CPC 33259, from loc. 707/16; 12, partial librigena, x4, CPC 33260, from loc. 707/16; 13, small (meraspid?) pygidium with thoracic segment attached, x8, CPC 33261, from loc. 707/16; 14, small (meraspid?) pygidium with thoracic segment attached, x9, CPC 33262, from loc. 707/16; 15a–b, small weathered cranidium in dorsal and oblique lateral views respectively, x6, CPC 33263, from float; 17, partial hypostome, x2, CPC 33264, from float; 18, stereo pair of partly silicified librigena, x4, CPC 33265, from locality 707/17B; 19, silicified fragment of librigena, x2, CPC 33266, from loc. 707/17A; 20, stereo pair of silicified hypostome, x2, CPC 33267, from loc. 707/17A. 16, indeterminate ?asaphid 5: internal mould of pygidium, x2, CPC 33268, from loc. 707/10.

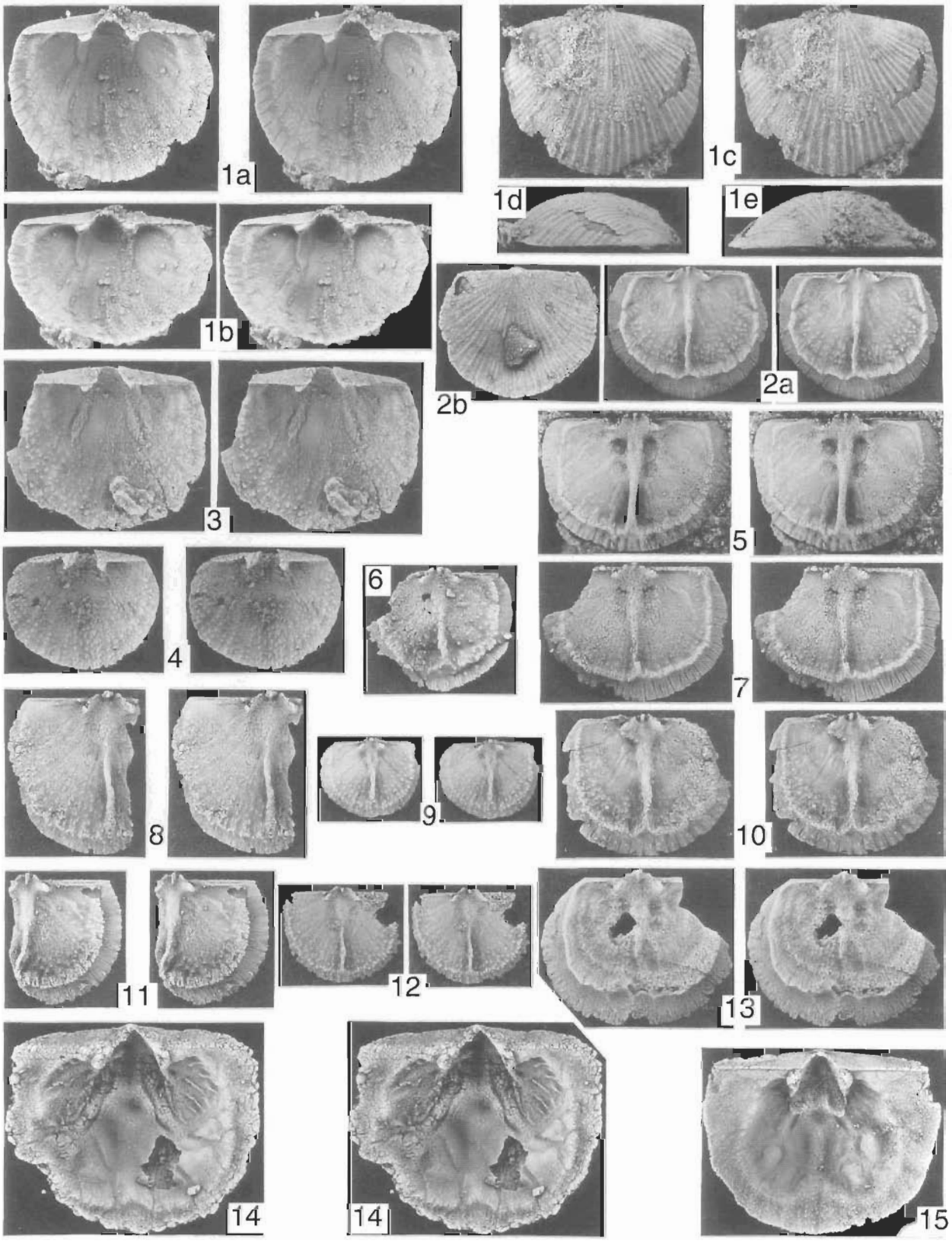

Figure 8. 1–13, *Tinopena shergoldi* gen. et sp. nov., all x4, all stereo pairs except figs. 1d, 1e, 2b, and 6, all from loc. 707/21: 1a–e, well-preserved paratype ventral valve, interior, interior oblique, exterior, lateral, and posterior views respectively, CPC 33269; 2a–b, well-preserved paratype dorsal valve, interior and exterior view respectively, CPC 33270; 3, paratype ventral interior, CPC 33271; 4, paratype small ventral interior, CPC 33272; 5, holotype dorsal interior, CPC 33273; 6, paratype dorsal interior, CPC 33274; 7, paratype dorsal interior, CPC 33275; 8, paratype partial dorsal interior, CPC 33276; 9, paratype small dorsal interior, CPC 33277; 10, paratype dorsal interior, CPC 33278; 11, paratype partial dorsal interior, CPC 33279; 12, paratype small dorsal interior, CPC 33280; 13, paratype (gerontic?) dorsal interior with median ridge broken off, CPC 33281. 14–15, *Spanodonta hoskingiae* Prendergast, 1935, both x3, both from loc. 707/21: 14, stereo pair of ventral interior showing mantle canal systems, CPC 33282; 15, ventral interior showing mantle canal systems, CPC 33283.

hypostomes, and two small pygidia. The glabella is very strongly constricted at about the level of the eyes, but expands strongly forward such that its widest point is near its anterior extremity. Its anterior margin is evenly and broadly rounded and steeply inclined towards the narrow cephalic border. The posterior limbs of the fixigenae are short (exsag.). The eyes are large, and the librigenal field convex and laterally bounded by a flattened border. The genal angle is produced into a large spine.

The hypostome is typically asaphine. It has a short (sag.) ovate middle body, at the posterolateral extremities of which are located two transverse ridge-like maculae. The posterior border notch is deep (sag.) and wide (tr.), and the prolongations occupy nearly half the total length of the hypostome. The pygidia available are quite small and have a wide unsegmented axis, a convex, smooth pleural field, and a wide flattened border.

This species has a combination of characters which makes it difficult to interpret. It has a cranidium with the constricted, anteriorly expanded glabella and narrow (tr.) anterior fixigenae similar to *Asaphus* and closely related genera. Similarly, the hypostome is unusual in being similar in dimensions to that of *Lycophron*, but different in character, insofar as it possesses a small but clearly defined middle body.

Indeterminate ?asaphid 5

Figure 7.16

Comments. This specimen, from locality 707/10, is represented by a single pygidium (CPC 33268) which may belong to an asaphid species.

Phylum Brachiopoda Duméril, 1806

Class Calciata Popov, Bassett, Holmer & Laurie, 1993

Order Orthida Schuchert & Cooper, 1932

Suborder Orthidina Schuchert & Cooper, 1932

Family Plectorthidae Schuchert & LeVene, 1929

Genus *Pseudomimella* Xu & Liu, 1984

Type species. *Mimella formosa* Wang, 1955.

?Pseudomimella sp.

Figures 10.3–10.5, 11.2

Material. One complete, unsilicified, weathered specimen (CPC 33290) found in float; and two silicified partial dorsal valves (CPC 33287, CPC 33289) and a partly silicified fragmentary ventral valve (CPC 33288) all from locality 707/17B.

Comments. Xu & Liu (1984) distinguished *Pseudomimella* from *Mimella* by its smaller ventral muscle field and the considerable difference in the arrangement of both ventral and dorsal mantle canal systems. Although the Gap Creek specimens exhibit little of their mantle canal systems, the single associated fragmentary ventral valve seems to have a rather small ovate muscle field, unlike that characteristic of species assigned to *Mimella* Cooper. For this reason the Gap Creek specimens are tentatively assigned to *Pseudomimella* Xu & Liu.

Genus *Oligorthis* Ulrich & Cooper, 1936

Type species. *Oligorthis arbucklensis* Ulrich & Cooper, 1936.

?Oligorthis sp.

Figure 10.6

Material. One nearly complete dorsal valve (CPC 33291) and several fragmentary specimens, all from locality 707/21.

Comments. This species is represented by several, mostly fragmentary dorsal valves, one of which is illustrated. It is a small brachiopod with a multicostellate ornament, a well-developed sulcus in the dorsal valve, well-developed brachiophore bases which converge onto a low broad median ridge, well-developed small fulcral plates, and a short broad quadripartite adductor field whose anterior scars are separated from the posterior ones by narrow oblique ridges. The cardinal process is developed as a very low blade.

Genus *Tritoechia* Ulrich & Cooper, 1936

Type species. *Deltatreta typica* Schuchert & Cooper, 1932.

Tritoechia sp.

Figures 10.1–10.2

Material. One nearly complete ventral valve (CPC 33285) from locality 707/17B; and several nearly complete small dorsal valves, one of which is illustrated (CPC 33286), and several fragmentary small ventral valves from locality 707/21.

Comments. This species is represented by only one large, nearly complete silicified ventral valve, several small dorsal valves, and many fragmentary specimens. It is similar in general proportions to the type species, but possesses a weak ventral sulcus and lacks the hollow costellae of the latter.

Family Taffiidae Schuchert & Cooper, 1931

Comments. Cocks & Rong (1989) included several subfamilies within the Taffiidae, but their scheme is not followed here for reasons outlined by Laurie (1991, pp. 52 and 62). This family therefore includes the genera *Taffia* Ulrich, *Aporthophyla* Ulrich & Cooper, *Aporthophylina* Liu, *Spanodonta* Prendergast [=*Archambona* Cooper], and the new genus *Tinopena*, which is described below.

Genus *Spanodonta* Prendergast 1935

[=*Archambona* Cooper, 1988]

Type species. *Spanodonta hoskingiae* Prendergast 1935.

Comments. The reasons for assigning *Spanodonta* to the Taffiidae and for including *Archambona* in its synonymy are explained by Laurie (1987) and Laurie & Burrett (1992).

Spanodonta hoskingiae Prendergast 1935

Figures 8.14–8.15, 9, 11.3

1935 *Spanodonta hoskingiae* Prendergast, p. 13, pl. 3, figs. 1–3.

1987 *Spanodonta hoskingae* (sic) Prendergast; Laurie, p. 44, figs. 2–4.

1989 *Spanodonta hoskingiae* Prendergast; Cocks & Rong, p. 98, figs. 36–40.

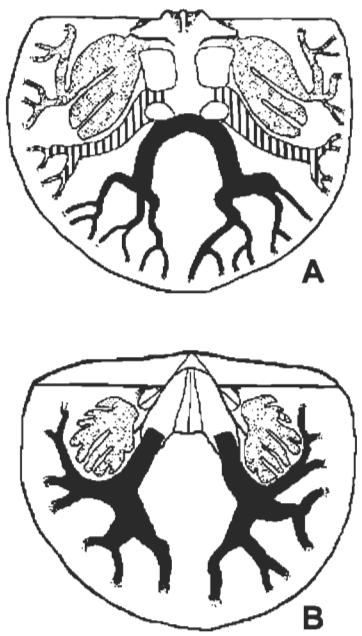

Figure 9. Interpretation of mantle canal systems of dorsal (A) and ventral (B) valves of *Spanodonta hoskingiae* Prendergast, 1935. In both valves the vascula media are black, the vascula genitalia stippled, and in the dorsal valve the vascula myaria are ornamented with parallel lines.

1992 *Spanodonta hoskingiae* Prendergast; Laurie & Burrett, pp. 16–17 (no description).

Material. Several unsilicified complete specimens, one of which is illustrated (CPC 33284), all from float; many unsilicified specimens from localities 707/10, 707/12, and 707/16; several hundred silicified specimens from localities 707/17A, 707/17B and 707/21, of which two (CPC 33282, CPC 33283) from this last locality are illustrated.

Comments. Details are much as described by Laurie (1987), but some specimens which are better preserved than most allow further details of the mantle canal systems to be discerned. One specimen, although somewhat damaged, shows the ventral mantle canal system in detail. A reconstruction of the saccate ventral mantle canal system based on this and one other specimen is shown in Figure 9. The reconstruction of the lemniscate dorsal mantle canal system is included in Figure 9 for the sake of completeness, and was obtained almost entirely from specimens illustrated by Laurie (1987).

Genus *Tinopena* gen. nov.

Etymology. Random selection of letters; the accent is on the o: feminine.

Type species. *Tinopena shergoldi* sp. nov.

Diagnosis. Concavoconvex, subcircular to transversely ovate, parvicostellate. Ventral interarea orthocline to apsacline; delthyrium with apical pseudodeltidium. Dorsal interarea catacline. Chilidium completely covering notothyrium.

Ventral muscle field subcordate, diductor scars extending beyond but not enclosing triangular adductor field. Teeth with narrow shelf-like fossettes, dental plates receding. Subperipheral rim present.

Cardinal process bladelike to knob-shaped. Socket ridges short. Subperipheral rim well developed, usually undercut. Posterior dorsal adductor scars ovate, larger than subcircular anterior pair. Median ridge narrow, extending to subperipheral rim.

Comments. Despite the lack of knowledge of details of the musculature and mantle canal systems in *Taffia*, this genus is assigned to the Taffiidae because the morphology of its ventral and dorsal musculature, dorsal cardinalia, and mantle canal system is consistent with a close relationship to other genera, such as *Aporthophyla* and *Spanodonta*, commonly assigned to that family.

In most respects, *Tinopena* is very similar to *Spanodonta*, with which it occurs. However, it differs in being only slightly more than half the dimensions of the latter, and in having a thinner shell and a consequently shorter trail in the dorsal valve. *Spanodonta* also lacks the well-defined narrow dorsal median ridge so characteristic of *Tinopena*.

Aporthophyla is similar to *Tinopena* in the arrangement of the mantle canal systems and musculature, general shell shape, and valve thickness, but is larger and lacks the dorsal median ridge.

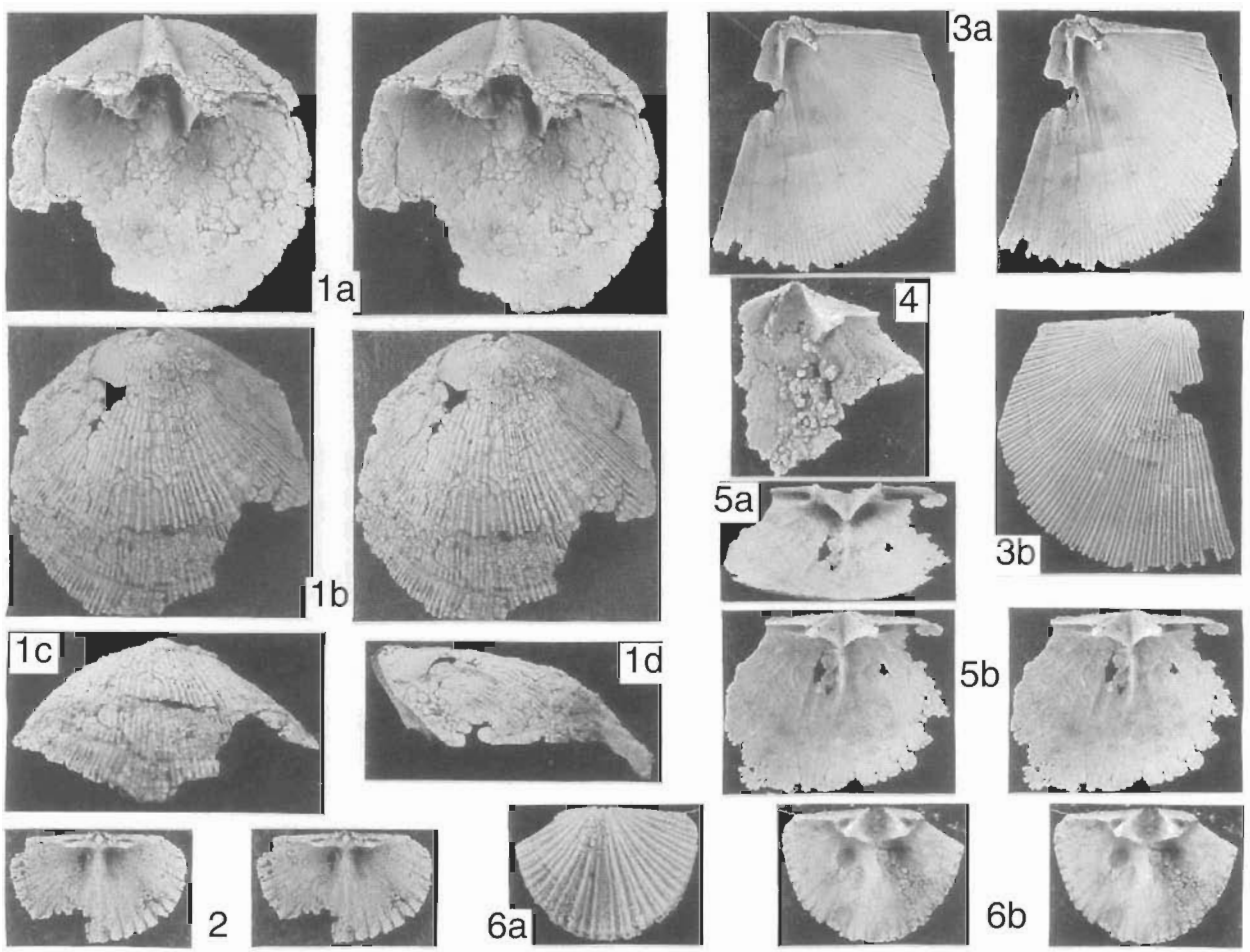

Figure 10. 1–2. *Tritoechia* **sp.: 1a–d, ventral valve, stereo pair of interior, stereo pair of exterior, anterior, and lateral views respectively, x3, CPC 33285, from loc. 707/17B; 2, stereo pair of small dorsal valve, x6, CPC 33286, from loc. 707/21. 3–5,** *?Pseudomimella* **sp., all from loc. 707/17B: 3a–b, partial dorsal valve, stereo pair of interior and exterior views respectively, x3, CPC 33287; 4, interior of fragmentary ventral valve, x6, CPC 33288; 5a–b, partial dorsal valve, oblique interior view and stereo pair of interior in normal view respectively, x3, CPC 33289. 6a–b,** *?Oligorthis* **sp.: dorsal valve, exterior and stereo pair of interior respectively, x6, CPC 33291, from loc. 707/21.**

Aporthophylina Liu is also reported to possess a dorsal median ridge, but from Liu's (1976, pl. 2, fig. 12) illustration it appears to be a much broader structure than the narrow blade-like dorsal median ridge in *Tinopena*. *Aporthophylina* also has subparallel ventral vascula media, unlike those of *Tinopena*, which are strongly divergent anteriorly.

Tinopena shergoldi sp. nov.

Figures 8.1–8.13

Etymology. After Dr J.H. Shergold, for his work on the Canning Basin Ordovician

Material. About 50 silicified specimens, all from locality 707/21, of which thirteen are illustrated (CPC 33269–33281)

Description. Concavoconvex, transversely ovate, ventral valve 83% as long as wide; dorsal valve 79% as long as wide. Maximum width at or behind midlength of valve; hinge width about 81% maximum width. Ornament parvicostellate; costellae on dorsal valve fine and poorly defined, on ventral valve they are broader and more clearly defined, with about 10 per 5 mm at the anterior margin. Ventral interarea planar, orthocline to apsacline, about 11% as high as wide. Delthyrium with broad, convex, apical pseudodeltidium. Dorsal interarea planar, low, catacline. Chilidium broad, convex, completely covering notothyrium.

Ventral muscle field subcordate, extending about one-third of the distance to the anterior valve margin; narrow diductor scars extend beyond but do not enclose the broad triangular adductor field. Vascula media diverge anteriorly from each other at about 40°. Remainder of vascular system obscure. Teeth moderately large, and have narrow shelf-like fossettes, dental plates receding, and low ridge-like extensions laterally bounding muscle field. Subperipheral rim present laterally, fading out anteriorly.

Cardinal process well developed, posteriorly directed, ranging from bladelike to knob-shaped, posteriorly ankylosed to chilidium. Socket ridges short, diverging anteriorly from one another at about right-angles, anteriorly bounding triangular rearward-opening sockets. Subperipheral rim well developed, usually undercut; in some specimens forming a low wall around visceral disc. Visceral disc large, planar. Dorsal adductor field commonly well defined, occupying 25% of valve width, and extending anteriorly about 43% of valve length. Posterior dorsal adductor scars longitudinally ovate, larger than anterior pair. Anterior scars subcircular, separated from posterior pair by low rounded transverse ridges. Median ridge broad posteriorly, narrowing towards anterior, extending to subperipheral rim as narrow blade, reaching maximum height anterior to dorsal adductor field. Dorsal mantle canal system with vascula media diverging anteriorly from the median ridge at about 20°; vascula myaria diverging anteriorly at about 50° from midline of valve. Remainder of vascular system obscure.

Comments. This species is uncommon at the type locality, and its juveniles can be distinguished from those of *Spanodonta hoskingiae* only by the presence of the characteristic dorsal median ridge.

Order Pentamerida Schuchert & Cooper, 1931

Suborder Syntrophiidina Ulrich & Cooper, 1936

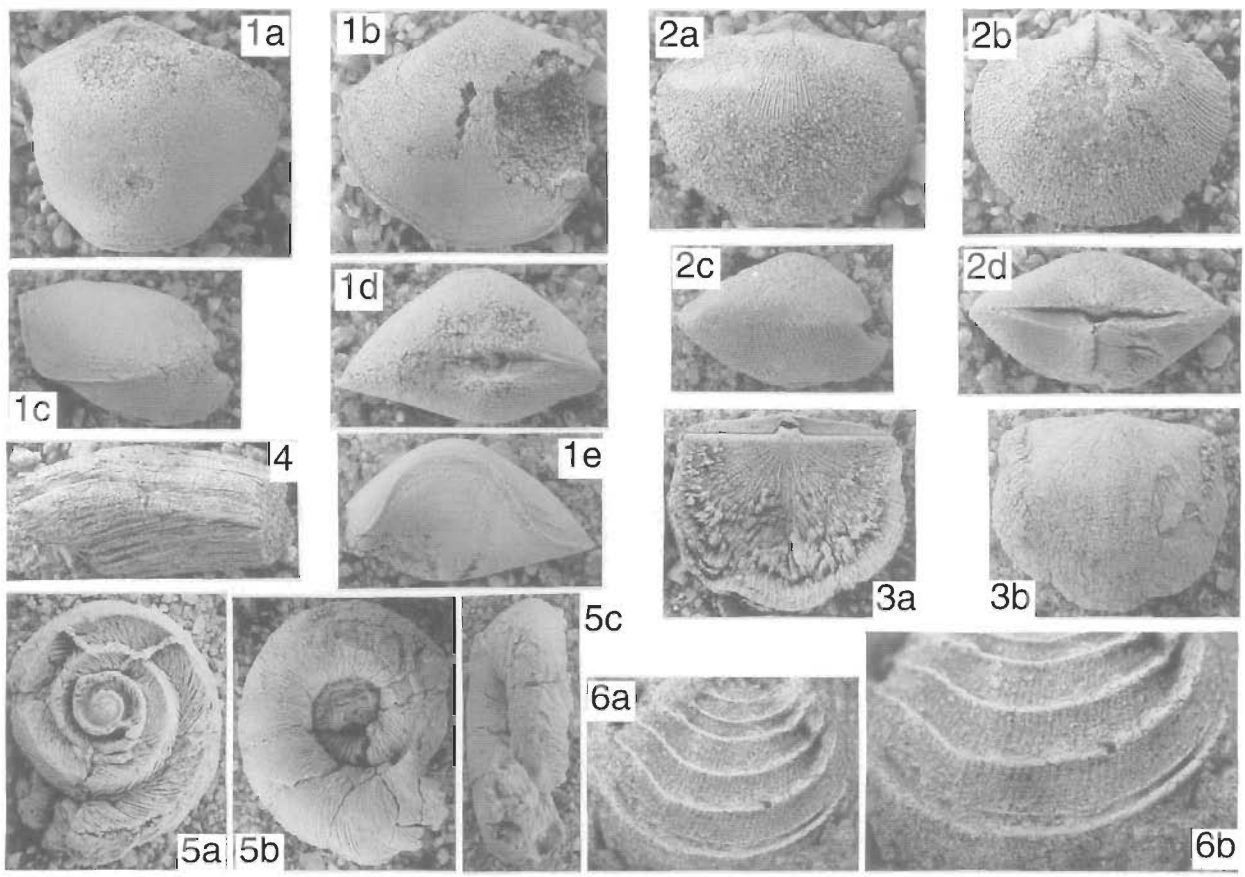

Figure 11. 1a–e, indeterminate syntrophiidine: complete but weathered unsilicified articulated specimen in dorsal, ventral, lateral, posterior, and anterior views respectively, x2, CPC 33292, from float. 2a–d, *?Pseudomimella* sp.: complete but weathered unsilicified articulated specimen in dorsal, ventral, lateral, and posterior views respectively, x2, CPC 33290, from float. 3a–b, *Spanodonta hoskingiae* Prendergast, 1935: complete unsilicified articulated specimen in dorsal and ventral views respectively, x2, CPC 33284, from float. 4, *Teiichispira* sp.: fragment of unsilicified operculum, x1.5, CPC 33293, from float. 5a–c, *Helicotoma* sp.: complete unsilicified shell, in apical, umbilical, and apertural views, x1, CPC 33294, from loc. 707/10. 6a–b, problematicum, nearly complete plate: 6a, entire specimen, x8; 6b, detail of distal portion showing ornament, x12. CPC 33295, from loc. 707/16.

Indeterminate syntrophiidine

Figure 11.1

Material. One unsilicified complete but weathered specimen (CPC 33292) found in float.

Comments. Only one reasonably well preserved unsilicified specimen is available; no silicified specimens have been found. This specimen is a typical Early Ordovician syntrophiidine: it is smooth and slightly transverse, and has a strongly plicate anterior commissure.

Phylum Mollusca

Class Gastropoda Cuvier, 1797

Order Archaeogastropoda Thiele, 1925

Suborder Macluritina Cox & Knight, 1960

Superfamily Macluritoidea Fischer, 1885

Family Macluritidae Fischer, 1885

Genus *Teiichispira* Yochelson & Jones, 1968

Type species. *Teiichispira kobayashi* Yochelson & Jones, 1968.

Teiichispira sp.

Figure 11.4

1973 *Teiichispira* sp. indet.; Gilbert-Tomlinson, p. 85, pl. 33, figs. 5, 10.

1993 *Teiichispira kobayashi* Yochelson & Jones; Yu, p. 446, figs. 4g–k.

Material. Several unsilicified specimens were obtained from float, one of which is illustrated (CPC 33293); many unsilicified specimens were found at localities 707/10, 707/12, and 707/16; many fragmentary specimens were also found silicified at localities 707/17A, 707/17B, and 707/21.

Comments. The opercula of this large macluritid gastropod are very common in the Gap Creek Formation. However, no detailed examination was attempted. The species is left under open nomenclature despite the opinion of Yu (1993) that it belongs to the type species. This is because, in his discussion of the specimens, he noted that they are different in size and possibly in shape (the phrasing is ambiguous) to the type species, but are possibly conspecific with *T. cornucopiae* Gilbert-Tomlinson (1973).

Family Helicotomidae Wenz, 1938

Genus *Helicotoma* Salter, 1859

Type species. *Helicotoma planulata* Salter, 1859.

Helicotoma sp.

Figure 11.5

Material. Two well-preserved specimens, one from float and one from locality 707/10. Only the latter is illustrated (CPC 33294).

Comments. Compared with the Pulau Langgun species of *Helicotoma* (Kobayashi 1959), this specimen has a lower rate of increase in whorl diameter.

Phylum Problematicum

Figure 11.6

Material. Several dozen specimens, all from locality 707/16, only one of which is illustrated (CPC 33295).

Comments. These ridged plates were at first thought to be fragmentary bivalves or gastropods, but they occur in both dextral and sinistral versions, are uniform in shape, essentially planar and the distance between the concentric ridges is quite variable. It is considered most likely that they are either conchostracan valves or machaeridian plates.

Acknowledgments

I thank the following Australian Geological Survey Organisation colleagues: Dr R.S. Nicoll for his conodont determinations, for assistance in the field, for many useful discussions, and for his constructive criticism of the manuscript; Drs J.H. Shergold and P.J. Jones for many useful discussions and their constructive criticisms of the manuscript; Messrs R.W. Brown and C. Thun for assistance in the field; and Mr H.M. Doyle for assistance with preparation and photography. I also thank Associate Professor B.D. Webby (Macquarie University) and Dr I.G. Percival (Geological Survey of NSW) for facilitating examination of the Warris Collection from western New South Wales, and also Dr A.T. Nielsen (Copenhagen University) for constructive criticism of the manuscript.

References

Ahlberg, P., 1992. Agnostid trilobites from the Lower Ordovician of southern Sweden. Transactions of the Royal Society of Edinburgh: Earth Sciences, 83, 539–570.

Cocks, L.R.M. & Rong Jiayu, 1989. Classification and review of the brachiopod superfamily Plectambonitacea. Bulletin of the British Museum (Natural History), Geology, 45(1), 77–163.

Cooper, G.A., 1988. A new genus of Plectambonitacea (Brachiopoda) from Malaysia. New Mexico Bureau of Mines and Mineral Resources, Memoir 44, 185–187.

Cooper, R.A. & Fortey, R.A., 1982. The Ordovician graptolites of Spitsbergen. Bulletin of the British Museum (Natural History), Geology, 36(3), 157–302, pls. 1–6.

Fortey, R.A., 1974. A new pelagic trilobite from the Ordovician of Spitsbergen, Ireland and Utah. Palaeontology, 17(1), 111–124, pls. 13–14.

Fortey, R.A., 1975. The Ordovician trilobites of Spitsbergen. II. Asaphidae, Nileidae, Raphiophoridae and Telephinidae of the Valhallfonna Formation. Norsk Polarinstitut Skrifter, 162, 207 pp.

Fortey, R.A., 1980. The Ordovician trilobites of Spitsbergen. III. Remaining trilobites from the Valhallfonna Formation. Norsk Polarinstitut Skrifter, 171, 163 pp.

Fortey, R.A. & Shergold, J.H., 1984. Early Ordovician trilobites, Nora Formation, central Australia. Palaeontology, 27(2), 315–366.

Gilbert–Tomlinson, J., 1973. The Lower Ordovician gastropod *Teiichispira* in northern Australia. Bureau of Mineral Resources, Australia, Bulletin 126, 65–88, pls. 29–34.

Guppy, D.G., Lindner, A.W., Rattigan, J.H. & Casey, J.N., 1958. The geology of the Fitzroy Basin, Western Australia. Bureau of Mineral Resources, Australia, Bulletin 36, 116 pp.

Guppy, D.G. & Öpik, A.A., 1950. Discovery of Ordovician rocks, Kimberley Division, W.A. Australian Journal of Science, 12, 205–206.

Henderson, R.A., 1983. Early Ordovician faunas from the Mount Windsor Subprovince, northeastern Queensland. Memoirs of the Association of Australasian Palaeontologists, 1, 145–175.

Hill, D., Playford, G. & Woods, J.T., 1969. Ordovician and Silurian fossils of Queensland. Queensland Palaeontographical Society, Brisbane, 32 pp.

Hintze, L. F., 1952. Lower Ordovician trilobites from western Utah and eastern Nevada. Utah Geological and Mineralogical Survey, Bulletin 48, 249 pp.

Hintze, L. F., 1973. Lower and Middle Ordovician stratigraphic sections in the Ibex area, Millard County, Utah. Brigham Young University, Geology Studies, 20(4), 3–36.

Holub, K., 1912. Doplňky ku fauně Eulomového horizontu v okolí Rokycan. Rozpravy České Akademie Ved, Tr.2, 21/33, 1–12.

Jell, P.A. & Stait, B., 1985. Revision of the Early Arenig

trilobite faunule from the Caroline Creek Sandstone, near Latrobe, Tasmania. Memoirs of the Museum of Victoria, 46, 35–51.

Kennard, J.M., Jackson, M.J., Romine, K.K., Shaw, R.D. & Southgate, P.N., 1994. Depositional sequences and associated petroleum systems of the Canning Basin, WA. In: Purcell, P.G & Purcell, R.R. (Editors), The sedimentary basins of Western Australia. Proceedings of the Petroleum Exploration Society of Australia Symposium, Perth, 1994, 657–676.

Kobayashi, T., 1959. On some Ordovician fossils from northern Malaya and her adjacence. Journal of the Faculty of Science, University of Tokyo, Section 2, 11, 387–407, pls. 24–27.

Laurie, J.R., 1987. A re-assessment of the brachiopod genus *Spanodonta* Prendergast from the Lower Ordovician of Western Australia. Alcheringa, 11, 43–49.

Laurie, J.R., 1991. Articulate brachiopods from the Ordovician and Lower Silurian of Tasmania. Memoir of the Association of Australasian Palaeontologists, 11, 1–106.

Laurie, J.R. & Burrett, C.F., 1992. Biogeographic significance of Ordovician brachiopods from Thailand and Malaysia. Journal of Paleontology, 66(1), 16–23.

Laurie, J.R. & Shergold, J.H., 1996. Early Ordovician trilobite fauna of the Emanuel Formation, Canning Basin, Western Australia. Part 1. Palaeontographica Abteilung A, 240, 65–103, pls. 7–21.

Laurie, J.R. & Shergold, J.H., in press. Early Ordovician trilobite fauna of the Emanuel Formation, Canning Basin, Western Australia. Part 2. Palaeontographica Abteilung A.

Legg, D.P., 1973. Ordovician stratigraphy and palaeontology (Trilobita, Graptolithina), Canning Basin, Western Australia. Ph.D. Thesis, University of Western Australia (unpublished).

Legg, D.P., 1976. Ordovician trilobites and graptolites from the Canning Basin, Western Australia. Geologica et Palaeontologica, 10, 1–58.

Legg, D.P., 1978. Ordovician biostratigraphy of the Canning Basin, Western Australia. Alcheringa, 2, 321–334.

Liu Diyong, 1976. Ordovician brachiopods from the Mount Jolmo Lungma region. Report of the Scientific Expedition to the Mount Jolmo Lungma Region (1966–1968), Palaeontology 2, 139–155, pl. 1–2. (in Chinese).

McTavish, R.A., 1973. Prioniodontacean conodonts from the Emanuel Formation (Lower Ordovician) of Western Australia. Geologica et Palaeontologica, 7, 27–58.

Nicoll, R.S., Laurie, J.R. & Roche, M.T., 1993. Revised stratigraphy of the Ordovician (late Tremadoc–Arenig) Prices Creek Group and Devonian Poulton Formation, Lennard Shelf, Canning Basin, Western Australia. AGSO Journal of Australian Geology & Geophysics, 14, 65–76.

Palfreyman, W.D., 1984. Guide to the geology of Australia. Bureau of Mineral Resources, Australia, Bulletin 181, 1–111.

Pek, I., 1977. Agnostid trilobites of the central Bohemian Ordovician. Sborník geologickych věd, paleontologie 19, 7–44, pls. 1–12.

Prendergast, K.L., 1935. Some Western Australian Upper Palaeozoic fossils. Journal and Proceedings of the Royal Society of Western Australia, 21, 9–35.

Ride, W.D.L., Sabrosky, C.W., Bernardi, G. & Melville, R.V. (Editors), 1985. International Code of Zoological Nomenclature, 3rd Edition. University of California Press, Berkeley, 338 pp.

Ross, R.J., 1951. Stratigraphy of the Garden City Formation in northeastern Utah, and its trilobite faunas. Peabody Museum of Natural History, Yale University, Bulletin 6, 161 pp.

Ross, R.J. & 27 others, 1982. The Ordovician System in the United States. International Union of Geological Sciences, Publication 12, 1–73.

Ross, R.J., Hintze, L.F., Ethington, R.L., Miller, J.F., Taylor, M.E. & Repetski, J.E., 1993. The Ibexian Series (Lower Ordovician) a replacement for "Canadian Series" in North American chronostratigraphy. United States Geological Survey, Open File Report 93–598.

Shergold, J.H., 1971. Resume of data on the base of the Ordovician in northern and central Australia. Mémoire de la Bureau de Recherches Géologique et Mineralogique, 73, 391–402.

Shergold, J.H., Laurie, J.R. & Nicoll, R.S., 1995. Correlation of selected late Lancefieldian–Bendigonian (Early Ordovician) successions. In: Cooper, J.D., Droser, M.L. & Finney, S.C. (Editors), Ordovician Odyssey: short papers for the Seventh International Symposium on the Ordovician System Las Vegas, Nevada, USA. SEPM, Pacific Section, 89–92

Warris, B.J.S., 1967. The Stratigraphy and Palaeontology of North Western New South Wales. Ph.D. Thesis, University of Sydney (unpublished).

Webby, B.D, VandenBerg, A.H.M., Cooper, R.A., Banks, M.R., Burrett, C.F., Henderson, R.A., Clarkson, P.D., Hughes, C.P., Laurie, J.R., Stait, B.A., Thomson, M.R.A. & Webers, G.F., 1981. The Ordovician System in Australia, New Zealand and Antarctica. International Union of Geological Sciences, Publication 6, 64 pp.

Xu Hankui & Liu Diyong, 1984. Late Lower Ordovician brachiopods of southwestern China. Bulletin of the Nanjing Institute of Geology and Palaeontology, 8, 147–235, pls. 1–18.

Yochelson, E.L. & Jones, C.R., 1968. *Teiichispira*, a new Early Ordovician gastropod genus. United States Geological Survey, Professional Paper 613B, 1–13.

Young, G.E., 1973. An Ordovician (Arenigian) trilobite faunule of great diversity from the Ibex area, western Utah. Brigham Young University, Geology Studies, 20(4), 91–115.

Yu Wen, 1993. Early Ordovician gastropods from the Canning Basin, Western Australia. Records of the Western Australian Museum, 16, 437–458.

Appendix 1: Index of figured specimens

CPC number	*Classification*	*Illustration*	*Horizon*
Geragnostus aff. *splendens* (Holub, 1912)			
33223	Figured specimen	Fig. 5.1	707/16
33224	ditto	Fig. 5.2	707/float
33225	ditto	Fig. 5.3	707/12
Carolinites ?genacinaca Ross, 1951			
33226	ditto	Fig. 5.4	707/16
33227	ditto	Fig. 5.5	707/16
Opipeuter angularis (Young, 1973)			
33228	ditto	Fig. 5.6a–c	707/12
33229	ditto	Fig. 5.10a–c	707/12
Opipeuter ?inconnivus Fortey, 1974			
33230	ditto	Fig. 5.7a–b	707/16
33231	ditto	Fig. 5.8	707/16
33232	ditto	Fig. 5.9	707/16
Canningella hardmani Legg, 1976			
33233	ditto	Fig. 5.11	707/float
33234	ditto	Fig. 5.12	707/16
33235	ditto	Fig. 5.13a–b	707/float
33236	ditto	Fig. 5.14a–b	707/float
33237	ditto	Fig. 5.15	707/float
33238	ditto	Fig. 5.16	707/float

33239	ditto	Fig. 5.17	707/12
33240	ditto	Fig. 5.18	707/16
33241	ditto	Fig. 5.19	707/16
33242	ditto	Fig. 5.20a–b	707/16
Encrinurella ?reedi Legg, 1976			
33243	ditto	Fig. 5.21	707/12
Indeterminate ?hystricurid 1			
33244	ditto	Fig. 5.22 left	707/12
33245	ditto	Fig. 5.22 right	707/12
33246	ditto	Fig. 5.23	707/float
33247	ditto	Fig. 5.24	707/12
33248	ditto	Fig. 5.25	707/12
Indeterminate asaphid 1			
33249	ditto	Fig. 6.1a–c	707/float
Indeterminate ?hystricurid 2			
33250	ditto	Fig. 6.2	707/12
33251	ditto	Fig. 6.3	707/16
Indeterminate asaphid 2			
33252	ditto	Fig. 6.4	707/12
33253	ditto	Fig. 6.5	707/12
33254	ditto	Fig. 6.7	707/12
33255	ditto	Fig. 6.8	707/12
Indeterminate asaphid 3			
33256	ditto	Fig. 6.6	707/10
33257	ditto	Fig. 6.9	707/10
Indeterminate asaphid 4			
33258	ditto	Fig. 6.10	707/float
33259	ditto	Fig. 6.11	707/16
33260	ditto	Fig. 6.12	707/16
33261	ditto	Fig. 6.13	707/16
33262	ditto	Fig. 6.14	707/16
33263	ditto	Fig. 6.15a–b	707/float
33264	ditto	Fig. 6.17	707/float
33265	ditto	Fig. 6.18	707/17B
33266	ditto	Fig. 6.19	707/17A
33267	ditto	Fig. 6.20	707/17A
Indeterminate ?asaphid 5			
33268	ditto	Fig. 6.16	707/10
Tinopena shergoldi gen. et sp. nov.			
33269	paratype	Fig. 7.1a–e	707/21
33270	paratype	Fig. 7.2a–b	707/21
33271	paratype	Fig. 7.3	707/21
33272	paratype	Fig. 7.4	707/21
33273	holotype	Fig. 7.5	707/21
33274	paratype	Fig. 7.6	707/21
33275	paratype	Fig. 7.7	707/21
33276	paratype	Fig. 7.8	707/21
33277	paratype	Fig. 7.9	707/21
33278	paratype	Fig. 7.10	707/21
33279	paratype	Fig. 7.11	707/21
33280	paratype	Fig. 7.12	707/21
33281	paratype	Fig. 7.13	707/21
Spanodonta hoskingiae Prendergast, 1935			
33282	figured specimen	Fig. 7.14	707/21
33283	ditto	Fig. 7.15	707/21
33284	figured specimen	Fig. 10.3a–b	707/float
Tritoechia sp.			
33285	figured specimen	Fig. 9.1a–d	707/17B
33286	figured specimen	Fig. 9.2	707/21
?Pseudomimella sp.			
33287	figured specimen	Fig. 9.3a–b	707/17B
33288	figured specimen	Fig. 9.4	707/17B
33289	figured specimen	Fig. 10.2a–d	707/float
?Oligorthis sp.			
33291	figured specimen	Fig. 9.6 a–b	707/21
Indeterminate syntrophiidine			
33292	figured specimen	Fig. 10.1a–e	707/float
Teiichispira sp.			
33293	figured specimen	Fig. 10.4	707/float
Helicotoma sp.			
33294	figured specimen	Fig. 10.5a–c	707/10
Problematicum			
33295	figured specimen	Fig. 10.6a–b	707/16

Appendix 2: Collections from the Gap Creek Formation

Section 707

707/10: indeterminate asaphid 3, indeterminate ?asaphid 5, *Spanodonta hoskingiae*, *?Pseudomimella* sp., *Helicotoma* sp., *Teiichispira* sp.

707/12: *Geragnostus* aff. *splendens*, *Opipeuter angularis*, *Canningella hardmani*, *Encrinurella ?reedi*, indeterminate asaphid 2, indeterminate ?hystricurid 1, indeterminate ?hystricurid 2, *Spanodonta hoskingiae*, *Teiichispira* sp.

707/16: *Geragnostus* aff. *splendens*, *Carolinites ?genacinaca*, *Opipeuter ?inconnivus*, *Canningella hardmani*, indeterminate asaphid 4, indeterminate ?hystricurid 1, *Spanodonta hoskingiae*, problematicum, *Teiichispira* sp., indeterminate gastropods

707/17A: indeterminate asaphid 4, *Spanodonta hoskingiae*, *Teiichispira* sp.

707/17B: indeterminate asaphid 4, *Spanodonta hoskingiae*, *Tritoechia* sp., *?Pseudomimella* sp. *Teiichispira* sp.

707/21: *Spanodonta hoskingiae*, *Tinopena shergoldi*, *Tritoechia* sp., *?Pseudomimella* sp., *?Oligorthis* sp., *Teiichispira* sp.

Section 708

708/10: indeterminate trilobite fragments, *Spanodonta hoskingiae*, *?Pseudomimella* sp., indeterminate gastropods

708/11: *Spanodonta hoskingiae*

708/48: indeterminate asaphid 4, *Spanodonta hoskingiae*, *?Pseudomimella* sp., *?Oligorthis* sp.

708/55: *Spanodonta hoskingiae*

708/60: *Spanodonta hoskingiae*, *Tinopena shergoldi*, *Tritoechia* sp., indeterminate plectambonitoidean, indeterminate trilobite

708/62: *Spanodonta hoskingiae*, *?Pseudomimella* sp., indeterminate trilobite

708/66: *Spanodonta hoskingiae*

708/75A: *Spanodonta hoskingiae*, *Tinopena shergoldi*

708/86B: *Tinopena shergoldi*.

708/98: *Tinopena shergoldi*, indeterminate gastropods

708/134: indeterminate gastropods

AGSO Journal of Australian Geology & Geophysics, 16(5), 717–730

A non-marine Lower Cretaceous rift-related epiclastic volcanic unit in southern Australia: the Eumeralla Formation in the Otway Basin. Part I: Lithostratigraphy and depositional environments

E. Anne Felton[1]

The Early Cretaceous non-marine volcaniclastic Eumeralla Formation accumulated in a rift basin on the southern margin of Australia during the break-up of eastern Gondwana. Wireline-log analysis and a range of sedimentary data have helped to discriminate three major basin-wide informal lithostratigraphic units in the formation. From the base of the formation they are: Eumeralla I: siltstone/mudstone/sandstone/coal; Eumeralla II: siltstone/mudstone/thin lithic sandstone; and Eumeralla III: volcaniclastic sandstone. A fourth unit — Eumeralla IV: siltstone/sandstone/coal — occurs throughout the western Otway Basin, but is absent, probably because of erosion, from the central and eastern parts of the basin. The bases of all four lithostratigraphic units are probably diachronous.

The succession of lithostratigraphic units Eumeralla I–IV is interpreted as representing coal swamps and flood plains of low-energy streams; shallow and deep freshwater lakes; channel tracts and flood plains of high-energy streams; and channel tracts, flood plains and coal swamps of low- energy streams respectively. Sedimentary facies analysis of outcropping Eumeralla II and Eumeralla III in the eastern Otway Basin confirms the interpretations for these units.

The basin-wide extent of the three lower lithostratigraphic units implies that a single integrated drainage system for the entire basin was established at the onset of Eumeralla Formation deposition, and persisted at least until the late Albian. This inference is supported by the close correlation between variations in lithology and depositional environments and the Aptian–Albian sea-level changes. However, intrabasinal volcanism significantly influenced sedimentation and was probably the primary control on basin drainage.

Introduction

The Eumeralla Formation, part of the Lower Cretaceous Otway Group, was deposited in a variety of non-marine environments in the Otway Basin, one of several extensional sedimentary basins which developed along the southern margin of Australia (Fig. 1) before and during the break-up of eastern Gondwana (Falvey 1974; Yu 1988). The formation overlies ?Upper Jurassic–Lower Cretaceous sedimentary and basaltic rocks deposited during an earlier rift phase in the basin, and pre-Mesozoic basement (Fig. 2). It occurs throughout the basin, mainly in the subsurface, where it has been intersected in more than 100 petroleum exploration wells (both onshore and offshore) and water-bores.

The only onshore outcrops of the Otway Group are in the Otway Ranges and Barrabool Hills near the eastern Otway Basin margin and in western Victoria (Fig. 3). Coastal exposures in the Otway Ranges along 100 km of shoreline southwest of Melbourne probably represent most of the upper 2000 m of the Eumeralla Formation (Felton 1992). The exposed thickness of the Otway Group in western Victoria is not known. Maximum thickness of the Eumeralla Formation is estimated at 3500 m (Gleadow & Duddy 1981; Megallaa 1986).

The formation has been described as mainly chloritic mudstone and shale with subordinate thinly bedded lithic sandstone and coal (Reynolds 1971; Morton 1986). However, coastal outcrops in the eastern Otway Basin consist principally of thick-bedded sandstone forming rugged cliffs up to 70 m high. The sandstone consists mainly of first-cycle epiclastic volcanic detritus of unknown provenance, and interbedded

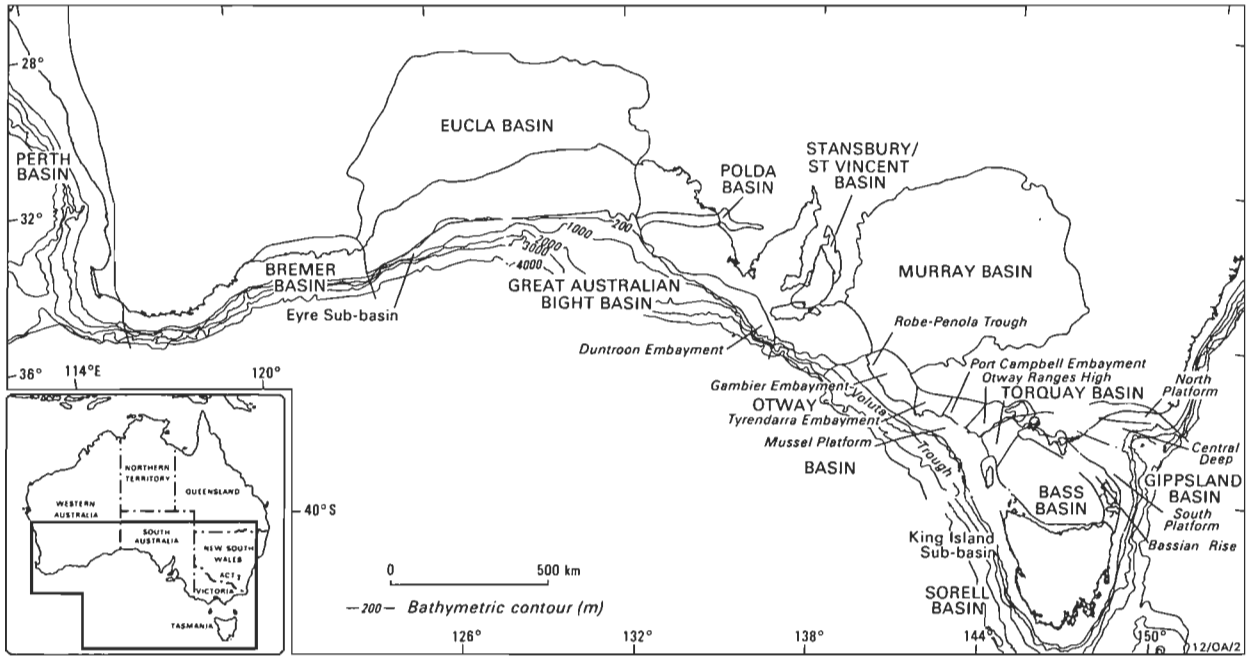

Figure 1. Location and regional setting of the Otway Basin (after Willcox & Stagg 1990).

[1] Department of Geology, The University of Wollongong, Wollongong, NSW, Australia; present address: SOEST Hawaii Institute of Geophysics and Planetology, University of Hawaii, 2525 Correa Road, Honolulu, HI 96822, USA.

AGE		STAGE	PALYNOLOGICAL ZONE (L. & basal U. Cret. only)	STRATIGRAPHIC NAME	
Tertiary		Miocene Oligocene		Heytesbury Group	
		Eocene Palaeocene		Wangerrip Group	
Cretaceous	Upper	Maastrichtian Campanian Santonian Coniacian Turonian Cenomanian	*A. distocarinatus*	Sherbrook Group	
	Lower	Albian	*P. pannosus*	Eumeralla Formation	Otway Group
			U.*C. paradoxa*		
			L.*C. paradoxa*		
			C. striatus	Windermere Sst Member	
		Aptian	U.*C. hughesi*		
			L.*C. hughesi*	Crayfish Subgroup	
		Barremian	*F. wonthaggiensis*		
		Neocomian	*C. australiensis*	Casterton Formation	
			?	?	
Jurassic	Upper				
Pre-Mesozoic				Basement	

Figure 2. Stratigraphy of the Otway Basin (after Morton 1990).

siltstone, minor conglomerate, mudstone, and coal. Finer-grained rock types predominate in the subsurface (Felton 1992). Prevailing opinion concerning the 'uniformity' or 'monotony' of the Eumeralla Formation (Edwards & Baker 1943; Reynolds 1971; Gleadow & Duddy 1981; Morton 1986) does not withstand detailed scrutiny from the perspectives of petrology (Duddy 1983; Felton 1992), depositional style (Duddy 1983; Felton 1989a, 1989b, 1992), or lithological variety (Felton 1992).

The character and evolution of Eumeralla Formation deposition in the basin is presented as a two-part paper. Part I, herein, describes the informal lithostratigraphic units and interpreted depositional environments which successively dominated sedimentation throughout the basin, and the sedimentology of lacustrine and fluvial deposits of parts of the sequence. Part II applies the geometry and relationships of sedimentary facies associations in the eastern Otway Basin to discriminate two discrete fluvial systems: an older proximal to medial alluvial fan and a younger braid plain to distal fan. Palaeocurrent directions of the fluvial systems indicate that the source(s) of the volcaniclastic sediment which dominates the Eumeralla Formation lay to the south and southeast of the present coast. Elevated Palaeozoic and Proterozoic basement blocks contributed non-volcanic quartz-lithic detritus locally.

Previous sedimentary studies

Early work in the Otway Basin mainly focused on establishing basin stratigraphy and regional correlations to assist with petroleum exploration. The stratigraphy erected in the late 1960s and early 1970s was based largely on contrasts in sandstone petrology. Changes in depositional facies were noted in several formations in the basin (James 1968; Eyles 1974), and their importance to regional correlation recognised (Morton 1986; 1990). From petroleum exploration drilling and seismic data, Kopsen & Scholefield (1990) and Morton (1986, 1990) presented depositional models for the lower Otway Group in the western Otway Basin (in South Australia). These models, based on seismic stratigraphic analysis and a limited study of sandstone provenance according to the methods of Dickinson & Suczek (1979), are continuing to evolve (Morton & Drexel 1995).

Published information on the Eumeralla Formation records few details of its sedimentary facies and depositional environments. The Otway Group, including the Eumeralla Formation, has been interpreted —mainly from macrofloral evidence — as reflecting deposition in a variety of fluvial and lacustrine environments (Douglas 1969; Dettmann 1986). Duddy (1983) described the character of Eumeralla Formation river channels as braided, and described palaeosols from their flood plains. Felton (1989b; 1992) also identified braided-stream systems in the Eumeralla Formation. Struckmeyer & Felton (1990) linked studies of organic and sedimentary facies to refine palaeoenvironmental interpretations in the Otway Group. Biomarker studies of hydrocarbons have suggested a variety of subenvironments in the lower parts of the Otway Group (Padley et al. 1995).

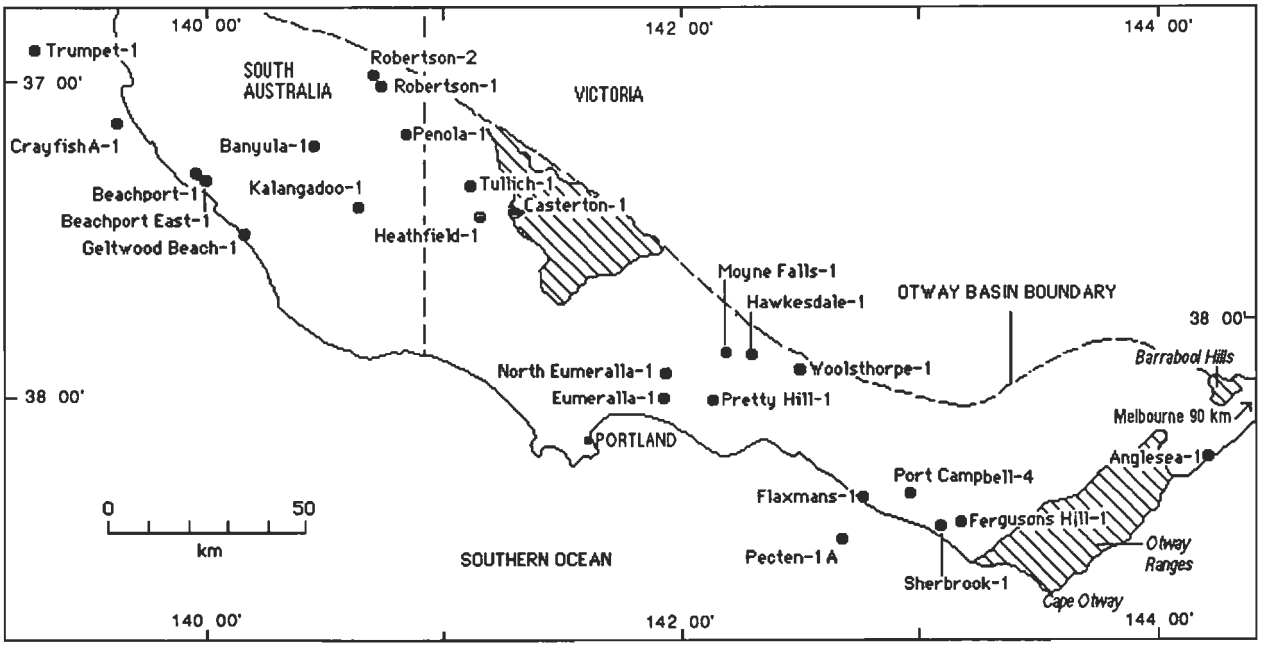

Figure 3. Otway Group outcrops (hachured) and petroleum exploration wells examined in this study.

Several authors have attempted to account for the source of the abundant volcanic detritus in the Eumeralla Formation. They have proposed both extra- and intrabasinal sources, such as Palaeozoic basement volcanics (Edwards & Baker 1943) and contemporaneous volcanic flows, despite the absence of primary volcanic rocks of Cretaceous age within or near the basin (Reynolds 1971). Applying fission-track dating of detrital apatite grains to a study of the thermal history of the basin, Gleadow & Duddy (1981) dated two pulses of Cretaceous volcanism and deposition at 126 and 106 Ma. They considered that this volcanism occurred within the basin. Duddy (1983) carried out comprehensive work on the petrology and geochemistry of the Eumeralla Formation, and mapped its burial metamorphic facies. Felton (1992), who also studied the petrology of Otway Basin sandstones, linked variations in Eumeralla Formation sandstone framework composition with palaeocurrent data, and with lithological and sedimentary facies changes, to present an argument for contemporaneous intrabasinal volcanism southwest to southeast of Cape Otway.

Methods and data

Selected wireline logs, cores, and cuttings from wells throughout the basin were used to identify associations of sedimentary rock types comprising distinct lithostratigraphic units, and to delineate their lateral and vertical distribution in the basin. Interpretation of the depositional environments represented by each unit relied on a range of sedimentary data derived mainly from cores and cuttings, supplemented by observations of age correlatives in outcrop, and of wireline-log characteristics.

A seismic-facies analysis was not included in this study because the quality of the older data is generally poor, particularly in the eastern onshore part of the basin, and recently acquired non-proprietary data are scant. The lack of structural control afforded by good-quality seismic data precluded construction of structurally correct regional cross-sections. Identification, description, and correlation of lithostratigraphic units may still proceed as presented here, but the relative thicknesses of the units across the basin may bear little relationship to original depositional thicknesses, even if compaction corrections are applied.

Twenty-five petroleum exploration wells, each penetrating a substantial thickness of the Otway Group and Casterton Formation, most with good palynological age control and reasonable wireline-log quality, were selected for study (Table 1). Digitised wireline-log data were unavailable for these wells, so self-potential (SP), gamma-ray, and resistivity logs for these wells were redrawn by hand and reduced to a common scale. These logs were selected from the range of wireline logs available for each well because they were considered to have the most value in contributing to lithological and facies interpretation.

Sedimentary rock types (sandstone, siltstone/mudstone, coal) in the wells were reinterpreted from the wireline logs, and checked against cores and cuttings, from which additional observations of composition, grainsize, fossils, and sedimentary structures were made. The rock types were closely cross-checked against their corresponding log responses, to ensure consistent interpretation of rock types in intervals poorly represented by core-and-cutting material.

Comparison of palynological ages with the lithostratigraphic boundaries interpreted during this study gives an indication of any diachroneity of the units. The apparent thicknesses of biostratigraphic zones in wells are affected by the structure, and cannot be used to calculate or infer relative rates of deposition. The palynological data recorded from wells, including those of Morgan (1985), relate to the zonation of Helby et al. (1987); however, recent changes to zonation (Morgan et al. 1995) affect the interval at the boundary of the Crayfish Subgroup and overlying Eumeralla Formation, and are discussed below. Changes to the apparent ages of lithostratigraphic units, while affecting assessments of their diachroneity, does not alter their spatial distribution or environmental interpretation.

The stratigraphic nomenclature in this paper is that proposed by Morton (1990). The recent elevation of the Crayfish Subgroup to group status (Morton et al. 1994) invalidates the term

Table 1. Otway Basin petroleum exploration wells selected for this study

West	*Northwest*	*Centre*	*East*
Trumpet 1	Banyula 1	North Eumeralla 1	Pecten 1A
Crayfish A1	Penola 1	Eumeralla 1	Flaxmans 1
Beachport 1	Robertson 1	Pretty Hill 1	Port Campbell 4
Beachport East 1	Robertson 2	Hawkesdale 1	Fergusons Hill 1
Kalangadoo 1	Tullich 1	Woolsthorpe 1	Sherbrook 1
Geltwood Beach 1	Heathfield 1	Moyne Falls 1	Anglesea 1
	Casterton 1		

Table 2. Key features of Eumeralla lithostratigraphic units

Lithofacies	*Distribution*	*Age and palynological zones*	*Relationships with other Eumeralla lithofacies*
Eumeralla IV			
Siltstone/sandstone/coal	Mainly west and northwest; may be present elsewhere	Albian (–?Cenomanian); upper *C. paradoxa–P. pannosus*	Overlies E III, its time equivalent in W and NW
Eumeralla III			
Volcaniclastic sandstone	Basin-wide; best developed in centre and E	Middle–late Albian; near base lower *C. paradoxa–P. pannnosus*	Overlies E II; overlain by E IV. Partial time equivalent of E II and E IV
Eumeralla II			
Siltstone/mudstone/thin lithic sandstone	Basin-wide	Late Aptian–early to mid-Albian; upper *P. notensis–C. striatus*; extends into upper *C. paradoxa* in W and NW	Overlies E I, overlain by E III; a time equivalent of both
Eumeralla I			
Siltstone/mudstone/sandstone/coal	Basin-wide; not recognised in Pecten 1A	?Late Barremian–Albian; ?upper *F. wonthaggiensis–C. striatus*	Overlain by E II. Overlies top Pretty Hill unconformity

Otway Group as a consequence. Morton et al. (1994) also suggested that the term Otway Supergroup would be inappropriate owing to the angular unconformity at the base of the Eumeralla Formation in the western Otway Basin. As stratigraphy and relationships within the Otway Group below the Eumeralla Formation in the central and eastern Otway Basin are uncertain, and no subgroups have been proposed for the 'Crayfish Group', the terms Crayfish Subgroup and Otway Group are retained here.

Lithostratigraphic units

During the lithological study, seven major lithostratigraphic units were recognised in the Otway Group and Casterton Formation — three within the section below the Eumeralla Formation. These lower units are not dealt with here. Three informal units comprising the Eumeralla Formation, termed Eumeralla I to III, can be correlated throughout the basin; a fourth unit, Eumeralla IV, is extensive in western and northwestern parts of the basin, but sparse in central and eastern parts, from which it has probably been removed by erosion (Figs. 4–7; Table 2).

Eumeralla I. Siltstone/mudstone/sandstone/coal

Description and interpretation

Siltstone is the main rock type, but mudstone, lithic (mainly volcaniclastic) fine-grained sandstone, and coal beds which in places contain much mineral matter (dull coal) are interbedded with it. In several wells in the northwest, the proportion of sandstone increases towards the top of Eumeralla I; in Heathfield 1 well the unit is sandy throughout.

This unit was probably deposited by low-energy meandering streams in one or more fluvial flood basins; coal swamps were common, and shallow ponds or lakes well developed. These depositional conditions appear to have prevailed throughout the basin.

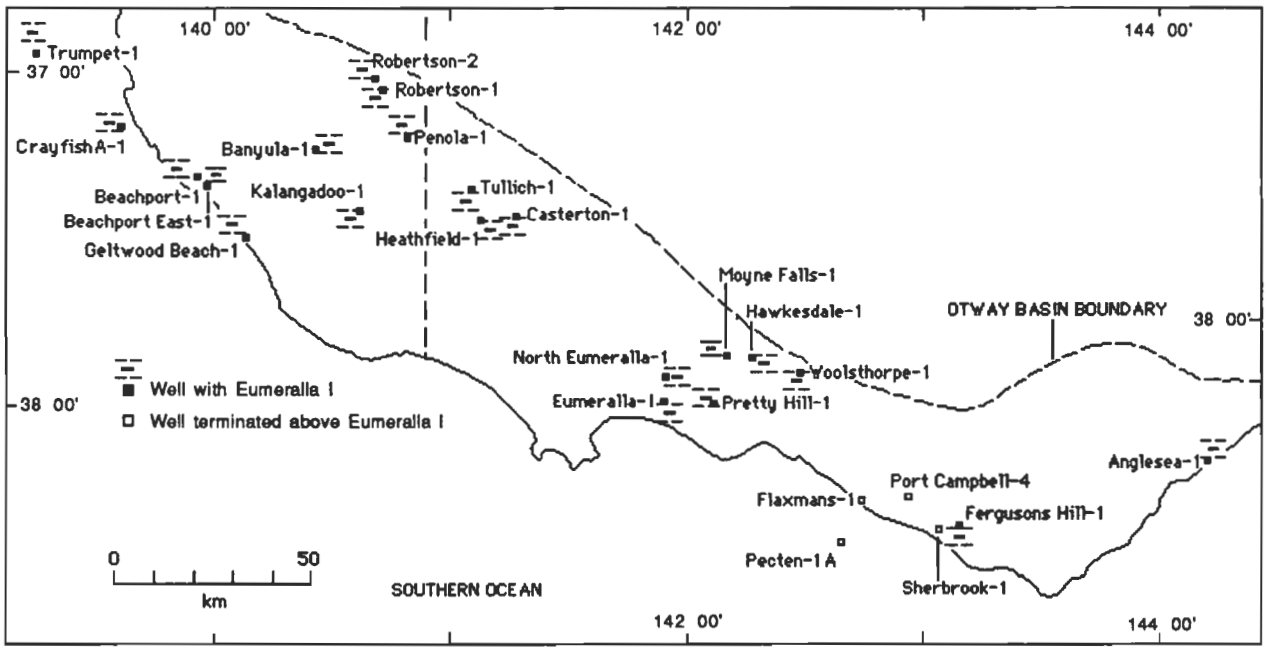

Figure 4. Distribution of Eumeralla I.

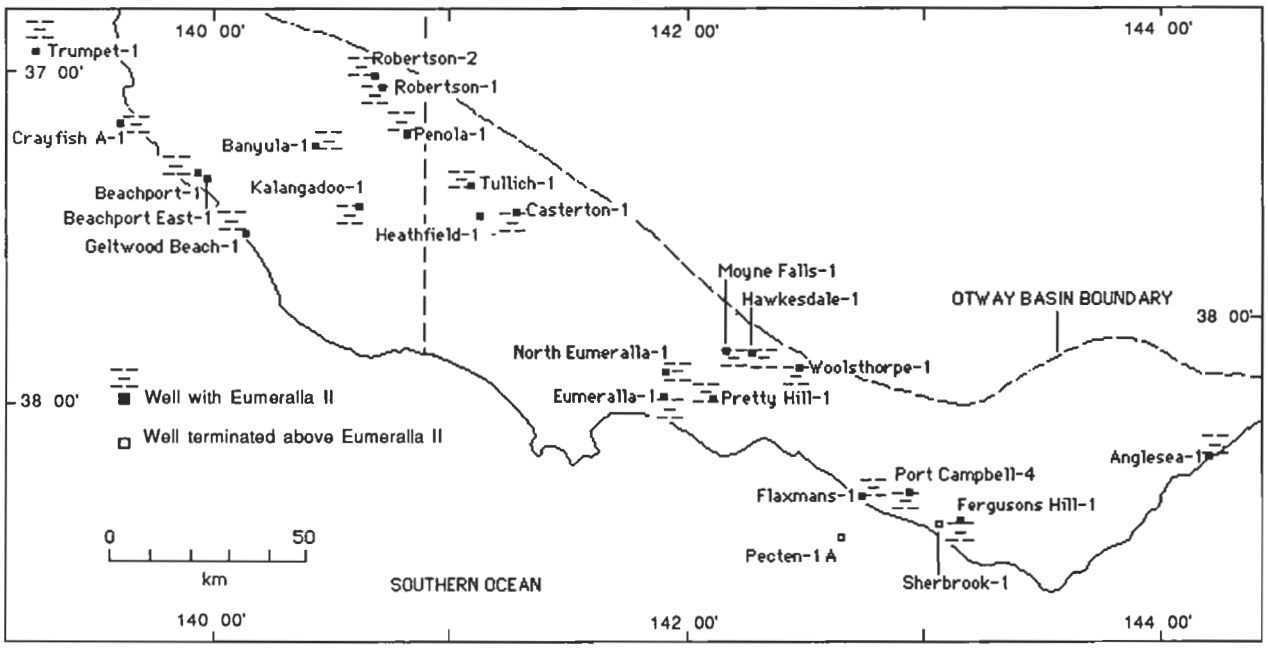

Figure 5. Distribution of Eumeralla II.

Coal beds are characteristic of Eumeralla I, but are absent from the lower part of the unit in the northwest, and in Hawkesdale 1, Woolsthorpe 1, and Moyne Falls 1 wells, near the central northern basin margin. A possible lacustrine environment is interpreted for the lower part of the unit in these areas, where lakes eventually filled with sediments and evolved into coal swamps more characteristic of Eumeralla I (Figs. 8, 9). Coaly facies are particularly well developed at the top of Eumeralla I in wells in the centre.

Discussion

The base of Eumeralla I appears to correspond to the seismic unconformity recognised by Rochow (1971) and Williamson et al. (1990; their 'top Pretty Hill' seismic horizon) at the base of the Eumeralla Formation. The base of Eumeralla I is therefore interpreted as the base of the Eumeralla Formation.

Felton (1992) suggested that the base of Eumeralla I (i.e., the Eumeralla Formation) might be diachronous. However, Morgan et al. (1995) considered that the base of the Eumeralla Formation lies at the base of their lower *P. notensis* Zone and is synchronous in at least the western (South Australian) part of the Otway Basin. Different ranges have been reported for *P. notensis* (Morgan et al. 1995), so the question of diachroneity remains unresolved (cf. Figs. 8 and 9).

Tupper et al. (1993) recognised a siltstone/mudstone/coal sequence in the lower Eumeralla Formation in wells on the Chama Terrace, in the western Otway Basin. Oils in the central-eastern Otway Basin are probably sourced from Eumeralla Formation peat swamp environments (Padley et al. 1995) which may be part of Eumeralla I.

A basal Eumeralla I sandstone corresponding to the Windermere Sandstone Member of the Eumeralla Formation (Morton 1990) has not been recognised in the wells studied.

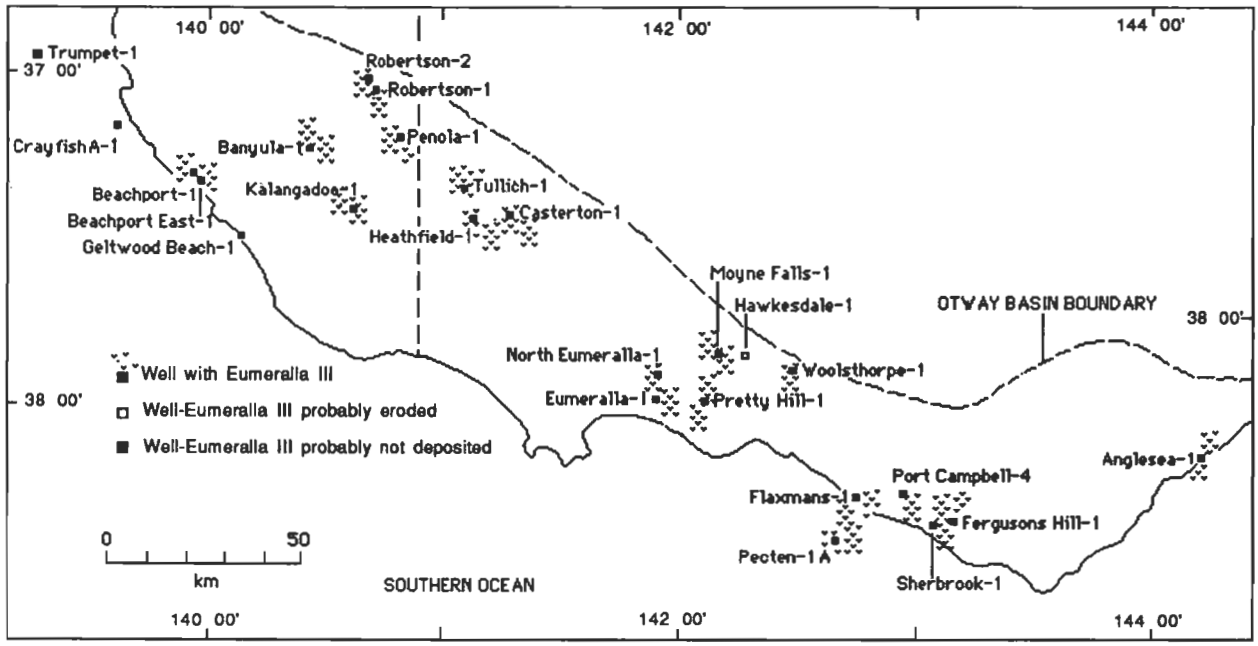

Figure 6. Distribution of Eumeralla III.

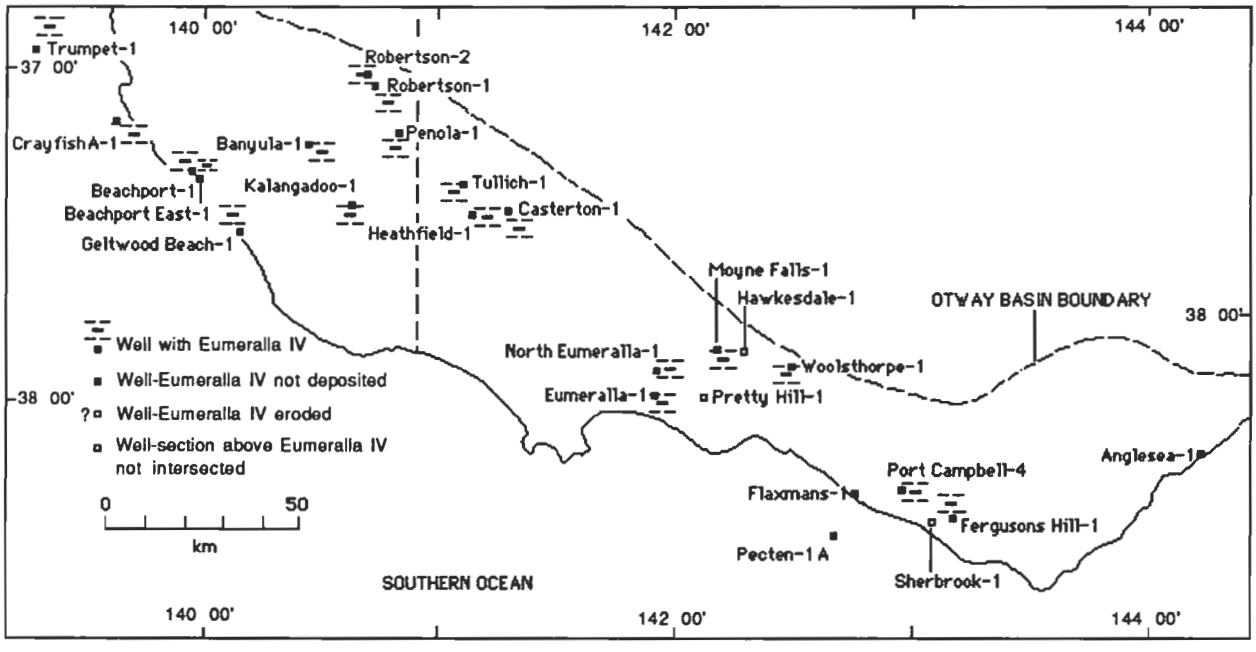

Figure 7. Distribution of Eumeralla IV.

Eumeralla II. Siltstone/mudstone/thin lithic sandstone

Description and interpretation

Eumeralla II consists mainly of fine-grained sedimentary rocks (siltstone and mudstone). Thin fine- to very fine-grained lithic (volcaniclastic) sandstone beds are common to abundant. Lack of abundant coal distinguishes Eumeralla II from Eumeralla I.

Eumeralla II is developed throughout the Otway Basin. It is interpreted as mainly lacustrine in origin. In a study of organic and sedimentary facies in the basin, Struckmeyer & Felton (1988, 1990) correlated an organic facies characteristic of a deep-freshwater lacustrine origin with this unit. Freshwater lakes succeeded and drowned the coal swamps of Eumeralla I over most of the basin.

A mainly fine-grained clastic section exposed in a road-cutting in the eastern Otway Basin has been interpreted as lacustrine in part (Felton 1992), and probably corresponds in part to Eumeralla II. The sedimentology of the cutting is described below.

Discussion

The base of Eumeralla II may be diachronous: it appears to lie within the *C. hughesi* Zone in the northwest (Robertson 1, ?Robertson 2, Tullich 1, and Casterton 1) and parts of the central area (Pretty Hill 1, Hawkesdale 1, ?Woolsthorpe 1, and possibly Moyne Falls 1), whereas elsewhere it lies at the base of or within the *C. striatus* Zone.

Eumeralla II is not recognised in Heathfield 1, in which a mainly siltstone unit containing several coal beds correlated with the *C. hughesi* Zone is interpreted as Eumeralla I.

Eumeralla III. Volcaniclastic sandstone

Description and interpretation

Eumeralla III consists mainly of fine- to coarse-grained volcaniclastic sandstone, and subordinate interbedded volcaniclastic siltstone and minor conglomerate containing intraclasts and/or exotic clasts. Its thickest and coarsest development is in the east, notably on- and offshore southwest of Cape Otway. Sandstone bodies in Pecten 1A and Fergusons Hill 1 are interpreted from wireline logs to be up to 60 m thick, but are mostly less than 25 m thick and separated by siltstone a few metres thick in other wells in the east. Gamma-ray-log signatures of these sandstones have a blocky character, defined by sharp flat bases and inclined tops, which indicate gradational fining upwards of the sandstone bodies. Blocky gamma-ray-log signatures of non-marine sequences are commonly interpreted as braided-stream-channel sandstones (Selley 1988).

Outcropping sandstone and siltstone in the eastern Otway Basin are considered to be part of Eumeralla III because they are similar in sandstone thickness and grainsize, incidence of siltstone partings, and age to Eumeralla III in the subsurface in nearby wells. These rocks are interpreted from their sedimentary facies as the deposits of high-energy braided fluvial channels and their adjacent flood plains (see below and part II of this paper).

The sandstone:siltstone ratio in the east is 80:20. Although the ratio is lower elsewhere, a change from siltstone- to sandstone-dominated deposition is apparent throughout most of the basin, and defines the Eumeralla II–Eumeralla III boundary. In the west and northwest, a marked increase in sand deposition corresponds to the base of the unit elsewhere

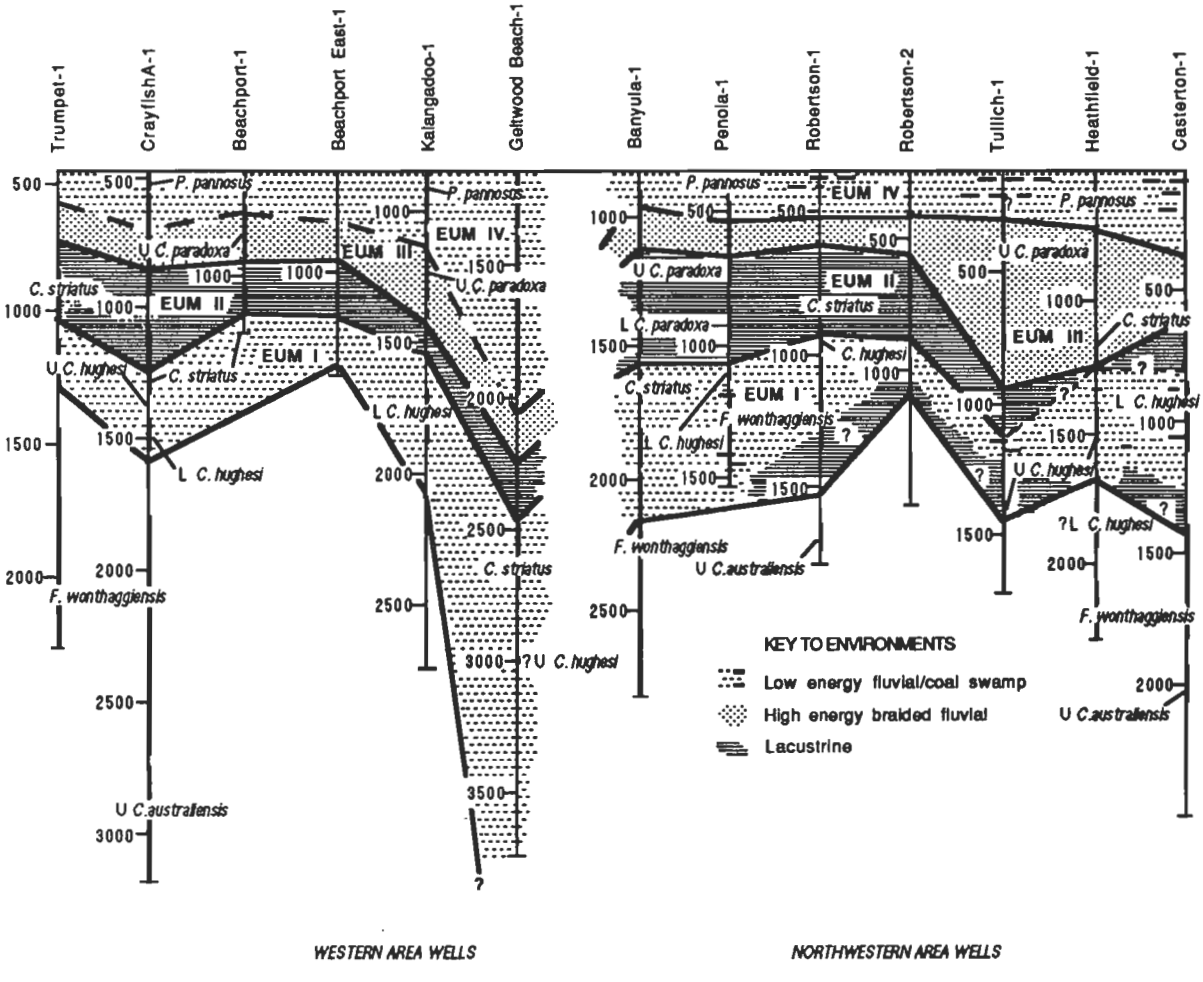

Figure 8. Time–space plot of Eumeralla lithostratigraphic unit correlation and depositional environments in the western and northwestern Otway Basin (modified from Felton 1992).

(Felton 1992). Even so, the sandstone:siltstone ratio in these areas is less than 40:60, a feature that could be applied to discriminating a lithostratigraphic unit correlative with but distinct from Eumeralla III.

Discussion

Eumeralla III marks a substantial change in the prevailing depositional regime from low-energy stream systems and large freshwater lakes to high-energy streams which transported large amounts of sand. The dominance of contemporaneous medium-grained volcanic detritus in the sand, and the spread of sand-dominated sediment throughout the basin apparently from southeast to northwest, (Figs. 8, 9) are indications either that major volcanic eruptive activity began, that its locus changed, or that dormant or extinct volcanic terrains were newly uplifted. The base of Eumeralla III is a major sequence boundary within the Eumeralla Formation.

Volcanic eruptions and/or uplift of volcanic source areas were accompanied by rejuvenation of drainage in the basin. Rain and/or snow precipitation might have increased, or the pattern of precipitation changed, as a consequence of the rapid growth of large active volcanoes. Tectonic and eruptive activity, with or without increased precipitation, would account for both the rapid erosion and redeposition of loosely consolidated volcanic products and high-energy stream flow in the newly established drainage systems.

The very thick sandstones in Pecten 1A and Fergusons Hill 1, and their coarse to medium grainsize, relative to other areas of the basin (Felton 1992) may indicate that this area lies closest to a volcanic sediment source. The character and palaeocurrent directions of correlative Otway Group outcrops near Cape Otway support this interpretation (see part II of this paper).

From palynological evidence, the base of this unit is probably diachronous. It lies close to the *C. striatus*–lower *C. paradoxa* Zone boundary in the centre and east, and near the base of the upper *C. paradoxa* Zone in many wells in the west and northwest. This observation is consistent with the spread of sandy volcaniclastic sediment through the basin from sources in the southeast. The pick of the base of Eumeralla III in Heathfield 1 is difficult in the overall sandy sequence that it intersected. As the base of Eumeralla III is no lower than the *C. striatus*–lower *C. paradoxa* Zone boundary elsewhere in the basin, the pick at the base of the *C. striatus* Zone in Heathfield 1 (Fig. 8) may be too low.

Eumeralla IV. Siltstone/sandstone/coal

Description and interpretation

Eumeralla IV consists largely of siltstone. Subordinate sandstone is volcaniclastic, thinner, and finer than in the underlying Eumeralla III. The siltstone lacks distinctive gamma-ray- and SP-log signatures, but its lower electrical response helps distinguish it from the sandstone. In general, although the sandstone in Eumeralla IV is similar in composition and grainsize to the siltstone, it shows up distinctly on the SP logs as sharp kicks to the left (e.g., Heathfield 1).

Coal beds are present in Robertson 1, Casterton 1, and Tullich 1 — all located near the northern margin of the basin. Coal beds, fragments of which are evident in well-cutting samples, may be indicated on the resistivity log by sharp kicks to the right, but, in 'dirty' coals (i.e., containing much mineral matter) characteristic of the Otway Group (e.g., table 7.6 of

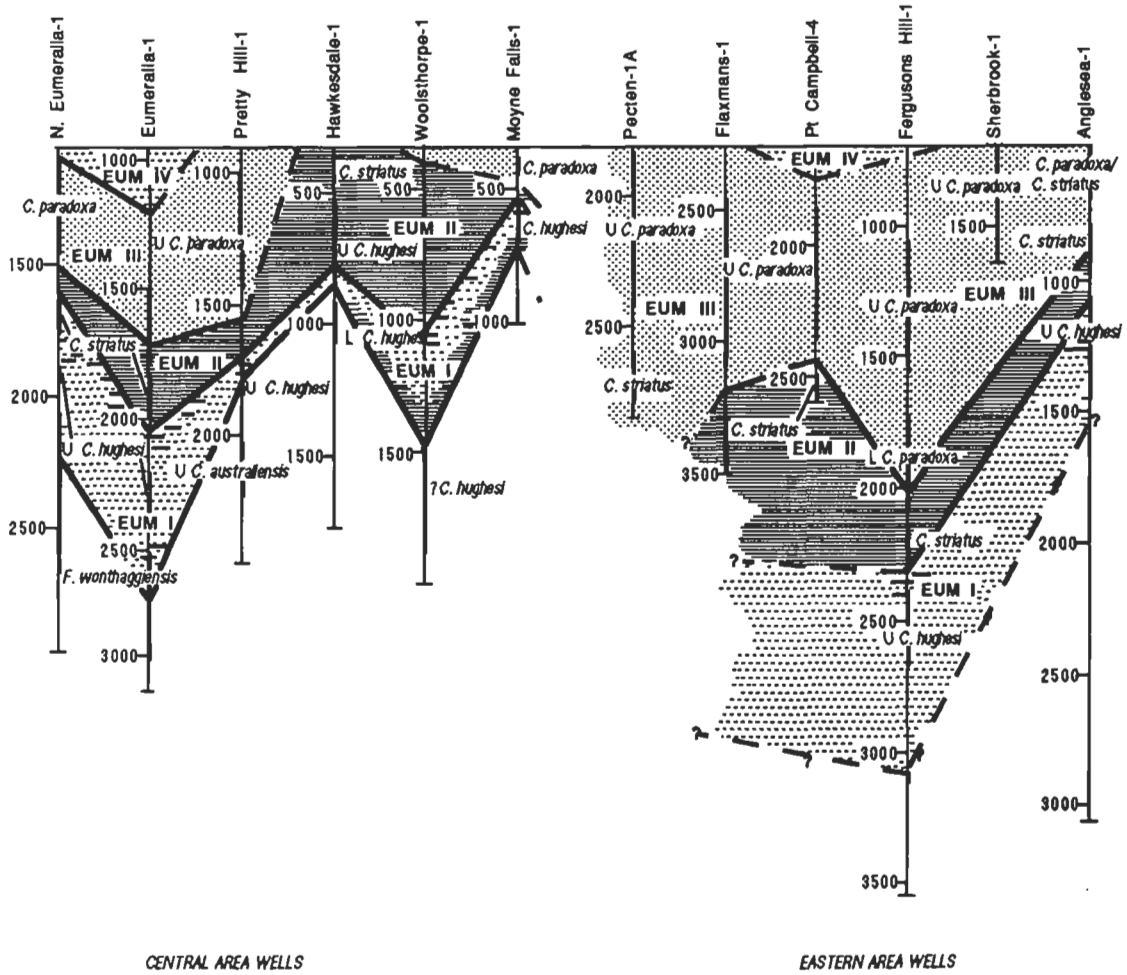

Figure 9. Time–space plot of Eumeralla lithostratigraphic unit correlation and depositional environments in the central and eastern Otway Basin (modified from Felton 1992). The pattern symbols are explained in Figure 8.

Kenley 1976), this log response is commonly suppressed.

Eumeralla IV is absent from most wells in the centre and east (Figs. 7, 9). Its presence in Port Campbell 4 and Fergusons Hill 1 is equivocal. Some wells in these areas were collared in the Eumeralla Formation below this unit. Others were collared in the Upper Cretaceous marine sequence overlying the formation below Eumeralla IV, whose absence is probably due to erosion before the younger sediments were deposited.

Eumeralla IV represents flood-plain, lake, and local coal-swamp environments with low-gradient meandering streams.

Discussion

The change from high- to low-energy depositional conditions is thought to result from a diminution of the sediment supply, and a loss of flow competence in streams draining volcanic sources as active volcanism waned, volcanic edifices subsided, and erosion further reduced elevation of the source areas. Basin drainage systems also might have been truncated by rising base levels due to rising sea level or tectonic subsidence, causing drainage to pond and favouring mainly fine-grained sedimentation.

Sedimentology of Eumeralla II and III in outcrop

Methods

Fresh natural and man-made exposures include sections up to several hundred metres parallel and transverse to depositional strike along the coast in the eastern Otway Basin. The depositional data for a number of long profiles, including details of inaccessible cliff outcrops examined with binoculars, were superimposed onto photographs. A number of vertical profiles were logged in detail to supplement the long profiles. Although vertical profiles are limited in their usefulness when characterising fluvial styles (Miall 1985), they are a convenient means of summarising the scales and relative abundances of sedimentary facies, and may have particular value for comparison with the subsurface. The vertical profiles presented here (and located in Fig. 10) are representative of the range of facies in Eumeralla II and III in the eastern Otway Basin.

The sedimentary facies recognised in outcrop can be grouped into a number of genetically distinct facies associations, described in part II. The relationships and thicknesses of facies associations compared for different parts of Eumeralla II and III outcrops in the eastern Otway Basin, and integrated with other sedimentary data, provide the basis for interpreting and characterising at least two local fluvial systems in the outcrop area.

Outcrop descriptions

Eumeralla II

Skenes Creek Road vertical profiles. Three vertical profiles recorded in Skenes Creek Road summarise the evolution of a 270-m coarsening-upwards section which is interpreted as a flood-plain and lake sequence recording fluctuating water levels in a flood-basin lake (profiles SCR1 and 2; Figs. 11–14), and gradual filling of the lake and migration of a fluvial channel across its flood plain (profile SCR3; Fig. 12). Higher in the section (not illustrated), lacustrine silty mudstone succeeds the fluvial interval, and a lake-beach sandstone is apparent (Felton 1992).

Most coal seams in the profiles are enclosed by lacustrine deposits (laminated and thinly bedded siltstone, mudstone, and fine to very fine sandstone), have no associated seat earths, and may be allochthonous.

Seat earths underlie some of the coal beds in the Skenes Creek Road section. One, at the top of unit 6 in profile SCR1 (Fig. 11), is 40 cm thick and forms the upper part of a discrete fining-upwards sequence capped by a thin coal bed. Units 7–9 in profile SCR 2 (Fig. 12) are similar but lack a well-developed seat earth. Such sequences are interpreted as the fill of abandoned lacustrine delta-distributary channels in which ponded water lay. Ponds eventually filled with fine sediments; buried vegetation formed thin coal beds.

Eumeralla III

Cat Reef vertical profile. A vertical profile at Cat Reef records aggradation and abandonment (units 1–11; Fig. 15) of a broad channel tract in which fining-upwards sheet sand accumulated repeatedly over intraclast gravel-filled scour hollows (bases of units 3 and 4, Fig. 15) in the bases of channels. Clasts range from boulders (1 m in diameter) to granules (Fig. 16). The cobble to granule size fraction consists of a mixture of intraclast siltstone and dark, altered glassy volcanic rocks. The boulders are intraclasts of (1) plane- and cross-bedded sandstone and (2) sandy conglomerate whose clasts are similar in size and composition to the cobble and granule fraction of the host conglomerate.

Sedimentary structures in the channel-tract sandstone are dominated by plane-bedding; minor backset cross-bedding and low-angle bedding indicate high-stage flows (Figs. 15, 16). Ripple and climbing-ripple laminations occur near the tops of

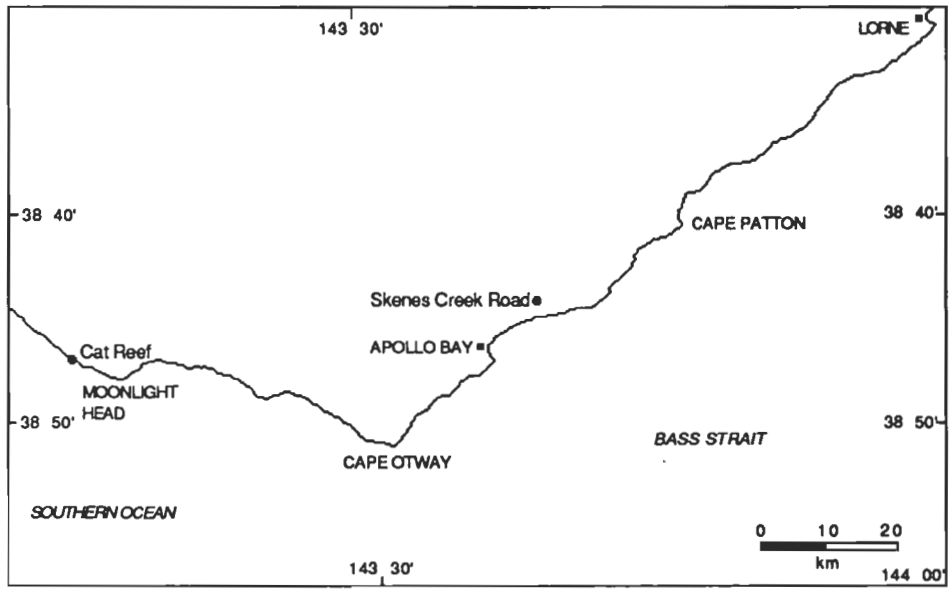

Figure 10. Outcrop locations, eastern Otway Basin (after Felton 1992).

thick multistorey sandstones as sandy beds pass upwards into finer-grained sediments (e.g., Figs. 15). Palaeocurrent directions in the sheet sandstone vary, but have an overall northwesterly to northeasterly trend.

The channel tract was abandoned a number of times, sometimes long enough for soils to develop and plants to grow (Figs. 15, 17). Much of the fine-grained part of the section is interpreted as suspension fall-out from turbid floodwater entering a flood-plain pond.

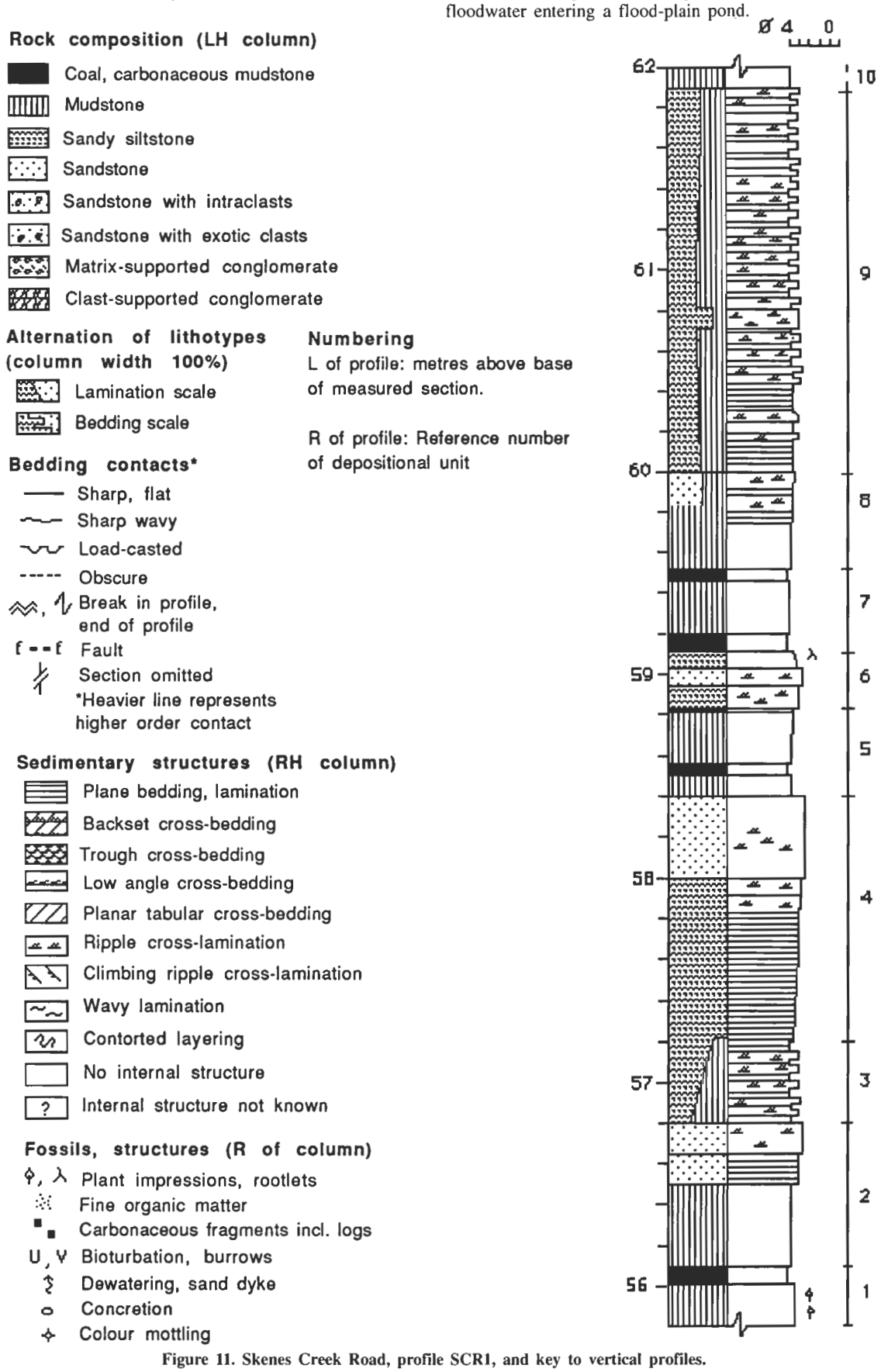

Figure 11. Skenes Creek Road, profile SCR1, and key to vertical profiles.

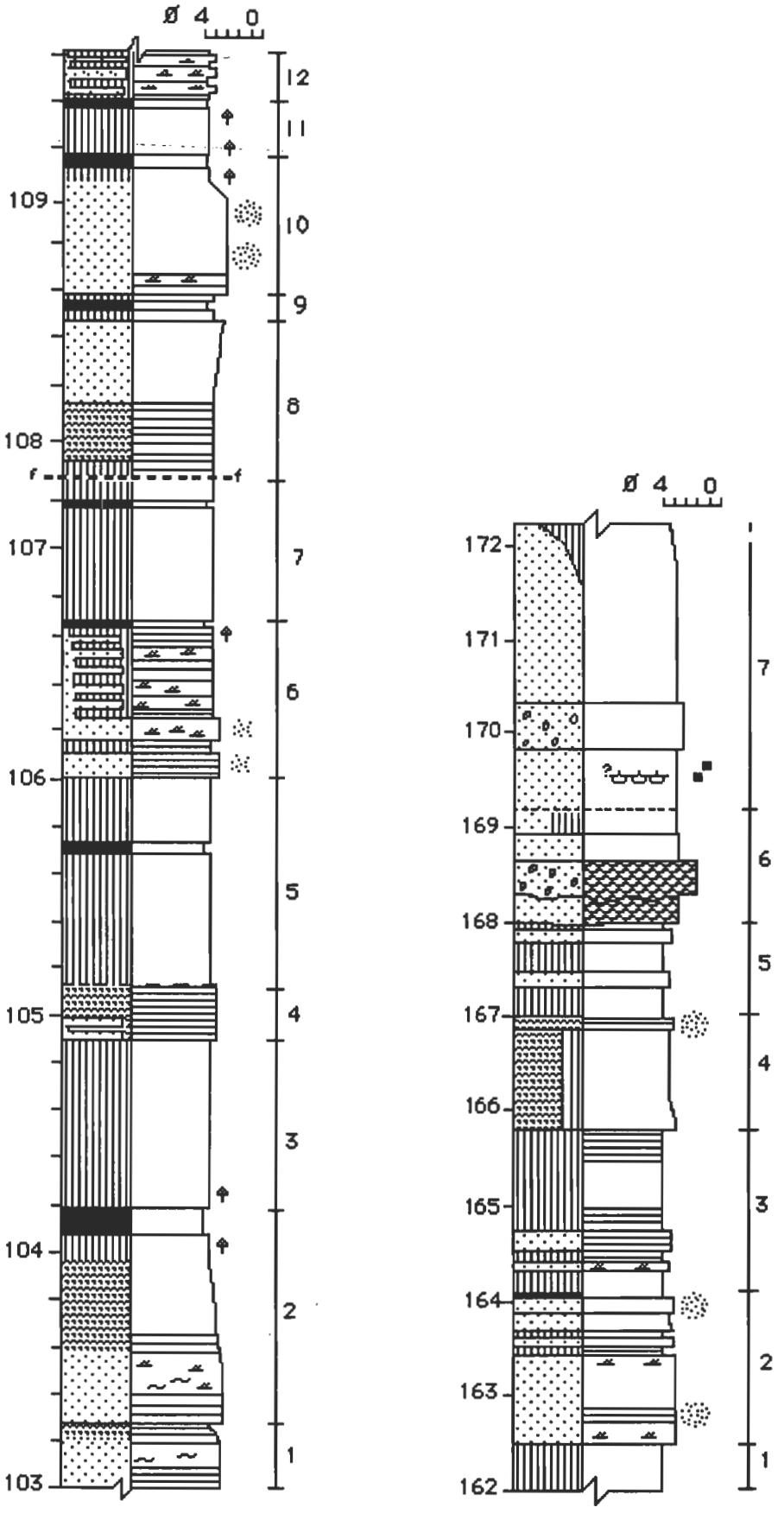

Figure 12. Skenes Creek Road, profiles SCR2 (left) and SCR3 (right).

Figure 13. Skenes Creek Road. Flood-plain and lake sequence. The coal seam near the base of the measuring staff is the lowest seam (top of unit 1) in profile SCR1. The top of the staff rests on rippled fine-grained sandstone at the top of unit 4. The staff is 2 m long.

Figure 14. Skenes Creek Road. Flood-plain swamp sequence; the top is 10.5 m below the base of profile SCR2. Several coal seams up to 50 cm thick overlie structureless carbonaceous mudstone (grey), some of which contain plant rootlets. Interseam rocks are composed of thinly bedded siltstone, mudstone, and fine sandstone. The staff is 2 m long.

Sedimentary evolution of the Eumeralla Formation

By the mid-Barremian, older depositional sub-basins were largely filled with sediment before the onset of Eumeralla Formation deposition. The basin-wide extent of Eumeralla I suggests that the basin was acting as a single depositional entity, and reflects the establishment of a single, integrated basin-wide drainage system. The succession of distinct lithostratigraphic units across the basin can be interpreted as products of evolution of such a system, which persisted to the end of the Albian.

More than one drainage system may have existed early in the history of Eumeralla Formation deposition. Felton (1992) presented evidence for the existence of two major fluvial systems — in the northwest and centre — before Eumeralla Formation deposition. She suggested that lakes developed in these areas at the onset of Eumeralla Formation sedimentation because renewed tectonism in the basin had caused the two systems to pond; lake development is a consequence of interior drainage in rift basins (Leeder & Gawthorpe 1987). The change from lacustrine to extensive flood-plain and swamp deposition in the northwest and centre may indicate that through-basin drainage had developed. Leeder & Gawthorpe (1987) described through-basin drainage in rifts as being characterised by a meandering fluvial system. Alexander & Leeder (1987) noted that both lakes and meandering systems tend to be developed close to the hanging walls of rift grabens (i.e., close to the bounding fault of a basin). This fits the lithological succession observed in Eumeralla I in the northwest and north-centre, close to the former basin-bounding fault.

If the basin had supported more than one drainage system, they must have been closely connected because the depositional conditions throughout the basin were quite uniform, particularly during the deposition of Eumeralla II and III; any changes to depositional controls would have affected all systems similarly in order to maintain that uniformity. Factors controlling/affecting fluvial drainage and sediment deposition are related to tectonics and climate and are not reviewed here, but include — among others — sediment supply, base level, precipitation, relief, and vegetation.

Ponding of drainage along the northern basin margin and establishment of widespread flood-plain and swamp environments in Eumeralla I may have been a consequence of a rising base level. The coincidence of these environments with a major marine transgression during the Barremian (Haq et al. 1987; Morgan 1980) and a maximum on the marine flooding curve derived by Struckmeyer & Brown (1990) is strong evidence that base level for drainage in the basin may have been controlled by sea level at this time. A rise in base level is also consistent with an increased rate of subsidence across the basin during a second phase of rifting (Williamson et al. 1990).

The change in sandstone composition from mainly quartz-lithic in the Crayfish Subgroup (Felton 1992; Little & Phillips 1995) to volcaniclastic in the Eumeralla Formation (Duddy 1983; Felton 1992) reflects the onset of major volcanism in the basin, which accompanied the second stage of rifting. This event may be the pulse of volcanism dated at 126 Ma by Gleadow & Duddy (1981). Subsidence in the central part of the rift could have been offset by elevation of the rift floor, driven by increased heat flow and expansion of magma; subsequent volcanic eruptions along the axis of the rift produced a substantial edifice. Evidence presented in part II of this paper suggests that a major source of the epiclastic volcanic detritus comprising the Eumeralla Formation was located in the axial part of the extensional basin resulting from the second stage of rifting. The coincidence of the Barremian marine transgression (Haq et al. 1987; Morgan 1980) with the changes in depositional conditions in the Otway Basin therefore might be entirely circumstantial; drainage in the basin could have been controlled entirely from within.

The widespread development of freshwater lakes (Eumeralla II), and a restriction of the flood-plain and coal-swamp environments represented by Eumeralla I, imply that the base level continued to rise. However, a model of facies relationships in continental half-grabens proposed by Schlische & Olsen (1990) predicts that — under conditions of constant water volume and sediment input, uniform subsidence, and a fixed outflow level from the half-graben — initially fluvial conditions will be replaced in time by lacustrine conditions. The lakes eventually fill and fluvial/alluvial conditions return throughout the half-graben system.

Deposition in the basin seems to accord with Schlische & Olsen's (1990) model. Fluvial conditions were re-established in the basin, whose central and eastern parts were blanketed by thick volcaniclastic sands (Eumeralla III) deposited by large active rivers during the early Albian (*C. striatus*–lower *C. paradoxa* Zone). However, the 106-Ma Cretaceous volcanic event identified by Gleadow & Duddy (1981) may have been the major influence on Eumeralla III sedimentation (Felton 1992).

Early development of Eumeralla III in the east, especially in Pecten 1A and Anglesea 1, and in Heathfield 1 and Kalangadoo 1 in the northwest and west respectively, suggest

that these sites were adjacent to active volcanic centres or located on major distributaries from such centres. Other sedimentary and petrographic data offer some support for this (Felton 1992). The later appearance of Eumeralla III elsewhere in the west and northwest might indicate that those sites were remote from source volcanoes or distributaries and/or that topographic highs were reactivated or maintained, such as Beachport High, which existed in the Aptian (Reynolds 1971).

The deposition of Eumeralla III apparently coincided with a late Aptian marine regression (Haq et al. 1987); this observation again suggests that the marine base level wielded an influence on non-marine sedimentation in the basin. The lowering of base level due to the marine regression could have contributed to the expansion of Eumeralla III across the basin, particularly westwards, where the first marine connection with the basin is thought to have been established (Morgan 1980; Mutter et al. 1985). Eumeralla III is less well developed in the west and northwest, areas which apparently were

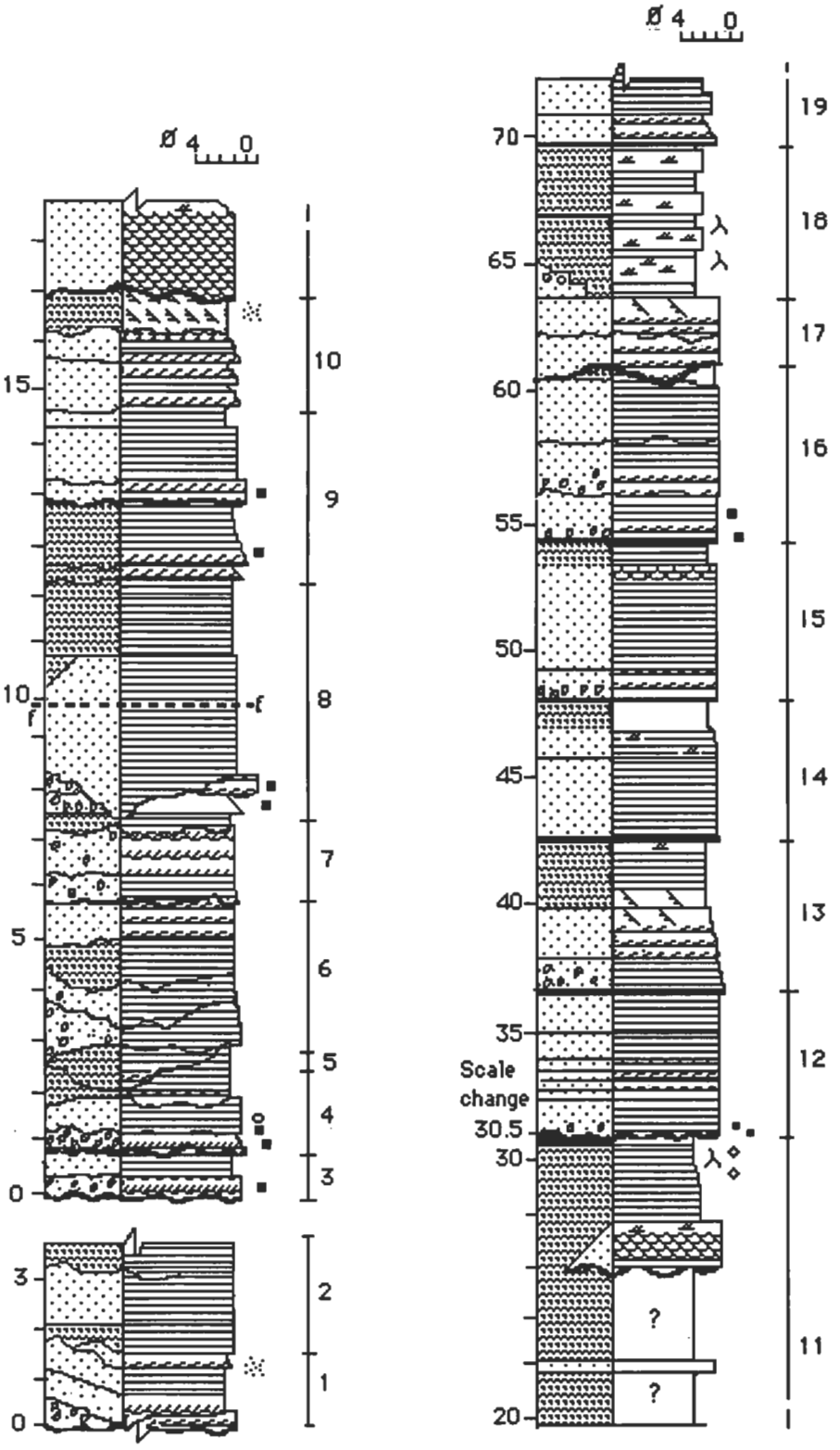

Fig. 15. Cat Reef, profile CR1.

Fig. 16. Massive intraformational conglomerate at the base of unit 3, profile CR1, comprises sandstone-intraclast boulders in an intraclast-supported small-pebble conglomerate filling a scour hollow. The pebbles are siltstone and devitrified glassy volcanic rocks. The overlying channel-fill consists of backset cross-bedded sandstone with a plane-bed set near the top of the photograph. The circular structure in the plane-bed set is a broken carbonate concretion. Short intervals on the measuring staff are 10 cm long.

Fig. 17. Soil profile overlain by a coal bed and the scoured base of a channel sandstone in unit 11, profile CR1. Mudstone at the top of the soil profile is reddened and bleached, and peds are developed. Rootlets demonstrate that the coal formed in situ.

bypassed by the major trunk rivers. Palaeocurrent data from Eumeralla III outcrops (see part II of this paper) imply that mainly westerly flowing rivers drained the basin at this time.

The expansion of Eumeralla IV and restriction of Eumeralla III towards the end of the Early Cretaceous suggest that sedimentation was responding to the late Albian marine transgression (Haq et al. 1987; Morgan 1980) and/or continued subsidence. Waning and cessation of volcanism, and a resultant reduction in sediment supply and lower relief in the source area(s), perhaps contributed to the restriction of Eumeralla III.

Conclusions

It seems likely that the non-marine sedimentation in the basin was influenced, at least in part, by changes in sea level from the Barremian onwards, as Morgan (1980) first suggested, since several sedimentary events apparently coincide with sea-level changes. Volcanism was also a major influence on sedimentation, and dominated the sediment supply from the Barremian to the end of the Albian (Felton 1992). However, the relative importance of volcanism, sea-level change, and tectonic subsidence on basin sedimentation from the Barremian onwards cannot be fully evaluated on present sedimentary evidence. The models for rift sedimentation were developed for rift systems without major infra-rift volcanic activity, and may be of limited use in interpreting the Eumeralla Formation.

References

Alexander, J. & Leeder, M.R., 1987. Active tectonic control on alluvial architecture. In: Ethridge, F.G., Flores, R.M. & Harvey, M.D. (editors), Recent developments in fluvial sedimentology. Society of Economic Paleontologists and Mineralogists, Special Publication 39, 243–252.

Dettmann, M.E., 1986. Early Cretaceous palynoflora of the subsurface strata correlative with the Koonwarra Fossil Bed, Victoria. Association of Australasian Palaeontologists, Memoir 3, 79–110.

Dickinson, W.R. & Suczek, C.A., 1979. Plate tectonics and sandstone composition. American Association of Petroleum Geologists, Bulletin 63, 2164–2182.

Douglas, J.G., 1969. The Mesozoic floras of Victoria, parts 1 and 2. Geological Survey of Victoria, Memoir 28.

Duddy, I.R., 1983. The geology, petrology and geochemistry of the Otway Formation volcanogenic sediments. PhD Thesis, University of Melbourne, Melbourne.

Edwards, A.B. & Baker, G., 1943. Jurassic arkose in southern Victoria. Proceedings of the Royal Society of Victoria, 55, 195–228.

Eyles, D.R., 1974. Well completion report, Trumpet No. 1, S.A. Esso Exploration and Production, Australia Inc., Report.

Falvey, D.A., 1974. The development of continental margins in plate tectonic theory. Australian Petroleum Exploration Association, Journal 14, 95–106.

Felton, E.A., 1989a. Evolution of Early Cretaceous braided fluvial depositional systems, eastern Otway Basin, southern Australia. Fourth International Fluvial Conference, Barcelona, Spain, Abstracts.

Felton, E.A., 1989b. Non-marine sedimentation in an intracontinental rift setting: the Early Cretaceous Otway Group, southern Australia. Twenty-Eighth International Geological Congress, Washington D. C., Abstracts 1, 479.

Felton, E.A., 1992. Sedimentary history of the Early Cretaceous Otway Group, Otway Basin, Australia. PhD Thesis, The University of Wollongong, Wollongong.

Gleadow, A.J.W. & Duddy, I.R., 1981 Early Cretaceous volcanism and the early breakup of south eastern Australia: evidence from fission track dating of vol-

caniclastic sediments. Fifth International Gondwana Symposium, Wellington, Proceedings, 295–300.

Haq, B.U., Hardenbol, J. & Vail, P.R., 1987. Chronology of fluctuating sea levels since the Triassic. Science, 235, 1156–1167.

Helby, R., Morgan, R. & Partridge, A. D. 1987. A palynological zonation of the Australian Mesozoic. Association of Australasian Palaeontologists, Memoir 4, 1–94.

James, E.A., 1968. Esso Crayfish A–1 well completion report. Esso Standard Oil Ltd, Report.

Kenley, P., 1976. Otway Basin, western part. In: Douglas, J.G. & Ferguson, J.A. (editors), Geology of Victoria. Geological Society of Australia, Special Publication 5, 217–222.

Kopsen, E. & Scholefield, T., 1990. Prospectivity of the Otway Supergroup in the central and western Otway Basin. Australian Petroleum Exploration Association, Journal 30(1), 263–279.

Leeder, M.R. & Gawthorpe, R.L., 1987. Sedimentary models for extensional tilt-block/half-graben basins. In: Dewey, J. & Hancock, P.L. (editors), Continental extension tectonics. Geological Society of London, Special Publication 28, 139–152.

Little, B.M. & Phillips, S.E., 1995. Detrital and authigenic mineralogy of the Pretty Hill Formation in the Penola Trough, Otway Basin: implications for future exploration and production. Australian Petroleum Exploration Association, Journal 35, 538–557.

Megallaa, M., 1986. Tectonic development of Victoria's Otway Basin — a seismic interpretation. In: Glenie, R.C. (editor), Second southeast Australia oil exploration symposium. Petroleum Exploration Society of Australia, 201–218.

Miall, A.D., 1978. Lithofacies types and vertical profile models in braided river deposits: a summary. In: Miall, A.D. (editor), Fluvial sedimentology. Canadian Society of Petroleum Geologists, Memoir 5, 597–604.

Miall, A.D., 1985. Architectural element analysis: a new method of facies analysis applied to fluvial systems. Earth Science Reviews, 22, 261–308.

Morgan, R., 1980. Eustasy in the Australian Early and Middle Cretaceous. Geological Survey of New South Wales, Bulletin 27, 1–105.

Morgan, R., 1985. Palynology of Argonaut A1, Banyula 1, Beachport 1, Breaksea Reef 1, Burrungule 1, Crayfish 1A, Geltwood Beach 1, Lake Eliza 1, Lake George 1, Lucindale 1, Kalangadoo 1, Morum 1, Neptune 1 and Penola 1. Reports for Ultramar Australia; Department of Mines & Energy, South Australia, Open-File Envelope 5011 (unpublished).

Morgan, R., Alley, N.F., Rowett, A. I. & White, M. R., 1995. Biostratigraphy. In: Morton, J.G.G. & Drexel, J.F., 1995 (editors), Petroleum geology of South Australia. Volume 1: Otway Basin. Department of Mines and Energy, South Australia.

Morton, J.G.G., 1986. Stratigraphy of the Otway Basin in South Australia. In: Gravestock, D.I., Hill, A.J. & Morton, J.G.G. (editors), A review of the structure, geology and hydrocarbon potential of the Otway Basin in South Australia. Department of Mines and Energy, South Australia, Report Book 86/77.

Morton, J.G.G., 1990. Revisions to stratigraphic nomenclature of the Otway Basin, South Australia. Geological Survey of South Australia, Quarterly Geological Notes 116, 1–19.

Morton, J.G.G., Hill, A.J., Parker, G. & Tabassi, A., 1994. Towards a unified stratigraphy for the Otway Basin. Extended abstracts, NGMA/PESA Otway Basin Symposium. Australian Geological Survey Organisation, Record 1994/14.

Morton, J.G.G. & Drexel, J.F., 1995. Petroleum geology of South Australia. Volume 1: Otway Basin. Department of Mines and Energy, South Australia.

Mutter, J.C., Hegarty, K.A., Cande, S.C. & Weissel, J.K., 1985. Breakup between Australia and Antarctica: a brief review in the light of new data. Tectonophysics, 114, 255–279.

Padley, D., McKirdy, D.M., Skinner, J.E., Summons, R.E. & Morgan, R.P., 1995. Crayfish Group hydrocarbons — implications for palaeoenvironment of Early Cretaceous rift fill in the western Otway Basin. Australian Petroleum Exploration Association, Journal 35, 517–537.

Reynolds, M.A.(compiler), 1971. A review of the Otway Basin. Bureau of Mineral Resources, Australia, Report 134.

Rochow, K.A., 1971. Subdivision of the Otway Group based on a sedimentary study and electric log interpretations. In: Wopfner, H. & Douglas, J.G. (editors), The Otway Basin of southeastern Australia. Geological Surveys of South Australia and Victoria, Special Bulletin, 155–176.

Schlische, R.W. & Olsen, P.E., 1990. Quantitative filling model for continental extensional basins with applications to early Mesozoic rifts of eastern North America. Journal of Geology, 98, 135–155.

Selley, R.C., 1988. Ancient sedimentary environments and their sub-surface diagnosis. Chapman & Hall, London.

Struckmeyer, H.I.M. & Brown, P.J., 1990. Australian sealevel curves. Part 1: Australian inundation curves. Bureau of Mineral Resources, Australia, Record 1990/11.

Struckmeyer, H. I. M. & Felton, E. A., 1988. Organic and sedimentary facies of the Early Cretaceous Otway Group, Otway Basin, southern Australia. Geological Society of Australia Convention, Abstracts 21, 383–384.

Struckmeyer, H. I. M. & Felton, E. A., 1990. The use of organic facies for refining palaeoenvironmental interpretations: a case study from the Otway Basin, Australia. *Geological Society of Australia, Journal 37, 351–364.*

Tupper, N.P., Padley, D., Lovibond, R., Duckett, A.K. & McKirdy, D.M., 1993. A key test of Otway Basin potential: the Eumeralla-sourced play on the Chama Terrace. Australian Petroleum Exploration Association, Journal 33, 77–93.

Willcox, B. & Stagg, H.M.J., 1990. Australia's southern margin — a product of oblique extension. Tectonophysics, 173, 269–281.

Williamson, P.E., Swift, M.& O'Brien, G.W., 1990. Two-stage Early Cretaceous rifting of the Otway Basin margin of southeastern Australia. Geology, 18, 75–78.

Yu, S.M., 1988. Structure and development of the Otway Basin. Australian Petroleum Exploration Association, Journal 28, 243–254.

AGSO Journal of Australian Geology & Geophysics. 16(5). 731–757

A non-marine Lower Cretaceous rift-related epiclastic volcanic unit in southern Australia: the Eumeralla Formation in the Otway Basin. Part II: fluvial systems

E. Anne Felton[1]

Relationships, thicknesses, and palaeocurrent and other sedimentary data applying to facies associations in Eumeralla Formation outcrops in the eastern Otway Basin distinguish at least three discrete depositional systems (A–C). Each system is characterised by high-energy fluvial flows in broad channel tracts.

The multistorey sandstone bodies of system A, between Cape Otway and Apollo Bay, are up to 70 m thick and contain varying proportions of basement-derived quartzose gravel and sand intermixed with mainly volcaniclastic sand. Interchannel siltstones also up to 70 m thick separate the sandstone bodies. Palaeocurrents in system A have an overall southerly trend. This system is interpreted to represent deposition in a medial alluvial fan to proximal braided-stream system.

System B occurs around Moonlight Head, and may extend southeast to Rotten Point. It is characterised by multistorey sandstone bodies up to 14 m thick separated by siltstones of similar thickness which locally contain thin coal beds, rooted horizons, and reddened soil profiles. It lacks basement-derived gravel. Palaeocurrents trend northeasterly to northwesterly. The sediments of system B accumulated on a medial to distal braid plain.

Facies associations and fluvial architecture of system C, seen in outcrop north of Skenes Creek, resemble those of system B, from which it is distinguished by consistently northwest palaeocurrent vectors, a basement-derived gravel component, and the absence of debris flows and volcanic pebbles. System C also represents deposition on a braid plain or in a braided-river system.

The three depositional systems are accommodated in a model for the Eumeralla Formation which suggests that its volcanic detritus was derived largely from infrarift volcanic complexes in the axial parts of the Otway rift basin, which during the Aptian–Albian lay to the south of the present coastline. A volcaniclastic apron spread northwest to northeast across the basin (system B). Elevated basement blocks shed quartzose detritus into flanking alluvial fans, the more distal parts of which mixed with volcaniclastic detritus (systems A, C). The onset of axial volcanism in the Aptian may have displaced a former westerly axial drainage towards the northern basin margin (system C).

Introduction

Part I of this paper describes four lithostratigraphic units comprising the Eumeralla Formation (Eumeralla I–IV), and presents an interpretation of their depositional environments, mainly from subsurface data. Part II describes the facies architecture and facies associations of those parts of Eumeralla II and Eumeralla III which crop out in the eastern Otway Basin. These associations, together with other sedimentary data, discriminate at least three depositional systems, and lend further support to the environmental interpretation of Eumeralla II and III.

Methods and data

The field methods used to gather sedimentary data are described in part I. Field locations are shown in Figure 1.

Six long and seven vertical profiles (Appendix) are representative of outcropping lacustrine and fluvial systems (Eumeralla II and III) respectively. The following discussion of facies associations is based on the profile descriptions.

Facies associations, Eumeralla II and III

Lithostratigraphic units Eumeralla II and III can be described in terms of their facies associations, sediment bodies distinguished by overall geometry, and internal architectural elements comprising assemblages of lithofacies. Each association represents a particular part (e.g., fluvial channel tract) of a larger depositional system. The internal arrangements of facies associations reflect the depositional processes and sedimentary controls (Miall 1985), while the relationships between the

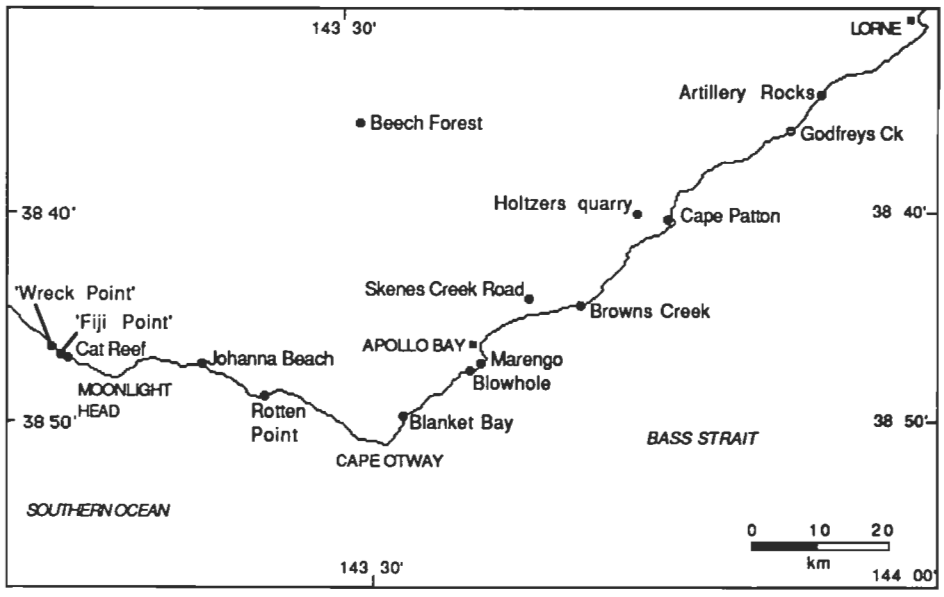

Figure 1. Field locations.

[1] Department of Geology, The University of Wollongong, Wollongong, NSW, Australia; present address: SOEST Hawaii Institute of Geophysics and Planetology, University of Hawaii, 2525 Correa Road, Honolulu, HI 96822, USA.

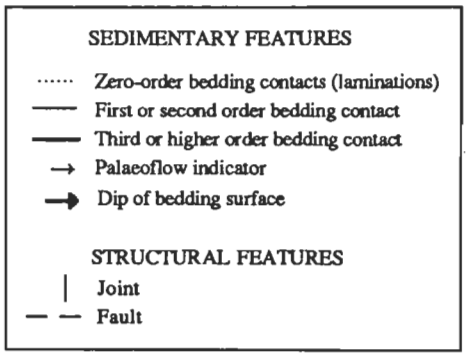

Figure 2. Key to long profiles.

associations define the character of the depositional systems.

The several architectural element classification schemes proposed for fluvial systems (e.g., Friend 1983; Allen 1983; Miall 1985) vary in complexity, but in general rely on excellent three-dimensional exposures for their application. Although the Eumeralla Formation is well exposed in cliff sections and wave-cut platforms in the eastern Otway Basin, the overall lack of three-dimensional exposures limits the application of Miall's (1985) classification. However, the simpler schemes of Friend (1983) and Allen (1983) proved useful starting points for developing the sedimentation models described later in this paper.

Fluvial-channel-tract facies association

The lithofacies assemblages present in this association are listed in Table 1. The association is dominated by plane-bedded and low-angle cross-bedded medium- to fine-grained sandstone (facies Sh and Sl; Table 2) and climbing-ripple-laminated fine sandstone (facies Src).

Facies architecture

All the geomorphic and depositional elements of modern fluvial channel tracts — channels, bars, bar complexes, and banks — have been observed in Eumeralla III sandstones (Appendix; Figs. 2–15). The relationships of these depositional elements were illustrated by Walker & Cant (1984). Each is characterised by one or more particular lithofacies, as described and interpreted in part I.

Single sets of lithofacies are separated by first-order contacts. Groups of genetically related lithofacies in bars, bar complexes, and dunes are separated by second-order bedding contacts which are usually discordant or concordant erosional (Allen 1983); the amount of erosion varies along the contact (e.g., surface **b**, Johanna Beach profile; Appendix; Fig. 12). These groups correspond to the 'storeys' of Friend et al. (1979), and the bounding erosion surfaces to their description of 'storey-scours'. All the channel-tract sandstone bodies observed in Eumeralla III are multistorey.

The sandstone storeys form sheets, or very broad channel forms with width>>depth (e.g., at Cape Patton; Appendix; Figs. 3, 4a, 4b), which are locally mud-draped. They are separated by sharp, flat to irregular scoured contacts of third or higher order (cf. Cant & Walker 1978), which are usually discordant erosional. These major scour surfaces are usually overlain by discontinuous stringers of muddy siltstone intraclasts (lithofacies Gs; Fig. 15); intraclast-supported massive conglomerate is locally present in scour hollows (fig. 16 in part I). In sandstone sequences lacking intraclasts, both second- and third-order contacts can be difficult to discern, particularly in weathered, inaccessible cliff sections (e.g., Fig. 3).

Variable amounts of erosion associated with the scour surfaces are reflected by the presence of intraclasts (lithofacies Gmi, Gs), and the overall lack of fining-upwards sequences commonly associated with channel occupation and abandonment. Where completely developed in Eumeralla III, a typical fining-upwards channel-fill sequence consists of basal Gmi or Gs overlying a third- or higher-order contact, succeeded by medium-grained Sh/Sl with or without St, then fine-grained Src, Sr, and Fl/Fm. However, finer-grained lithofacies (Sr, Fl, Fm) are generally eroded away, and appear only as intraclasts, mainly lithofacies Gs. Although making up less than 5 per cent of the channel-tract thickness, Gs is very common.

Channel margins and banks rarely crop out. Only one has been recognised unequivocally, by its associated levee: at Cape Patton lookout, a sandstone bed at the base of a palaeochannel cuts into overbank siltstone and coal, and wedges out against a levee; an overlying sandstone passes laterally into interbedded sandstone and siltstone, also interpreted as a levee (Figs. 4a, 4b).

Sandstone body geometry

Large-scale tabular or sheet geometry can be inferred for at least some Eumeralla fluvial-channel-tract sandstone bodies, although the dimensions of the bodies relative to outcrops

Table 1. Eumeralla facies associations: constituent facies

	Fluvial channel tract		*Fluvial flood plain*		*Lacustrine*	
Letter code	*Channel floor*	*Bars*	*Flood basin*	*Levee*[1]	*Basin*	*Margin*
Gmi[2]	X					
Gm	x					
Gs	X	x	x			
Sb	x					
Sm	x					
Sh	X	X	X	x	x	
Sl	X	X	x			x
Ss	X		x			
St	X	x	x			x
Sp		x	x			
Sr		x	X	X	X	X
Src		X	x	x		
Fl		x	X		X	x
Fm		x	X	X	X	X
C			x	x	x	x

[1] Only two examples observed.

[2] Facies codes generally follow the scheme of [Miall, 1978 #388]. See Table 2 for facies descriptions.

X = common occurrence: x = uncommon occurrence; no symbol = not observed.

preclude mapping their full extent. Sandstone body dimensions almost invariably exceed outcrop dimensions, and have overall minimum lateral dimensions of tens to hundreds of metres (Table 3).

Two other observations support the inference of sheet form for channel-tract sandstone bodies. Facies and facies architecture in the sandstone bodies, whose wide lateral extent (Table 3) can be unequivocally demonstrated, are similar to those observed in outcropping thick sandstone bodies throughout Eumeralla III, and imply similar depositional processes and hence channel formation and filling. Also, evidence for large-scale channel incision is lacking. As described above, third-order basal contacts of the sandstones, although locally scoured, are flat overall, and channel-bank contacts are rare. Gradational top contacts to the sandstones are also moderately flat.

The geometry and architecture of the sandstone bodies, their relationships with flood plains (see below), and lack of evidence of channel confinement suggest that deposition took place in very broad tracts composed of vertically and laterally stacked broad channels whose widths greatly exceeded their depths.

Fluvial-flood-plain facies association

The lithofacies present in this association are listed in Table 1. Although not as well represented in outcrop as the fluvial-channel-tract facies association, the flood-plain facies association is widely distributed in Eumeralla III — for example, at Cat Reef and west of Johanna Beach (Table 4).

Flood-plain deposits

Geomorphic and depositional elements of flood plains include small channelways (flood-plain distributary channels, moderately flat interchannel areas inundated at high flood stages, and basin-like shallow depressions that were the locations of flood-plain lakes and swamps in those areas; Popov & Gavrin 1970; Simpson & Doutch 1977). These elements comprise the flood basin. Levees are elevated areas forming the most proximal part of the flood plain relative to the river channel (Kesel et al. 1974).

Flood-plain deposition in the outcropping Eumeralla Formation is inferred for mainly fine-grained sandstone and siltstone deposits which are tens of metres thick and hundreds of metres in lateral extent, and occur between channel-tract sandstones. Compositional details of several flood-plain-inter-

Table 2. Summary of sedimentary facies, Eumeralla Formation.

*Facies**	*Description*	*Major associated facies*	*Occurrence*	*Interpretation/ bedforms*
Gmi	Massive clast-supported conglomerate; intraclast-dominated; lacks internal structure	Gs, Sl	Scour hollows	Scour fill; ?debris flow
Gm	Massive sandy conglomerate; pebble imbrication to structureless; mainly exotic clasts	St	Locally in channel tracts	Bar; channel fill
Gs	Mudclast-stringer conglomerate	Gmi, Sl, Sh	Scour surfaces	Rip-up clasts from stream bank or redistributed Gmi
Sb	Back-set cross-bedded sandstone	Sh	Locally in channel tracts	Upper-regime flow; locally developed chute-and-pool
Sm	Massive (structureless) sandstone	Sh	Channel tracts	?Hyperconcentrated flow; locally developed antidunes
Sh	Plane-bedded sandstone	Sl, St, Src	Channel tracts; sheets in overbanks	Upper-regime plane-bed flow; bars and sheets
Sl	Low-angle cross-bedded sandstone	Sh, St, Src	Channel tracts; thick sheets in overbanks	Upper-regime plane-bed to transition flow; forward and lateral accretion of bars and sheets
Ss	Scour-filling low-angle cross-bedded sandstone	Sh	Channel tracts; thick sheets in overbanks	Upper-regime flow
St	Trough-cross-bedded sandstone	Sh, Sl, Sp	Channel tracts; thin sheets in overbanks	Lower-regime flow; distal or waning floods; dunes
Sp	Planar tabular cross-bedded sandstone	St	Channel tracts; thin sheets in overbanks	Lower-regime flow; waning floods; sand waves, transverse bars
Src	Climbing-ripple-laminated sandstone	Sh, Sl	Channel tracts; thin sheets in overbanks	Rapid sediment fall-out; sudden loss of flow strength due to waning flood or flow diversion
Sr	Ripple-laminated fine sandstone, wavy laminated fine sandstone	Fl	Thin beds in channels and overbanks	Low flow strength; sinuous-crested ripples
Fl	Laminated, wavy-, and cross-laminated siltstone and mudstone	Sr, Fm	Lenses and thin beds in channels and overbanks	Suspension fall-out
Fm	Structureless siltstone and mudstone	Sr, Fl	Tops of channel tracts	Suspension fall-out; includes seat earths

* Based on lithofacies codes of Miall (1978).

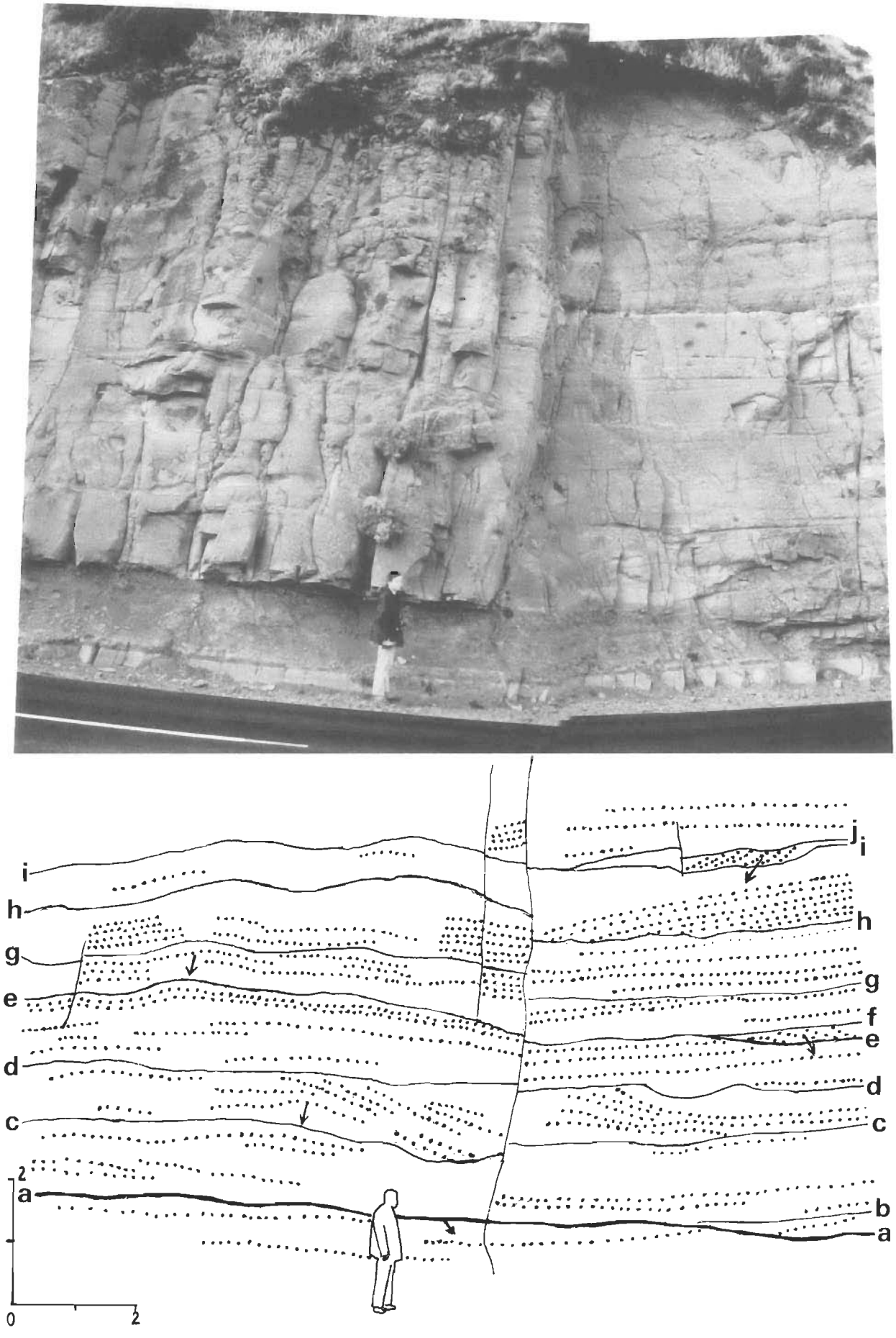

Figure 3. Cape Patton road-cutting. Cape Patton profile CP1. Flood-plain siltstone (the recessive unit behind the person) is overlain by a channel-tract sandstone whose base is at the level of the person's neck.

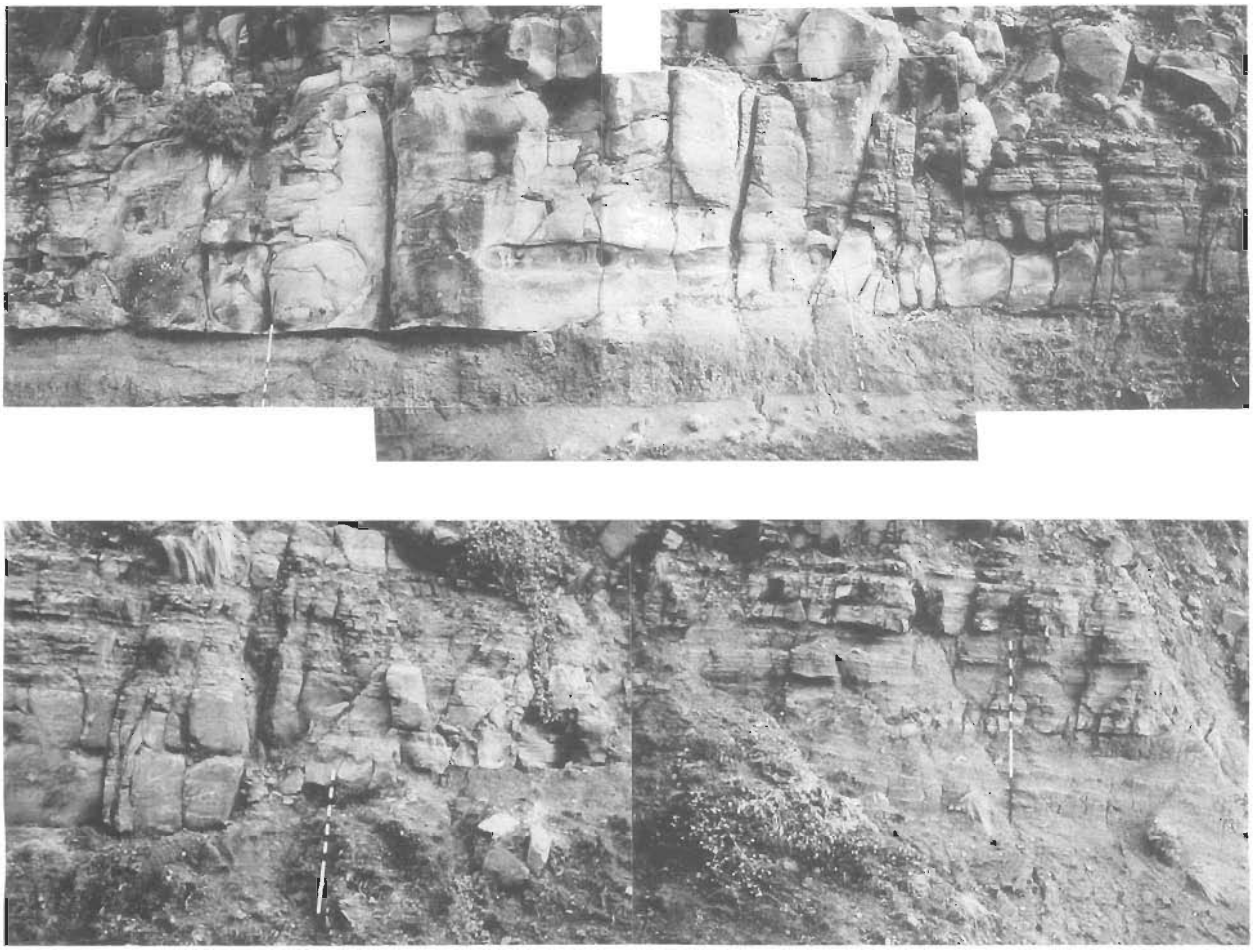

Figure 4. Cape Patton road cutting: the base of the channel-tract sandstone illustrated in and 10 m along strike to the right of Figure 3. The two photographs (a, top; b, bottom) are continuous, but are reproduced at different scales. The lowermost sandstone unit, a channel fill containing large elongate concretions (channel 1) is cut into flood-plain siltstone. It thins sharply towards its margin, and interfingers with fine-grained sedimentary rocks in a levee (right-hand side of b). Channel 1 and its levee have been partly eroded by the overlying channel 2, which also passes laterally into a levee sequence containing thin fining-upward splay sands. The levees are displaced relative to the channel-tract sandstone owing to greater compaction of the interbedded finer rocks, apparent at the right-hand side of a and in b. The staff is 2 m long, and has divisions at 50 cm and 10 cm.

preted rock bodies are presented in Table 4; thin coal and carbonaceous mudstone beds are conspicuous but minor components of some of them. Whereas abandoned channel-fills become finer-grained in vertical sequence, and their upper parts commonly consist of several fining-upwards units (e.g., Fig. 8, units 10–11), flood-plain deposits generally show no consistent grainsize trend (e.g., Fig. 14, units 1–8).

Sheet siltstone. These bodies are usually no more than 3 m in (compacted) thickness (Table 4), and are areally extensive. Thin coal and carbonaceous mudstone are conspicuous but minor components of some bodies. They represent low-energy deposition in (i) moderately flat interchannel areas inundated at high flood stages, and (ii) basin-like shallow depressions — the locations of flood-plain lakes and swamps — within those areas.

Sheet sandstone. Sheet sandstone bodies in the association are of wide lateral extent and tabular form, and have varying thicknesses up to 3 m. They usually have one storey, and are composed of few lithofacies. Most sheet sandstones have palaeocurrent directions divergent from over- and underlying channel-tract sandstones, and probably represent splay/sheet-flood deposits. Some may be distributary channelways.

Lenticular sandstone. Lenticular sandstone has a similar thickness to sheet sandstone, from which it differs mainly in lateral extent. Those bodies with erosional bases and internal cross-bedding are interpreted as flood-plain distributary channels (e.g., Rotten Point; Table 4; Fig. 6). Those which have gradational relationships with flood-plain siltstone and channel-tract sandstone are probably levee deposits (e.g., Cape Patton; Table 4; Figs. 3, 4a, 4b).

Lacustrine facies association

The lacustrine facies association is thickest and most widespread in the lower part of the Eumeralla Formation (lower Albian *C. striatus* Zone; Struckmeyer & Felton 1990), although outcrops are limited. The lacustrine facies association is exposed at Browns Creek (Fig. 14), and in cuttings along Skenes Creek Road north of Apollo Bay (figs. 11–14, part I), where much of the 270-m exposed section consists of lake-basin mudstone and siltstone. Parts of thick intervals of flood-plain facies association sediments at Blanket Bay (Table 4) may be deposits in shallow flood-plain lakes.

The lateral extent of the assocation is unknown, although parts of Eumeralla II have been correlated with this association (part I). Felton (1992) discussed evidence for a deep perennial lake origin for the thick sequences of uniform, dark silty mudstones in a water well near Apollo Bay, and in petroleum exploration wells near the northeastern margin of the Otway Basin.

This association is distinguished from fine-grained parts of the fluvial-flood-plain facies association by its general lack of sandy lithofacies, overall finer grainsize, and thickness.

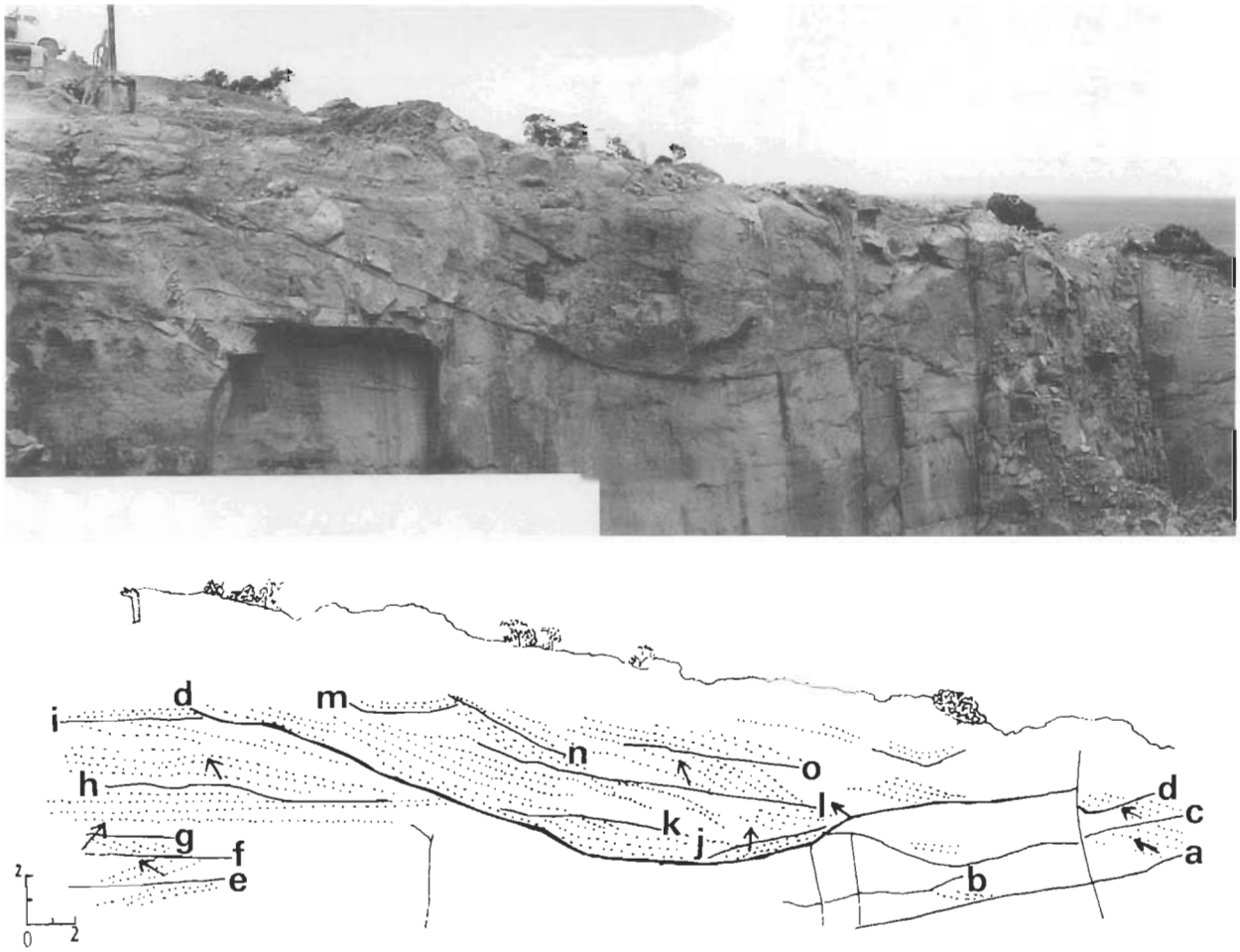

Figure 5. Holtzers Quarry profile HQ1. The person standing next to the drilling rig (upper left) provides the scale.

Distal overbank deposits — recognised by intercalations of thin fine-grained rippled and laminated sheet sandstones — interfinger with interpreted lake-margin sedimentary rocks at Browns Creek (Fig. 14).

Lacustrine deposits

Two styles of deposition, described below, are recognised in outcrop.

Lake basin. Lake-basin deposits consist mainly of finely laminated mudstone and siltstone (figs. 11–14, part I). Laminae less than 2 mm thick are distinguished by subtle colour variations that correspond to grainsize changes. Regularly alternating light and dark laminae which might suggest varves are not apparent. At the Skenes Creek Road locality, rare thin light beds with compact texture and blocky fracture may be airfall tuffs. Their origin is obscured by weathering.

Local starved ripples with amplitudes of 8 mm or less, and single ripple trains with amplitudes of 1–2 cm, consist of silt and fine sand; such ripples have commonly sunk into underlying muds. Vertical to subvertical burrows and bioturbated layers occur in places in shallow lake deposits. Macerated plant debris, now coalified, is abundant in both shallow and deeper lake-basin sediments (Struckmeyer & Felton 1990).

Lake margin. Fine- to medium-grained lithic-quartz sandstone bodies are enclosed by lake-basin sedimentary rocks as described above. Their characteristics and interpretation were discussed in detail by Felton (1992), and are summarised in Table 5. These sands mostly represent different parts of small deltas prograding into the lakes.

The interpreted lake-beach sandstone (Table 5) differs from other sandstones in lacustrine sequences in being more quartz-rich and well sorted. Internally it is well bedded; it is cross-bedded in part, and the thicknesses of individual beds do not exceed 30 cm. The cross-bedding may be low angle. This sandstone is isolated in thick lake-basin mudstone, with which it has sharp planar upper and lower contacts; if it is a lake-beach deposit, it would have accumulated at the lake margin during a rapid fluctuation in lake level.

Fluvial regime of Eumeralla rivers

Depositional processes

Bedforms

Bed mesoforms identified in outcrop are interpreted as bars of various types which formed and moved in stream channels, and were presumably stable over at least part of the prevailing flow regime (Rust & Koster 1984). Three types of bed mesoforms are recognised in the Eumeralla Formation channel tracts. Plane-bedded bars, of both simple and complex type (Allen 1983), are dominant. Dunes may occur throughout the channel tract, but sand waves are largely confined to the upper parts of channel deposits.

Plane-bedded bars. The margins of large plane-bedded bars may rarely be visible (cf. Allen 1983), depending on the scale and orientation of both outcrop and bar. In the study area, low-angle accretion surfaces at bar margins are common because the bars are generally smaller than outcrop scale (tens of metres). Both simple and complex plane-bedded bars in the Eumeralla Formation channel tracts are commonly a few metres to tens of metres long and wide, less than 1.5 m thick, and tabular, rather than elongate. The largest plane-bedded bar noted in the study area, south of Blanket Bay, was 150 m long in the downstream direction, and 4 m thick (Fig. 15); its lateral extent could not be observed.

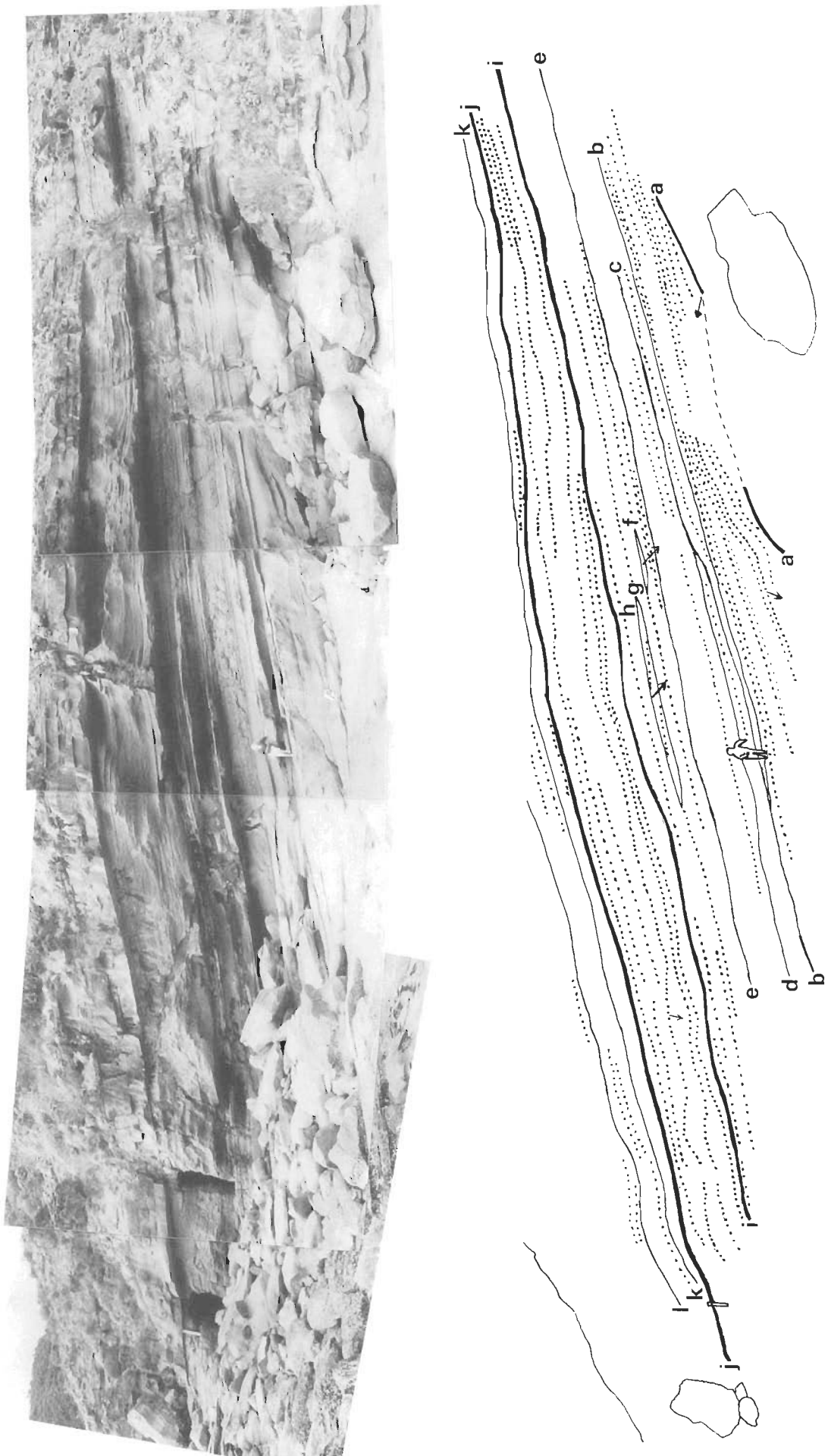

Figure 6. Rotten Point profile RP1.

Table 3. Parameters of fluvial-channel-tract sandstone bodies

Field location	*Lateral dimensions*	*Thickness (m; range observed)*	*Max. relief (m) on base*[1]
Cat Reef/Fiji Point (4 bodies)	150 m+ normal & parallel to depositional dip (all)	12–14	Flat (all)
West of Johanna Beach (1 body)	Updip extent not known; 1.5 km+ normal to depositional dip	10–15 E to W	2.5
Rotten Point (1 body)	400 m+ normal; 200 m+ parallel to depositional dip	35	Not seen in detail
Blanket Bay (1 body)	100 m+ normal & parallel to depositional dip	70	6
Marengo (1 body)	100 m+ normal & parallel to depositional dip	70+	2.5
Cape Patton (2 bodies)	150 m+ normal to depositional dip (each)	60+; 30+	6; flat

[1] All basal contacts are third- or higher-order, erosional.

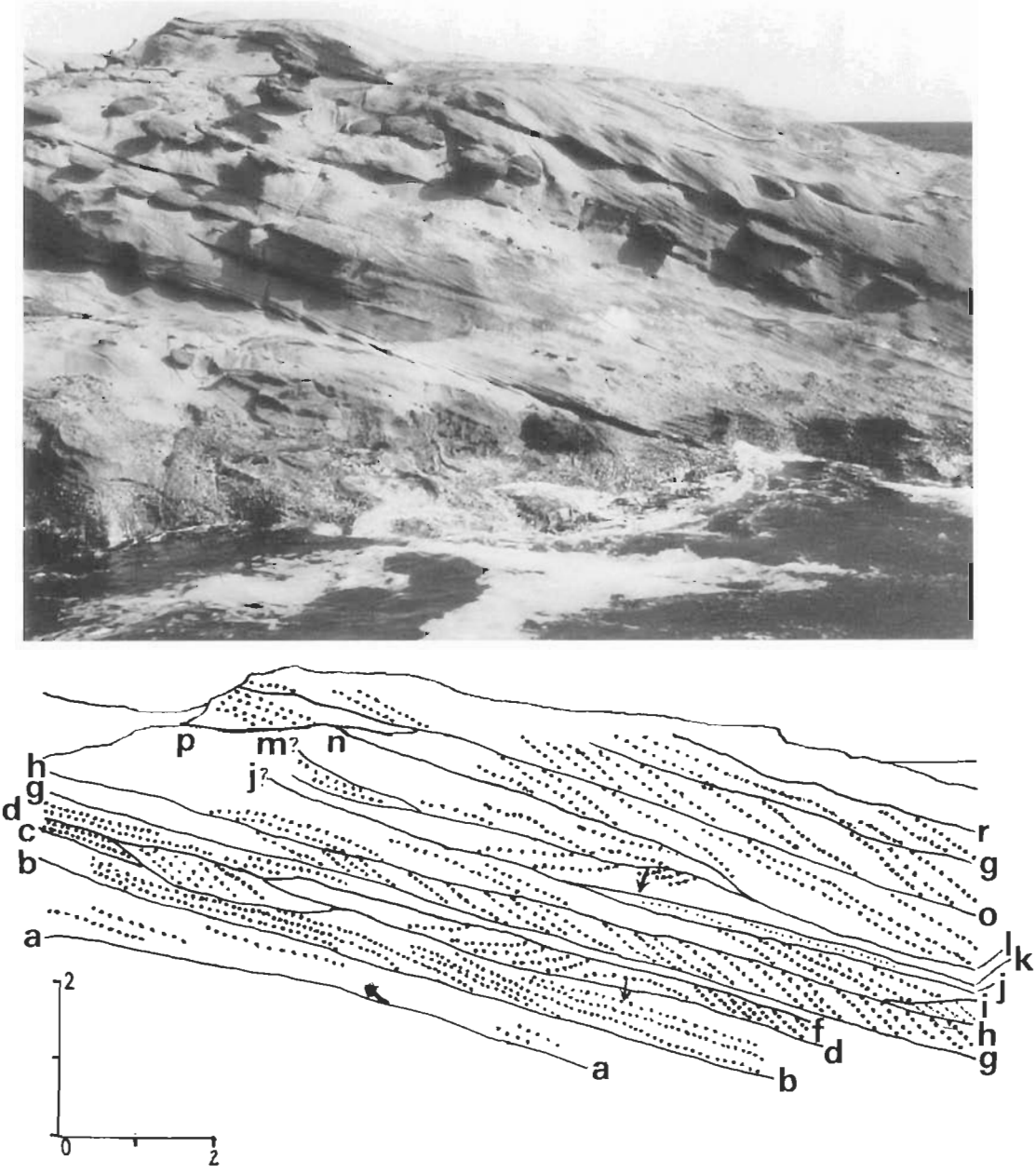

Figure 7. Rotten Point profile RP2.

Table 4. Characteristics of the flood-plain facies association

Field location	*Architectural element*	*Sedimentary structures*	*Lateral dimensions*	*Maxium thickness*	*Nature of contacts*
Cat Reef/Fiji Point (3 bodies up to14 m thick[1]; fig. 15, part I)	1. Sheet siltstone ± coal (90%)	Laminae, ripples, rootlets, bioturbation, pedogenesis	50 m+ along strike and updip	6 m	Gradational bases; sharp or erosional tops
	2. Lenticular sandstone (10%)	Trough X-beds	4 m+ updip	1 m	Erosional bases; sharp tops
West of Johanna Beach (1 body 30m thick)	1. Sheet siltstone (60%)	Laminae, ripples	1.5 km+ along strike; 150 m+ updip	3 m	Gradational base; sharp or erosional top
	2. Sheet sandstone (40%)	Trough cross-beds	As above	3 m	Sharp base; gradational top
Rotten Point (2 bodies with maximum thicknesses of 19 and 35 m; Fig. 8, units 10–13 & 15–21)	1. Sheet siltstone (70%)	Laminae, ripples, rootlets, bioturbation, pedogenesis	400 m+ along strike; 200 m+ updip	3 m	Gradational bases; sharp or erosional tops
	2. Sheet sandstone (25%)	Low-angle and trough cross-beds; plane bedding	As above	2.5 m	Sharp bases; gradational tops
	3. Lenticular sandstone (5%)	Low-angle and trough cross-beds; ripples	4 m updip	1 m	Sharp bases and tops
Blanket Bay (2 bodies 70 m and 64 m thick; Fig. 13)	1. Sheet siltstone (85%)	Laminae, ripples, bioturbation, rootlets	100 m+ updip and transverse	22 m	Gradational bases; third- or higher-order erosional tops
	2. Sheet sandstone (15%)	Ripple lamination	As above	0.5 m	Sharp bases; second- or higher-order and sharp or gradational tops
Cape Patton (1 body 30+ m thick; Figs. 3–4)	1. Sheet siltstone, minor coal	Laminae, ripples, ?rootlets, ?pedogenesis	150 m+ transverse to depositional dip	3 m+	Base grades to underlying channel tract; third- or higher-order erosional top
	2. Lenticular sandstone	Ripple and wavy laminae; thin silty interbeds	6 m down depositional dip	2 m	Gradational base; passes laterally into and overlain by channel-tract sandstone
Skenes Creek Road (1 body 10+ m thick; fig. 12, part I, units 1–7)	1. Sheet siltstone/fine sandstone ± thin coal	Laminae (internal structure obscure)	7 m+ along depositional strike	3 m	Gradational base with underlying lacustrine mudstone; erosional top
	2. Sheet sandstone	Trough cross-beds	As above	0.7 m	Erosional base; sharp or gradational top
Browns Creek (1 body 20+ m thick; Fig. 14, units 4–7)	1. Sheet siltstone/fine sandstone ± thin coal	Laminae (internal structure obscure)	700 m+ along depositional strike	2 m	Gradational base with underlying lake mudstone or distributary-channel sandstone; erosional top
	2. Sheet sandstone	Trough cross-beds	Several hundred metres along depositional strike	1 m	Erosional base; gradational top

[1] All bodies of the flood-plain facies association are gradational, underlie channel tracts, and have third- or higher-order erosional upper contacts.

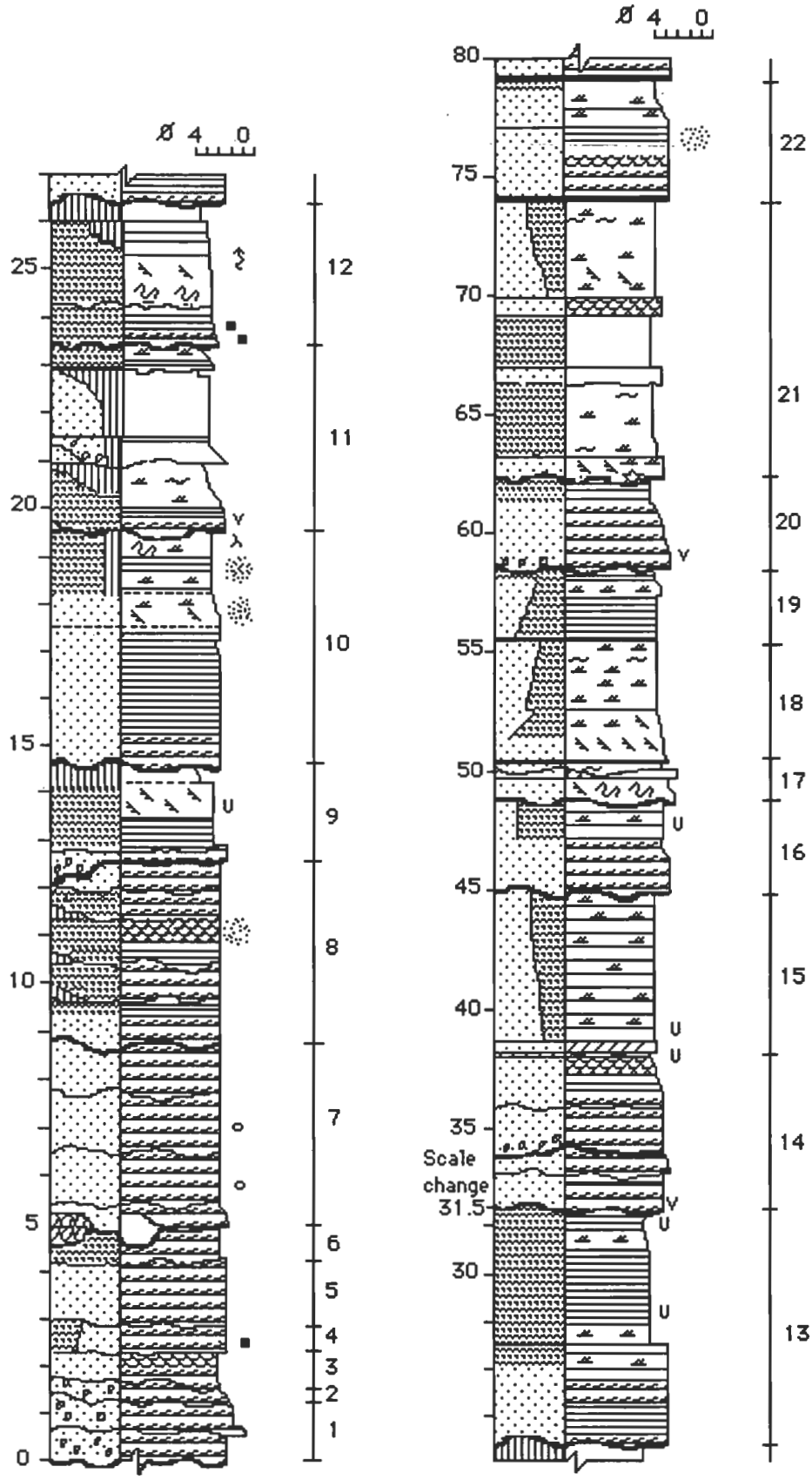

Figure 8. Rotten Point profile RP3.

Table 5. Parameters of lake-margin sandstones

Sandstone body	*Thickness (m)*	*Base*	*Top*	*Facies*	*Overlain by*	*Interpretation*
Browns Creek, tops of units 1, 2 (Fig. 13)	0.75–1	Gradational; coarsens upward	Gradational; fines upward	Sr, Src	Fm, Fl	Distributary mouth bar succeeded by lake basin
Skenes Ck Rd, unit 4 (fig. 11, pt I)	0.4	Gradational; coarsens upward	Sharp, planar	Sr	Fm, C	Distributary mouth bar succeeded by infill marsh
Browns Creek, near top of unit 3 (Fig. 14)	0.5	Gradational; coarsens upward	Sharp, planar	Fl	Fl	As above; partly eroded by distributary channel
Skenes Ck Rd, unit 2, (fig. 11, pt I)	0.3	Gradational; coarsens upward	Sharp, planar	Sh, Sr	Fm, Sr	Mouth bar succeeded by levee
Skenes Ck Rd	1.8	Sharp, planar	Sharp, planar	Sl, ?Sp	Fm, Fl	Lake beach succeeded by lake basin

Internal bedding in the marginal parts of plane-bedded bars in the Eumeralla Formation commonly has low-angle relationships with underlying surfaces. Further, the low-angle bedding on the bar margins commonly is highly differentiated in grainsize, bed thickness, and internal structure (Figs. 9, 10).

Bar formation was probably initiated on fairly flat stream beds which developed after an initial cut-and-fill episode associated with the onset of flooding. The mechanism of bar initiation may have been similar to that suggested by Leopold & Wolman (1957): longitudinal bars nucleate about small accumulations of the coarsest bedload fractions, deposited as flow decreases; they grow mainly in the downstream direction by the addition of material to their downstream ends. This process in Eumeralla rivers permitted local bed aggradation and bar growth, and the concomitant development of low relief in the stream bed. Flow separation induced by relief in the bed, which — in conditions of falling-stage flow — would normally result in the formation of lower-flow-stage dunes and sand waves, was suppressed as high-stage flows continued. Weak separation eddies prevailed locally, as did flow fluctuations, inducing sediment deposition on the downstream and lateral margins of the bars. Low-angle accretion surfaces thus developed at high angles to the palaeoflow.

The high variances observed in measurements of current directional indicators in the mainly upper-stage-flow Eumeralla rivers (Felton 1992) are consistent with the model for sediment deposition and bar growth discussed above. The bi-directional trends observed in many palaeocurrent roses (Fig. 16) lend support to the suggestion that much of the sediment accumulated on the sides of plane-bedded bars.

Plane-bedded bars and bar complexes formed at the high-fluvial-flow stage were modified during falling- and low-flow stages (cf. Smith 1971). Modifications observed in this study include erosion of the sides of bars; channelling-in and erosion of their tops; and deposition of reworked sediment in low-stage channels surrounding the bar complexes. Repeated cut-and-fill, reactivation surfaces, abundant intraclasts strewn along those surfaces, and rare in-situ fine-grained sediments all attest to considerable fluctuation of flow stage in Eumeralla III fluvial-channel tracts.

Dunes. Trough cross-beds are developed throughout the channel-tract sandstone. Where they occur near storey bases in multistorey sandstones, they represent dunes which formed and moved on channel floors after the initial scouring of a channel during the rising stages of floods.

Small trough and planar tabular cross-bed sets in places are interbedded with finer sediments at the tops and sides of plane-bed cosets; they are usually isolated single sets, or consist of two to three sets separated by reactivation surfaces. They developed as flow fluctuated over the tops of bars in the stream channel. They also formed in response to waning flow at the tops of channel-tract sandstones as the tract was abandoned.

Sand waves. Sand waves, or planar tabular cross-bedded bars, are uncommon in the Eumeralla Formation. Small planar tabular cross-sets (30 cm thick) in places formed above or lateral to plane-bedded bars, an indication that local decreases in current velocity occurred around larger bars.

Larger planar tabular sets and cosets, up to 2 m thick, are best developed at Fiji Point, where they overlie mainly plane-bedded sandstone. They represent simple bars or sand waves. They record not only a lower flow regime in the channel tract, possibly resulting from loss of flow competence in wider, shallower channels, but also current directions divergent from the vector mean of palaeocurrent directional indicators in the area (Felton 1992, appendix 4A). An inspection of Walker & Cant's (1984) illustration of the morphology of simple bars indicates that measurements of these bedforms, whose downstream side may consist of one or more arcuate lobes, may diverge from the direction of palaeoslope by up to 180°.

Fluvial style

Eumeralla river systems were dominated by high-stage flow. The small scale and general lack of sedimentary features formed under lower flow regimes attests to rapidly rising and falling flows that were not conducive either to the formation or preservation of such features. Scour channels probably formed during the rising and peak stages of floods, when nearly all sediment was entrained. At peak flood stage, the sediment-charged water overtopped the banks of deep scour channels to spread out laterally as upper-flow-regime sheet floods. The ensuing drop in flow competence in the channels enhanced in-channel sediment aggradation as channel-floor dunes [facies St, low-angle cross-beds (Ss), and small-scale plane-bedded bars (Sh/Sl)]. Elsewhere in the channel tract, sediments were deposited mainly as plane-bedded bars (Sh/Sl) as high-stage flows continued after peak flood. These bars prograded laterally into the scour channels, and merged with the in-channel deposits. The resulting channel tracts were broad and moderately flat, and lacked well-defined margins.

Palaeohydrology

Water depths

According to the method of Allen (1984), water depths of 2 to 6 m are estimated from trough cross-beds in secondary and tertiary channels near the tops of channel-tract sandstone bodies at Fiji Point. The mean measured thickness of the trough cross-beds here is 40 cm, to which is added 25 per cent to yield an estimate of the group mean for the original dune heights (50 cm). Water depths estimated by this method

Figure 9. Rotten Point profile RP3, unit 4: detail of facies Sl. Thickened beds near the base of a low-angle cross-bedded bar consist of fine and coarse-grained sandstone, both of which are internally laminated.

Figure 10. Rotten Point profile RP3, unit 4: detail of facies Sl. A thickened bed consists of climbing-ripple muddy fine-grained sandstone with mud flasers; the basal contact of the overlying coarse sandstone is load-casted into the finer unit. The light-coloured pebbles are muddy siltstone intraclasts.

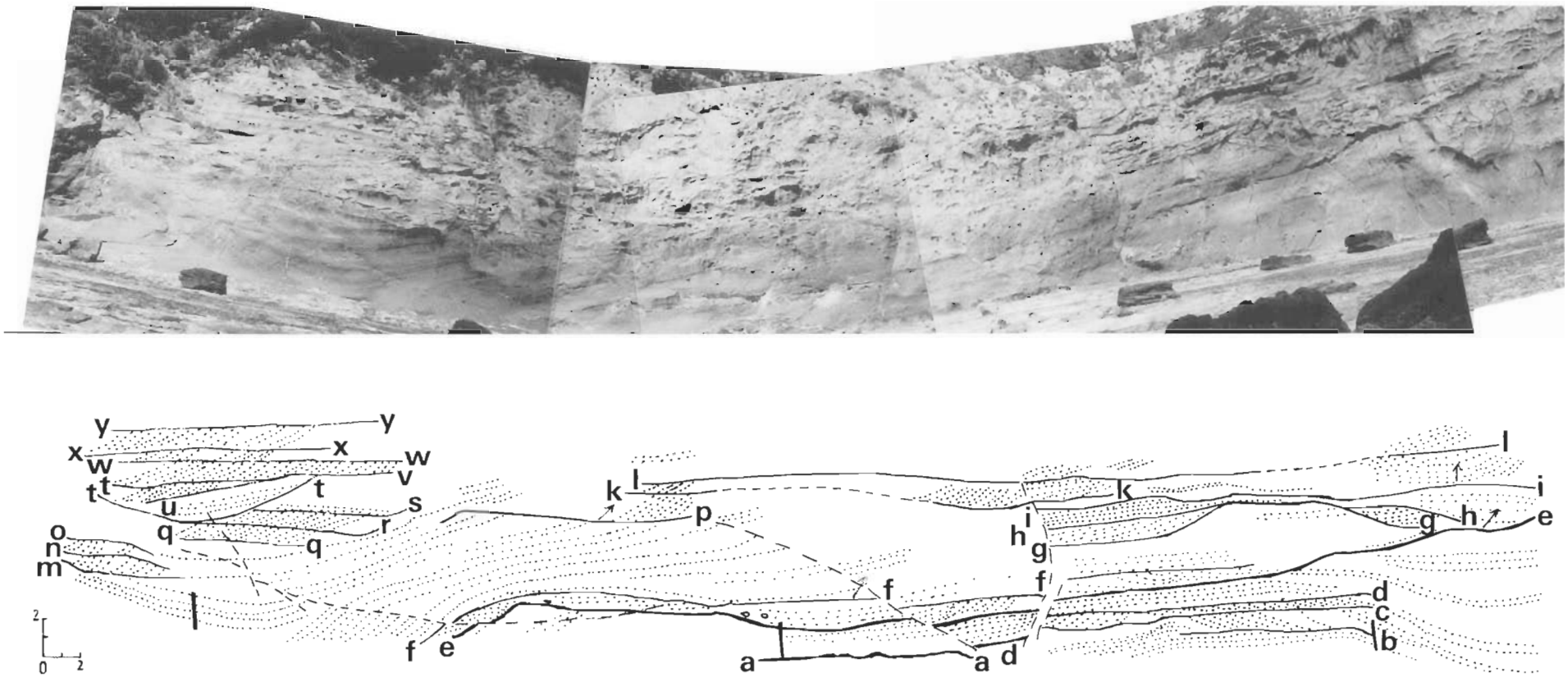

Figure 11. Cat Reef profile CR2. The measuring staff is 2 m long.

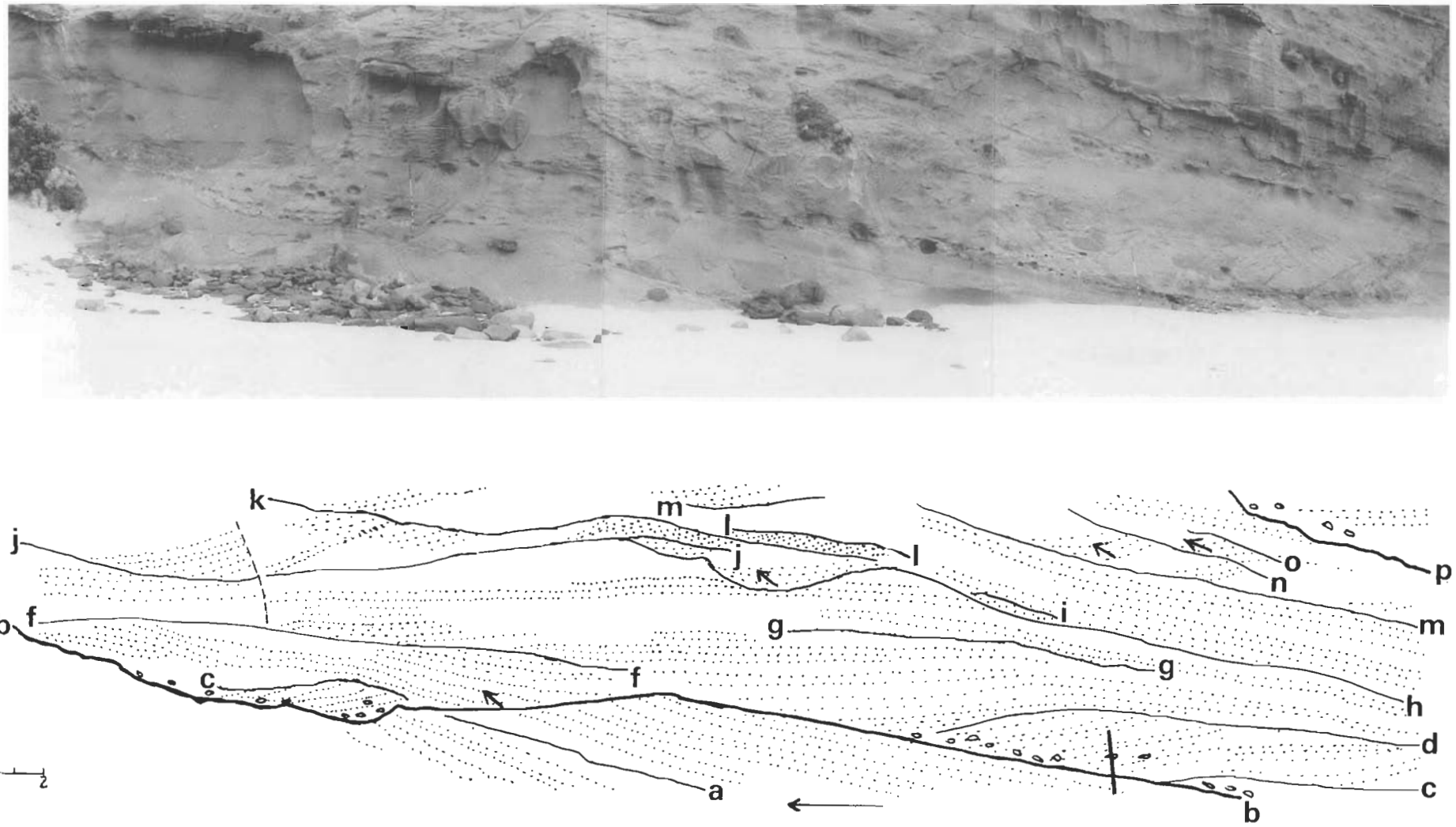

Figure 12. Johanna Beach profile JB1. The measuring staff (with 0.5- and 0.1-m graduations) is 2 m long.

are similar to channel depths estimated from the maximum preserved thickness of filled channel forms at nearby Cat Reef.

The bank-full depths of Eumeralla streams are not less than the depths of the major scours and the maximum thicknesses of bars (cf. Allen 1983). Scour depths range from 2–6 m at Blanket Bay and Marengo, and 2–4 m elsewhere (Table 6). Maximum preserved thicknesses of bars are 5 and 4 m respectively (Table 6); however, the mean height of plane-bedded bars, rarely more than 1 m, indicates a minimum depth of water in channels during bar formation as 1 m.

Slopes, sinuosities, and discharges

From determinations of the silt/clay percentages of bank and channel material, and channel width:depth ratios, in modern fluvial systems, Schumm (1960, 1972) developed methodologies for estimating discharges in straight reaches of stable alluvial channels. These methods are designated I and II respectively in the discussion which follows.

Schumm's equations may have limited application to Eumeralla rivers, whose channels were probably not stable although they probably had straight reaches. Also, Eumeralla channel forms are rarely preserved, so estimates of slope, sinuosity, and discharge based on parameters associated with them will be representative of only small parts of the fluvial system(s). Despite the limited data, internal comparisons of different parts of the system(s) are possible (Table 7).

Blanket Bay channel. The Blanket Bay channel is a moderately deep sand-and-gravel-filled scour cut into medium-grained volcaniclastic sandstone containing about 10 per cent coarse quartzose sand. It was probably cut during the rising stage of a flood. If its margins were eroded at peak flood, the estimates of its dimensions, especially width, might be too low. Percentages of silt and clay (method I), difficult to determine accurately in weathered rock, were estimated for the stream bed and bank (Table 7). Method II is preferred for calculations associated with this channel.

The estimated width:depth ratio according to method II is low, and may reflect the greater power of gravel-charged fluvial flows to cut deeper channels, or the preservation of only the deepest part of a larger channel. Sinuosity, slope, mean annual discharge, and bedload are all similar to the Cat Reef channels (Table 7). A calculated average sinuosity of 1.5 is similar to that of sandy mixed-load streams of braided or meandering character (e.g., Schumm 1972).

Cat Reef channels. These two channel forms (Table 7) are incised into older sandy deposits (Fig. 11). At least one of the margins of each of the channels is eroded. As a result, the estimates of channel widths are low, and consequently so too are the method II calculations of width:depth ratios, the lowest for any of the channels examined in this study. Despite the difficulty of determining bank and channel silt/clay percentages in weathered rocks, method I is preferred over method II owing to the uncertainty of the original widths and depths of these channels.

The estimated width:depth ratios for the two channels according to method I are intermediate between the ratios estimated by method II for the Blanket Bay and Cape Patton channels.

Cape Patton channel. The Cape Patton channel, overlying and incised into flood-plain siltstone (Figs. 4a, 4b), is probably the most completely preserved of the four channels studied, and — having silty banks — was the most stable. Both margins of the Cape Patton channel (channel 1 in Figs. 4a, 4b) are exposed in a road-cutting oriented normal to palaeoflow; a

Table 6. Comparison of Eumeralla depositional systems

	Depositional system A	*Older depositional system B*	*Depositional system B*	*Depositional system C*
Outcrops	NE of Cape Otway, SW of Apollo Bay	NW of Cape Otway (Rotten Point–Johanna Beach)	NW of Cape Otway (Cat Reef–Fiji Point)	NE of Apollo Bay
Age	Early Albian (*C. striatus Zone*)	Early Albian (*C. striatus Zone*)	Late Albian (*C. paradoxa–P. pannosus* Zones)	Early–late Albian *C. striatus, C. paradoxa*, and *?P. pannosus* Zones
Sediment composition	Volcaniclastic sand (2 Ø), granitic detritus (–1 Ø), metamorphic pebbles	Volcaniclastic sand (1–2 Ø)	Volcaniclastic sand (1 Ø), glassy volcanic pebbles	Volcaniclastic sand (2 Ø), minor granitic metamorphic pebbles and metamorphic detritus (–1 Ø) including pebbles
Character of channel tracts:				
Floor	Scours to 6 m	Scours to 2.5 m	Scours to 2.5 m, channel forms	Scours to 2.5 m, channel forms
Fill	Plane-bedded bars to 5 m thick; channel-tract sandstones to 70 m thick	Plane-bedded bars to 3 m thick; channel-tract sandstones to 40 m thick	Plane-bedded bars to 2 m thick; planar tabular cross-channel bars to 2 m thick; channel-tract sandstones to 14 m thick	Plane-bedded bars to 3 m thick; channel-tract sandstones >50 m thick
Character of flood plain (interchannel):				
Max. observed thickness	70 m	30 m	14 m	15 m
Lateral extent	?100s of metres	?100s to 1000s metres	?100s to 1000s metres	
Palaeoslope	S or N to NW	SE to NE	NE	

Table 7. Slopes, sinuosities, and discharges calculated from palaeochannel data[1]

Location and method	*Uncorrected width/stream width (m)*	*Uncorrected depth/stream depth (m)*	*% silt and clay in bank*	*% silt and clay in bed*	*Calculated width: depth ratio [range]*	*Estimated sinuosity [range]*	*Mean annual discharge ($m^3 s^{-1}$) [range]*	*Mean annual flood ($m^3 s^{-1}$) [range]*	*Slope [range]*	*Meander wavelength (m) [range]*	*Estimated radius of curvature (m)*	*% total load as bedload*
Blanket Bay												
Method I			10.0	5.0	41.3 [16.7–101.8]	1.43 [1.09–1.88]	37.79 [20.09–71.08]	358.55 [199.40–644.68]	0.00060 [0.00030–0.00118]	1910.67 [928.08–3933.57]	243.0	10.1
Method II[2]	**60.0/90.0**	**6.0/3.9**	**N/A**	**N/A**	**23.08**	**1.50** [1.14–1.97]	**45.61** [18.49–112.47]	**407.40** [165.21–1004.67]	**0.00043** [0.00021–0.00088]	**1466.32** [568.37–3782.94]	**429.2**	–
Cat Reef channel 1												
Method I			**5.0**	**5.0**	**44.8** [18.2–110.6]	**1.41** [1.07–1.84]	**34.93** [18.57–65.70]	**341.42** [189.88–613.88]	**0.00063** [0.00032–0.00125]	**1968.88** [956.35–4053.39]	**243.0**	**11.0**
Method II	60.0/90.0	10.0/6.5	N/A	N/A	13.85	1.72 [1.31–2.26]	81.23 [32.94–200.32]	570.75 [231.44–1407.49]	0.00026 [0.00013–0.00054]	1118.53 [433.56–2885.68]	429.2	–
channel 2												
Method I		**As for Channel 1**										
Method II	55.0/82.5	8.0/5.2			15.87	1.66 [1.27–2.18]	56.37 [22.86–139.03]	455.49 [184.70–1123.25]	0.00032 [0.00016–0.00067]	1132.16 [438.84–2920.85]	390.0	–
Cape Patton												
Method I			10.0	30.0	20.28 [8.22–50.01]	1.69 [1.29–2.21]	460.06 [244.58–865.40]	1802.39 [1002.42–3240.77]	0.00020 [0.00011–0.00041]	2746.55 [1334.10–5654.41]	486.0	5.28
Method II	**120.0/180.0**	**3.0/2.0**	N/A	N/A	**92.31**	**1.03** [0.79–1.35]	**51.31** [20.81–126.54]	**481.14** [195.11–1186.51]	**0.00081** [0.00039–0.0017]	**4932.09** [1911.75–12724.23]	**919.9**	–

[1] Correction for compaction of all channel-fill sandstones was estimated to be 10 per cent, and added to the measured depth of all channels.

[2] The preferred method and parameters calculated from it for each palaeochannel are emboldened.

levee is apparent at its right-hand margin (Fig. 4b). A second channel (channel 2 in Figs. 4a, 4b) partly eroded the initial incised channel; only one of its margins, adjacent to its levee, was exposed.

Owing to the erosion of channel 1, both its width and depth are underestimated; however, the exposed channel is wide, and any errors introduced into the determination of its parameters are probably less significant than for the narrower eroded channel at Blanket Bay. For this reason, calculations based on the Cape Patton channel width:depth data (method II;

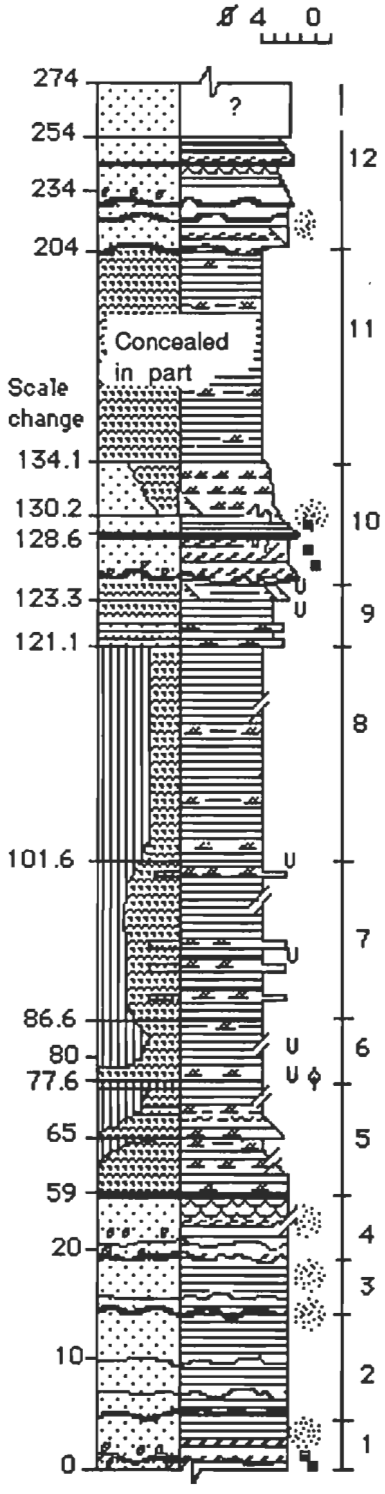

Figure 13. Blanket Bay profile BB1.

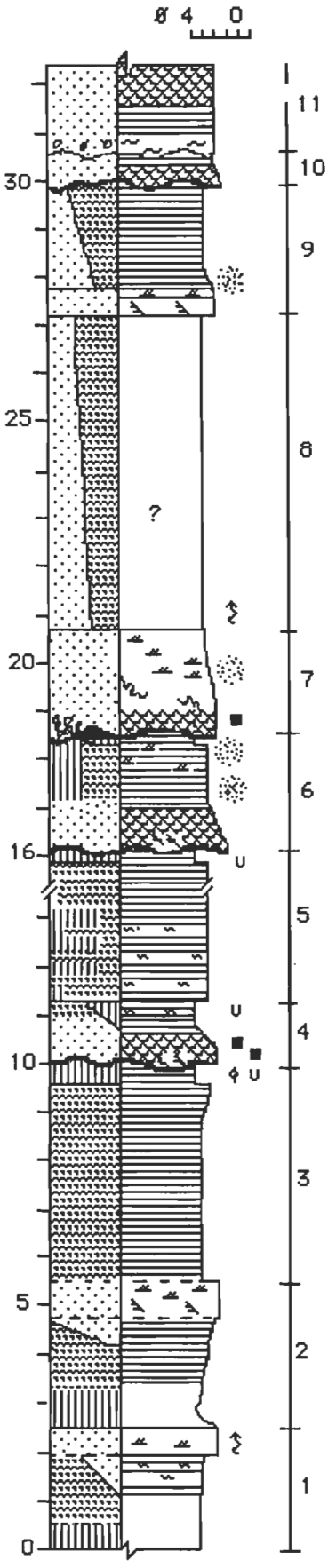

Figure 14. Browns Creek profile BC1.

Table 7) probably give the best estimates of parameters associated with Eumeralla rivers; even so, there is still considerable uncertainty in these estimates.

The Cape Patton channel has a much greater calculated width:depth ratio (92:1) than any other Eumeralla fluvial channel. It also has the lowest calculated average sinuosity and the highest calculated slope, mean annual discharge, and mean annual flood of any channel investigated.

Discussion. Even the upper limits of calculated width:depth ratios for Eumeralla stream channels (Table 7) are much less than the reported width:depth ratios of channels in sandy braided stream systems (around 200:1; Smith 1971; Cant & Walker 1976). However, the systems in these published studies have stable channels, are dominated by lower-flow-regime deposition, and are unlike the Eumeralla system(s). Eumeralla scour channels cut by rising floods are probably narrower and deeper than channels in these systems.

Calculated mean annual discharges are almost meaningless in fluvial systems for which discharge is highly variable or 'flashy'. The 'mean annual flood' would not approximate maximum discharge in an unconfined system, but may be a reasonable estimate of the discharge associated with channel cutting and scouring, before a flood peak. Calculated bedloads are low, consistent with sandy systems dominated by high-stage flow, in which most sand and all finer material would be entrained in a turbulent flow.

Regional palaeocurrents

Measured current directional features include sedimentary structures (filled channel forms, trough and planar tabular *cross-bedding*, and ripple and climbing-ripple cross-lamination marks) and linear features (sand-filled flutes and coalified logs on bedding planes). The vector trends reported here are based on two-dimensional vectorial analysis of data according to the method of Jones (1970), which corrects the data for structural dip — provided that the strata were not rotated during deformation. Felton (1992) presented a detailed statistical analysis of the data.

Vector means of large numbers of measurements of palaeocurrent directional data from channel-tract sandstone are considered best to approximate regional palaeoslopes, as large eddies may cause current movements on flood plains to vary considerably from the regional downslope direction (cf. Popov & Gavrin 1970). Dispersion (variance) of the directional data from Eumeralla channel tracts is high (Felton 1992), so vector means calculated from small numbers of measurements are much less reliable than those calculated from larger numbers, and might approach random distribution. Palaeocurrent roses incorporating the vector ranges and means of measurements are plotted in Figure 16. The data define four broad groups based on geographic location, age, and vector mean in channel-tract sandstone (Table 8).

In the Otway Ranges, three major palaeocurrent trends are apparent. Southwest of Apollo Bay, the trend is southeasterly to southwesterly; a southeasterly trend is also apparent at Rotten Point (Fig. 16). Northeast of Apollo Bay, a northwesterly trend is dominant, a direction also reported by Medwell (1977, 1988). In almost all these areas, the age of the rocks is early Albian (Wagstaff & McEwen Mason 1989). The northwesterly trend at Godfreys Creek is apparently in younger strata. An overall northerly trend, with variations from northwesterly at Red Johanna locality to northeasterly at Fiji Point, is apparent in younger (*P. pannosus* Zone) strata near Moonlight Head. Deep, northeasterly trending scour channels at Cat Reef, formed during the initial stages of major floods, are likely to be oriented parallel to the regional palaeoslope, and support the northeasterly trend at nearby Fiji Point.

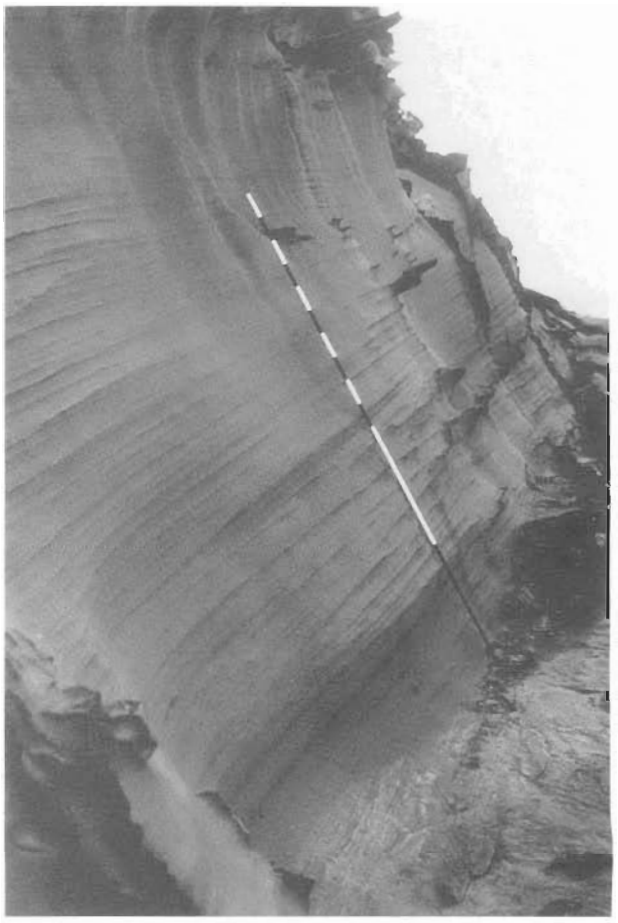

Figure 15. Blanket Bay locality. Part of a wind-eroded single set of plane-bedded sandstone, 150 m long and 4 m thick, representing a large plane-bedded simple bar. Note the carbonate-cemented siltstone intraclast stringer conglomerate (facies Gs) at the base of the bar. Elongate concretions are oriented parallel to bedding in the bar. The measuring staff (with 0.5- and 0.1-m graduations) is 2 m long.

Depositional systems

At least three discrete fluvial systems, A–C, can be recognised in the outcropping Eumeralla Formation in the eastern Otway Basin. They are distinguished by their ages, sandstone compositions, palaeocurrent directions, and dimensions of the fluvial-channel-tract and flood-plain deposits (Table 8).

Depositional system A

Marengo and Blanket Bay areas

Deposits of system A are exposed along the coast between Cape Otway and Apollo Bay (Fig. 1). System A may have evolved from an earlier fluviolacustrine system (Fig. 17) whose remnants crop out immediately north of Apollo Bay; J. Douglas (Geological Survey of Victoria, personal communication 1986) suggested that the palaeoflora in this area represent an older assemblage of his macrofloral zone C (Douglas 1969, 1986).

Although gravels are present, they are a minor part (<10%) of the observed outcrops. Roughly equal amounts of sandstone and siltstone/mudstone make up the remainder of the sedimentary section, although particles of quartz grit and weathered feldspar are common in the sandstone. A substantial part (>30%) of the framework grains in the sandstone is fine to medium epiclastic volcanic sand, whose source area is conjectural.

Mixed sandy and gravelly detritus from both basement and volcanic sources was deposited in stream channels, at least

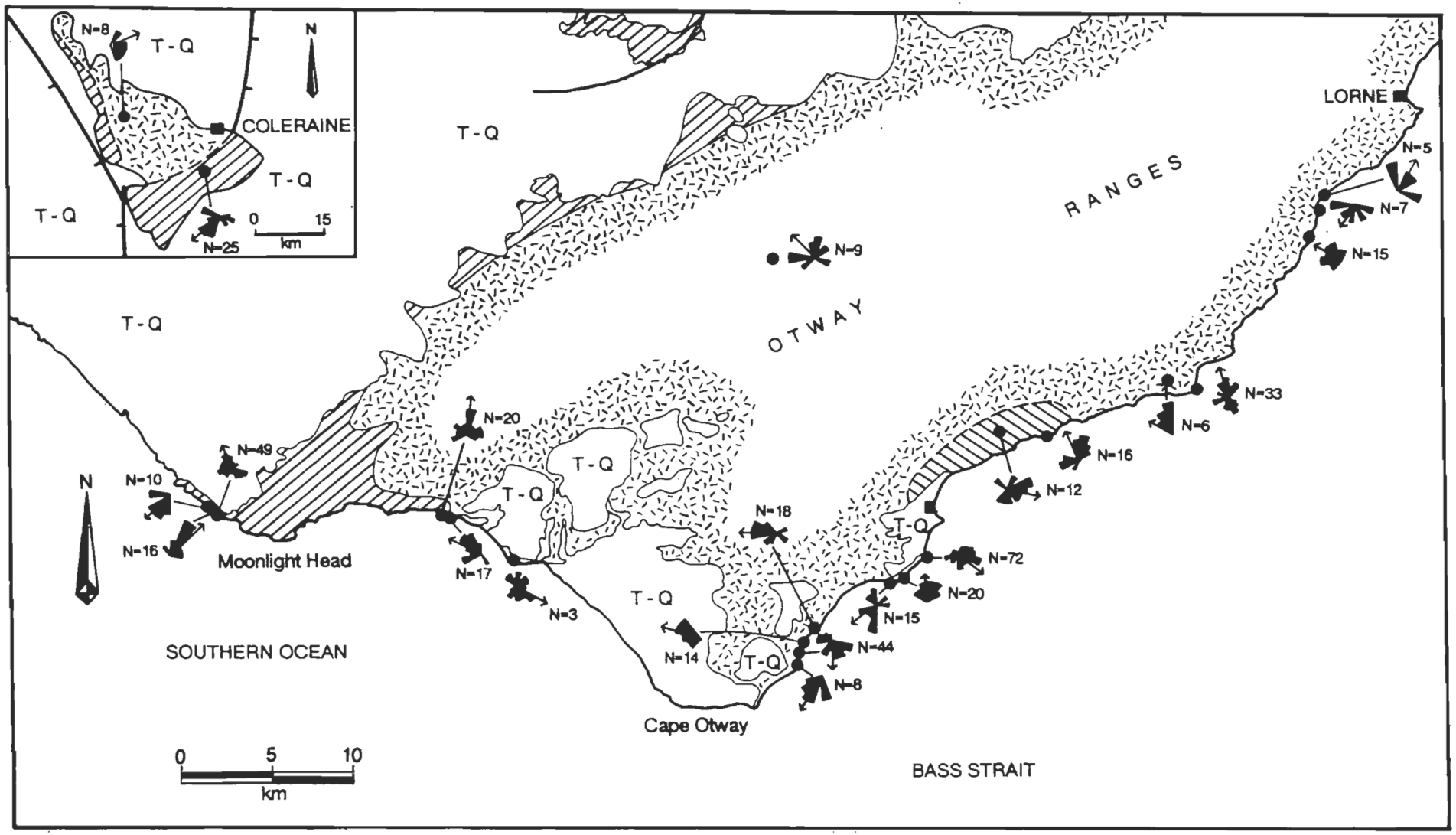

Figure 16. Palaeocurrent data for outcrops in the Otway Ranges and western Victoria.

Table 8. Summary of palaeocurrent data, Otway Group outcrops

Area	*Microfloral/ macrofloral zone*	*Vector mean(°)*	*Direction*	*Facies association*	*Depositional system*
Southwest of Apollo Bay					
Marengo	*C.* striatus[1]	127.46	S	Channel tract	A
Blowhole	*C. striatus*[2]	5.22	N	Channel tract	A
		239.21	SW		
Blanket Bay	*C.* striatus[1]	275.70	W	Channel tract	A
		284.34	WNW		
		178.67	S		
		211.32	SSW		
Northeast of Apollo Bay					
Skenes Ck Rd	'lowest zone C'[3]	105.73	ESE	Lacustrine	?A
Browns Creek	'lowest zone C'[3]	333.01	NW	Flood plain/ lacustrine	?A
Cape Patton	*C. striatus*[2]	342.17	NW	Channel tract	C
Holtzers Quarry	*C. striatus*[4]	300.30	NW	Channel tract	C
Beech Forest Quarry	*Speciosus* assemblage[5]	319.17	NW	Channel tract	C
Godfreys Creek	?*P. pannosus*[2]	299.28	NW	Channel (abandonment)	C
Artillery Rocks	*Speciosus* assemblage[5]	212.65 26.73	SSW NNE	Channel tract	C
Near Rotten Point					
Rotten Point	*C. striatus*[1, 2]	115.62	SE	Channel tract	B
Moonlight Head					
Johanna Beach	*C. paradoxa*[2]	7.48	N	Channel tract	B
Red Johanna	*C. paradoxa*[2]	296.28	NW	Channel tract	B
Cat Reef	*P. pannosus*[2]; zone D[6]	339.24	NNW	Channel tract	B
Fiji Point	zone D[6]	43.61	NE	Channel tract	B
Wreck Point	zone D[6]	223.44	SW	Channel tract	B

[1] Wagstaff & McEwen Mason (1989).
[2] Burger (1987).
[3] J. Douglas (personal communication 1986).
[4] Burger (1985).
[5] Geological Survey of Victoria (1973).
[6] Benedek & Douglas (1988, p. 225).

6 m deep in places, cut by the scouring action of the coarser material. Sediment-laden waters overspilled channel banks and deposited thick (up to 70 m) siltstone- and mudstone-dominated sequences in interchannel areas. Facies architecture, sediment composition, and texture suggest that the Apollo Bay deposits accumulated in a medial-fan to proximal braided-stream setting (Fig. 17).

Discussion

The common presence of granitic grit, subrounded to well-rounded schist pebbles, and weathered granite pebbles attests to erosion of nearby pre-Mesozoic basement, and transportation of the clasts several kilometres by water from an area northwest of Apollo Bay.

The maximum size of clasts in alluvial sequences is an indicator of proximity to source, according to Rust & Koster (1984), who used plots of maximum clast size versus distance from source to derive fields for modern alluvial-fan and alluvial-plain environments. The largest clasts observed at Blanket Bay and Marengo are granite, 25 cm in diameter, and fall within the area of overlap of fields from alluvial fans and braided rivers/alluvial plains. If system A is part of a fan, these clasts are 2 to 10 km from their source; if part of a braided river system, the range of distances may be much greater, up to 80 km.

Depositional system B

Moonlight Head and Rotten Point areas

Depositional system B is best developed along the coast northwest of Cape Otway. Near Moonlight Head (Fig. 1), system B lacks a basement-derived gravel component, and has palaeocurrent vectors markedly dissimilar to those of system A, which is older (Table 6). In addition, a greater, although still minor, proportion of lower-flow-regime deposits — mainly medium- to large-scale planar tabular cross-channel bars — is preserved in parts of depositional system B, although many other aspects of fluvial style are common to both systems.

Some features of the sequence at Rotten Point are common to systems A and B (Table 6). This sequence is about the same age as system A (*C. striatus* Zone), and has a southeasterly palaeocurrent vector mean. However, it lacks basement-derived gravel, and its multistorey channel-tract sandstone bodies are thinner than those of system A, but thicker than those of system B. The prevailing fluvial regime under which it evolved did not favour the development of coal swamps or incipient

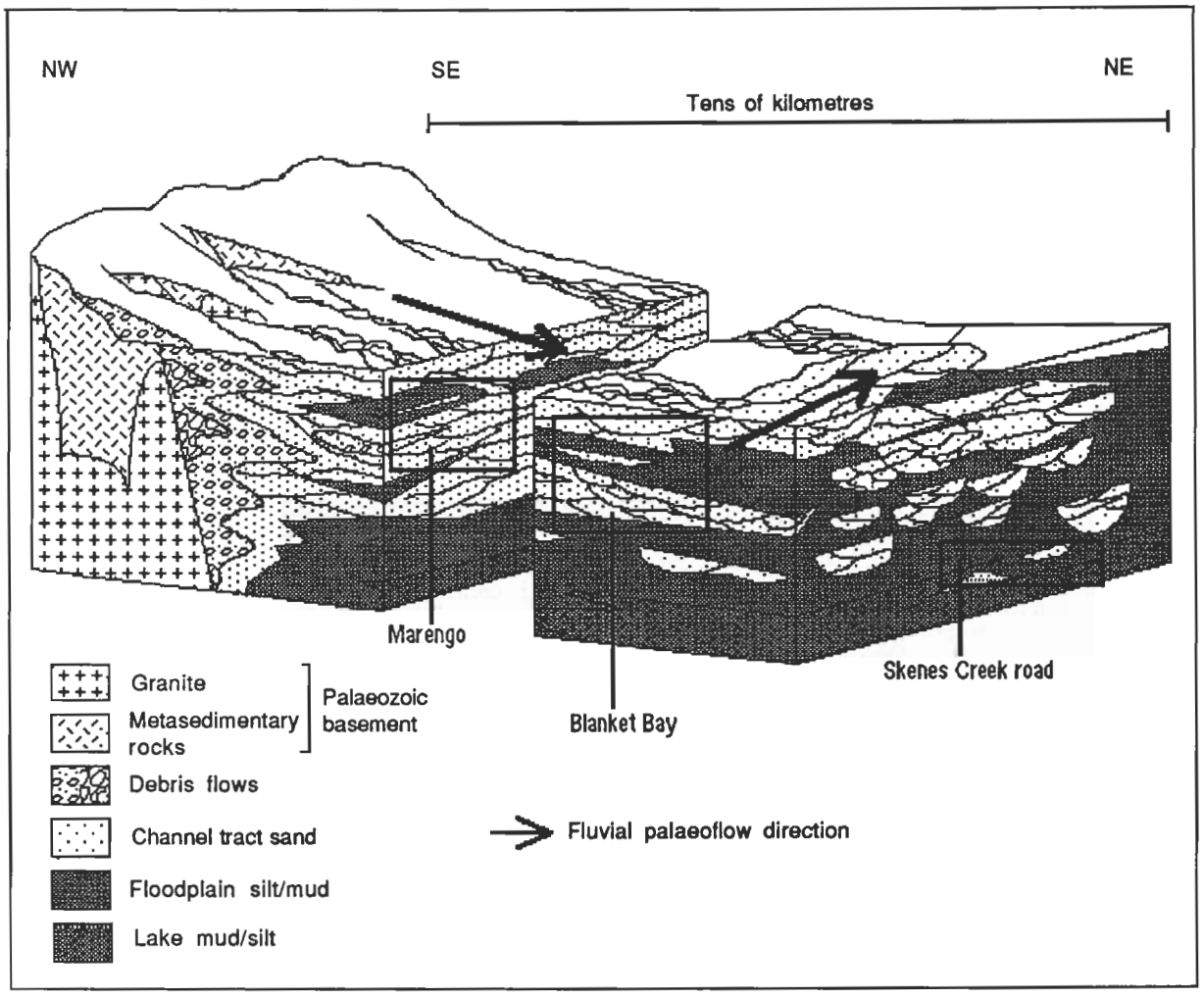

Figure 17. Block diagram of depositional system A: alluvial-fan/braid-plain deposition adjacent to structurally elevated basement.

soils, unlike system B. The sequence is interpreted as an older part of system B.

Discussion

Depositional systems in which sand-size and finer debris comprise the entire depositional products, and in which high-stage flows are the norm, are rarely described (e.g., Allen 1983; Tunbridge 1984); the few modern examples are attributed to rare catastrophic flooding whose depositional products are isolated within sediments reflecting more 'normal' depositional conditions (Osterkamp & Costa 1982), or are exposed to low-flow reworking or likely to undergo other substantial post-depositional modification (e.g., McKee et al. 1967). Most sandy systems described in the literature are characterised by low-flow-stage deposition of sand in braided or meandering streams subject to moderate hydrodynamic regimes (see reviews by Miall 1977; Walker & Cant 1984).

Such models are inappropriate for depositional system B, whose interpretation must rely on lithofacies, bedforms, and geometry. In system B, scour-and-fill accompanied the initial stages of floods which subsequently spread widely beyond the scour channels to form broad active stream tracts. System B is characterised by multistorey sandstone bodies up to 14 m thick, representing channel-tract deposition, separated by interchannel siltstones of similar thickness which locally contain thin coal beds, rooted horizons, and reddened soil profiles. The soil profiles, best developed immediately below thick sandstones, indicate that some interchannel (flood-plain) areas were inactive and exposed for long periods before they were reoccupied by new channel tracts.

This fluvial system is interpreted as a braid plain (Fig. 18). Multiple active stream tracts, dominated by upper-regime fluvial flow, were only weakly channelised. The absence of gravel (apart from mudstone intraclasts) in depositional system B is atypical of braid-plain deposition described in the literature (see Rust & Koster 1984 for a review of braid-plain sedimentology), but the lithofacies and bedforms of gravelly systems described by Rust & Koster (1984) are analogous to the depositional features of the Eumeralla sandy channel tracts. A number of features — namely, the dominance of sandy volcaniclastic sediment, rare pebbles of devitrified glassy volcanic rocks, and the local presence of possible debris-flow and hyperconcentrated stream-flow deposits — suggest that depositional system B was part of an apron flanking source volcanoes. Palaeocurrent vectors indicate that the volcanic sources were located southwest to southeast of Moonlight Head, perhaps in the axial part of the rift.

Depositional system C

North of Skenes Creek

Fluvial sedimentary rocks that crop out along 20 km of coastline between Skenes Creek and Lorne have some features in common with both systems A and B (Table 6), but have northwesterly palaeocurrent vectors and are interpreted as part of a third, distinct, depositional system (depositional system C). The ages of these outcrops are mainly early Albian (Wagstaff & McEwen Mason 1989), corresponding to the *C. striatus* and lower *C. paradoxa* Zones, but some are younger (*P. pannosus* Zone; Burger 1985).

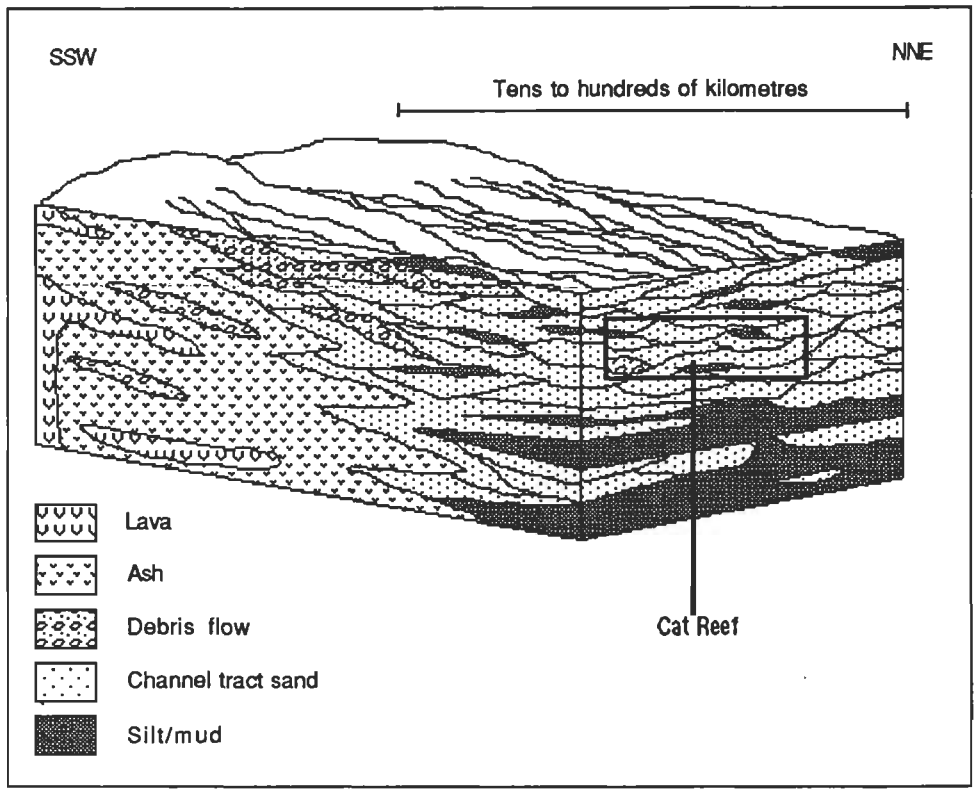

Figure 18. Block diagram of depositional system B: braid-plain deposition on the distal flanks of rift-axis volcanic complexes.

This system is sandstone-dominated (>90% of the coastal section), and its facies associations and fluvial architecture are similar to depositional system B. As for systems A and B, stream tracts of system C were dominated by upper-regime fluvial flow. Some channels initially were deeply scoured (up to 6 m at Cape Patton; Table 3), but the bases of most channels were flat or gently undulating (Figs. 3, 4a, 4b, 5).

The multistorey channel-tract sandstones of system C are several tens of metres thick (e.g., at Cape Patton; Table 3; see also Fig. 5). Dark grey interchannel siltstone and fine sandstone, where exposed, are seldom more than a few metres thick. Fossil soil has not been observed, but thin coal is locally preserved beneath channel bases (Fig. 3). Coalified logs up to 25 cm in diameter are common in the channel sandstones at many locations. These features indicate that system C consisted of large active channel tracts with fluctuating but probably perennial flow.

Discussion

This fluvial system is interpreted as representing a large braided river or possibly a braid plain. Unweathered volcaniclastic sandy detritus, which constitutes the bulk of the system, suggests that the major source of sediment supply was from contemporaneous volcanism, to the southeast. If this source was near the axis of the Otway rift, it was more distal to system C than to system B, consistent with the absence of debris flows and volcanic pebbles from system C.

System C might represent a late stage in the evolution of a formerly axial west-draining trunk stream (south of the present Otway Ranges) displaced to the north as volcanism developed at several locations along the rift axis. Alternatively, northerly drainage from extensive volcanic complexes near the rift axis south of Moonlight Head may have been diverted around the elevated basement block interpreted to have been present west of Apollo Bay. The presence of granitic and metamorphic clasts in gravel in system C could support either interpretation.

Other systems

Western Victoria

Exposures of fine-grained fluvial deposits at several localities in western Victoria consist mainly of siltstone, and subordinate thin sandstone with small-scale trough cross-bedding, indicating low-energy depositional conditions. Stacked soil profiles at one locality (see Felton 1992 for details) indicate long periods of exposure and low rates of sediment accretion. These sedimentary features are consistent with the interpretation of a distal braid plain, and the outcrops may represent the distal parts of system B.

A few outcrops indicate higher-energy depositional conditions in the fluvial system. They include a high proportion of basement-derived quartzose gravel. The well-rounded pebbles in the gravel may indicate second-cycle deposition and/or considerable transport. Most of these outcrops are mapped as part of the older *speciosus* microfloral assemblage of Dettman (1963; Geological Survey of Victoria 1971), but cannot otherwise be correlated with Eumeralla Formation outcrops elsewhere in the basin, or with the finer-grained outcrops, which are mapped as part of Dettman's (1963) *paradoxa* assemblage.

Barrabool Hills, west of Geelong

The northern Otway Ranges in the Barrabool Hills (fig. 3 in part I) consist of a fault-bounded elevated block composed of Palaeozoic basement and Eumeralla Formation rocks. Cobble beds containing rounded clasts of locally derived metasediments and greenstones near the faults are probably basal conglomerates in the Cretaceous (?Eumeralla Formation) sequence, but no contacts with basement are exposed. The cobble beds are interbedded with mud-draped pebbly cross-bedded quartz-lithic sandstone, poorly sorted and containing a volcaniclastic component. Eumeralla Formation mudstones higher in the same section along the Barwon River are dated as Albian on microfloral evidence (Cookson & Dettmann 1958).

The sequence probably represents part of an alluvial fan

or valley fill flanking elevated basement, exposed less than 1 km away. Although it is not part of depositional system A, its setting is similar to but more proximal than the exposed parts of system A.

Conclusions

At least three discrete fluvial depositional systems are apparent in the Eumeralla Formation. Depositional systems A–C are distinguished by sediment composition, geography, age, sandstone geometry, and facies architecture.

The systems are sand-dominated. They are characterised by high-stage flow regimes, and 'flashy' discharge. Multistorey sandstones accumulated to tens of metres in thickness in broad active stream tracts which were largely unconfined by banks. The stream tracts have an overall braided character, but do not conform to published models of sandy braided stream systems. Bedforms and sedimentary structures are more akin to those of gravelly systems.

Depositional system C represents a northwest-flowing, formerly axial drainage in the Otway rift system. It was displaced to the north by the onset of axial volcanism and an associated volcaniclastic apron. System B is part of the epiclastic medial to distal apron formed on the northern flank of a volcanic complex on or near the rift axis. System A is of more local extent, and represents part of an alluvial fan flanking an elevated basement block of Palaeozoic metasediments and granite west of Apollo Bay. The block may also have contributed to displacement and diversion of a west-flowing trunk stream in the Otway rift towards the northern basin margin.

The depositional model proposed for the outcropping Eumeralla Formation implies that the contemporaneous volcanism which contributed the bulk of the detritus to the unit occurred largely at the rift axis. Sedimentary evidence suggests that at least one substantial volcanic complex was located southwest of Cape Otway, probably close to the present-day shelf edge. Other volcanic complexes farther southeast supplied epiclastic detritus to system C.

Acknowledgments

I thank Professor Alan Cook, former Head of the Department of Geology, the University of Wollongong, for encouraging me to undertake a PhD study of the Otway Basin; and my supervisor, Dr Brian Jones, for advice, encouragement, and the opportunity to examine modern braided ephemeral river systems in northern Australia in 1988. I also thank Mr John Cramsie and Dr Bob Dalgarno, who, as successive Directors of the Geological Survey of Victoria, permitted me to examine and sample core and cuttings from the Otway Basin. I thank staff at government core laboratories in Victoria, South Australia, and the ACT for their assistance in locating relevant material, in particular Mr Joe Staunton of the Core & Cuttings Laboratory, Canberra, ACT.

The PhD study was undertaken with the assistance of a Commonwealth Postgraduate Study Award during 1986–1988.

References

Allen, J.R.L., 1983. Studies in fluviatile sedimentation: bar-complexes and sandstone sheets (low-sinuosity braided streams) in the brownstones (L. Devonian), Welsh Borders. Sedimentary Geology, 33, 237–293.

Allen, J.R.L., 1984. Sedimentary structures. Their character and physical basis. Elsevier, Amsterdam.

Benedek, S. & Douglas, J.G., 1988. Otway Basin, eastern part. In: Douglas, J.G. & Ferguson, J.A. (editors), Geology of Victoria. Geological Society of Australia, Melbourne, 222–228.

Burger, D., 1985. Palynological report on samples from Holtzers Quarry, Otway Basin, Victoria. Bureau of Mineral Resources, Australia, Professional Opinion, Geology, 85.004

Burger, D., 1987. Palynological examination of samples from the Otway Group in the Otway Basin, Victoria. Bureau of Mineral Resources, Australia, Professional Opinion, Geology, 87.006

Cant, D.J. & Walker, R.G., 1976. Development of a braided fluvial facies model for the Devonian Battery Point Sandstone, Quebec. Canadian Journal of Earth Science, 13, 102–119.

Cant, D.J. & Walker, R.G., 1978. Fluvial processes and facies sequences in the sandy braided South Saskatchewan River, Canada. Sedimentology, 25, 625–648.

Cookson, I.C. & Dettmann, M.C., 1958. Some trilete spores from upper Mesozoic rocks from the eastern Australian region. Proceedings of the Royal Society of Victoria, 70, 95–128.

Dettman, M.E., 1963. Upper Mesozoic microfloras from southeastern Australia. Proceedings of the Royal Society of Victoria, 77, 1–148.

Douglas, J.G., 1969. The Mesozoic floras of Victoria, parts 1 and 2. Geological Survey of Victoria, Memoir 28.

Douglas, J.G., 1986. The Cretaceous vegetation and palaeoenvironment of the Otway Group sediments. In: Glenie, R.C. (editor), Second southeast Australia oil exploration symposium. Petroleum Exploration Society of Australia, 233–240.

Felton, E.A., 1992. Sedimentary history of the Early Cretaceous Otway Group, Otway Basin, Australia. PhD Thesis, The University of Wollongong, Wollongong, Australia.

Friend, P.F., 1983. Towards the field classificiation of alluvial architecture in sequence. In: Collinson, J.D. & Lewin, J. (editors), Modern and ancient fluvial systems. International Association of Sedimentologists, Special Publication 6, 345–354.

Friend, P.F., Slater, M.J., & William, R.C., 1979. Vertical and lateral building of river sandstone bodies, Ebro Basin, Spain. Journal of the Geological Society, London, 136, 39–46.

Geological Survey of Victoria 1971. Hamilton 1:250 000 geological sheet SJ54–7. Geological Survey of Victoria, Melbourne, Australia.

Geological Survey of Victoria 1973. Colac 1:250 000 geological sheet SJ54–12. Geological Survey of Victoria, Melbourne, Australia.

Jones, B.G., 1970. A computer programme for analysing directional data designed for use on a CDC3600. Bureau of Mineral Resources, Australia, Record 1970/67.

Kesel, R.H., Dunne, K.C., McDonald, R.C., Allison, K.R. & Spicer, E., 1974. Lateral erosion and overbank deposition in the Mississippi River in Louisiana caused by 1973 flooding. Geology, 2, 461–464.

Leopold, L.B. & Wolman, M.G., 1957. River channel patterns: meandering, braided and straight. United States Geological Survey, Professional Paper 282–B, 1–85.

McKee, E.D., Crosby, E.J. & Berryhill, H.L., 1967. Flood deposits, Bijou Creek, Colorado. Journal of Sedimentary Petrology, 37, 829–851.

Medwell, G.J., 1977. Palaeocurrent directions on Otway Group sediments, Otway Ranges, southeastern Australia. Proceedings of the Royal Society of Victoria, 89, 27–50.

Medwell, G.J., 1988. Otway Ranges. In: Clark, I. & Cook, B.J. (editors), Victorian geology excursion guide. Australian Academy of Science, 133–156.

Miall, A.D., 1977. A review of the braided river depositional environment. Earth Science Reviews, 13, 1–62.

Miall, A.D., 1978. Lithofacies types and vertical profile models in braided river deposits: a summary. In: Miall, A.D. (editor), Fluvial sedimentology. Canadian Society

of Petroleum Geologists, Memoir 5, 597–604.
Miall, A.D., 1985. Architectural element analysis: a new method of facies analysis applied to fluvial systems. Earth Science Reviews, 22, 261–308.
Osterkamp, W.R. & Costa, J.E., 1982. Changes accompanying extraordinary flood in a sand-bed stream. In: Mayer, L., (editor), Catastrophic flooding. Binghamton Symposia in Geomorphology, International Series, 18. Allen & Unwin, Boston, 201–224.
Popov, I.V. & Gavrin, Y.S., 1970. Use of aerial photography in evaluating the flooding and emptying of river flood plains and the development of flood-plain currents. Soviet Hydrology, 5, 413–425.
Rust, B.R. & Koster, E.H., 1984. Coarse alluvial deposits. In: Walker, R.G. (editor), Facies models, second edition. Geoscience Canada Reprint Series, 1, 53–69.
Schumm, S., 1960. The shape of alluvial channels in relation to sediment type. United States Geological Survey, Professional Paper, 352–B, 17–30.
Schumm, S., 1972. Fluvial palaeochannels. In: Recognition of ancient sedimentary environments. Society of Economic Paleontologists and Mineralogists, 16, 98–107.
Simpson, C. & Doutch, H.F., 1977. The 1974 wet-season flooding of the southern Carpentaria Plains, northwest Queensland. BMR Journal of Australian Geology & Geophysics, 2, 43–52.
Smith, N.D., 1971. Transverse bars and braiding in the lower Platte River, Nebraska. Geological Society of America, Bulletin 82, 3407–3420.
Struckmeyer, H.I.M. & Felton, E.A., 1990. The use of organic facies for refining palaeoenvironmental interpretations: a case study from the Otway Basin, Australia. Australian Journal of Earth Sciences, 37, 351–364.
Tunbridge, I.P., 1984. Facies model for a sandy ephemeral stream and clay playa complex: the Middle Devonian Trentishoe Formation of north Devon, U.K. Sedimentology, 31, 697–715.
Wagstaff, B.E. & McEwen Mason, J., 1989. Palynological dating of Lower Cretaceous coastal vertebrate localities, Victoria, Australia. National Geographic Research, 5, 54–63.
Walker, R.G. & Cant, D.J., 1984. Sandy fluvial systems. In: Walker, R.G. (editor), Facies models, second edition. Geoscience Canada Reprint Series, 1, 71–89.

Appendix. Profile descriptions

The profiles described below are representative of Eumeralla lacustrine and fluvial systems. They are located in Figure 1, and supported by keys presented in Figure 2 (for the long profiles) and figure 11 in part I of this paper (for the vertical profiles). Bedding contacts are classified according to the hierarchical system of Allen (1983).

Cape Patton

Profile CP1 (Fig. 3; Figs. 4a, 4b). Profile CP1, in a road cutting at Cape Patton (Fig. 3), is 14 m long and 11 m high and trends 070°, roughly normal to the depositional dip (towards 340°; away from camera). Figures 4a and b are continuous with profile CP1, but at a larger scale. They illustrate the passage of a basal channel sandstone body into levee siltstones at its right-hand margin. An overlying channel sand also passes laterally into a levee sequence containing thin fining-upward splay sand beds. The levees have an apparent dip away from the channel sandstones owing to the greater compaction of interbedded finer sediments.

Bedding contact **a** (Fig. 3) is a concordant to discordant erosional third- or higher-order contact at the base of a sandstone body at least 12 m thick overlying sediments of lithofacies Fl, Fm, and C (Table 2). Erosional relief on contact **a** is probably less than 50 cm. Other major bedding contacts in the profile are planar concordant to discordant erosional surfaces, usually truncating zeroth-order internal lamination in underlying beds. Contact **e** truncates fining-upward bed **de**, and is probably second order, but all other bedding contacts are first order.

Most individual beds consist of single plane-bed or low-angle cross-bed sets (lithofacies Sh and Sl) 70 cm to 1.2 m thick, which are sheet-like or elongate-lenticular within the length of the outcrop (60 m). These beds are probably simple plane-bedded bars. Shallow scours in places are filled by lithofacies Ss (**ab**, **ef**, **ij**).

Holtzers quarry

Profile HQ1 (Fig. 5). This profile is exposed in a quarry face trending 250°, 50° oblique to the vector mean palaeocurrent direction of 300° (away from camera) determined from measurements at the base of the opposite face of the quarry. Apparent structural dip is to the right (true dip is 30°/140°). The profile is about 50 m long and 12 m high. The total height of the quarry face is about 30 m.

The nature and extent of many low-order bedding contacts cannot be ascertained with certainty. Most appear to be first-order concordant to discordant erosion surfaces bounding plane-bed or low-angle cross-bed sets (**h**, **i**, **k**, **e**, **f**, **g**, **c**); **o** may be a reactivation surface.

d is a second- or third-order bedding contact defining the base of a channel form. Its oblique cross-section width in outcrop is about 30 m, and its depth 4 m. A lateral component is apparent in the channel fill **do**, which consists of lithofacies Sh and Sl. **l** may be a lateral accretion surface. **dj** is a small low-angle bed set in the channel base.

Facies Sl and Sh are prominent in the sandstone underlying the channel. Intervals **ef** and **fg** may be parts of large cross-bed sets or the low-angle margins of bars. Intervals **ac** and **cd**, which extend laterally for several tens of metres and are 2 to 3 m thick, are probably simple plane-bedded bars.

Elsewhere in the quarry, but not apparent in the profile, small-scale trough and planar tabular cross-bed sets, up to 35 cm thick, are locally developed in silty sandstone at the tops of plane-bed cosets; they are usually isolated single sets, or consist of two to three sets separated by reactivation surfaces. Thin intervals of laminated mudstone and siltstone may drape their tops, and commonly pass laterally into a thin layer of mudclasts (lithofacies Gs) at the base of a succeeding plane-bed set. Small-scale cross-bedded sandstone a few centimetres thick may be interbedded with the mudstone and siltstone.

The exposures in the quarry are interpreted as part of the channel tract of a large river in which rising floodwater or increasing flows cut shallow channels in underlying sands. Plane-bed cosets topped by cross-beds represent large compound bars developed during upper-regime fluvial flows. Flow fluctuations and waning flows promoted deposition of the cross-bedded finer-grained sediments atop the bars; mud and silt were deposited during periods of slack-water.

Rotten Point

Profile RP1 (Fig. 6). Profile RP1 is located on the eastern side of a small headland 150 m east of Rotten Point. The profile is 44 m long. About 10 m of vertical section is exposed, including units 10, 11, and 12 in the vertical profile RP3 (Fig. 8); intervals **ai**, **ij**, and **jl** are units 10, 11, and part of 12 respectively. The trend of the profile is 240°, 60° oblique to the depositional dip towards 180° (to the left). True structural dip is 22°/300° (away from the camera).

Profile RP1 consists of lithofacies Sh, Sl, and rarely St (70% of section), which sharply fine upwards into Sr, Fl, and

Fm (30% of section).

Bedding contacts **a**, **i**, and **j** are concordant to discordant erosional surfaces of third order or higher. **c**, **f**, and **g** are second-order erosional contacts forming the lower boundaries of small, fine- to medium-grained sand-filled channel forms. **e** is also a second-order contact at the base of a thin laminated and rippled sandstone sheet within interval **ai**. Other contacts (**b**, **k**, and **l**) are first-order concordant to discordant erosional to non-erosional surfaces bounding plane-bedded sandstone sheets within thicker sandstone/mudstone sheets (intervals **ai**, **ij**, and **jl**) bounded by higher-order contacts.

The sandstone/mudstone units are interpreted as the products of sheet-floods which, during high-stage flow, deposited considerable thicknesses of laminated sand as essentially unchannelled sand sheets on a flat fluvial plain, such as a braid plain or distal alluvial fan. Six probable floods can be identified in units 10–12 (Fig. 8). Flow waned abruptly, but deposition of fine sand, silt, and mud continued, and built up considerable thicknesses of sediments (up to 2 m compacted thickness), too thick to be attributed to a single flood. Much accumulated fine sediment might have been supplied by periodic overbank deposition from remote fluvial channel tracts (e.g., upper half of unit 10; Fig. 8). Some sediment might have been deposited by overbank deposition from minor flood-plain distributaries, represented in the profile by the small sandstone-filled channel forms bounded by surfaces **g** and **h**.

Profile RP2. Profile RP2 (Fig. 7) exemplifies the nature of deposition in part of a 35-m-thick sandstone forming cliffs 30 m high 500 m east of Rotten Point. The top of the outcrop illustrated in Figure 7 lies about 5 m below the base of profile RP3 (Fig. 8), in which units 1–9 constitute the top of the thick sandstone.

The outcrop comprising RP2 is inaccessible to detailed examination, so that depositional and structural dip could not be determined from actual outcrop measurement. Structural dip is assumed to be 22°/300°, the same as much of the Rotten Point sequence nearby. The depositional dip is assumed to be oriented about 170°, according to the vector mean palaeocurrent direction determined for units 1–7 in RP3 (Fig. 8). Profile RP2 trends 190° (to the right of Fig. 7), and so is oriented about 20° oblique to the depositional dip, away from the camera. It represents about 5 m of section, and is 13 m long.

Mainly first-order bedding contacts appear to be present in RP2, which consists almost entirely of low-angle cross-beds (lithofacies Sl) with similar orientations. The surfaces are concordant to discordant erosional, and truncate zeroth-order contacts within individual beds; most are subparallel to one another, and define principal bedding in the sequence. Contacts **d** and **l** may be second-order contacts; they are locally scoured, and separate beds with distinctly different orientations of laminae which reflect different palaeocurrent vectors.

Intervals **de** and **lm** are scours filled by lithofacies Ss. All other beds are sheets or elongate lenses ranging in thickness from 20 to 60 cm. In beds **df**, **hj**, **jk**, and **mn**, the internal laminae reverse their dip direction over a few metres. In other beds (e.g., **bd**), the dip angle of internal laminae varies along the bed, and locally is parallel to the bed base. Also, in beds **jl** and **lo**, dip angles of internal laminae steepen toward the bed top, and the laminae increase in thickness.

In the centre and right of bed **bd**, the gently dipping internal laminae thicken downdip to an estimated maximum of 15 cm where they meet the base of the bed. Similar thickened beds in lithofacies Sl in unit 4 of profile RP3 (Fig. 8) consist of laterally persistent interbeds of internally laminated upper fine-grained (to 15 cm thick) and lower coarse-grained (to 20 cm) sandstone (Fig. 9). One interbed 15 cm thick consists of climbing-ripple fine-grained sandstone with mud flasers (Fig. 10); the basal contact of overlying coarse sandstone is load-casted into the finer unit.

The beds in RP2 are interpreted as low-relief cross-bedded simple bars deposited in upper-flow-regime conditions. The low angle of the cross-bedding is due to suppression of flow separation at the bar margins. Lateral and oblique accretionary growth of the bar margins relative to mean palaeocurrent direction is evident from the development of thickened laminae in bed **bd**, and is inferred from the predominance of low-angle cross-bedding in other beds. Although some of the plane-bedded tops of bars have been removed by erosion, I suspect that only small amounts of sand were deposited on the bar tops, and that most deposition took place on the downstream and side margins of bars in conditions of somewhat lower (but still upper- or transitional-stage) flow regime than that prevailing on the bar top. Small-period fluctuations in flow along the sides and fronts of bars promoted the development of thicker laminae and thin beds as sediment was dumped in conditions of lower flow.

Profile RP3 (Figs. 8–10). The succession at Rotten Point represents deposition in an active flood basin, probably on a braid plain. Units 1–9, the upper part of a multistorey channel-tract sandstone 35 m thick, are representative of deposition throughout the sandstone. Units 8–9 record abandonment of the active channel. The remaining 62 m consists of fining-upward sheet sandstones of different thicknesses — probably splay sandstones spilt from sandy channels during floods — separated by intervals of laminated and rippled siltstone; units 10–12 are illustrated in Figure 6. Bioturbation, soft-sediment deformation, and water-escape features also attest to frequent inundation.

The absence of coal beds and pedogenic features distinguishes the environment of this flood-plain sequence from that represented in Cat Reef profile CR1.

Cat Reef

Profile CR1 (figs. 15–17 in part I). This profile is described in part I. The base of unit 3 corresponds to the bedding contact **aa** in profile CR2.

Profile CR2 (Fig. 11). The Cat Reef locality, in the youngest known part of the exposed Eumeralla Formation, is close to the western limit of the Otway Ranges coastal outcrops (fig. 3 in part I). The cliff face exposure illustrated is 10 m high and 55 m long; it trends 330°, roughly normal to the trends of the major channels (030°). The calculated vector mean palaeocurrent direction of 340° for the entire Cat Reef section (Felton 1992, appendix 4A) diverges from vector means calculated for individual units from the lower part (units 3, 4, 7, and 8 of fig. 15 in part I), including this profile. The structural dip of the profile is 15°/290° (towards and to the left of the camera).

Overall, the section at Cat Reef/Fiji Point consists of 93 per cent sandstone, including rare thin lenticular muddy siltstones filling shallow depressions in the tops of sandstone storeys. The remaining 7 per cent consists of siltstone and mudstone, pedogenised in part (fig. 18 in part I), thin lenticular sandstones, and rare beds of carbonaceous mudstone and coal.

Two large channel forms (**ae** and **ey**), filled by medium- and coarse-grained sandstone with local gravel, are major features of profile CR2. Both **a** and **e** are third-order, broadly concave-up bedding contacts at the bases of the two channels. The relationship of **a** to the right-hand channel, **ae**, is not apparent from the profile, but this major scour surface can be traced across the wave-cut platform in the foreground to the base of a headland about 10 m to the right of CR2. The scour surface is overlain by a sandstone-intraclast boulder and pebble bed (base of unit 3, fig. 15 in part I; see also fig. 16 in part I). If surface **a** in the profile, including its associated sandstone-intraclast boulders, lay close to a channel cutbank margin, the total channel width must have exceeded 60 m.

The fill of **ae**, mainly plane-bedded sandstone, is at least 8 m thick, and the deepest part of the channel, at the right of the profile, about 10 m across. Shallower parts of the channel are filled by plane-bed and low-angle cross-bed sets (**bc** and **cd**; which are laterally equivalent to the upper part of unit 3 in figs. 15 and 16 in part I) in which chute-and-pool backset cross-beds locally overlie **a** (fig. 16 in part I). The first-order discordant erosional bounding surfaces of **bc** and **cd** roll over into the main channel to become concordant with the channel-fill laminae, and ultimately merge with them. **bc** and **cd** are interpreted as broad low-relief bars which developed in shallower parts of the channel, probably during flood-falling stage (but still in upper-regime flow conditions). The bars, growing by lateral and forward accretion, prograded laterally into the adjacent deeper channelised part of **ae**, which probably formed by scour during initial stages of a major flood. Sedimentation in the channel may have been continuously vertically accreting, without the development of bars, in conditions of upper-regime flow.

The size and form of channel **ey**, and the organisation of its sedimentary fill, are similar to those of **ae**. Surface **e** has associated siltstone intraclasts (lithofacies Gs), and defines deeper and shallower parts of a scour channel at least 60 m across with a deep section 11 m across. The shallower part of the channel is filled mainly by single sets of Sl and Sh, some of which flank a larger plane-bed set (**fg**) of minimum thickness 3.4 m. The upper bounding surface of this set, a second-order concordant to discordant erosional surface, separates larger and smaller bedforms. **fg** is thought to represent part of a large plane-bedded simple bar that developed in the channel at high-flood-flow stage, and was partly eroded during a lower stage — perhaps after a fairly rapid decline in flow strength when smaller bedforms grew around (**gh'**, **gh**) and across (**h'i**) it. At least some of these bedforms, probably small bars, also prograded laterally into channel **eq**; bedding contacts and bedforms cannot be readily traced across the central fault-bounded block into the marginal part of channel **eq**, but surface **p**, a possible correlative of **i**, rolls over and merges with bedding in **eq** in a similar manner to surfaces **c** and **d** in channel **ae**. The large bar **eg** probably wedges out on the deep channel margin near the convex-upwards part of surface **f**.

Above the deep channel **eq**, planar tabular sandstone sets 1 m thick or less comprise the bulk of the remaining exposed channel-fill; some sets may extend across the entire width of the channel (e.g., **kl** and a possible correlative in the sequence, **qy**). The planar tabular sets formed and grew in lower-flow-regime conditions following the flood peak. A brief scouring episode is recorded by scour-fill unit **tv**.

This profile represents part of a fluvial-channel-tract sandstone. Simple and complex plane-bedded bars are the main bedforms, developed during consistent upper-regime flows. Flow fluctuations influenced the local development of dunes and simple bars in lower-flow-regime conditions, and, during periods of high or rapidly rising flows, might have promoted the scouring of broad and shallow channel forms that were later filled by migrating bars. Mass flows and hyperconcentrated flood flows may have presaged the larger floods.

Johanna Beach

Profile JB1 (Fig. 12). Profile JB1 is a cliff section 47 m long that trends about 350°, about 20° oblique to the depositional dip direction of 007°, which is away from the camera; 10 m of vertical section is exposed. The apparent structural dip is about 20° to the right.

Two subparallel third- (or higher-) order (**b**) and second-order (**p**) bedding contacts are about 8 m vertically apart. **p** is a low-relief discordant to concordant contact which extends for at least 40 m in outcrop. **b** is a discordant erosional contact, and has a relief of at least 2 m; in places up to 2.5 m of silty mudstone (Fl and Fm) are preserved beneath the contact. The mudstone rests disconformably on another sandstone body (**ab** in profile), but, in the profile as figured, has been eroded and redistributed as lithofacies Gs along the contact.

Contact **b** has been traced 300 m east to the end of Johanna Beach and possibly extends west for about 1.5 km to a headland where it appears above a recessive unit at the base of a cliff. The overlying sandstone here has an estimated thickness of 13 m. The sandstone at Johanna Beach is equivalent to the basal part of this sandstone body.

In profile JB1, most bedding surfaces are concordant to discordant erosional, and are identified as first-order contacts. Lithofacies Sh and Sl are dominant; Ss is locally developed in scours. **bh**, apparently a sandstone sheet or elongate lens, is probably a large plane-bedded bar.

Discontinuous minor surfaces (**f** and **g**) are interpreted as reactivation surfaces. **f** bounds a shallow scour (minor channel) fill. **c** and **d** may also be reactivation surfaces, or the margins of downstream accreting sandy bedforms, probably simple bars.

First-order contacts **h** and **j** have local erosional relief of about 1 m on top of the sandy bedform **bh**. Scour-filling units **be** and **hk** consist of lithofacies Ss. Units **jk**, **kl**, and probably **hm** are plane-bedded bars of various scales. Cross-strata in **jk** may locally approach avalanche steepness. Minor surfaces **n** and **o** are interpreted as reactivation surfaces.

bh and **hp** resemble the plane-bedded simple bars from the Devonian Welsh brownstones, illustrated in summary by Allen (1983, fig. 12b). Like the bars in the brownstones, they have variably scoured lower contacts and numerous reactivation surfaces. However, where plane bedding rolls over into accretionary foresets, these dip at 10° or less.

Plane-bedded bars dominate this profile, which represents the basal part of a channel-tract sandstone. Cross-bedding at bar margins ('foresets') has a low angle, and implies extremes of high-stage flow accompanying deposition. The basal third-order scour surface observed defines a number of scour hollows a few square metres in area but is only weakly channelised. The channel tract is interpreted as broad and shallow, and as having essentially unconfined fluvial flow over a flat or low-slope alluvial plain.

Blanket Bay

Profile BB1 (Fig. 13). Profile BB1 represents two channel-tract sandstone sequences separated by flood-plain and lacustrine deposits. Units 5–9 record the depositional history of the flood plain.

Stacked fining-upward cycles of sandstone to mudstone are dominant in units 5–6. They record the final abandonment of the underlying channel tract (unit 5), and drowning of the abandoned channel by a flood-plain lake (unit 6). The accumulation of lacustrine mud and silt (units 7–8) was interrupted frequently by incursions of fine sand (especially in unit 7). The burrowed and bioturbated unit 7 probably represents deposition in a shallow lake. The upward decrease in rippled intervals in unit 8 may record deepening of the lake; the upper 10 m is ripple-free.

In addition to its increasing grainsize, the overall coarsening-upward unit 9 includes ripple laminae succeeded by a climbing-ripple interval, and reflects increasing energy in the system. Bioturbated beds indicate either or both shallowing of the lake or an increased nutrient supply. The succeeding channel-tract sandstone (unit 10) is thinner than other channel-tract sandstones (at least 70 m thick; Felton 1992) in the Blanket Bay area, and has a palaeocurrent vector mean which differs from that in units 1–4; it may be a large splay or distributary channel.

Browns Creek

Profile BC1 (Fig. 14). The profile was measured at one end of a wave-cut platform 700 m long in which the sheet-like geometry of the bedding was accentuated by preferential carbonate cementation of the thin sandstones present. Most of its units extend laterally for several hundred metres subparallel to the depositional dip.

Laminated siltstone (lithofacies Fl) is the dominant rock type. Wavy lamination and local rippled coarse silt laminae are the only other sedimentary structures. Single ripple sets 1 to 3 cm thick are common. Straight-crested ripples are confined to fine-grained intervals in the lower half of the profile; in the upper half, only sinuous-crested ripples were found. Both ripple types have north-northwesterly palaeocurrent directions similar to the north-northwesterly directions indicated by trough cross-strata.

Units 1–3 represent lacustrine deposition. The rippled thin sandstone bodies at the tops of units 1 and 2 are lenticular, and have gradational bases and tops. The gradational tops consist of sharply fining-upward structureless sandy siltstone 20 cm thick. The sandstone bodies are enclosed by laminated mudstone and siltstone of probably lacustrine origin. They are interpreted as the mouth bar deposits of a small distributary developed during the lowstand of a flood-plain lake.

Unit 3 consists of laminated lacustrine siltstone which coarsens upwards to very fine sandstone with a sharp planar top, which is succeeded by carbonaceous marsh mudstone. The sandstone is a distributary mouth bar deposit similar to those described above, but represents a lake-filling episode culminating in marsh deposits which are partly eroded by a small splay or distributary channel.

Units 4–7 are probably flood-plain deposits. Units 6 and 7 are sheet sandstones which fine upwards through rippled and laminated fine sandstone, siltstone, and mudstone to rare thin carbonaceous mudstone and coal. The basal contacts of these sheet sandstones are sharp, planar to locally concave-upward, and overlie lithofacies Fl and Fm. Because of their extent, they are interpreted as medial to distal-splay and/or sheet-flood sands which spread over essentially flat flood-plain surfaces that were locally scoured. Unit 4 appears to be lenticular; it is not as extensive as units 6 and 7, and may be a distributary channel.

Units 8 and 9 probably represent a return to shallow lacustrine conditions. The composite sand body represented by units 10–11 contains several cosets of small trough cross-beds, and may be a proximal splay or small flood-plain distributary channel.

Skenes Creek Road

Profiles SCR1, SCR2, SCR3 (figs. 11–14 in part I). These profiles are described in part I of this paper. They represent parts of a flood-plain/lake sequence.

AGSO JOURNAL

OF AUSTRALIAN GEOLOGY & GEOPHYSICS

VOLUME 16
1995–97

AUSTRALIAN GEOLOGICAL SURVEY ORGANISATION
CANBERRA

REVIEWERS OF MANUSCRIPTS FOR V0LUME 16

The Editorial Board of the *AGSO Journal of Australian Geology & Geophysics* sincerely thanks the following reviewers for their efforts at maintaining the *Journal*'s standard and in selecting papers for publication.

Bob Abell
Ravi Anand
Chris Ballhaus
A.W.R. Bevan
P.N. Bierwirth
Lance Black
R.S Blewett
Simon Bolster
Bob Bourman
D.M. Boyd
Albert Brakel
Charles Butt
Richard Carver
David Champion
Colin Chartres
X.Y. Chen
Lee Chenoweth
Max Churchward
J. Claoué-Long
Geoffrey Clarke
Jon Clarke
Dave Cohen
J. Creasey
John Dohrenwend
M.B. Duggan
Tony Eggleton
Pauline English
Christopher Fanning
John Foden
Bob Galloway
Andrew Glikson
R.A.F. Grieve
Ken Grimes
Reiner Grun
A.R. Hildebrand
Mark Hinman
Dean Hoatson
Mart Idnurm
Jim Jago
R.W. Johnson
Bernie Joyce
J.R. Leven
J.F. Lindsay
Steve Lucas
L.F. Macias
Doug Mackenzie
Ken McQueen
John Morton
Arne Thorshøj Nielsen
Jon Nott
Cliff Ollier
Brian Oversby
Colin Pain
John Percival
M. Pilkington
Brad Pillans
Patrick Quilty
John Rexilius
John Rigby
Ian Robertson
R.D. Shaw
John Sheraton
E.M. Shoemaker
A.J. Stewart
P.G. Stuart-Smith
Shen-su Sun
S.R. Taylor
A.M. Therriault
David Tilley
Bob Tingey
Jennie Totterdell
Elizabeth Truswell
M.W. Wallace
J. Webb
A.T. Wells
A. Whitaker
Lisa Worrall
G.E.Williams
Bob Young
Jian-xin Zhao

VOLUME 16, NUMBERS 1 & 2, 1995

Thematic issue: The Giles mafic–ultramafic complex and environs, western Musgrave Block, central Australia

VOLUME 16, NUMBER 3, 1996

Thematic issue: Australian Regolith Conference '94

VOLUME 16, NUMBER 4, 1996

Thematic issue: Australian impact structures

Guest associate editor: Andrew Y. Glikson

VOLUME 16, NUMBER 5, 1997

AGSO
AUSTRALIAN GEOLOGICAL SURVEY ORGANISATION

AGSO Journal of Australian Geology & Geophysics

Volume 16, Number 5

CONTENTS